Smart Rocks and Wireless Communication System for Real-time Monitoring and Mitigation of Bridge Scour – a Proof-of-concept Study

Final Report No. RITARS-11-H-MST

Submitted by
G.D. Chen, D. Pommerenke, R. Zheng, A. Radchenko, Y. Tang,
B. Schafer, Y. Huang, and Z.L. Yang

Missouri University of Science and Technology

December 30, 2013

TECHNICAL REPORT DOCUMENTATION PAGE

1. Report No. RITARS-11-H-MST	2. Government Accession No.	3. Recipient's Catalog No.

4. Title and Subtitle Smart Rocks and Wireless Communication System for Real-time Monitoring and Mitigation of Bridge Scour – a Proof-of-concept Study	5. Report Date December 30, 2013
	6. Performing Organization Code Missouri University of Science and Technology
7. Author(s) G.D. Chen, D. Pommerenke, R. Zheng, A. Radchenko, Y. Tang, B. Schafer, Y. Huang, and Z.L. Yang	8. Performing Organization Report No. RITARS-11-H-MST
9. Performing Organization Name and Address Missouri University of Science and Technology 328 Butler-Carlton Hall, 1401 N. Pine Street Rolla, MO 65409-0030	10. Work Unit No.
	11. Contract or Grant No. RITARS-11-H-MST
12. Sponsoring Agency Name and Address U.S. Department of Transportation Research and Innovative Technology Administration (RITA) 1200 New Jersey Avenue, S.E., Room # E33-467 Washington, DC 20590	13. Type of Report and Period Covered Final Report
	14. Sponsoring Agency Code USDOT

15. Supplementary Notes

The investigation was conducted in cooperation with the Missouri Department of Transportation through field test support at two bridges and in-kind match funds.

16. Abstract

This study aims to integrate commercial measurement and communication components into a scour monitoring system with magnets or electronics embedded in smart rocks, and evaluate and improve its performance in laboratory and field conditions for the movement of smart rocks. Properly-designed smart rocks were found to be automatically rolled into the very bottom of a scour hole and can give critical information about the maximum scour depth and effectiveness of rip-rap mitigation strategies. Four types of smart rock technologies were investigated in this proof-of-concept phase of study, including passive with embedded magnets, active with magneto-inductive communication, active with controllable magnet rotation, and active with acoustic communication. Their performances were evaluated against three criteria: 1) movement accuracy within 0.5 m, 2) transmission distance between 5 and 30 m, and 3) at least one measurement every 15 minutes. Test results demonstrated that the proposed smart rocks are cost-effective, viable technologies for bridge scour monitoring.

17. Key Words Smart rocks, wireless communication, scour depth, rip-rap mitigation, magnetic field, magneto-inductive coupling, acoustic communication	18. Distribution Statement No restrictions. This document is available to the public through National Technical Information Center, Springfield, Virginia 22161

19. Security Classification (of this report) Unclassified	20. Security Classification (of this page) Unclassified	21. No. of Pages	22. Price

Form DOT F 1700.7 (06/98)

Final Report

RITARS-11-H-MST

SMART ROCKS AND WIRELESS COMMUNICATION SYSTEM FOR REAL-TIME MONITORING AND MITIGATION OF BRIDGE SCOUR

– a Proof-of-concept Study

U.S. DEPARTMENT OF TRANSPORTATION
RESEARCH AND INNOVATIVE TECHNOLOGY ADMINISTRATION (RITA)

By G.D. Chen, D. Pommerenke, R. Zheng, A. Radchenko, Y. Tang, B. Schafer,
Y. Huang, and Z.L. Yang

Acknowledgments: U.S. Department of Transportation, Research and Innovative Technology Administration - Commercial Remote Sensing and Spatial Information (CRS&SI) Technologies Program, Missouri Department of Transportation, and Federal Highway Administration – J. Sterling Jones Hydraulics Research Laboratory

WASHINGTON D.C.
DATE SUBMITTED: December 30, 2013

EXECUTIVE SUMMARY

Most bridge collapses in the U.S. are due to scour effects. Scour is an erosion process in which water flow in a river gradually carries away river-bed deposits and creates a scour hole around a bridge pier or abutment, resulting in bridge instability in hours or days. To prevent scour, protect properties and save lives during a severe flood event, the bridge scour process must be monitored, assessed, and responded in real time. Due to erosion and refilling of river-bed deposits, existing scour monitoring technologies face a challenge in locating and measuring the maximum depth of local scour even if they can survive the harsh environment.

In this study, the concept of smart rocks is introduced and demonstrated to be cost effective for real time scour monitoring in bridge applications. Smart rocks are either natural rocks or concrete encasements with embedded magnets or electronics. Properly-designed smart rocks roll to the deepest point of a scour hole when deployed in top river-bed deposits around a bridge foundation and can thus function as field agents to collect the maximum scour depth as scour develops. During a severe flood event, the critical scour data can be transmitted to the engineer-in-charge or decision makers through wireless communication with the electronics in smart rocks or remote measurement of the magnetic field strength of the magnets in smart rocks. In addition to the maximum scour depth, smart rocks can be used to evaluate in real time the effectiveness of a rip-rap scour countermeasure since rock movement is an indicator of its incipient failure.

Three smart rock technologies are proposed and tested for their feasibility in field implementation: passive, active, and semi-active. Passive smart rocks with one embedded magnet each provide the magnetic field intensity of the magnet group by a remote magnetometer. Active smart rocks with embedded electronics (e.g. pressure sensor, gyroscope, 3-axis accelerometer, timer, rock identifier, and battery level indicator) can be assigned with individual identification (ID) and potentially networked to provide spatial information on the evolvement of a scour hole. Active smart rocks can be linked among themselves and to a base station with either magneto-inductive or acoustic wireless communication. The relative strength of received signals with magneto-inductive communication and the time difference of arrived signals with acoustic communication are investigated. A semi-active smart rock includes one embedded magnet, a magnet flipping mechanism, and necessary electronics such as ID and battery. It also provides the magnetic field intensity of the magnet as it is being flipped but combines the advantages of simplicity in passive smart rocks and the individualism in active smart rocks.

To date, concrete encasements were designed based on the density requirement to ensure they can remain at the bottom of river without being washed away in strong water current. The ad-hoc design for smart rocks was proven effective during the August 7, 2013, flood event with a return period of over 100 years in Rolla, MO. The so-designed smart rocks were demonstrated to consistently roll to the deepest area of scour with multiple laboratory tests. However, the size and density of concrete encasements have not been optimized based on the bridge and river geometries, hydraulic environments, and riverbed profile and materials.

Passive Smart Rocks: The combined magnetic field intensity of a permanent magnet and the Earth was formulated for general cases. Two smart rock localization algorithms were proposed with known and unknown magnet orientations. Various intensity-distance curves and the localization algorithms were validated with field tests. Critical to the localization of smart rocks by triangulation, the intensity-distance relation of a passive smart rock with an embedded magnet was significantly affected by the polarization of the magnet. This influence can be effectively removed from a unique mechanism design that makes the magnet always oriented with the North Pole of the Earth magnetic field.

One smart rock was deployed at the US63 Gasconade River Bridge on September 24, 2012, and another at the I-44 Roubidoux Creek Bridge on October 3, 2012. The smart rock at the US63 Bridge was retrieved on October 4, 2013, after the August 7, 2013, flood event. The smart rock appeared to move downstream for approximately 1 m and stopped in a scour hole near the bridge foundation. It was in a good condition and remained effective for magnetic field intensity measurement. Although in general agreement with the calibration results, the intensity-distance curves measured around the I-44 Roubidoux Creek Bridge as the smart rock was manually dragged underwater locally fluctuated due to the uneven riverbed or varying magnet orientation. The measured intensities were consistent at the two bridge sites and over time at each bridge.

A measurement distance of over 50 m has been demonstrated in field condition based on the resolution of the used magnetometer (G858 Model). To achieve a rock localization accuracy of less than 0.5 m, the measurement distance can range from 21 to 42 m depending upon measurement accuracy and environmental influence. In multiple laboratory tests, 2 cm accuracy has been repeatedly achieved for a scour depth measurement of 18 cm with a small-scale pier model. It is practically impossible to separate the effects of individual magnets in a group.

The magnetometer can be set up for field measurement in less than 10 minutes. Each of the smart rocks deployed at bridge sites costs approximately $300. Passive smart rocks with Earth magnetic field oriented magnets are ready for implementation studies.

Active Smart Rocks with Magneto-inductive Communication: Active smart rocks with embedded electro-mechanical modules for magneto-inductive communication with a base station and among the smart rocks were developed as a rock positioning system. The battery-powered electronics received command from the base station, sensed the movement of rocks, and transmitted information back to the station. To save power, smart rocks were set in sleep mode until they received a wakeup signal from the base station. One localization algorithm was developed.

The electro-mechanical modules in active smart rocks were demonstrated to be waterproofed with no leakage even during the August 7, 2013, flood event. They successfully provided battery-powered magneto-inductive communication, whenever needed, for individual rocks and transmitted sensor data with low power. A measurement distance of over 20 m in field condition was tested. A distance and localization error of less than 0.5 m can be achieved based on numerical simulations.

Each active smart rock costs approximately $600. Additional cost for electronic components at the base station may be $800-$1,000. Overall, a network of around 10 active smart rocks is recommended as a comprehensive solution for bridge scour monitoring in real time, which gives water depth and tilt/head/rock data at the location of individual rocks in addition to the maximum scour depth. They will be ready for implementation studies after the electro-mechanical modules and localization algorithm have been further validated in field conditions.

Active Smart Rocks with Acoustic Communication: An underwater acoustic localization system was designed and tested both in laboratory and field conditions, including GPS receivers for timing synchronization, analog and digital converters for data reception and transmission, a digital signal processor, and the time-difference-of-arrival algorithm for transmitter localization.

The transmitter in smart rocks and receiver (hydrophones) modules were demonstrated to be robust and functional based on laboratory and field tests. The underwater acoustic localization system achieved a localization accuracy of 0.3 m over a measurement distance of up to 90 m. The cost for one transmitter and one receiver (hydrophone) is approximately $900 due to non-recurring engineering cost on the acoustic transducers.

The potential effect of concrete encasement on the acoustic wave propagation and the effectiveness of multiple transmitters for rock localization require further studies. As such, the acoustic communication system is recommended for implementation study after extensive packaging and system integration tests have been completed.

Semi-active Smart Rocks: Semi-active smart rocks with a free-to-rotate magnet were designed and tested for their dynamic range of measurement, localization accuracy, data repeatability, and differentiability between the effects of magnet and other ferromagnetic substances. The magnet rotation can be controlled with an electronic circuitry, resulting in a controllable pattern (e.g. periodic) of magnetic field intensity over time.

The performance of a magnet flipping mechanism is consistent and repeatable over time. The dynamic range of measurement of a semi-active smart rock can be five times as large as that of a passive smart rock. The periodic measurement allows additional verifications on the quality of obtained data. The time-varying magnetic field intensity taken from a semi-active smart rock is significantly different from the time-invariant intensity taken from a passive smart rock. This difference allows the separation of magnet effect from the effect of other ferromagnetic substances in practical application, further reducing the rock localization error.

The material cost for one semi-active smart rock is approximately $400. Overall, a few semi-active smart rocks with flipping magnets are recommended as the most reliable solution for bridge scour monitoring in real time. They will be ready for implementation studies after further performance characterization tests in laboratory and field conditions.

ACKNOWLEDGMENTS

Financial support for this study was provided in part by the U.S. Department of Transportation, Research and Innovative Technology Administration - Commercial Remote Sensing and Spatial Information (CRS&SI) Technologies Program, by the Missouri Department of Transportation through in-kind match funds, and by the Missouri University of Science and Technology through both in-kind and cash match funds. Thanks are also due to the Missouri Department of Transportation for their assistance provided during field tests with Ms. Jennifer Harper as coordinator and due to Federal Highway Administration – Turner-Fairbank Highway Research Center for their laboratory test assistance in J. Sterling Jones Hydraulics Research Laboratory with Drs. Kornel Kerenyi and Jerry Shen as coordinators. Deep appreciations are extended to assistant professor Dr. Zhibin Lin from North Dakota State University, retired research civil engineer David Hoffman, senior specialist Jason Cox, laboratory technician John Bullock, and many other graduate students (David Allen, Yi Bao, Alex Cains, Yizheng Chen, Bing Han, Pratik Maheshwari, Viswa Pilla, Hongya Qu, Satyajeet Shinde, and Richard Spengemann) for their contributions in various facets throughout the project. The views, opinions, findings, and conclusions reflected in this report are the responsibility of the authors only. They do not represent the official policy or position of the U.S. Department of Transportation Research and Innovative Technology Administration or any State or other entity.

TABLE OF CONTENTS

LIST OF FIGURES

LIST OF TABLES

1 INTRODUCTION

1.1 Background

Bridge piers and abutment corners in a river break the path of water flow, causing unsteady horseshoe vortices around them. The shedding of vortices drastically changes local hydraulics, creates both lifting and shear forces, and carries away deposits in the river bed. This process is referred to as local scour at bridge piers or abutments.

The 1993 flood in Midwest destroyed or severely damaged over 2500 bridges due to scour (Mueller and Wagner 2002). More recently, the center pier of a continuous steel-girder bridge over the Thompson River in north Missouri was washed away, as shown in Figure 1.1, due to the heavy rainfall on September 22, 2010. In the United States, scour and other hydraulic effects are responsible for 58% of over 1,500 bridge collapses in the past 40 years (Briaud and Hunt 2006), as indicated in Figure 1.2. They are also a growing problem (Lagasse et al. 1997, Hunt 2005a). As shown in Figure 1.3, the number of scour critical bridges (when their foundations have been determined to be unstable for the calculated or observed scour condition) increased from 2% by 1997 to 5% by 2005. Similarly, the number of scour susceptible bridges over water increased from 29% to 40% over a period of eight years.

Figure 1.1 Loss of a Center Pier of the Thompson River Bridge, Missouri

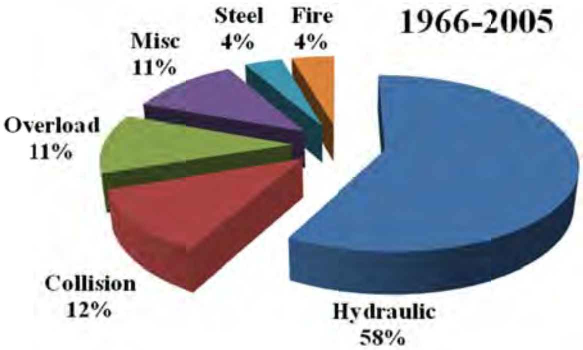

Figure 1.2 Scour-Induced Bridge Collapse Statistics

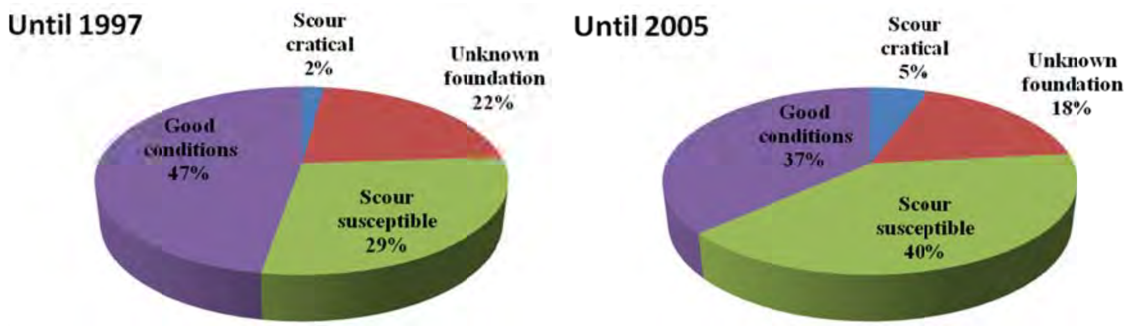

Figure 1.3 Growing Problems with Bridge Scour

The current diving practice in bridge maintenance for bridge scour inspection depends on visual check by inspectors every five years unless a problem is detected. This practice is both uneconomical when a bridge is in good condition and risky missing occurrence of bridge scour in between two inspections. Under strong current, it is also dangerous to have a special inspection of bridge scour condition visually, resulting in few or no field data available in real time. Furthermore, visual inspections are qualitative and subjective, particularly in muddy water during a flood event when riverbed profiles are not visible to the inspectors. Therefore, the primitive visual inspection technique with divers has a poor degree of accuracy (Fukui and Otuka, 2002). In addition, divers must have relevant experience to quantify the degree of scour (Forde et al.1999).

Due to lack of real time field data, most design guidelines and computer programs developed by Federal Highway Administration (Melville et al. 1989, Mueller and Landers 1999, Lagasse et al. 1997, 2001, Hunt 2005b), various state Departments of Transportation (Ettema 2006), and international communities (Ministry of Works and Development 1979) have not been validated for their performance during a scour process. Of empirical nature, most of the existing scour design regulations and computer programs do not accurately predict the degree of scour in some regions of our nation (Mueller and Wagner 2002, Richardson and Davis 2001) since they were derived for specific river, water flow, and structural conditions (Ali et al. 2002, Salaheldin et al. 2004). Specifically, they largely depend on the limited field data prior to and after a scour event. More importantly, almost all the existing technologies are not applicable to assessing the condition of bridge scour in real time because the continuous changes of the river and flow conditions required for the prediction of the maximum scour depth (Ali et al. 2002, Salaheldin et al. 2004) are not available during a flood event.

In addition to the above technical reasons, real time monitoring and assessment of bridge scour is not only critical to maintain ground transportation services, but also to ensure the transportation safety in hours or days during high flood seasons (NTSB 1998). On April 5, 1987, scour developed around the piers of the Schoharie Creek Bridge in New York, caused a catastrophic bridge collapse, and resulted in 10 fatalities (Boorstin 1987, NTSB 1998, Lagasse 2001). Therefore, real-time scour monitoring at bridge sites is crucial for a more accurate prediction of scour process, a more comprehensive calibration of bridge design equations, a more prompt alert of scour-induced foundation stability, and a safer operation of bridges during a severe flood.

1.2 Objectives and Expected Performance

The long-term goal of this study is to develop a pragmatic but highly innovative, real-time bridge scour management system with remote sensing and wireless communication technologies for integrated monitoring and mitigation of foundation scour. The specific objectives of this study are (1) to integrate several alternative commercial measurement and communication technologies into a scour monitoring system with passive and active sensors embedded in smart rocks or concrete encasements, (2) evaluate the comparative effectiveness of these communication technologies in laboratory and field conditions and improve them for better performances and/or reduced costs in bridge applications, and (3) analyze the movement of smart rocks during testing for the determination of scour depth and/or for the evaluation of rip-rap scour countermeasure effectiveness.

Smart rocks are smart in two senses. One is that properly-designed smart rocks can automatically be rolled into the very bottom of a scour hole. The other is that smart rocks can give critical information about the maximum scour depth and effectiveness of rip-rap mitigation strategies.

At the beginning of this project, the research team met with an advisory committee composed of end users, researchers, and vendors. The performance criteria for this proof-of-concept phase of study include:

a) Horizontal and vertical movement accurate to within 0.5 m,
b) Transmission distance between 5 and 30 m, and
c) At least one measurement every 15 minutes.

1.3 Application Scenarios and Overall Monitoring Strategies

1.3.1 Application Scenarios

Scour is responsible for most of the U.S. bridges that collapsed during the past 40 years. The maximum scour depth is the most critical parameter in bridge design and maintenance. This study is focused on two application scenarios for real time bridge scour monitoring: (1) determining the maximum scour depth around a bridge pier, and (2) monitoring a rip-rap scour countermeasure with rocks. They are schematically illustrated in Figures 1.4 and 1.5.

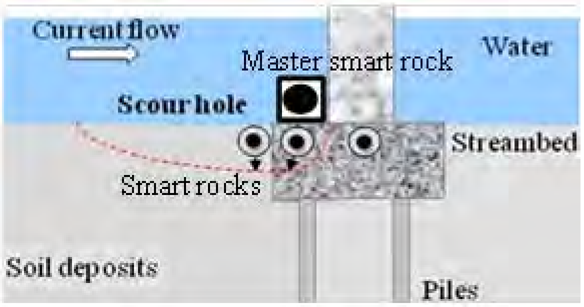

Figure 1.4 Maximum Scour Depth Monitoring

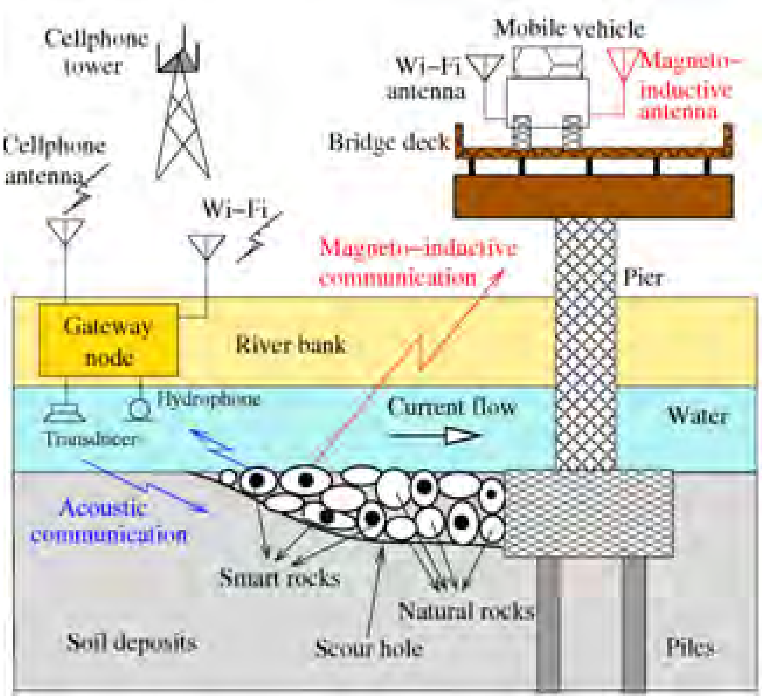

Figure 1.5 Scour Countermeasure Monitoring

As shown in Figure 1.4, Scenario 1 involves several smart rocks deployed against the side faces and around the perimeter of a footing or foundation cap of an existing (or new) pier. As it is undermined during a flood event, a properly-designed smart rock as large as natural rocks near the foundation falls and always stays at the bottom of a developing scour hole so that the maximum scour depth can be monitored and determined. If deemed necessary, a group of smart rocks can be designed to cover the range of natural rocks in size and weight. To facilitate the monitoring of smart rock positions, a master (heavy, square, and tied to the pier as needed) smart rock may be placed on top of the footing or foundation cap to serve as a reference point, collect data from nearby small smart rocks, and transmit data to a remote station. As a scour hole is developed during a flood event, smart rocks will roll into the very bottom of the hole. The change in spatial distribution of smart rocks resembles the formation process of the scour hole.

As shown in Figure 1.5, Scenario 2 involves smart rocks and natural rocks placed in an existing scour hole around a pier so that the effectiveness of the scour countermeasure can be evaluated over time. As it moves, a smart rock or a group of smart rocks changes its position; the change in spatial position of a smart rock or the change in distribution pattern of a smart rock group indicates the effectiveness of a rip-rap scour countermeasure.

Note that Figure 1.5 shows two wireless communication schemes: magneto-inductive and acoustic. Magneto-inductive communication can be established directly between active smart rocks and a mobile station parked on bridge decks or river banks. Acoustic communication can be established between active smart rocks and a gateway node in water near river banks. The acoustic signals received at the gateway node can then be transmitted through a Wi-Fi to a mobile station on bridge decks or through cellphone antenna and tower to an end user in the engineer-in-charge office.

1.3.2 Overall Monitoring Strategies

Due to erosion and refilling of river-bed deposits, strong current, and a variety of debris, existing technologies such as magnetic sliding collars, sonar systems, remotely controlled boats, buried probes, fathometers and optical sensors face a challenge in measuring the maximum scour depth during a strong flood. Therefore, real time scour monitoring is not only a technical issue but also a deployment problem.

In this study, sensors and wireless communication technologies are embedded into rocks that are deployed around a bridge pier and become an integral part of scour process (Chen et al. 2012, Radchenko et al. 2013). In doing so, the smart rocks with embedded sensors are sufficiently rugged to survive a harsh environment and can be integrated into a scour mitigation strategy with rip-rap countermeasure. Therefore, a smart rock system is the new strategy proposed in this study to tackle the grand challenge of scour monitoring in real time.

Specifically, permanent magnets can be embedded into rocks or concrete encasements. These passive smart rocks are deployed around the foundation of a bridge as field agents. Magnetic field changes of the smart rocks can be measured at distance from a magnetometer. With more than three remote measurements, passive sensors (magnets) allow the triangulation from the remote measurement stations to determine the location of smart rocks.

Electronics can be embedded into rocks or concrete encasements to form active smart rocks. With wireless communications, active sensors can send their position change information to a nearby mobile station. The active sensors can be various devices for different measurement parameters as needed, such as 3-axis accelerometers, 3-axis magnetometers, and pressure transducers. In addition, each sensor includes an ID, a timer, and a battery level indicator. A smart rock system enables the monitoring of the most critical scour condition and time by logging and analyzing sliding, rolling, tilting, and heading of the spatially distributed sensors.

1.4 Report Organization

A proof-of-concept study on the innovative concept of smart rocks and wireless communication for real time bridge scour monitoring is presented in this report. Included are four types of smart rocks with: a) passive sensors with permanent magnets, b) active sensors with flapping permanent magnets controlled by an electric circuit, c) active sensors with magneto-inductive communication, and d) active sensors with acoustic communication. In general, detailed discussion of the technology, design, fabrication, and validation of each type of smart rocks are described.

This report includes seven sections. Section 1 states the background, objectives and expected performance, application scenarios and overall strategies, and the report organization. Section 2 gives a comprehensive literature review on various technologies for scour monitoring. Section 3 introduces the definition, theory, localization algorithm, laboratory characterization, and field validation of passive smart rocks. Section 4 introduces the definition, design, theory, localization algorithm, laboratory characterization, and field validation of active smart rocks with magneto-inductive communication. Section 5 introduces the definition, design, and laboratory demonstration of active smart rocks with flapping permanent magnets. Section 6 introduces the definition, design, laboratory demonstration, and field validation of active smart rocks with acoustic communication. Section 7 summaries the main findings from this proof-of-concept study and the readiness of various smart rock technologies for field implementation.

2 LITERATURE REVIEW ON SCOUR MONITORING TECHNOLOGIES

2.1 General Overview

Over the past half century, the United States Geological Survey (USGS) along with the Federal Highway Administration (FHWA) and state Departments of Transportation (DOTs) in the U.S. have made significant efforts into the study of bridge scour at bridge sites. In 1987, the FHWA funded the USGS to initiate the National Bridge Scour Program. After many years of studies, the USGS published a national bridge scour report (Landers and Mueller 1996), which aimed to guide the practice of engineers. From the report released by the USGS, countermeasures to mitigate bridge scour usually involve physical protection, such as riprap, and/or monitoring. In case physical countermeasures are cost prohibitive, monitoring can be used to ensure that bridge foundations are stable. Monitoring can detect the evolvement of bridge scour around piers and abutments that are either always under river or flooded in heavy raining seasons, and provide warning prior to a sudden failure, thus protecting the lives of bridge users and preventing bridge collapse if promptly mitigated.

Over the past few decades, measurement and monitoring instrumentation has been developed for bridge scour (Nassif et al. 2002). FHWA's HEC-18 by Richardson and Davis (2001) first recommended the use of fixed instrumentation and sonic fathometers (depth finders) as scour monitoring countermeasures. The NCHRP Project 21-3 by Lagasse et al. (2009), *Instrumentation for Measuring Scour at Bridge Piers and Abutments*, developed, tested, and evaluated fixed scour monitoring methods both in laboratory and field. The NCHRP Synthesis 396 by Hunt (2009), *Monitoring Scour Critical Bridges,* assessed the state of knowledge and practice for fixed scour monitoring of scour critical bridges. In addition, the technical literature documented a number of scour detection and monitoring methods that have been developed over the past two decades.

Due to the criticality of bridge scour, over 15 monitoring methods have been developed by 2005 to improve the effectiveness of bridge scour inspection though there were no accepted methods or off-the-shelf equipment for collecting scour data prior to the early 1990s (Mueller and Wagner 2002). Scour monitoring methods can be classified into three groups: portable instruments, fixed instruments, and others (Lagasse et al. 1997). Their advantages and disadvantages can be found from Schall and Price (2004) and Ettema et al. (2006). Some of the main technologies are compared in Table 2.1 in terms of cost, measurement accuracy, durability, ease in installation, and applicability in various environments. Many of the existing technologies cannot provide the mission critical data – maximum scour depth due to unknown scour locations and refilled scour holes. In addition, almost all the existing technologies are applicable only in normal operations of bridges. During a flood event, the existing instrumentations are difficult to survive the harsh environment (debris/ice/muddy water/current) and thus face a challenge in providing the maximum scour depth in real time, which is critical for a timely warning, response, and prevention of scour-induced collapsing of bridges. The developed smart rock technology in this study expects to be superior to existing methods in most aspects as indicated in Table 2.1. Up to 10 smart rocks were considered in cost estimation.

Table 2.1 Performance Comparison among various Monitoring Technologies

Method	**Cost (×$1,000)**	**Acurancy**	**Durability**	**Ease in installation**	**Applicability**		
					Current	**Debris/ice**	**Mitigation**
Diver	0.5-1	Poor	NA	Good	NA	NA	NA
Probing rods	2	Fair	Poor	Fair	NA	NA	NA
Ground penetrating radar	3-10	Good	Fair	Poor	NA	NA	NA
Boats	0.5-1	Fair	NA	Poor	NA	NA	NA
Sonar	5-15	Good	Fair	Good	Good	NA	NA
Float-out	3	Fair	Poor	Fair	Poor	NA	NA
Magnetic collars	5-10	Good	Good	Good	Good	NA	NA
Optical sensors	5-10	Good	Fair	Fair	Good	NA	NA
Global positioning	5-20	Good	NA	Good	Good	Good	NA
Smart rocks	**0.3-9**	**Good**	**Good**	**Good**	**Good**	**Good**	**Good**

More recently, Lagasse et al. (2009) also classified various monitoring techniques into portable and fixed instrumentations. Portable instrumentation such as diving, sounding rod, radio controlled boat, reflection seismic profile, and ground penetrating radar, involves a manual operation of measuring stream bed elevations at bridge foundations. The portable devices can be used to monitor the entire bridge or transported from one bridge to another so that they are cost effective tools to address the scour monitoring needs in a bridge network. However, the portable devices cannot offer a continuous detection on the scour condition of bridge foundations. On the other hand, fixed instrumentations involves monitoring devices which are attached to bridge structures to detect scour at a particular location when frequent measurements or real-time monitoring are desirable.

Therefore, there are many options available for bridge scour monitoring. The selection of a most effective and appropriate monitoring method itself could be a challenge for practical engineers. Ideally, appropriate instrumentation should be selected based on site conditions, operational limitations of specific instrumentation and engineering judgment, the advantages and disadvantages of different technologies (Lagasse et al. 2009). To facilitate the selection of monitoring technologies, Lueker et al. (2010) developed a scour monitoring framework for instrumentation selection given site-specific bridge and stream conditions. The framework is a Visual Basic for Applications (VBA) enable excel workbook that requires the input for site specific information of one bridge at a time, such as the details of bridge, stream, and scour; it compares the application attributes with critical characteristics of fixed scour monitoring equipment. The final output is a list of instrument ranking in the framework and an overview of how various characteristics of this application affect the ranking score for each instrument.

Although various scour monitoring techniques have been developed, by 2005 only approximately 100 out of 25,000 over-water bridges in the U.S. were instrumented due to their limitations and associated costs, among which 90% were equipped by fixed instruments. The sonar scour system was the most popular device used at 51 bridge sites, followed by magnetic sliding collar at 23 sites and float-out device at 13 sites (Briaud and Hunt 2006). To date, little or no real time scour data exists from historic flood events.

2.2 Example Monitoring Technologies

Radar, particularly Ground Penetrating Radar as a geophysical technique, has been successfully applied to identify and determine the depth of scour (Gorin and Haeni 1989, Horne 1993, Millard et al. 1998, Forde et al. 1999, Webb et al. 2000, Lagasse et al. 2009, Schall and Price 2004, Park et al. 2004, Anderson et al. 2007). The measurement of scour depth through radar is based on the wave propagation and reflection at river bed. As shown in Figure 2.1, a diverging pulse of electromagnetic radiation from the transmitting antenna (Tx) propagates through water and experiences multiple reflections/transmissions at the bottom of the river when it encounters interfaces with different dielectric constants (e.g. sediment and river bed). The reflections propagate back to the water surface where the receiving antenna (Rx) is located. The variations recorded in the received radar signal represent the change in river bed profile.

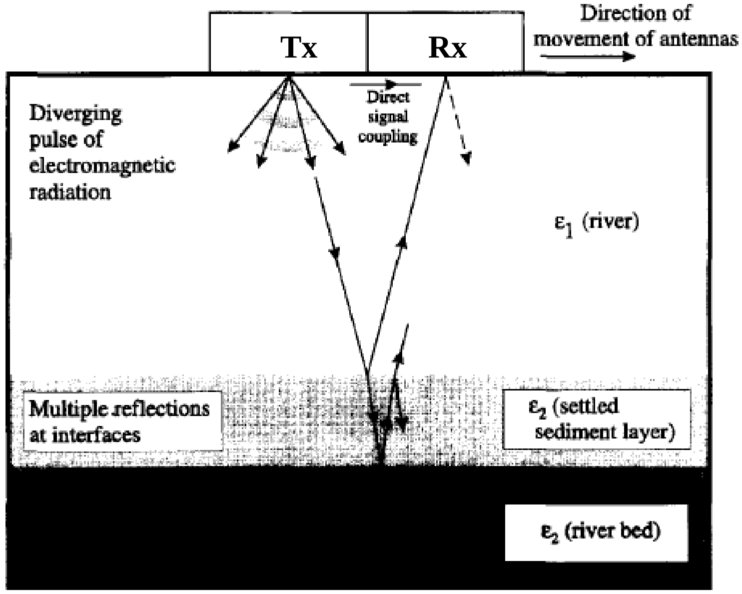

Figure 2.1 Transmission and Reflection of Radar Signal

Following the same principle as radar, a sonar device transmits a wave toward an object to measure the time and amplitude of the reflected wave or echo. In other words, the sonar technology is based on the round trip travel time of an acoustic pulse from a sensor to the riverbed (Mason and Shepard 1994, Hayes and Drummond 1995). Sonar instruments measure scour depth through a supersonic sensor mounted on the edge of a sounding rod extending from a bridge deck or an inspection scaffold on a bridge inspection vehicle (Okoshi and Fukui 2001). Sonar has been developed and used to characterize the sea bed by extracting the sediment type and properties from echo signals (Lu and Cai 2010). Alternatively, sonar as a non-optical underwater imaging technology has demonstrated the most potential application in scour monitoring (Browne 2010). Underwater acoustic imaging can provide photo quality visual images of submerged elements for structural inspection documentation and channel texture information for scour monitoring during a flood event in an easy, fast and safe approach.

Though both radar and sonar were successfully used to detect the profile of bridge scour and convenient to apply in the field. However, the monitoring results are sensitive to noise and are difficult to interpret especially when the water contains high concentration sediments, debris or rocks in a flooded river. Therefore, radar and sonar are usually good for applications after flooding and they cannot detect the maximum scour depth that is achieved during a flood at a peak discharge (Xiong 2012).

Magnetic sliding collar (MSC) is another effective device used for the detection of scour. This instrument consists of a collar wrapped around a rod with a series of magnetically activated switches at predetermined locations along the length of the rod. The rod is driven into the streambed and the collar is embedded into the streambed (Lagasse et al. 1997, Schall et al. 1997a, 1997b). The scour depth is determined by the movement of the collar, which slides down the magnetic rod as the deposits around the foundation is eroded away.

Lu et al. (2008) used an MSC and a steel rod to monitor the total bridge scour during floods. The lower tip of the steel rod was initially placed slightly below the riverbed in the main channel. When scour occurred, the steel rod would sink as the surface of the riverbed was lowered. The scour depth is determined based on the total lowering distance of the steel rod with respect to its initial position. One of the major disadvantages of this instrumentation is that it cannot detect the refilling process of the scour.

Tiltmeters are also simple devices for scour measurement. A tiltmeter basically detects scour-related settlements of pier or abutment foundations (Avila et al. 1999, Zarafshan 2011). However, it can be a challenge to differentiate the movement by scour and other factors such as traffic, thermal, wind and ambient perturbations.

A float-out device has a radio transmitter buried in the riverbed at particular locations (a certain depth) near bridge foundations or abutments. As scour develops and reaches that depth, the device floats up to the water surface and transmits a signal that can be detected by a receiver at a remote station such as bridge deck (Lagasse et al. 2009). Float-out devices are inexpensive, but only measure the particular depth where each is buried. Furthermore, such a device requires replacement once activated and washed away in the river.

Sounding rods are manual or mechanical (automated) gravity-based physical probes (Butch 1996, Lagasse et al. 2009, Hunt 2009). A gravity-based probe drops with the changes to the streambed depth. As a result of self-weight, the probe may penetrate in granular soils. To prevent self-penetration and vibration of the rod from flowing water, the foot of the rod must be sufficiently large.

Fukui and Otuka (2002) developed a Radio-Controlled Boat (RC Boat) to detect bridge scour. As shown in Figure 2.2, a RC Boat system consists of a digital fathometer for the measurement of scour depth, a telemeter transmitter of the measured data, a telemeter receiver of the measured data, a total station installed at the river bank to locate the boat, and a personal computer. The received data from the receiver and the location data from the total station are automatically transmitted into the computer for processing and evaluation of the scour depth at the streambed. The radio controlled boat can provide a precise streambed condition around bridge piers, but cannot be used during a flood event when debris or ice floats on water.

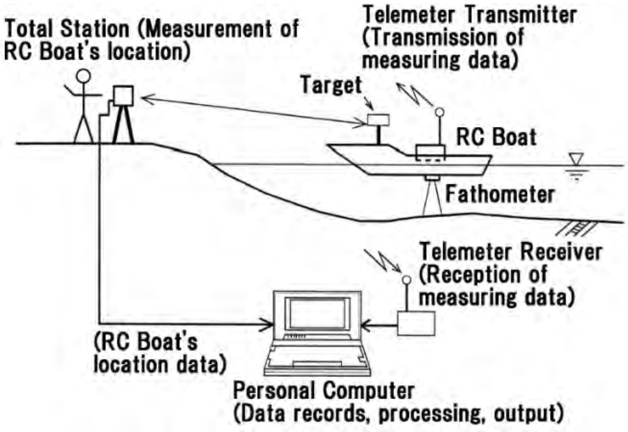

Figure 2.2 Outline of a RC Boat Monitoring System

In recent years, time domain reflectometry (TDR) has been developed and used for real-time monitoring of bridge scour. It operates by sending an electromagnetic pulse through a transmission line with a fixed velocity. The pulse propagates down the transmission line until the end of the line or some intermediate discontinuity (air/water interface and water/sediment interface), where part of the pulse is reflected back to the source. By measuring the returning time of the sent pulse, the physical distance between the line end or the discontinuity and the TDR source can be calculated. In 1994, Dowing and Pierce (1994) adopted a vertically buried TDR sensor in the sediments adjacent to a structural element. When scour occurred, a portion of the TDR sensor was exposed, broken off, and shortened by the stream flow, which can be detected and measured. However, the TDR sensor will be ruined and must be replaced after each scour event. Yankielun and Zabilansky (1999) first introduced a TDR probe to identify the sediment/water interface for scour monitoring. The TDR sensor made of steel pipe and can be permanently installed under the river bed. Field evaluation at several locations indicated that the sensor was sufficiently rugged. Even so, the intrinsic design of the probe made it difficult to install in the field condition. The acquired signals can be difficult to interpret and the application was limited to a relatively short sensing range. Attempts were made to develop a robust algorithm for scour measurements and systematically interpret TDR signals by understanding the electromagnetic wave phenomena and TDR system characteristics (Yu and Zabilansky 2006). The automatic scour monitoring system was demonstrated in laboratory experiments; the robust algorithm can accurately evaluate the thickness of sedimentation. Yu and Yu (2007) developed a theoretical framework for an automatic scour monitoring system using the TDR principle and analyzing the TDR signals to determine scour condition and sediment status. In addition, it is indicated that TDR could accurately measure the scour depth, the density of sediment materials and the electrical conductivity of river water. The robust algorithm for TDR signals was further described, assessed and evaluated by Yu and Yu (2009, 2011a, 2011b) and compared with the ultrasonic method to illustrate the advantages of the new TDR in Yu and Yu (2010). A new TDR sensor was designed with a coated metallic to increase the sensing depth and the level of protection by Yu et al. (2013). Tao et al. (2013) designed an innovative TDR scour sensor for field applications and the robust algorithm was used to retrieve scour information from TDR signals.

Fiber Bragg grating (FBG) sensors have also been applied for scour monitoring in recent years. They have many advantages such as long-term stability and reliability, resistance to environmental corrosion, high resolution, serial multiplexing capability, small size, geometrical and structural compatibility, immunity to electrical and electromagnetic noise, and low cost (Joan et al. 2003). The transduction mechanism of FBG sensors is based on the change in light wavelength under loading induced in scour process (Measures 2001, Li et al. 2004, Ansari 2007). Lin et al. (2004) proposed, developed, and tested a real time sensory system using FBG sensors to detect the bridge scour through laboratory experiments. The sensor was basically a rod instrumented with a number of FBG sensors at predetermined locations and embedded in the river sediment. The scour detection principle was based on the fact that individual sensors are subjected to increasing strains when exposed to the river flow as a result of scour.

Lin et al. (2005) designed two systems for local scour monitoring as shown in Figures 2.3a and 2.3b. In the first design, three FBG sensors were mounted on the surface of a cantilevered beam and arranged in series along one single fiber. In the second design, several FBG sensors were arranged along one single optical fiber, but mounted on cantilevered plates installed at different levels of a hollow steel pile attached to a pier or abutment. The beam or plates were bent in the scour process and the induced strains were measured by the FBG sensors as running water flows around the cantilevered beam or plates. The scour depth can be detected by knowing the strain information indicated from the explosion condition of the FBG sensors which were buried under the sediment or river bed (Lin et al. 2005). This FBG-based scour sensor was subsequently installed at the Dadu bridge site in Taiwan for scour monitoring during floods. The FBG monitoring system appeared robust and reliable for real-time scour depth measurements (Lin et al. 2006). Huang et al. (2007) developed a new type of optical FBG-based scour monitoring sensors which excluded the influences of soil pressure and static water pressure varying with the depth. In addition, FBG sensors were embedded in a fiber reinforced polymer beam to improve the accuracy and durability of measurement (Zhou et al. 2011). Three designs of the scour monitoring system using FBG sensors were introduced, described, discussed, compared and demonstrated in laboratory by Xiong et al. (2012). Such a system may potentially be applied to measure the water level, maximum scour depth, scour process, and deposition height due to refilling process (Xiong et al. 2012).

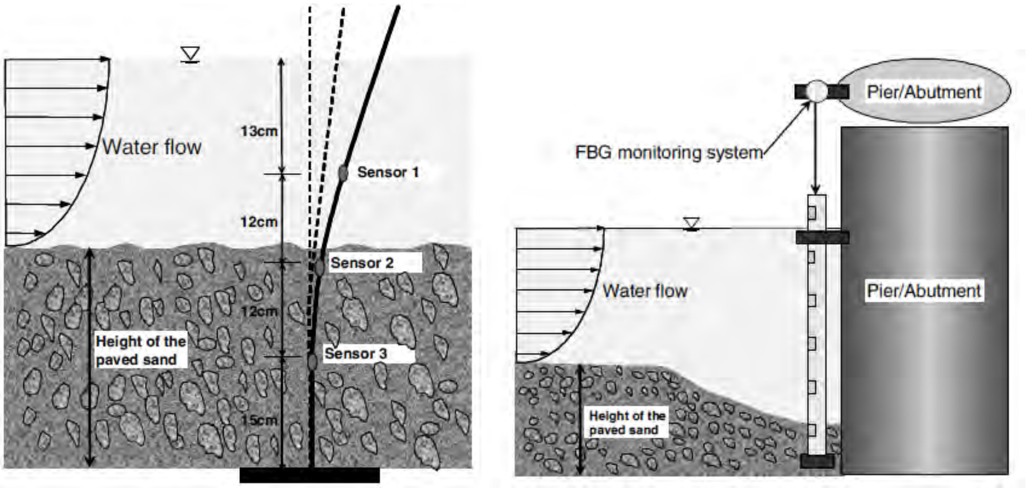

(a) Model 1 (b) Model II

Figure 2.3 Schematic of FBG Monitoring System for Bridge Scour

A single FBG sensor can be applied to measure the change in vibration frequency of a rod inserted into the scour depth in the river bed and then relate the fundamental frequency of vibration to the scour effect (Zarafshan et al. 2011). Attempt was also made to use an array of FBG sensors for temperature measurement and then relate the temperature data to scour depth around bridge structures under routine and flood conditions (Cigada et al. 2008, Manzoni et al. 2010). In this case, the operational mechanism is that optical fibers are heated by an electrical circuit because of Joule effect at the sediment/water interface due to different thermal behaviors. For example, the temperatures of sensors buried inside the river bed often exceeds those of sensors directly exposed to flowing water, thus indicating the presence of the river bed level when observed. In addition, a remote scour monitoring system including polymer fiber optic sensors (PFOSs) and MicroElectroMechnaical System (MEMS) such as switches, phototransistor, LED, amplifier, detector, and multiplexing system (Isley et al. 2007) was designed and fabricated for scour monitoring and detection at bridge piers and abutments. Since the response of sensors was greatly affected by the reflection property of different mediums, the scour depth was detected by identifying the change of various media.

More recently, Lin et al. (2010) used distributed MEMS sensors for pressure measurement. The piezoelectric films (Fan et al. 2008, Wang et al. 2012) were also applied to monitor the water flow condition since voltage is generated as the piezoelectric film is deformed (bent) under the water flow effect. Such a sensing device was built by mounting piezoelectric thin films on a rod at certain spacing and inserting the rod into a guide rail installed next to the bridge pier. If the embedded piezoelectric film in the riverbed was disturbed by the water current as a result of scour, the output voltage is large than that when not disturbed. Therefore, the signals from all the piezoelectric sensors can indicate the variation of soil/water interface before, during and after a food event. Chang et al. (2012) developed a multi-lens monitoring system that can track scour images and retrieve the scour information through an image recognition process. Another tracing technique for sediment transport and scour around bridges was developed by

Lauth and Papanicolaou (2008) using radio waves, a communication between a Radio Frequency Identification (RFID) and transponders embedded in an individual tracked particles allowed to estimate the scour. A combination of multi-beam ultrasonic echo sounders and vibrating wire piezometers was used to measure and map the riverbed topography and detect local scour appeared within and around the pile group (Chen et al. 2010, 2012). A three dimensional profiling of the bed form around bridge piers has also been attempted using a rotatable sonar profiler (Shin and Park 2010, Jesse 2011).

A motion sensor is considered as a method to monitor sensitive bridge columns by relating the fundamental frequency of the bridge itself to the scour depth (Yao et al. 2010). A reliable non-destructive and indirect scour evaluation technique with vibration measurement (Ko et al. 2010) was developed and analyzed to assess the scour of bridge foundations. For a pier-soil system, as the river bed is eroded by scour, the free length of the column is increased, leading to the decline of its lateral stiffness. If the scour is getting more severe and the foundations exposed, the foundation stiffness is degraded so that the total stiffness of the system is further reduced. The stiffness reduction can be reflected by the variation of the structural vibration characteristics (Ko et al. 2010).

3 PASSIVE SMART ROCKS WITH EMBEDDED MAGNETS

In this section, the concept and measurand, the measurement principle, and various validation tests of passive smart rocks are presented and discussed. Small (11 mm or 7/16” in diameter) and large (102 mm or 4” in diameter) magnets were used in laboratory and field tests, respectively.

3.1 Smart Rock Concept, Measurand, and Measurement Principle

3.1.1 The Concept and Measurand

As introduced in Section 1, a passive smart rock is basically a permanent magnet embedded inside a natural rock or concrete encasement. Once buried into and top flush with sediments around a bridge pier foundation, a smart rock can roll to the bottom of a gradually growing scour hole as the sediments are eroded away. Like a field agent, the smart rock can therefore provide the maximum scour depth if the position of the smart rock is tracked over time.

To locate a smart rock, a commercial magnetometer (Model G858) is used to measure the intensity of the total magnetic field of the Earth and the magnet inside the rock. Therefore, the measurand for bridge scour monitoring with passive smart rocks is the intensity of magnetic field. In practice, at least three measurements must be taken from three different stations. In an oversimplified term, the relation between the intensity and measurement distance can be used to locate the smart rock by triangulation. The actual localization scheme is significantly more complicated than direct triangulation as discussed below.

3.1.2 The Measurement Principle

The G858 is a Cesium optically pumped magnetometer. It is operated with the elemental Cesium metal vapor in a 25-mm-diameter and 25-mm-length absorption cell. Inside the cell, the Cesium atoms are pumped by a lamp (source of light) containing additional Cesium metal but at a slightly higher vapor pressure. Each Cesium atom has only one electron in the outer-most electron shell. The electron has an electrical charge and a spin. It will thus have a small magnetic moment whose magnitude depends on the direction of its spin axis relative to an ambient magnetic field vector. For example, the electron has lower energy as its magnetic field is aligned with the ambient magnetic field. In combination with the fact that the energy of a photon and its frequency are related by Planck’s Constant, the energy difference that an electron possess can be accurately determined by measuring the Larmor frequency associated with the light source.

Figures 3.1a and 3.1b respectively show a two-sensor head setup in a plane and a 3-D view of one sensor head of the G858 Magnetometer with active and dead zones. Each sensor head can effectively measure the change in ambient magnetic field when its centerline in Figure 3.1b is oriented from 15° to 75° to the lines of force of the magnetic field. For example, the magnetic intensity becomes smaller or nearly zero as a magnet is moved from the active to dead zone. In applications, the two sensor heads are used to increase the dynamic measurement range for subtle changes in ambient magnetic field since each head senses the combined Earth's and local magnetic fields as illustrated in Figure 3.2 and the Earth's magnetic field is significantly stronger than the local field. More importantly, the magnetic field is represented by a vector as indicated in Figure 3.2 and cannot be completely determined by one sensor head measurement unless the magnet's orientation is known *in priori*.

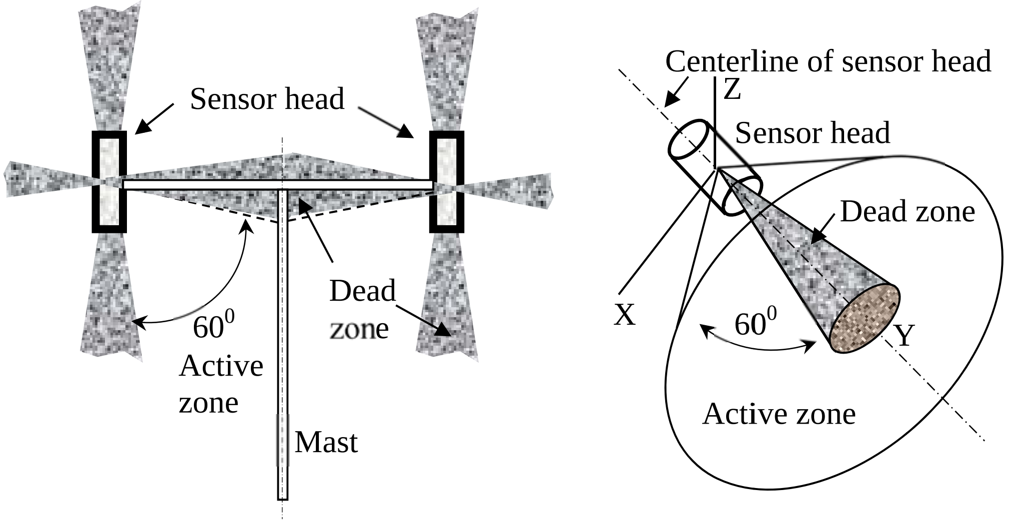

(a) Two Parallel Sensor Heads in a Plane (b) 3-D view with one sensor head

Figure 3.1 A Schematic View of Effective Measurement with Sensor Heads

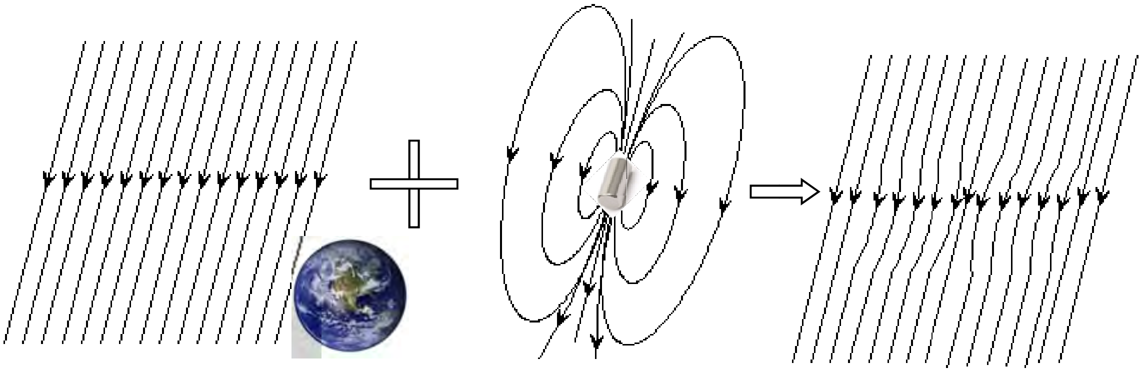

Figure 3.2 Schematics of the Resulting Field from the Earth's and Local Magnetic Fields

To test out its functionality, the G858 Magnetometer was used to measure the Earth magnetic field in an open football field at the Missouri University of Science and Technology. A sensor head was placed horizontally at various heights above the ground to ensure that no disturbance on the Earth magnetic field be observed from potential underground metal objects. Figure 3.3 presents two field strength distributions when the sensor head is rotated 360° in a horizontal plane at Location 1 and Location 2, respectively. The two locations are 3 m apart vertically. It can be seen from Figure 3.3 that each plot is approximately symmetrical about the Earth magnetic field orientation.

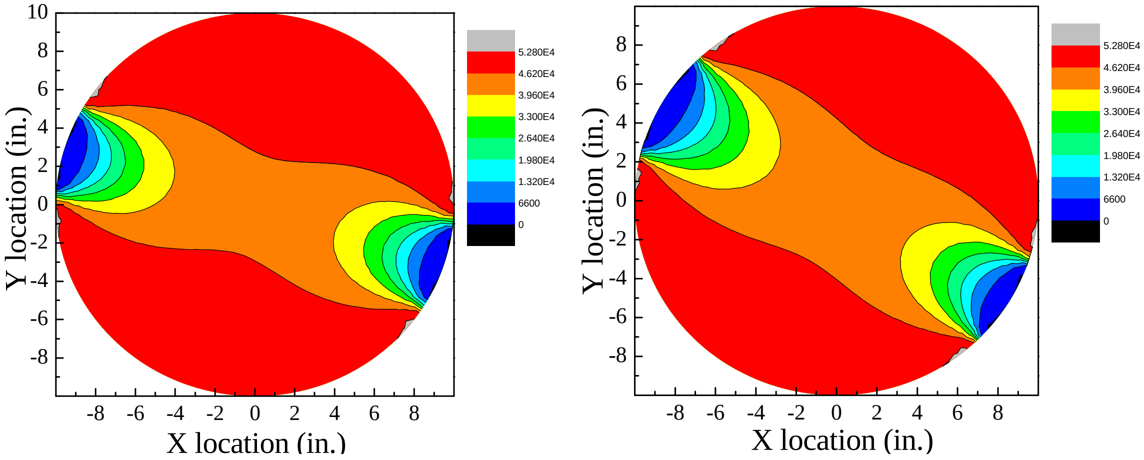

(a) Location 1: 130 in. above Ground (b) Location 2: 81 in. above Ground

Figure 3.3 Dead Zone Effect on Earth Magnetic Field Measurements

Figure 3.3 seemly indicates the different orientations of the Earth magnetic field at two locations. The difference was likely attributed to non-precise coordinate measurement.

The G858 comes with two measurement probes called sensor heads as indicated in Figure 3.1a. It measures the strength of an ambient DC magnetic field that combines the effects of the Earth magnetic field and other metal objects. To improve measurement sensitivity, a gradiometer with two sensor heads was acquired with the G858 Magnetometer. The two sensors are calibrated against each other so that their difference can be taken into account in applications. Figure 3.4 shows two measurements by the two horizontal sensors as they are moved away from a magnet that is 13 mm in diameter and 25 mm in length. The sensors were always placed 0.965 m above ground. It can be observed from Figure 3.4 that the two measurements at various distances are generally parallel. The significant variations within approximately 3 m result from the presence of the magnet at zero distance. At 6.1 m, both readings represent the strength of the Earth magnetic field. Figure 3.4 clearly indicates that the difference in two sensors is about 10 nT.

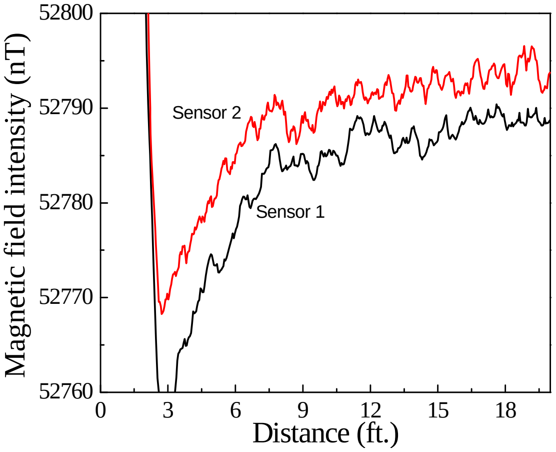

Figure 3.4 Field Strengths of a Magnet Measured at 0.965 m above Ground

3.2 Magnetic Fields of Permanent Magnets and the Earth

In this section, the magnetic field theory of a permanent magnet, the total magnetic field of the magnet and the Earth, and the proposed magnet localization scheme are presented and discussed in relation to their applications in passive smart rocks. They are validated by laboratory and field test results.

3.2.1 The Magnetic Field Theory of a Permanent Magnet

Consider a rod/cylinder magnet of 2a in diameter and 2b in length in cylindrical coordinate system as shown in Figure 3.5. Here, the origin of the coordinate system is located at the centroid of the magnet, y axis represents the centerline of the magnet from north to south, and ρ axis represents the radial direction perpendicular to the y axis.

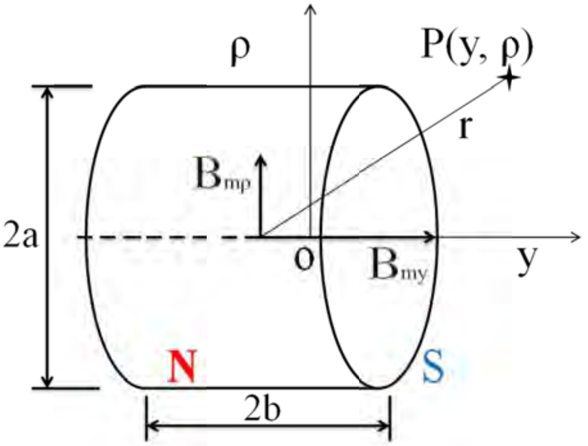

Figure 3.5 A Cylinder Magnet and Cylindrical Coordinate

Exact Solution: The magnetic field induced by the magnet is axis symmetrical about the centerline of the magnet and can be represented by a vector $\mathbf{B}_{m}$(y, ρ) at any point P. The magnetic field vector can be decomposed into a longitudinal component $\mathbf{B}_{my}$ and a radial component $\mathbf{B}_{m\rho}$. The two component magnitudes can be expressed into (Derby and Olbert 2009):

$$B_{my}(y,\rho)=\frac{B_{m0}a}{\rho+a}\int_{0}^{\frac{\pi}{2}}\frac{\cos^{2}\varphi+\gamma\sin^{2}\varphi}{\cos^{2}\varphi+\gamma^{2}\sin^{2}\varphi}\left(\frac{\beta_{+}}{\sqrt{\cos^{2}\varphi+k_{+}^{2}\sin^{2}\varphi}}-\frac{\beta_{-}}{\sqrt{\cos^{2}\varphi+k_{-}^{2}\sin^{2}\varphi}}\right)d\varphi \quad (3.1a)$$

$$B_{m\rho}(y,\rho)=B_{m0}\int_{0}^{\frac{\pi}{2}}(\cos^{2}\varphi-\sin^{2}\varphi)\left(\frac{\alpha_{+}}{\sqrt{\cos^{2}\varphi+k_{+}^{2}\sin^{2}\varphi}}-\frac{\alpha_{-}}{\sqrt{\cos^{2}\varphi+k_{-}^{2}\sin^{2}\varphi}}\right)d\varphi \quad (3.1b)$$

in which $B_{m0}=\mu_0 nI/\pi$ is the original intensity of the magnet, n is the number of turns per unit length, I is the magnitude of the electric current I, and μ_0 is the permeability of vacuum in N/m^2. Other parameters in Eq. (3.1a, b) are defined below:

$$y_{\pm} = y \pm b \tag{3.1c}$$

$$\alpha_{\pm} = \frac{a}{\sqrt{{y_{\pm}}^2 + (\rho + a)^2}} \tag{3.1d}$$

$$\beta_{\pm} = \frac{y_{\pm}}{\sqrt{{y_{\pm}}^2 + (\rho + a)^2}} \tag{3.1e}$$

$$\gamma = \frac{a - \rho}{a + \rho} \tag{3.1f}$$

$$k_{\pm} = \sqrt{\frac{{y_{\pm}}^2 + (\rho - a)^2}{{y_{\pm}}^2 + (\rho + a)^2}} \tag{3.1g}$$

Approximate Solution: When the radial coordinate ρ at Point P is significantly larger than the radius a of the magnet or the longitudinal coordinate y is significantly larger than half of the magnet length b, the magnitudes B_{my} and $B_{m\rho}$ of two components of the magnetic field vector can be approximated by

$$B_{my}(y,\rho) = \frac{\mu_0 \mu}{4\pi} \frac{(2y^2 - \rho^2)}{r^5} = k \frac{(2y^2 - \rho^2)}{r^5} \tag{3.2a}$$

$$B_{m\rho}(y,\rho) = \frac{\mu_0 \mu}{4\pi} \frac{3\rho y}{r^5} = k \frac{3\rho y}{r^5} \tag{3.2b}$$

$$B_m(y,\rho) = \sqrt{B_{my}^2(y,\rho) + B_{m\rho}^2(y,\rho)} \tag{3.2c}$$

where $k = \mu_0 \mu / 4\pi$ is the constant coefficient of the magnet (e.g. k=10^{-9}Nm^2/A), μ is the magnetic moment in Am^2, and $r^2 = y^2 + \rho^2$.

For example, the largest magnet used in smart rocks in this study has a=0.05 m and b=0.025 m and typically detected by a base station (at river bank or bridge deck) set away from the magnet by at least 2 m. In this case, Eq. (3.2) gives the following two magnetic field strengths at a distance of c in meter from the centroid of the magnet and their *approximate* ratio:

$$B_m(c,0) = \frac{2k}{c^3}, \quad B_m(0,c) = \frac{k}{c^3}, \text{ and } \frac{B_m(c,0)}{B_m(0,c)} = 2.$$

On the other hand, Eq. (3.1a) and (3.1b) can be numerically integrated out in MATLAB. The corresponding *exact* field strength ratio is given below:

$$\frac{B_m(1,0)}{B_m(0,1)} = 1.950, \quad \frac{B_m(2,0)}{B_m(0,2)} = 1.998, \text{ and } \frac{B_m(3,0)}{B_m(0,3)} = 1.999.$$

The above calculations indicate that, as Point P is moved away from the magnet, the field strength ratio approaches 2. In practical applications, the approximate solution is acceptable for a measurement distance of over 2 m. In this case, c/min(a, b)=2/0.025=80. This ratio requirement corresponds to a measurement distance of 44 cm for a magnet of 11 mm in diameter and 25.4 mm in length, which will be used in small-scale bridge pier tests. As such, the approximate solution can also be used for laboratory test cases provided that the magnetometer is set away from the magnet by at least 44 cm.

Determination of the Earth Magnetic Field Intensity B_E and Coefficients k and θ: The magnetometer G858 used in this study measures a total intensity of the magnetic fields of the Earth, the magnet, and nearby ferromagnetic substances. When the nearby substances are neglected, the total magnetic field intensity B depends upon the Earth's magnetic field intensity B_E, the dip angle θ of the Earth's magnetic field lines with a horizontal axis, and the coefficient k of the magnet in addition to the coordinates (x, y, z). That is, $B = B(B_E, \theta, k, x, y, z)$.

The Earth's magnetic field intensity changes from one place to another and the coefficient of the magnet may change over time as well. Therefore, k and θ must be evaluated for a specific study. The Earth's magnetic field lines are considered to be parallel at each bridge site. Since it is not axis-symmetrical, the xyz Cartesian coordinate system is used when the Earth's magnetic field is combined with the magnetic field of the magnet. Considering the geographical location in Rolla, MO, with latitude and longitude coordinates being 37°57′12″N and 91°45′27″W, respectively, and a magnet pointing due geographical south of the Earth, Figure 3.6 illustrates the xyz coordinate system and the relative directions of the magnetic fields of the Earth and the magnet. Here, x-axis points out of the paper and both magnetic fields are symmetrical about the yoz plane. In Figure 3.6, the dip angle θ represents the angle between the Y axis and the Earth's magnetic field lines.

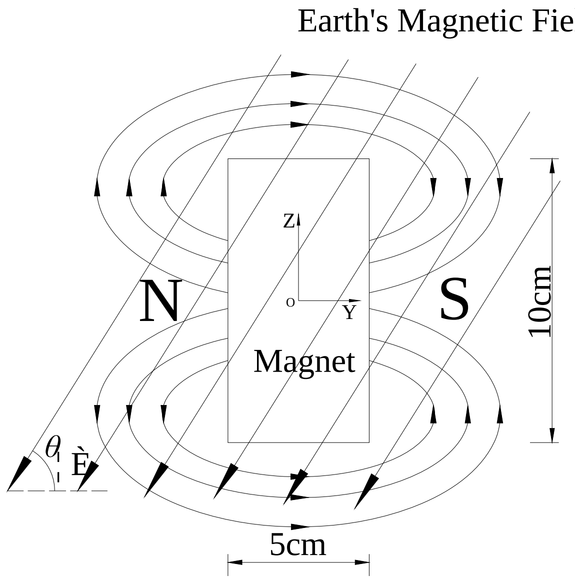

Figure 3.6 xyz Cartesian Coordinate and the Earth and Magnet's Magnetic Fields

Referring to Figure 3.6, the total magnetic field intensity vector at an arbitrary point P can be written as $\boldsymbol{B}=(B_x, B_y, B_z)$ in the xyz coordinate system. The magnetic field components of the magnet are given in Eq. (3.2), in which the radial component can be further decomposed into x- and z-components. The Earth magnetic field vector has two non-zero components along y- and z-axes. The x-, y-, and z-component of the total magnetic field intensity vector can then be expressed into:

$$B_x = k\frac{3xy}{r^5} \tag{3.3a}$$

$$B_y = k\frac{2y^2 - x^2 - z^2}{r^5} + B_E \cos\theta \tag{3.3b}$$

$$B_z = k\frac{3zy}{r^5} + B_E \sin\theta \tag{3.3c}$$

where $r^2 = x^2 + y^2 + z^2$. Finally, the total magnetic field intensity B=‖**B**‖ at any point P(x, y, z) around the cylindrical magnet can be expressed into:

$$B = \sqrt{(k\frac{2y^2 - x^2 - z^2}{r^5} + B_E\cos\theta)^2 + (k\frac{3zy}{r^5} + B_E\sin\theta)^2 + (k\frac{3xy}{r^5})^2} \tag{3.4}$$

The magnetic field intensity of the Earth was first evaluated with a series of field tests. To this end, an open field test site located at the Ber-Juan Park, Rolla, was selected to avoid the effects of electric lines, train tracks, and other ferromagnetic substances. During the tests, mobile phones and magnets were taken far away from the magnetometer sensor heads. Based on 15 measurements, the average Earth’s field intensity in Rolla was found to be 52442 nT with a standard deviation of 0.18 nT.

The coefficients *k* and *θ* were then evaluated with *n* sets of calibration test data collected at the Ber-Juan Park, Rolla, each including the total magnetic field intensity as a function of the magnet coordinates. A trial-and-error method through MATLAB was used to determine *k* and *θ* in three steps. In Step 1, *k* is assumed to vary from 30000 to 45000 with a step size of 50 based on the literature for various magnets. For each *k* value, Eq. (3.4) was used to calculate θ_i with each set of the test data ($i=1, 2,\ldots, n$). In Step 2, the *n* numbers of θ_i were used to determine the unbiased mean and standard deviation:

$$\overline{\theta} = \frac{1}{n}\sum_{i=1}^{n}\theta_i \,, \quad \sigma = \sqrt{\frac{\sum_{i=1}^{n}(\theta_i - \overline{\theta})^2}{n-1}} \,. \tag{3.5}$$

In Step 3, the *k* value corresponding to the minimum standard deviation and its corresponding average *θ* value are determined. They contributed to the least-squared error in comparison with the measured data.

As it will be detailed in Section 3.4.1, an Automatically Pointing South System (APSS) is designed with a floating magnet embedded in a smart rock. Analogous to the concept of compass, the floating magnet is always oriented to the south of the Earth magnetic field unless other ferromagnetic substances are present. For field tests at Ber Juan Park in Rolla to determine the *k* and *θ* coefficients, an APSS was realized with the use of two buckets. The small bucket with a magnet floated in the water contained in the large bucket as shown in Figure 3.6(c).

To minimize the uncertainty in test setup, a single sensor head of the magnetometer was fixed to measure the total magnetic intensity as the floating magnet was moved in various positions. As shown in Figure 3.7a, the sensor head was set at the origin of the test plan, which is fixed on a plastic bin and ensured to be level using a bubble level as indicated in Figure 3.7b. The other points labelled from M1 to M11 in Figure 3.7a are the locations of the floating magnet. To determine the exact locations of the magnet and sensor head, a total station was applied as shown in Figure 3.7d. The prism placed above the magnet as displayed in Figure 3.7e can ensure accurate measurements with the total station. The position of the total station itself was determined by ensuring that the station be 30 m due South with the aid of an army compass placed on top of the sensor head as shown in the insert of Figure 3.7b.

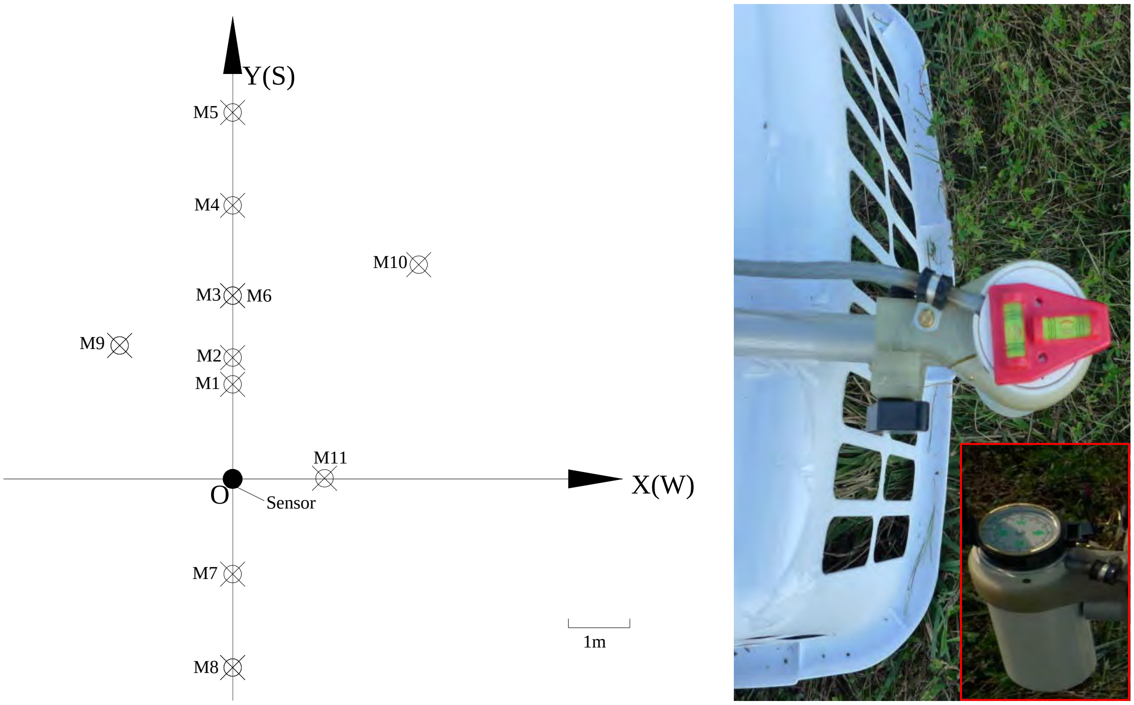

(a) Magnet and Sensor Head Locations (b) Sensor Head Setup with a Bubble Level

(c) Primitive APSS (d) Total Station for Positioning (e) Prism for Precision Positioning

Figure 3.7 Plan and Setup for Calibration Tests

The coordinates and the total magnetic field intensities at the 11 magnet locations are listed in Table 3.1. These coordinates were measured at the magnet centroid. Eight (M1 to M8) out of the 11 sets of data were used to determine k and θ values. The remaining three sets of data (M9 to M11) were used to verify the estimation accuracy by comparing the predicted total field intensities with their corresponding measurements.

Figures 3.8a and 3.8b show eight sets of θ changes and their standard deviation with various k values, respectively. It can be seen from Figure 3.7b that k = 37060.38 (×10^{-9} Nm^{2}/A) results in the minimum standard deviation σ of θ. The corresponding eight θ (from θ_1 to θ_8) are 64.8 °, 65.4 °, 64.8 °, 64.6 °, 63.5°, 63.8 °, 64.3 °, and 63.2 °, respectively. The mean and standard deviation of θ are 64.3 ° and 0.283°, respectively. The coefficient of variation of θ is 0.283°/64.3° = 0.44%.

Table 3.1 Relative Coordinates and Total Magnetic Field Intensities

Magnet Location	**x(m)**	**y(m)**	**z(m)**	**B_i (nT)**	
				Measured	**Predicted**
M1	0	1.538	-0.0418	63203.86	N/A
M2	0	1.973	-0.0488	56825.43	N/A
M3	0	2.980	-0.0671	53607.66	N/A
M4	0	4.466	-0.0723	52970.32	N/A
M5	0	5.957	-0.0979	52591.49	N/A
M6	0	2.978	0.255	54020.86	N/A
M7	0	-1.546	-0.213	66024.6	N/A
M8	0	-3.066	-0.140	53796.31	N/A
M9	-1.835	2.170	-0.140	52838.71	52859.21
M10	3.022	3.482	-0.0058	52560.14	52561.65
M11	1.492	0.011	-0.0811	48503.09	48726.87

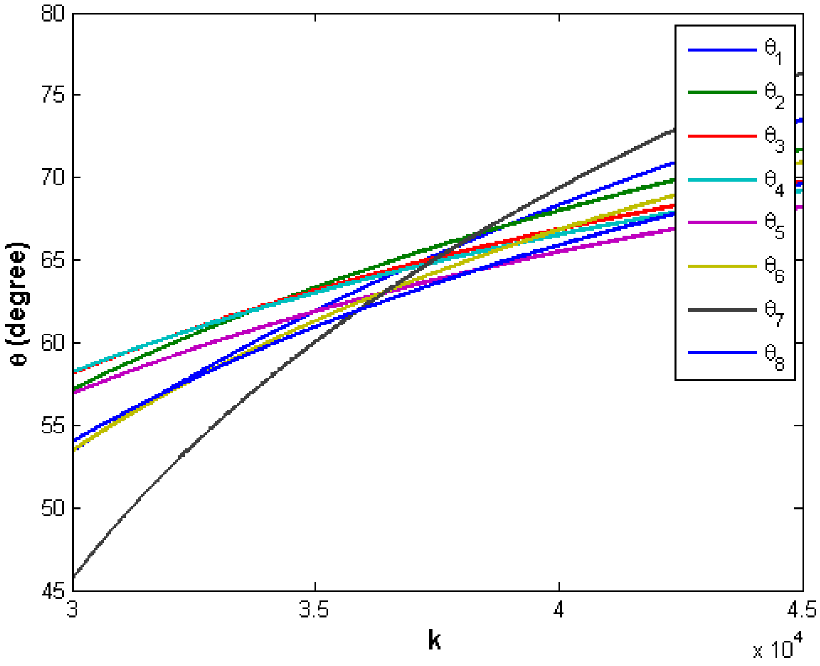

(a) n Numbers of θ Values for each k Value

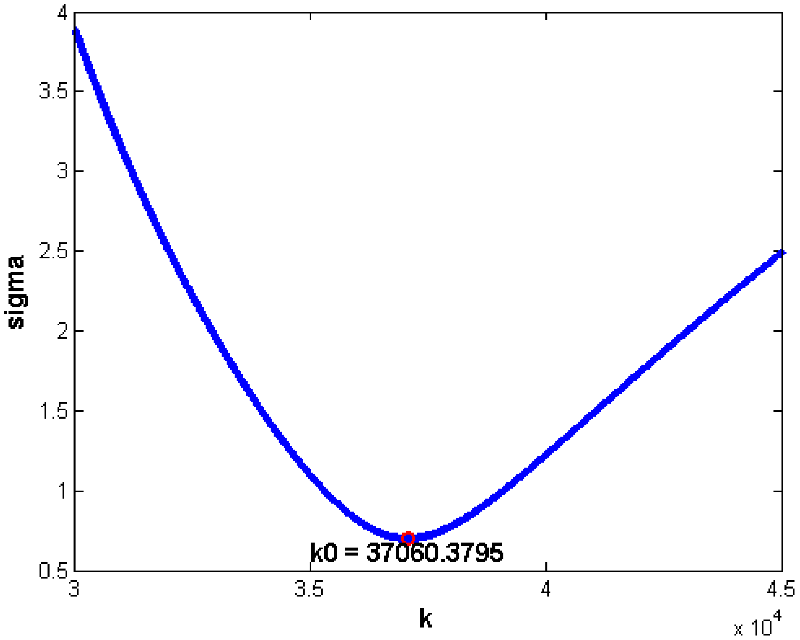

(b) Standard Deviation of θ Values as a Function of k Value

Figure 3.8 Least-square Error for the Determination of θ and k

With the estimated B_E, k, and θ values, the total magnetic field intensity at other three points (M9 to M11) in Table 3.1 can be predicted from Eq. (3.4). The predicted intensities are included in the last column of Table 3.1. The relative errors in the prediction of the total magnetic field intensities are used to 0.04%, 0.00%, and 0.46%, respectively. The largest error occurred at Point M11 due to its proximity to the sensor head within approximately 1.5 m so that the approximate solution in Eq. (3.2) is less accurate. Overall, the prediction errors are very small and thus the estimated k and θ values are acceptable. This result also demonstrates that the approximate solution is acceptable in engineering application even at 1.5 m away from the sensor head.

Characteristics of the Total Magnetic Field: As indicated by Eq. (3.4), the spatial distribution of the total magnetic field intensity is highly complicated near the cylinder magnet. To gain insight on this distribution, two visual results are presented: the intensity variation in a fixed plane and the three-dimensional surface with equal intensity.

Figure 3.9 shows the spatial distribution of the total intensity in vertical plane (YOZ). Note that the intensity at the origin of the Cartesian coordinate system is unbounded as indicated in Eq. (3.4). Therefore, the center portion of the spatial distribution with a radius of 0.1 m is not shown in Figure 3.9. Three distinct spikes are observed in the intensity distribution as shown from two perspectives in Figure 3.9. The near center area has the highest intensity shown in red color. The dark blue color indicates the lowest intensity nearby.

Figure 3.10 shows the spatial distribution of the total intensity in horizontal plane at different heights (constant z). The total intensity in South Pole of the magnet is always greater than that of the North Pole at all heights. With the increasing of the height, the difference between the maximum and minimum intensities becomes gradually reduced. The intensity distribution is symmetrical about x axis as observed from Figure 3.9.

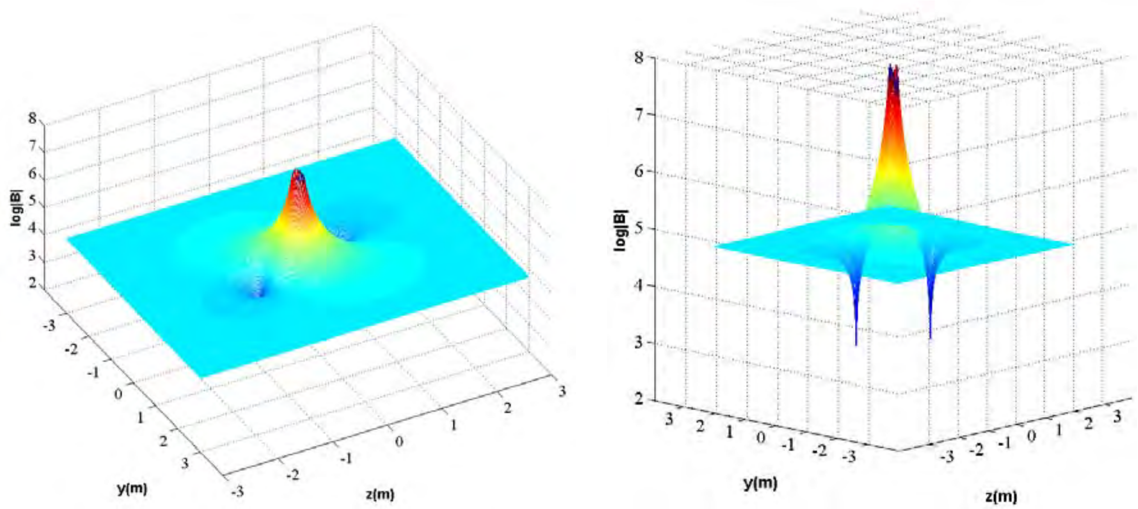

(a) Side View 1 (b) Side View 2

Figure 3.9 Change of Total Magnetic Intensity in YOZ Plane

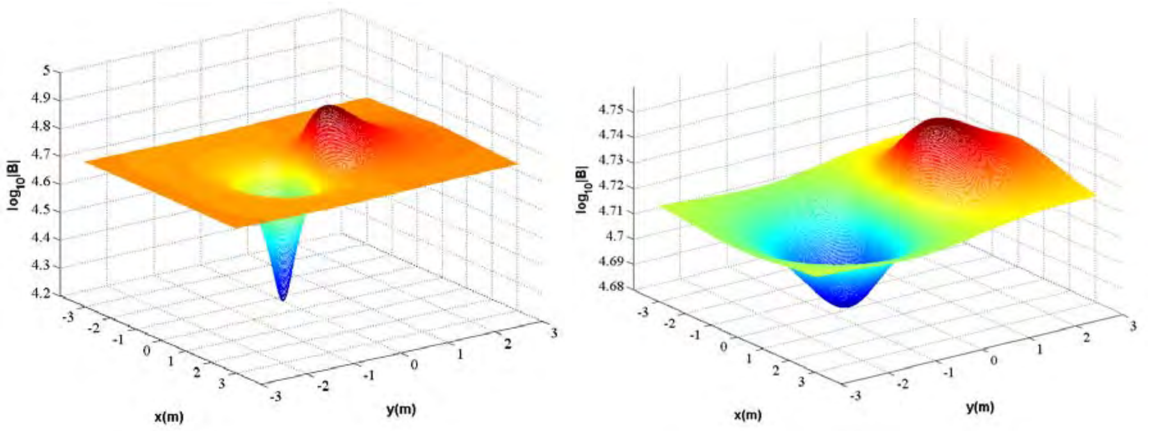

(a) z = 1 m (b) z = 2 m

Figure 3.10 Changes in Total Magnetic Intensity in Horizontal Planes

Figure 3.11 shows the equi-intensity surface where the total magnetic field intensity is constant. At the origin of the coordinate system, the magnetic intensity tends to approach infinite according to Eq. (3.4). Therefore, all equi-intensity surfaces do not pass through the origin. Figures 3.11a-3.11c represent the surfaces when the total intensity is less than the Earth's magnetic field strength, B_E=52442 nT. Figure 3.11d represents the surface when the total intensity is equal to the Earth's intensity. Figures 3.11e and 3.11f represent the surfaces when the total intensity exceeds the Earth's magnetic field strength. Note that all the equi-intensity surfaces are symmetrical about x axis as expected from Eq. (3.4).

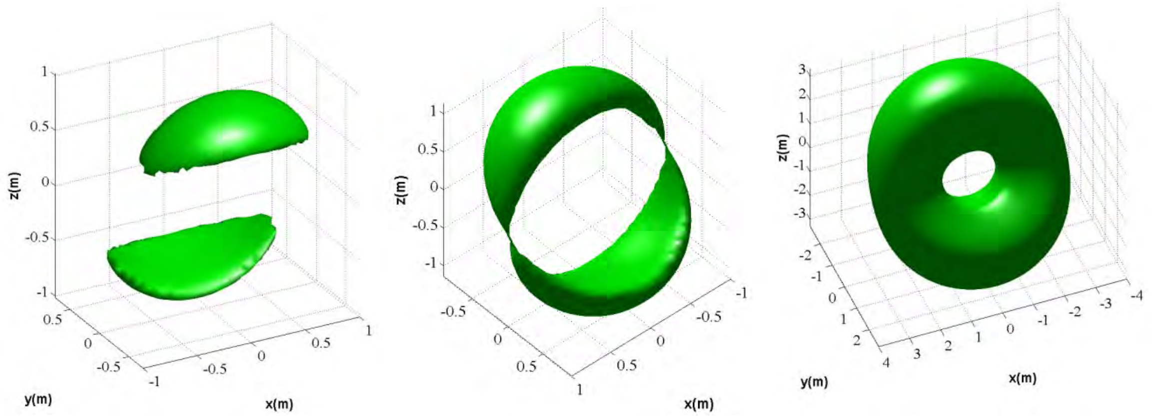

(a) B=40000 nT (b) B=47300 nT (c) B=52441 nT

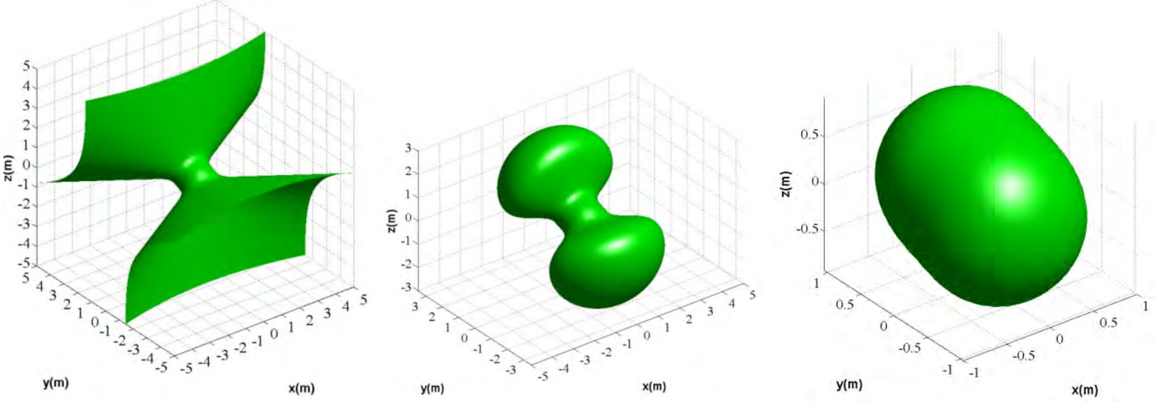

(d) B=52442 nT (e) B=52443 nT (f) B=70000 nT

Figure 3.11 Equi-intensity Surface of the Total Magnetic Field (B_E=52442 nT)

As the total intensity decreases below the Earth's intensity as shown in Figures 3.11a-3.11c, the equi-intensity surface resembles like a doughnut with its center hole enlarging and its wall thickness reduced, eventually becoming two separate pieces divided at z=0. It was observed from simulations that the minimum total magnetic field intensity is approximately 8000 nT.

As the total intensity increases above the Earth's intensity, the equi-intensity surface resembles like a dumbbell with its end plates shrinking and the neck in between the two plates growing. The rate of change in dumbbell size decreases from high, when the total intensity is slightly larger than the Earth's intensity, to low with further increasing of the total intensity. Indeed, the two end plates are open and unbounded when the total intensity is exactly equal to the Earth's magnetic intensity as indicated in Figure 3.11d. They decrease as the total intensity increases. The neck portion eventually disappears as shown in Figure 3.11f.

3.2.2 Effects of Magnet Geometry, Magnetometer, and Environment

Assuming the same Earth magnetic field in the City of Rolla, MO, magnetic fields of various permanent magnets in shape, size, volume, working environment (air/water), and measurement instruments (mini magnetometer and G858) were measured and compared for their relative intensities. To minimize the disturbance of potential metal objects near the test site, all tests in this study were conducted in a football field where no metals on the ground surface were observed. All the magnets used in field tests were manufactured with high grade Neodymium, Grade N45 (12,500 Gauss) or higher, by the United Nuclear Scientific LLC. They were in sphere, cube, rod, tube, plate, and disc shapes. In addition to the G858, a DC MilliGauss Meter with a model of MGM produced by AlphaLab Inc. was used for some measurements.

Geometry Effect: Figures 3.12a and 3.12b compare the theoretical predictions with test results for some of the magnets placed in air and underwater, respectively. Here the distance from the magnet is measured from the centroid of a sensor head of G858 Magnetometer to the centroid of the magnet. In air, the 25.4 mm × 25.4 mm × 6.4 mm (1″ × 1″ × ¼″ in length × width × thickness) plate gave the largest magnetic field strength and measurement distances. It is followed by the 12.7 mm × 25.4 mm (½″ × 1″ in diameter × thickness) rod, 25.4 mm (1″) diameter sphere, and 25.4 mm × 6.4 mm (1″ × ¼″ in diameter × thickness) disc. The theoretic predictions agree well with experimental results, validating the prediction accuracy of the theoretic analysis. To verify the well-known fact that water does not affect magnetic field, underwater tests were conducted by placing the permanent magnets inside a closed channel filled with water. In water, the magnetic fields of the plate, rod, and disc with similar sizes decreased with distance in a similar fashion. Based on the theoretic predictions and field test data, the plate and rod for a given size are the best candidates for smart rocks in scour monitoring. Their magnetic field strengths differ little in air and underwater, which confirms that magnetic field can penetrate through water without being disturbed.

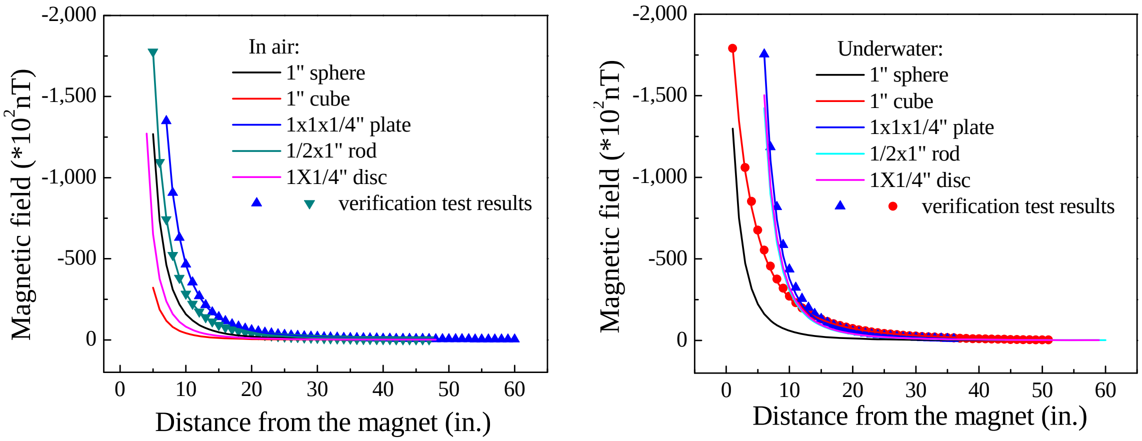

(a) Measured in Air with MGM

(b) Measured in Water with MGM

Figure 3.12 Magnetic Field Strengths for various Magnets: Prediction versus Experiment

Instrument Effect: Size effects of various magnets were investigated for the selected rod and plate shapes only. The measurements with the MGM (1 MilliGauss resolution) and the G-858 Magnetometer (0.01 nT resolution) are compared since the mini magnetometer is easier to carry around in practical applications.

Figure 3.13 shows the test procedure of rod- and plate-shaped magnets. The equipment, MGM or G-858, was placed at a particular location as a magnet moved away from the instrument/sensor heads along a predetermined direction by 25.4 mm (1″) at a time. Figure 3.14 compares the theoretic predictions with the test data for some cases and compares the measurements by the two magnetometers. With the mini magnetometer, the maximum measurement distance for a 12.7 mm × 25.4 mm (½″ × 1″) rod is 1.7 m (5′7″) and the maximum measurement distance for a 25.4 mm × 25.4 mm × 4 mm (1″ × 1″ × ¼″) plate is 1.9 m (6′3″). With the G-858, the maximum measurement distances of the rod and the plate reach 7.95 m (26′1″) and up to 8.5 m (28′) Figures 3.6a - 3.6d also indicate that the magnetic field of a permanent magnet highly depends on the in-plane dimension and the thickness of the magnet. The thicker the magnet and the larger its in-plane dimension, the stronger the induced magnetic field and the longer distance the magnet can be detected.

Field Strength Enhancement - Extended Steel Bar and Alternate Magnet Polarity: To increase magnetic field strengths, one 0.35 m No.13 (14″ #4) rebar was connected to each end of a 12.7 mm (½″) in diameter, 25.4 mm (1″) in length permanent rod magnet as shown in Figure 3.15a. The G858 Magnetometer was set at a specific location and measured the magnetic field of the Earth plus the extended magnet as the magnet moved away from the instrument/sensor by 305 mm (1′) at a time. In this case, the polarity of the extended magnet alternates at each stop. Figure 3.15b compares the field strengths measured by the G-858 between the original magnet and the extended magnet. The maximum measurement distance of the 12.7 mm (½″) in diameter and 25.4 mm (1″) in length rod magnet was found to be approximately 8.5 m (28′), which agrees with the previous theoretic prediction. The maximum measurement distance of the extended rod exceeded 21.3 m (70′). Therefore, extending a rod magnet by adding steel bars at both ends can increase the magnetic field strength by many times.

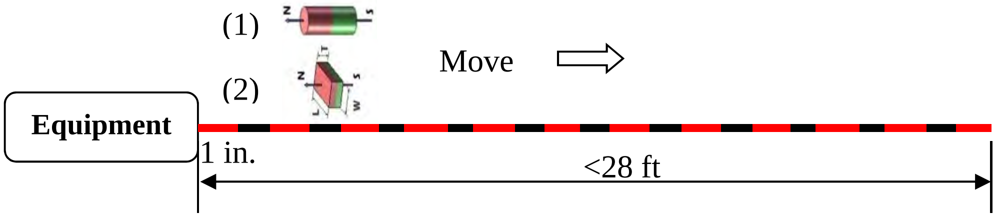

Figure 3.13 Test Procedure for Rod and Plate Magnets

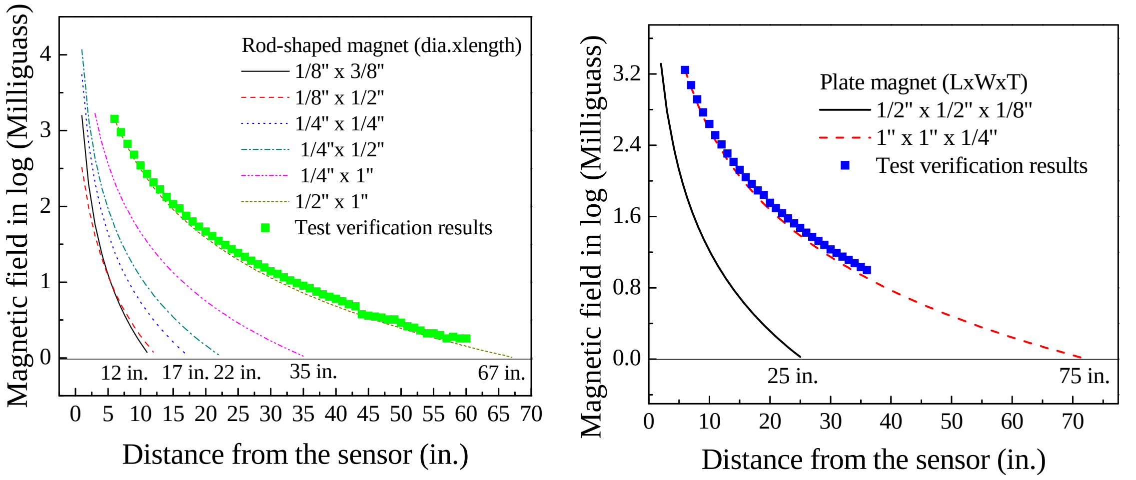

(a) Rod Magnet with MGM Measurement (b) Plate Magnet with MGM Measurement

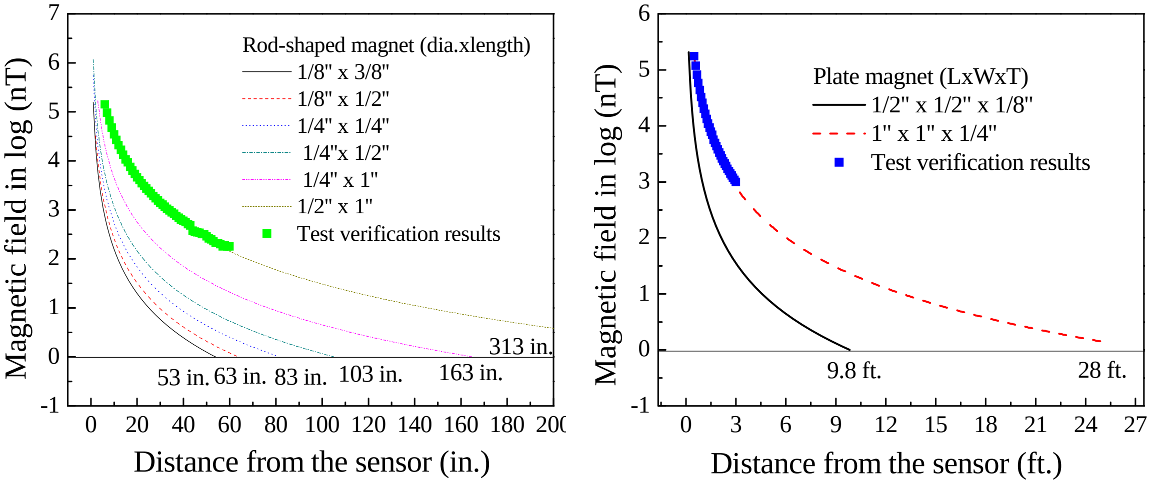

(c) Rod Magnet with G858 Measurement (d) Plate Magnet with G858 Measurement

Figure 3.14 Field Measurements of Rod and Plate Magnets with Two Magnetometers

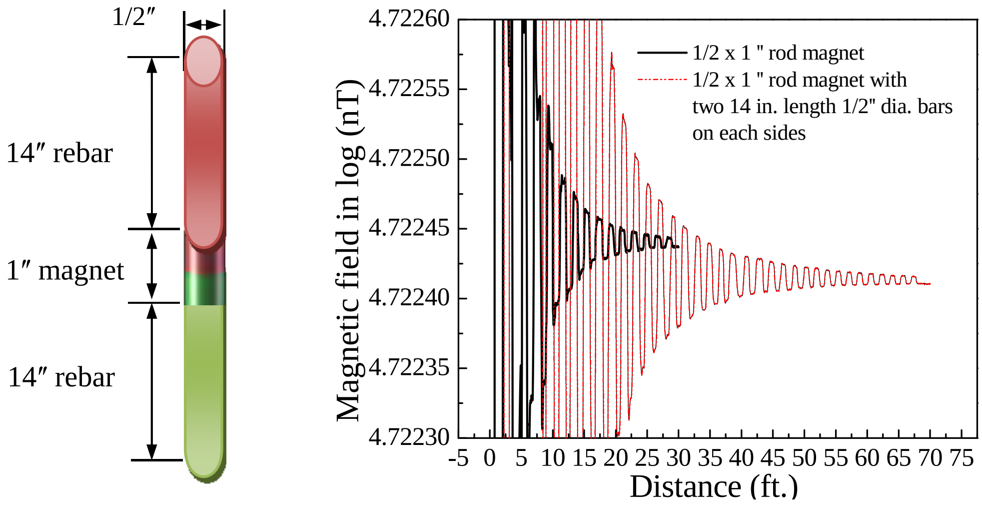

(a) Extended Magnet (b) Magnetic Strength

Figure 3.15 Strength-Distance Curves as Polarity Alternates at Every Foot

Strength Gradient Measurements: Figure 3.16a shows the orientations and the relation of two sensor heads (C3344 above C3372) in vertical gradient tests. The test procedure was the same as used to acquire data presented in Figure 3.15. Four rod magnets were tested, including 12.7 mm × 25.4 mm (½″×1″ in diameter × length), 25.4 mm × 25.4 mm (1″×1″), 50.8 mm × 25.4 mm (2″×1″), and 50.8 mm × 50.8 mm (2″×2″) Figure 3.16b presents the measured Earth magnetic vertical gradients and those for a 12.7 mm × 25.4 mm (½″×1″) rod magnet. The Earth magnetic vertical gradient is within 7.5 nT while that of the 12.7 mm × 25.4 mm (½″×1″) rod magnet changes significantly within a distance of 8.5 m (28′) from the location of the instrument/sensor. Figure 16c compares the vertical gradients and the maximum measurement distances with rod magnets of various sizes. Given a detectable strength threshold of 0.1nT, which is 10 times of the resolution of the G858 Magnetometer, a 50.8 mm × 50.8 mm (2″×2″) magnet yielded reliable data at 40.7 m (150′).

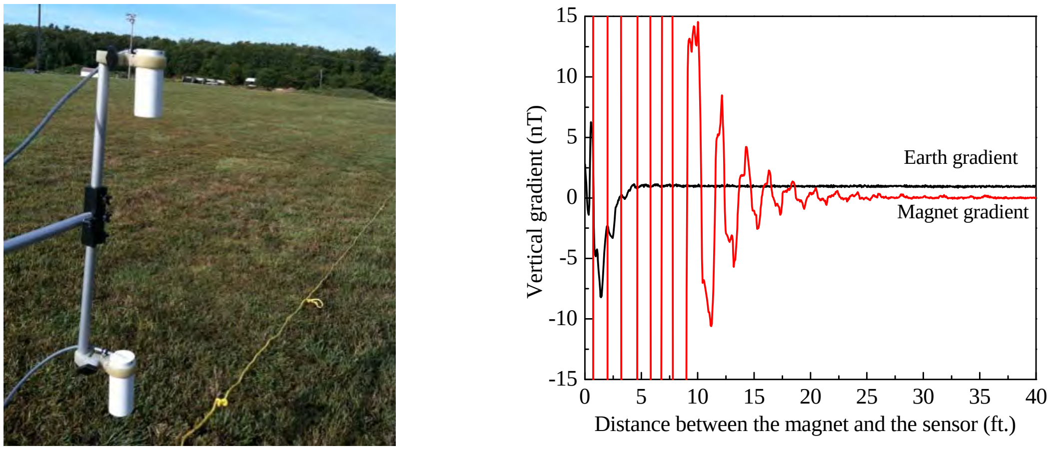

(a) Sensor Orientation

(b) Vertical Gradient for ½″×1″ Rod Magnet

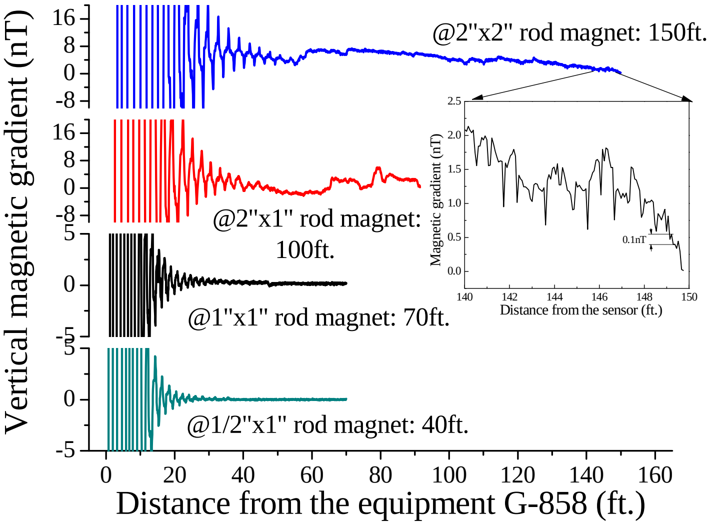

(c) Maximum Measurement Distance for Various Rod Magnets

Figure 3.16 Vertical Gradient versus Distance of Rod Magnets with G858 Magnetometer

Hollow and Solid Steel Spheres: To determine whether encasing a smaller magnet with a metal shell increases the gradient strength, the magnetic field strength and vertical gradient of a solid magnetic rod, 12.7 mm (½″) in diameter and 25.4 mm (1″) in length, were compared to those of a hollow tube magnet with the same length and outer diameter but an interior diameter of 6.4 mm (¼″). The test procedures are similar to Figure 3.13. To test the intensity of the magnetic field of each magnet, the magnetometer G-858 was held in a stationary position while each magnet moved at a constant speed in a straight line up to a distance of 12.2 m (40′) away from the sensor. Likewise, to find the gradient, each magnet moved along this same path while rotating at a constant speed every foot up to 12.2 m (40′).

Figure 3.17a and 3.17b compare the average field intensities and the average vertical gradient of two tested magnets, respectively. With the same length and outer diameter, the material reduction of the magnet affected little to the intensity or the gradient of the magnetic field. Therefore, using hollow magnets instead of solid magnets will provide similar sensing strength with less magnet weight and lower cost, indicating that the magnetic field strength of the smart rock could be potentially increased to a large extent by enclosing the smart rock in a large hollow steel bowl or as such.

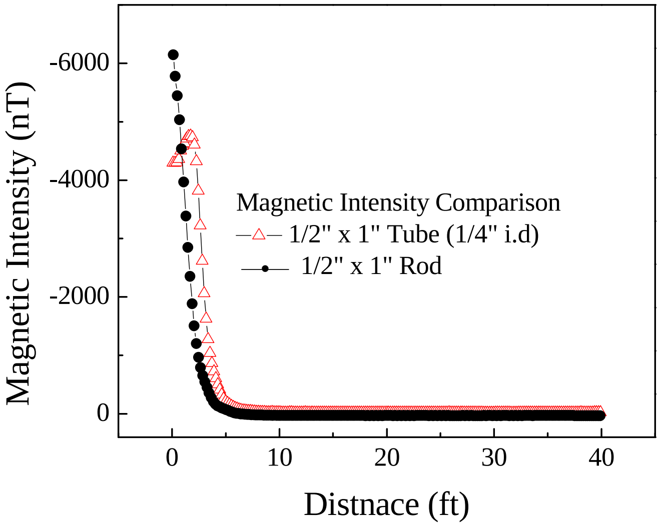

(a) Comparison of Magnetic Field Intensity

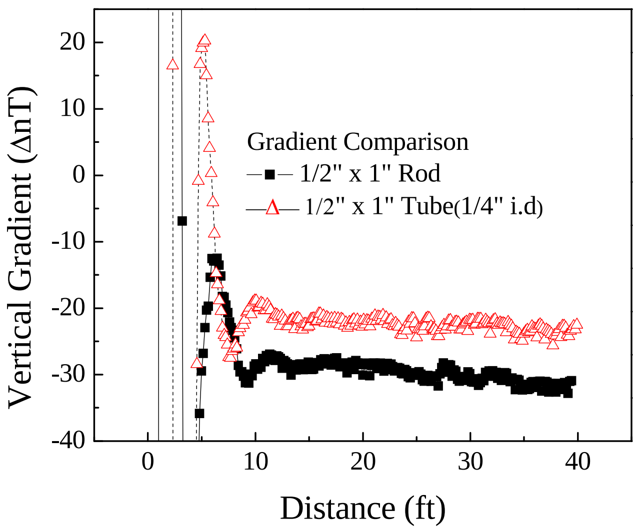

(b) Comparison of Vertical Gradient

Figure 3.17 Solid versus Hollow Rod/Cylinder Magnet

Rotation Speed Effect: To understand whether rotating a magnet can increase the sensitivity of magnetic field strength in application and thus the maximum measurement distance, a series of tests with magnet rotations were conducted. In this case, the magnetometer was placed 5′ away from the rotating magnet. For a consistent and accurate evaluation of the rotating effect on the magnetic field strength, a rotating apparatus shown in Figure 3.18 was designed to allow for a constant rotation speed (1 rpm) of a magnet. As illustrated in Figure 3.18, the magnet can independently rotate about the horizontal and vertical axes. Three tests were conducted with various rotations about the horizontal axis, the vertical axis, and both axes. For each test case, multiple runs were performed to test the data repeatability.

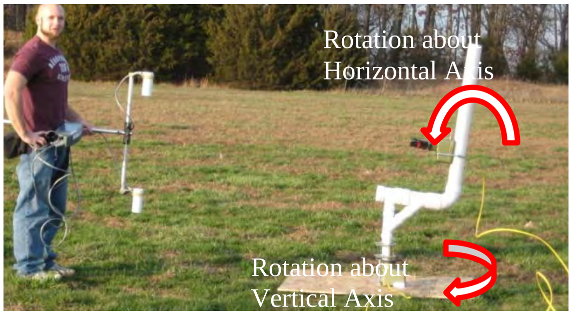

Figure 3.18 Field Test Setup

The vertical gradient was measured as the apparatus rotated the 12.7 mm × 25.4 mm (½″ × 1″ in diameter × length) magnetic rod. The test results were averaged and plotted as shown in Figures 3.19a – 3.19c for the three cases, respectively. Overall, the magnetic field strength followed a sinusoidal function of the magnet rotation as the dipoles of the magnet rotate in the same rotating plane.

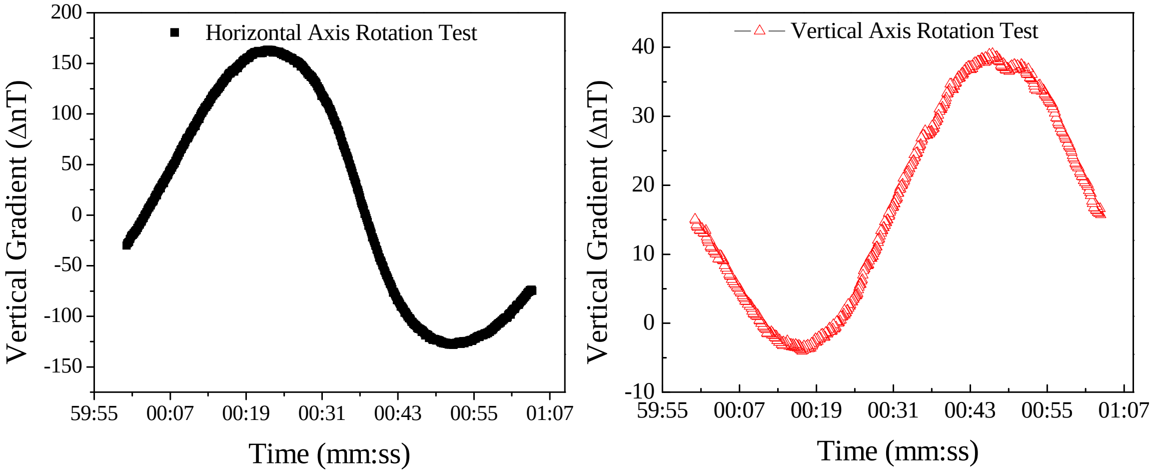

(a) Rotation about Horizontal Axis (b) Rotation about Vertical Axis

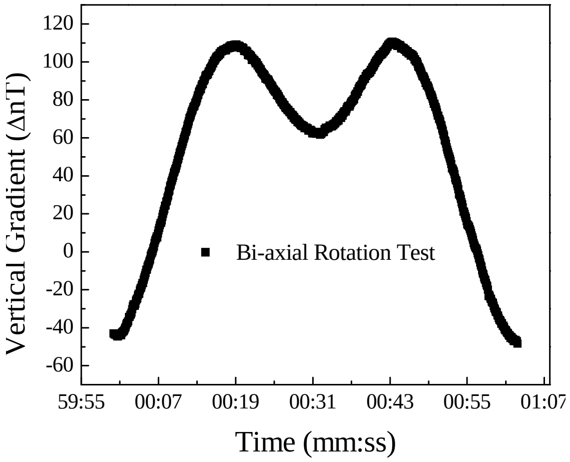

(c) Bi-axial Rotation

Figure 3.19 Effects of Stationary Magnet Rotation on Vertical Gradient

Figures 3.19a and 3.19b show that, in both horizontal and vertical planes, the intensity of the magnetic field reaches the maximum and the minimum when the magnet is parallel and perpendicular to the sensor heads, respectively, as illustrated in Figure 3.18. Figure 3.19c indicates that the maximum vertical gradient was achieved at 19 and 44 seconds, respectively. With this particular time period and a constant rotation speed of one revolution per minute, the angles when the maximum intensity of magnetic field was achieved can be estimated by:

$$\frac{19}{60}\times 360 = 114, \qquad \frac{44}{60}\times 360 = 250$$

Therefore, the rod magnets were estimated to obtain their maximum vertical gradient reading when the angle of the rod is 114 ° and 250 ° both to the horizontal and vertical axis, with the consideration of the Earth magnetic field in that particular test field. For the future field application, the field rotation tests should be operated at the particular job site before the installation of the smart rocks to search the maximum magnetic field intensity angle for the consideration of largest capacity of the installed “smart rock” system.

3.2.3 Scour Test and Depth Prediction with a Small-scale Pier Model

Prototype smart rocks were built and prepared for their characterization and validation tests in the Hydraulics Engineering Laboratory at Turner-Fairbank Highway Research Center (TFHRC), McLean, VA. First, the minimum flow velocities to set smart rocks of various size and density in motion were characterized in a small flume. Second, natural rocks with one embedded magnet each were then characterized in the small flume for localization of the rocks as they slide or rotate mainly in one direction. Finally, smart rocks were validated for maximum scour depth monitoring in a large flume with two small-scale bridge pier models. Following is a brief summary of the laboratory test results and analysis.

Minimum Water Flow Velocity to Set Smart Rocks in Motion: Three cylinder magnets of various sizes were embedded into acrylic balls to function like passive smart rocks. As exemplified in Figure 3.20a, each ball was individually tested in the small flume at TFHRC as the velocity of water flow increased. The 11.1 mm × 25.4 mm (diameter × length) Grade N42 cylinder magnet embedded in a 28.6 mm acrylic ball can resist a dragging force of water flow at 56 - 65 cm/sec when placed on top of the sand particles glued to a flat bottom of the small flume, as shown in Figure 3.20b. This velocity is slightly above the velocity (approximately 50 cm/sec) around the small-scale bridge piers tested in the large flume at TFHRC as discussed later. In practical design, the minimum water flow velocity depends on the size and density of smart rocks and the water flow condition in the river.


(a) Bottom Texture of the Flume (upstream) (b) Acrylic Ball with an Embedded Magnet

Figure 3.20 Minimum Velocity Tests of Passive Smart Rocks

Localization Tests in Small Flume: To locate a smart rock, the magnetic field intensity-distance curves for several controlled modes of the rock movement were recorded and used as basic patterns of the intensity-distance curve for any general rock movement. Therefore, a magnet was oriented either vertically or horizontally and tested as it moved away from a magnetometer in an open field at Rolla, MO. Figures 3.21a and 3.21b illustrate the test setup and magnet movement. Figures 3.22a and 3.22b show the change in magnetic field strength starting from approximately 38 cm away from the magnetometer through 60 cm. This range covered the measurement distances used during the small-scale scour monitoring tests in the large flume at TFHRC.

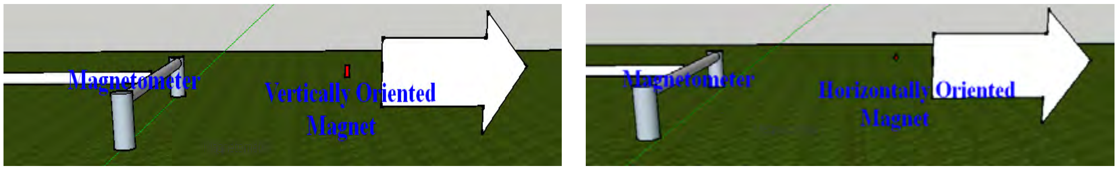

(a) Vertical Orientation (b) Horizontal Orientation

Figure 3.21 Intensity-distance Correlation Test Layout with Magnetometer Sensors

It can be seen from Figure 3.22 that the shapes of the two overall curves (shown in inserts) are similar. However, the vertical orientation gives more sensitive measurements than the horizontal orientation. For example, in the distance range of interest to the small-scale bridge pier tests, the magnetic field strength dropped 1100 nT over 23 cm in the vertical orientation and 900 nT over 25 cm in the horizontal orientation. Also note that there is an ascending stage of the intensity when the magnet was oriented horizontally.

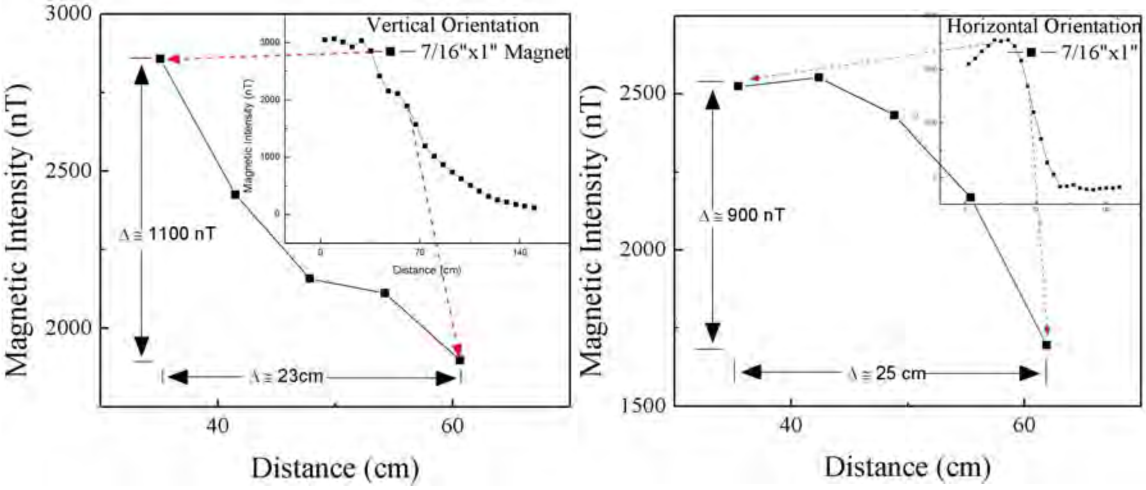

(a) Vertical Orientation (b) Horizontal Orientation

Figure 3.22 Intensity-distance Curves

Small Flume and Passive Smart Rock: The small flume used for various characterization tests of passive and active smart rocks is shown in Figure 3.23a. The velocity of water flow in the flume can be adjusted by simultaneously regulating the power of two hydraulic pumps and the angle of tail plates (see insert) at both ends of the flume. For characterization tests, passive smart rocks were made by drilling an oversize hole on a natural rock, placing a magnet into the natural rock and sealing the hole with a Great Stuff TM by DOW sealant as shown in Figure 3.23b. The magnet was embedded into the rock to demonstrate the flexibility of passive sensor encasement options and the reliability of passive sensors within the natural rock structure.

(a) Small Flume at TFHRC (b) Natural Rocks with and without an Embedded Magnet

Figure 3.23 Overview of the Small Flume and a Passive Smart Rock

Two test cases with one and two smart rocks were considered in the small flume with controllable water flow velocities. For each case, the flow velocity was increased until the passive smart rocks moved. For example, Figure 3.24 displays the movement of two smart rocks as the velocity increased. The magnetometer was placed nearby as shown in Figure 3.25 and took a continuous reading for each of these tests at 0° (the line of two sensors is perpendicular to the water flow direction).

(a) Rocks at rest (b) 1st rock rotating (c) 2nd rock moving

Figure 3.24 Movement of Two Rocks at Various Flow Velocities

Figure 3.25 Measurement with a Magnetometer in the Small Flume

The effects of rock distance, orientation, and group on magnetic field intensities were quantified in the small flume at TFHRC. To simulate a turbulence flow, an artificial block was placed inside the flume to locally increase the flow velocity as illustrated in Figure 3.24.

Figure 3.26a shows the magnetic gradient measurement from one smart rock (one magnet). Before 00:08, the smart rock was rocking back and forth at low amplitude, causing a low level disturbance on the magnetic field measurement. It was then sliding over some distance and finally rotated before it was slowly sliding away from the magnetometer.

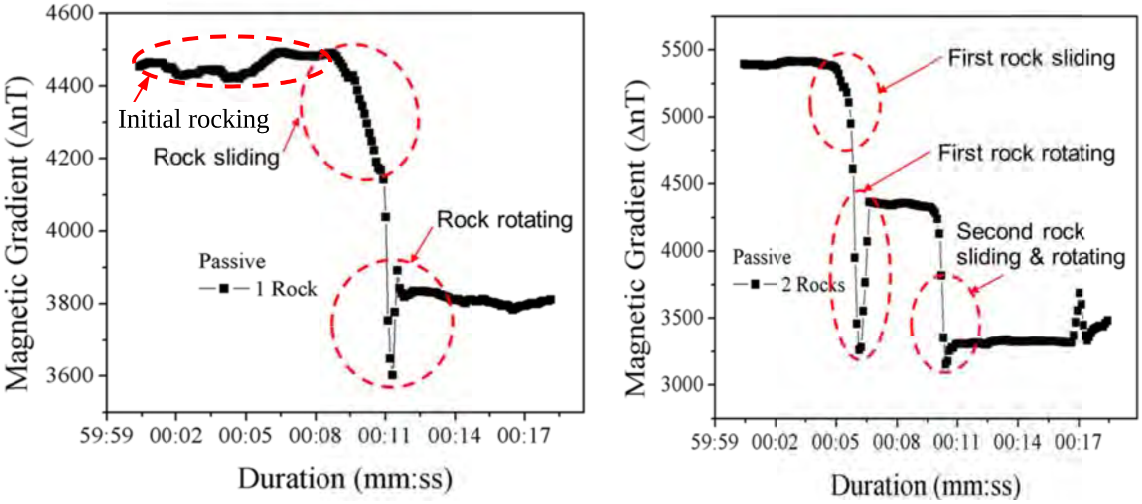

(a) One Passive Rock b) Two Passive Rocks

Figure 3.26 Test Results: Magnetic Field Gradient vs. Time

The gradient measurements from the two smart rocks are presented in Figure 3.26b. The first rock did not slide until around 00:05. Immediately after the initial sliding, the rock rotated under the increasing water flow. The first rock then remained at the same location. Meanwhile, the second rock began to slide at approximately 00:09. Immediately after that moment, the second rock almost rotated under the strong flow and then remained at the same position.

Small-Scale Bridge Scour Tests in Large Flume: Two small-scale bridge piers, circular and rectangular, were tested in the large flume as shown in Figure 3.27 to validate the proposed smart rock technology in the laboratory condition. The magnetometer was placed on top of the rectangular pier to simulate testing from the bridge deck. In order to determine if the change in magnetic field strength was due to rock moving or rotating, multiple measurements were taken approximately every 30^o for each reading period. A reading was recorded every ten minutes for the duration of the test which lasted approximately one and a half hours.

Figure 3.27 Test Setup and Details of Magnet Placement and Measurement

Throughout the scour test, visual observations on the development of the scour hole were made continuously for about 30 minutes and periodically afterward. It was visually observed that the scour depth continuingly increased for a period of 1.5 hours. About 70% of the scour hole was developed in the first half an hour. Smart rocks placed around the piers rolled at different times and then remained at the bottom of the scour hole developed over time. Three test cases with one, two, and five smart rocks were performed as described below.

First, one acrylic ball with an embedded magnet was placed in front of the rectangular pier as illustrated in Figure 3.28a. The model pier is 225 mm long (water flow direction), 750 mm wide, and approximately 500 mm deep.

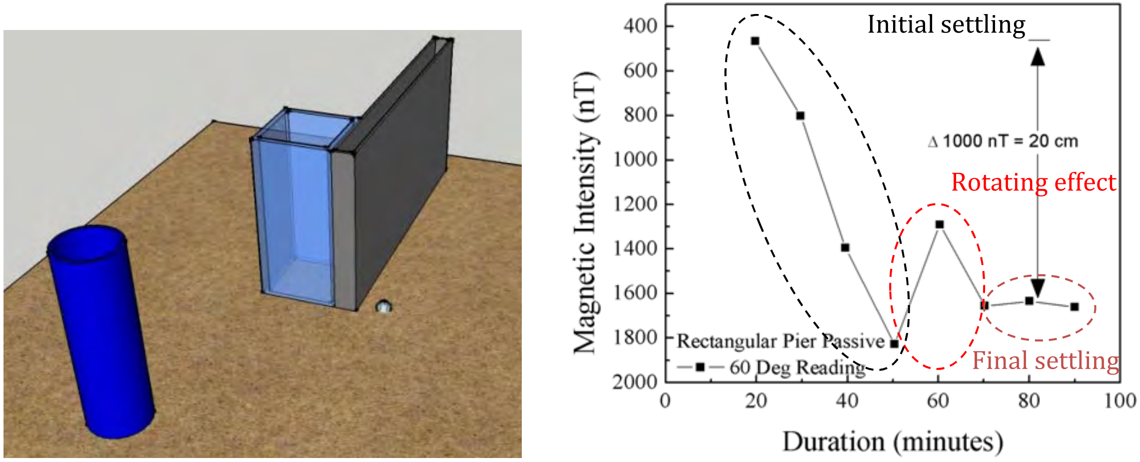

(a) One Smart Rock (b) Intensity Change over Time with Intensity-distance Correlation

Figure 3.28 Test Setup and Results with the First Scour Test

Figure 3.28b shows the change in magnetic field strength over time when the upstream flow velocity was 27 cm/sec. The overall change is approximately 1000 nT, which corresponds to a distance change of approximately 20 cm when compared with the previous test data in Figure 3.22. The post-test surface map taken from a laser device at 20 cm above the riverbed and the deepest points profile of the sand bed (D_{50}=1 mm), Figures 3.29a – 3.29c, confirm that the maximum scour at the rectangular pier was approximately 18 cm. The maximum scour depth was also verified by the post-test measurements as given in Figure 3.30. Note that the blue line and green line in Figure 3.29a represent the x–axis and y–axis deepest scour locations, respectively.

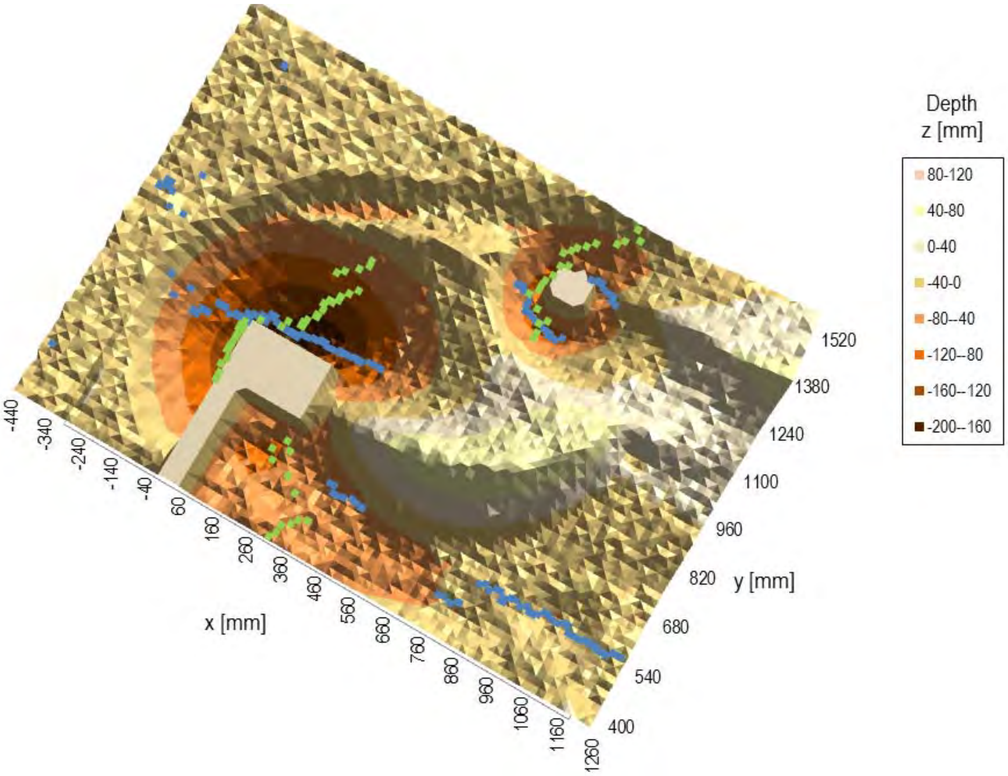

(a) Surface Mapping of the Sand Bed after the Scour Test

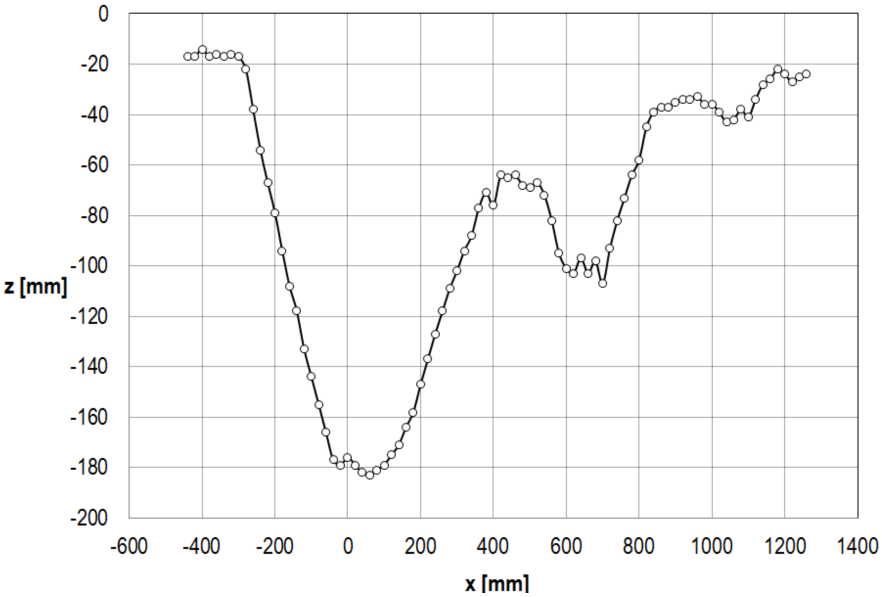

(b) *x*–axis Deepest Point Profile

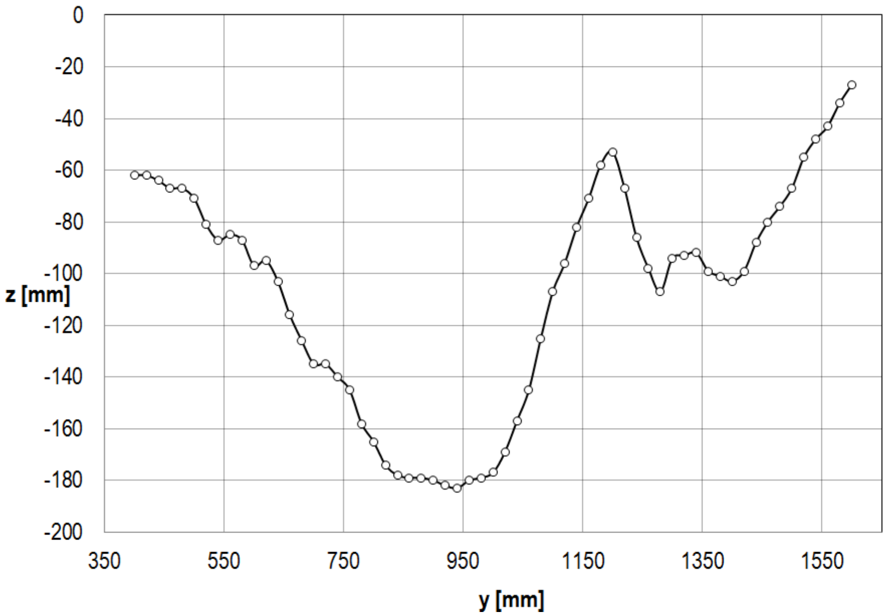

(c) *y*–axis Deepest Point Profile

Figure 3.29 Post-test Surface Mapping Results for Test One

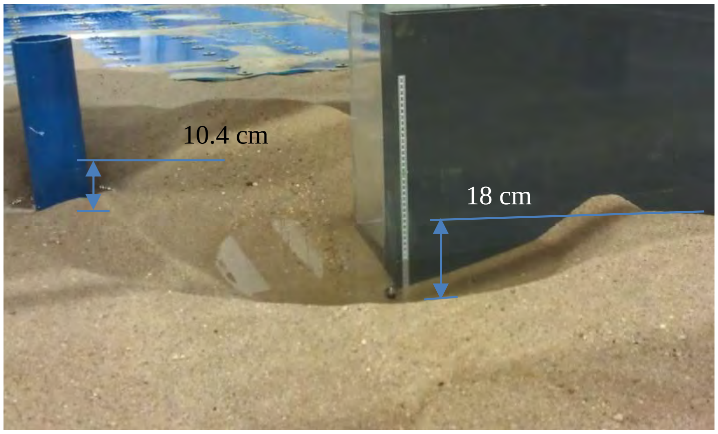

Figure 3.30 Maximum Scour Depth at the Completion of the Test

Then, two acrylic balls were placed in front of the rectangular pier and the circular pier, respectively, as shown in Figure 3.31a. The circular pier was 114.3 mm in diameter, and located 490 mm and 480 mm from the rectangular pier and the glass wall, respectively. It was situated downstream of the front face of the rectangular pier by 297 mm.

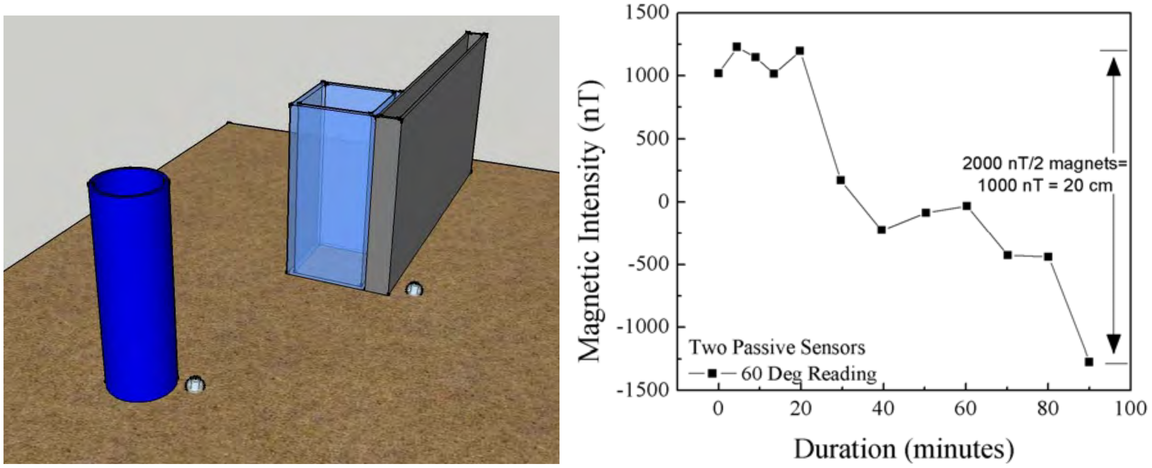

(a) Two Smart Rocks (b) Strength Change over Time with Intensity-distance Correlation

Figure 3.31 Test Setup and Results from the Second Scour Test

Figure 3.31b shows the change in magnetic field strength over time when the upstream flow velocity was 27 cm/sec. The overall change by the two rocks is 2000 nT, each contributing approximately 1000 nT. Like the first scour test, this result corresponds to a distance change of approximately 20 cm. The post-test surface map and the deepest point profile of the sand bed, Figures 3.32a – 3.32c, also confirm that the maximum scour at the rectangular pier was approximately 18 cm. However, the maximum scour depth at the circular pier is only approximately 11 cm. The magnetometer cannot distinguish between two different readings and the strength represents the combined effect of all magnetic interferences within the area. This makes it difficult to determine the depth of an individual passive smart rock if placed at different piers. This will not pose a problem in practice as bridge monitoring can be planned for one pier or two well-separated piers.

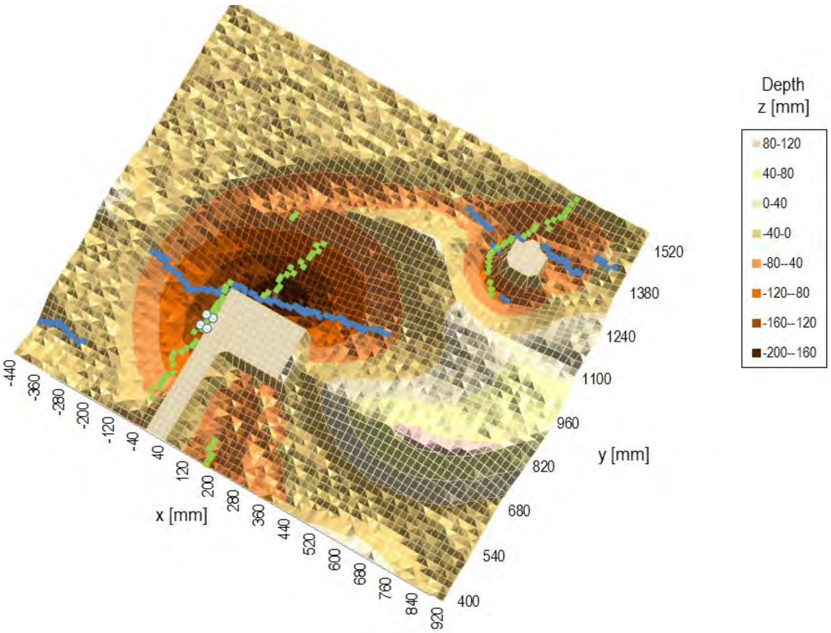

(a) Surface Mapping after the Scour Test

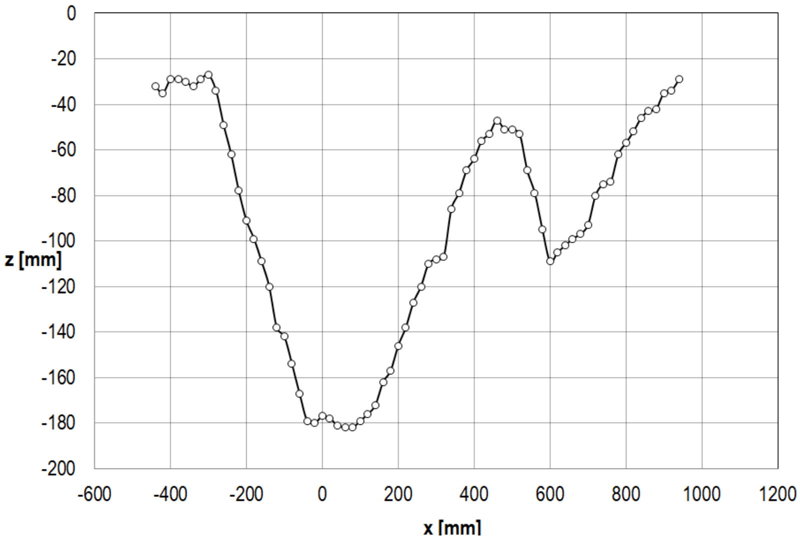

(b) *x*-axis Deepest Point Profile

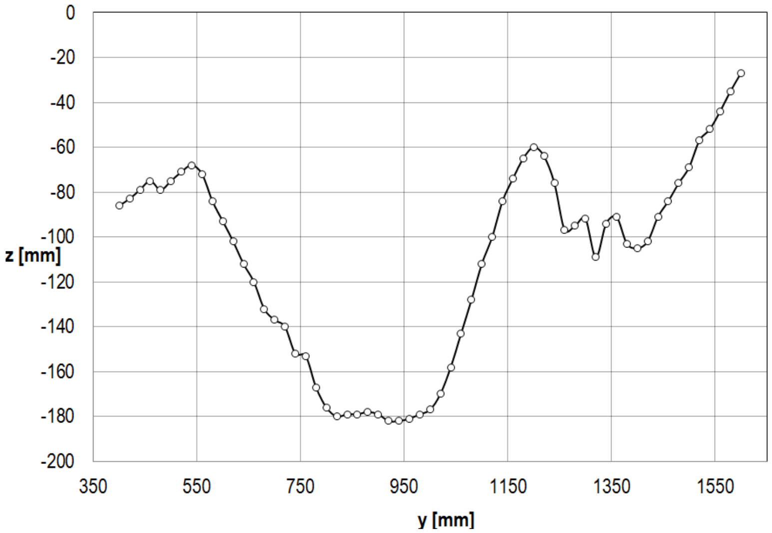

c) *y*–axis Deepest Point Profile

Figure 3.32 Post-test Surface Mapping Results for Test Two

Finally, five passive smart rocks were distributed around the rectangular bridge pier and one active sensor was deployed at the circular bridge pier. Figure 3.33a focuses on the passive sensors around the rectangular pier. Readings were taken after each passive sensor moved and joined another or every ten minutes until the final passive sensor, placed 28 cm away from the bridge pier, rolled into the scour hole and connected with the other passive sensors. Four sensors were placed directly in front of the rectangular bridge pier and connected together within the first 30 minutes of the test.

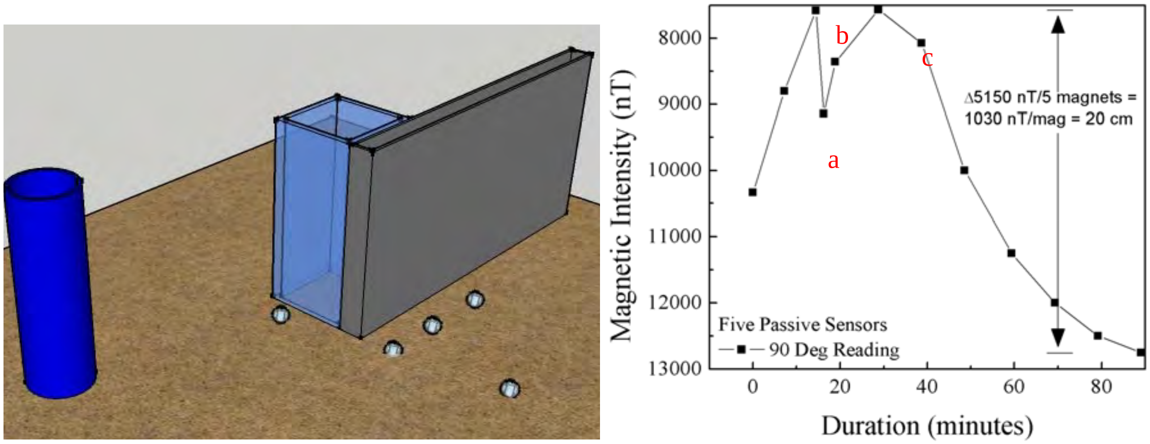

(a) Five Smart Rocks (b) Strength Chang over Time with Intensity-distance Correlation

Figure 3.33 Test Setup and Results from the Third Scour Test

Typically, the magnetic field strength doesn't increase drastically as a passive rock moves away from the magnetometer. In this case, however, as the passive rocks attached to each other, the magnetic strength actually increased. The red letters (a–c) in Figure 3.33b correlate with the scour models in Figures 3.34a – 3.34c. Figure 3.34 also illustrates the ability of the passive smart rocks to find the maximum scour location. The back smart rock actually rolled against the current to the bottom of the scour hole. The final location and orientation of the smart rocks can be seen in Figure 3.34d.

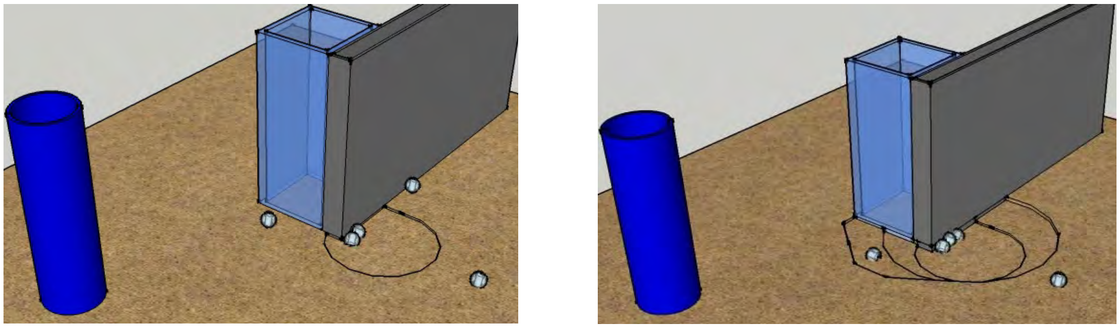

(a) First Two Rocks Connected (b) 3rd Rock Connected to the First Two

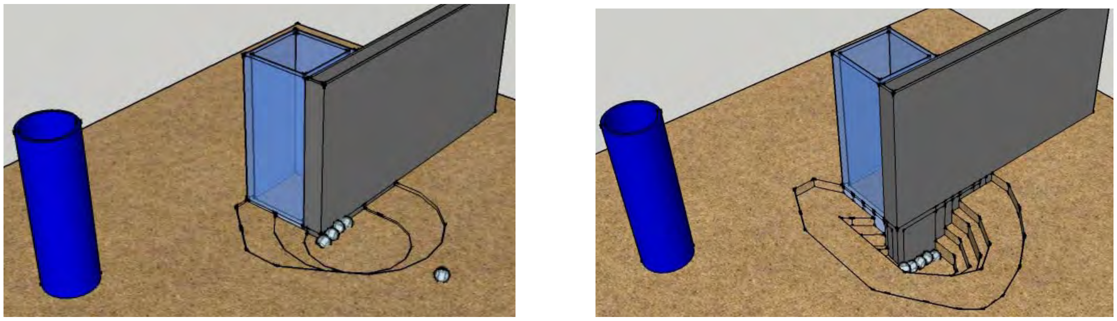

(c) 4th Sensor Connected to the First Three (d) 5th Rock Connected to the Remaining

Figure 3.34 Characteristic Behavior of Passive Smart Rocks in a Scour Event

Since there are five passive smart rocks within range of the magnetometer, the change in magnetic strength should be approximately five times greater than the correlated distance graph of Figure 3.22. Figure 3.33b shows a result of approximately 20 cm maximum scour depth, which is confirmed by the surface mapping results of Figure 3.35.

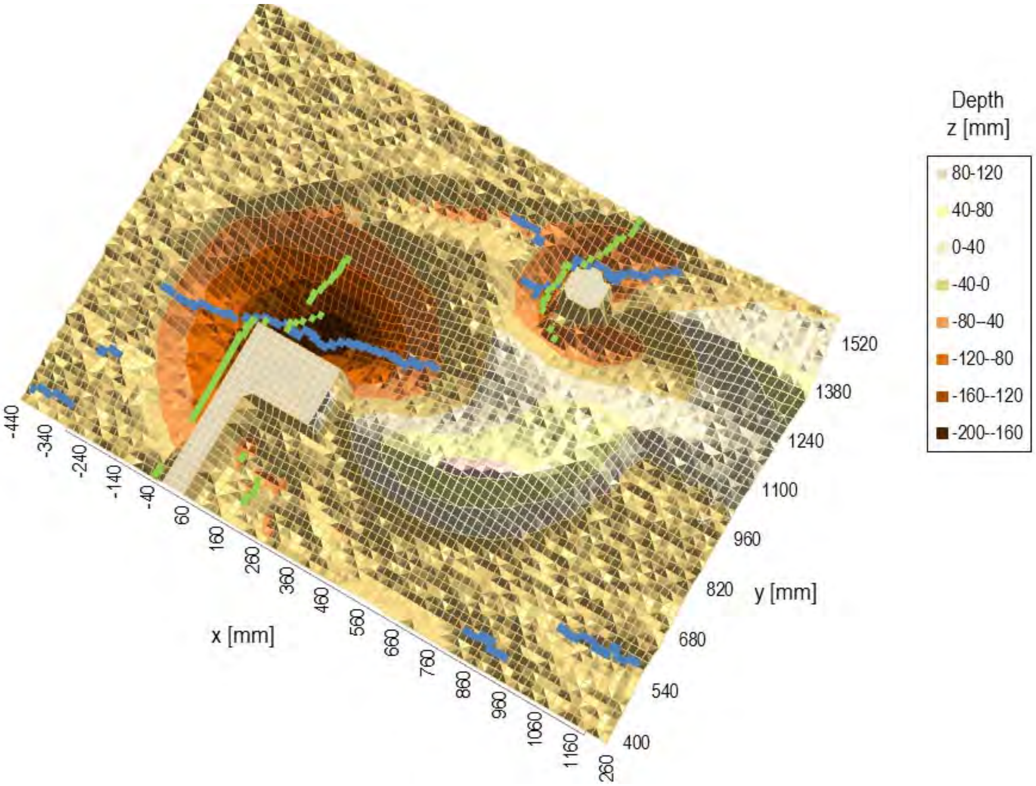

(a) Surface Mapping after the Third Scour Test

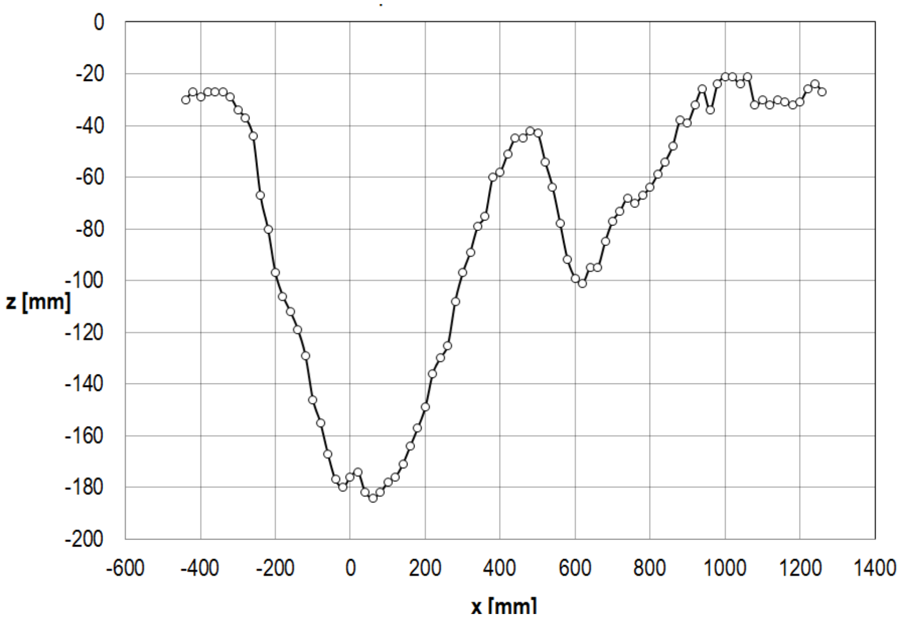

(b) *x*–axis Deepest Point Profile

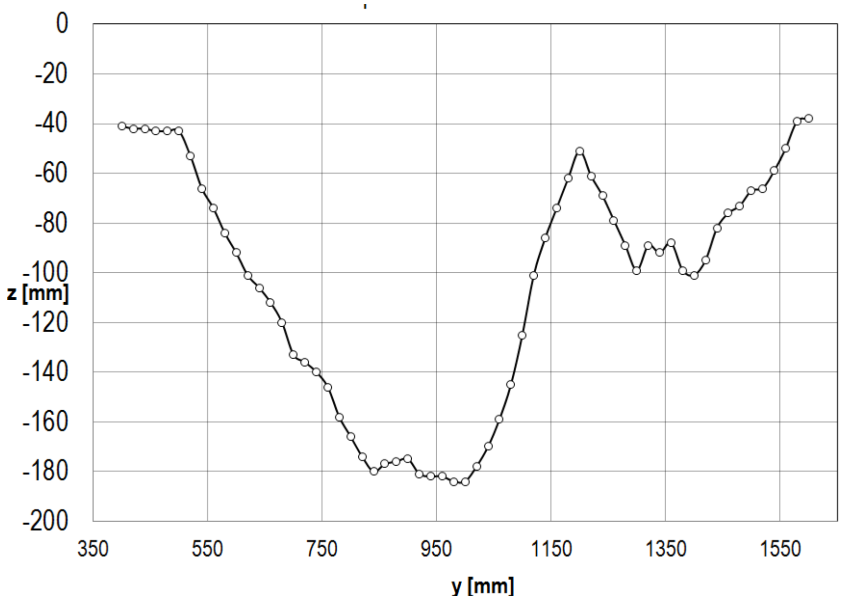

(c) *y*–axis Deepest Point Profile

Figure 3.35 Post-test Surface Mapping for Test Three

Gradient versus Individual Measurements: Figure 3.36a compares the individual readings from the two sensors of a magnetometer. Their difference was presented in Figure 3.36b as magnetic gradient. For a convenient comparison, the reading from the closest sensor was reproduced in Figure 3.36b using the same scale. By comparing Figure 3.36b with Figure 3.36b, it is observed that the gradient mainly removed the Earth's magnetic field. There is no clear sign of indication that the noise level in the gradient readings was reduced by the subtraction.

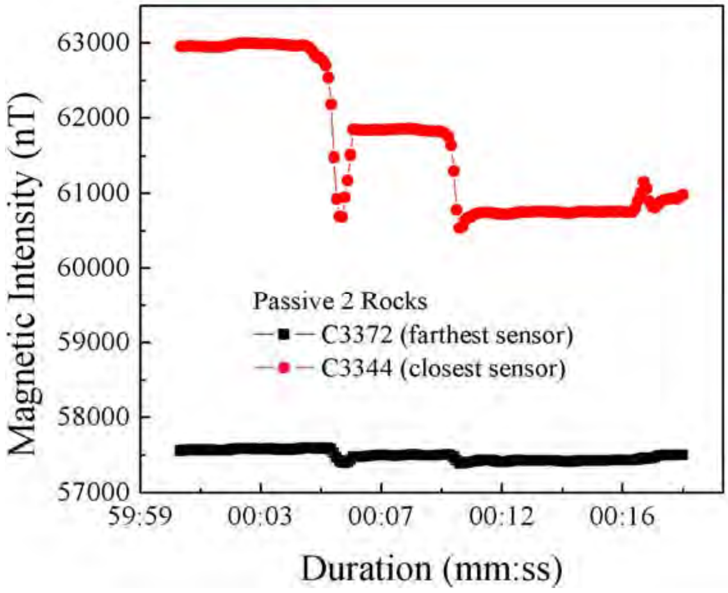

(a) Two Individual Measurements

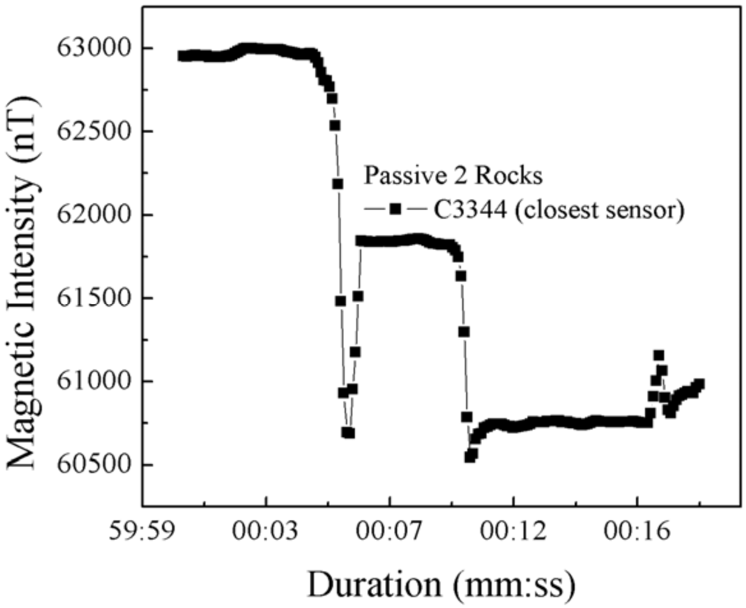

(b) Zoomed-in Measurement from One Sensor Head

Figure 3.36 Comparison between Individual and Gradient Readings

3.2.4 Intensity-distance Relations and Experimental Validations

Test Procedure and Results with a Small Magnet: The magnetic intensity was measured as a small magnet moved vertically sway from the magnetometer as illustrated in Figure 3.37. At each location, the magnet was rotated about x-, y-, and z-axis, respectively.

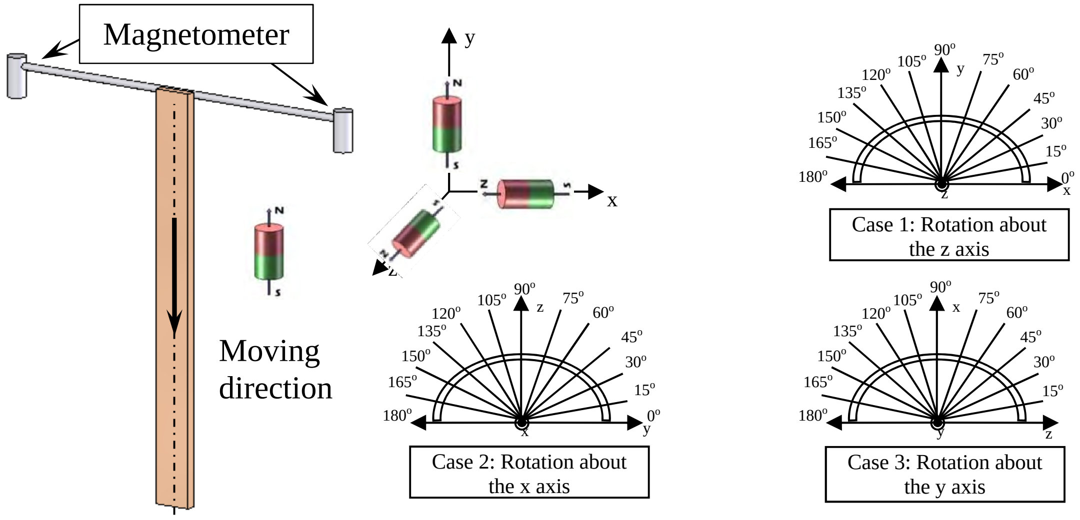

Figure 3.37 Intensity–distance Correlation Test Setup with 15° Magnet Rotations about Three Primary Axes and Vertical Change in 7.62 cm Increments

The magnet moved vertically in 76.2 mm increments from 0 to 762 mm and 152.4 mm increments from 762 to 1524 mm away from the magnetometer. At each location, the magnet was rotated about the respective axis (x-, y-, or z-) in 15° increments. A total number of 624 unique orientations were evaluated. This test was performed to simulate the movement of a smart rock at a bridge pier during a scour event.

Figures 3.38a – 3.38c display the intensity-distance correlation for each angle measurement about each axis in the desired range, approximately 38 – 70 cm (the actual distance away from the magnetometer during laboratory testing at the FHWA Hydraulics Lab). When the magnet is oriented within the strong area associated with the axis of rotation, the corresponding graph represents the decaying trend associated with the intensity-distance correlation. It has been concluded that the local discrepancies in the graphs, i.e. the graphs that do not follow the expected trend, are due to the method of data acquisition. Instead of collecting one orientation angle along the test path at one time, the orientation was changed from 0 to 180° in 15° increments before continuing along the test path. Because of this and the fact that the orientation was manually managed it is possible for the assumed angle to be slightly off and therefore creating the unexpected trend shown.

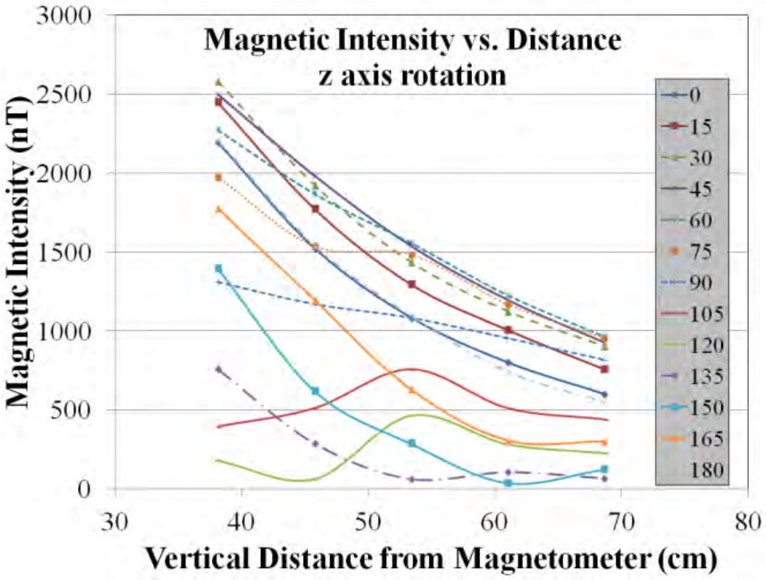

(a) Magnetic Rotation along *z*-axis

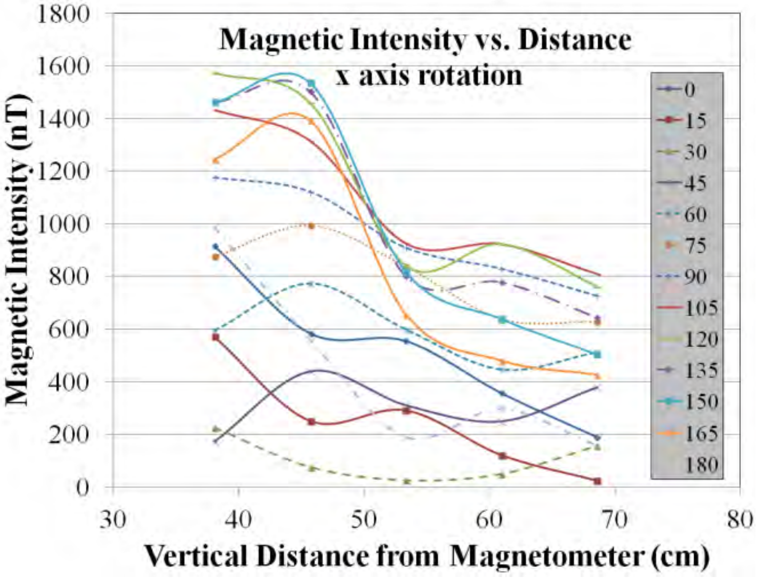

(b) Magnetic Rotation along *x*-axis

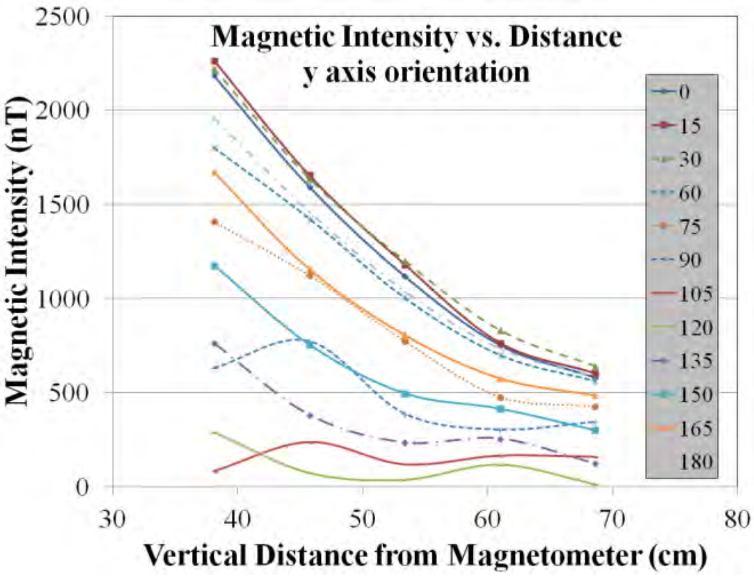

(c) Magnetic Rotation along *y*-axis

Figure 3.38 Intensity-distance Curves for Various Magnetic Orientations

The data in Figure 3.38 was re-plotted as a function of rotation angle as illustrated in Figures 3.39a – 3.39c. Clearly, the orientation of magnet has a large impact on the strength of magnetic field when the magnet at certain positions is rotated about x-, y- and z-axis, respectively. As expected, an increased depth results in a decreased magnetic intensity regardless of which axial rotation was being tested. Each orientation also shares the same general sinusoidal trend as well. Rotating about the z- or y-axis only a slight amplitude adjustment would need to be made. However, rotation about the x-axis shows not only a significant amplitude difference but also a phase shift of nearly 60°. With such database of characteristic behaviors of the tested magnet, the aim is to simulate the graph acquired from the scour testing event.

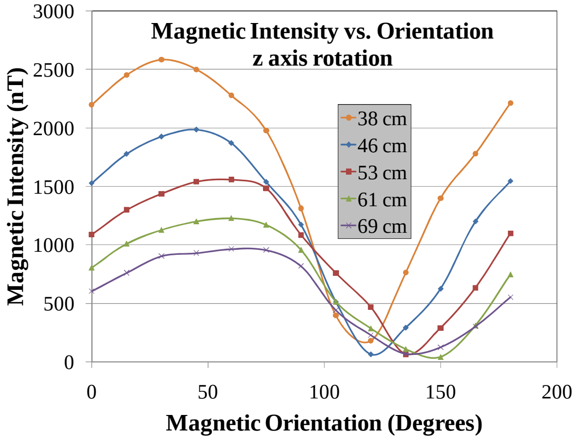

(a) Magnetic Rotation about *z*-axis

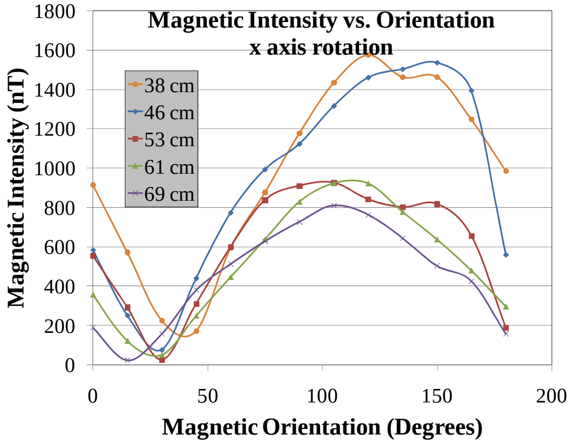

(b) Magnetic Rotation about *x*-axis

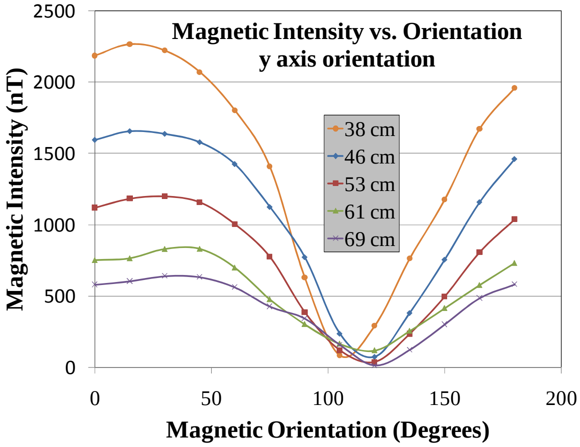

(c) Magnetic Rotation about *y*-axis

Figure 3.39 Orientation Effects at Various Distances

Scenario Reconstruction of Scour Process of the Small-scale Pier Model: Throughout the tests in the small flume, magnetic intensity readings were collected with the magnetometer at various time increments. This data was processed and displayed in the graph in Figure 3.40a. The magnetometer was located at top of the small scale pier directly over the smart rock and data was collected approximately every 10-15 minutes during the scour event.

Figure 3.40a also shows a graph derived from the characteristic behavior database. Table 3.2 displays the curve fitted data collected from the characteristic behavior database. The axis of orientation, column one, indicates which chart (Figures 3.38a – 3.38c) to look at for the given point; the second column, angle of orientation, indicates the graph used from the afore mentioned chart; and the fifth column, interpolation points, indicates which two measured points were used for interpolation to obtain the corresponding distance from the magnetometer. All interpolations were assumed to be straight lines between two points.

Figure 3.40b is the resulting scour depth over time relationship. It is not possible to obtain intermediate scour depths during the scour test to compare with the characteristic behavior. However, the trend shown seems to be representative of typical scour events. As the scour depth increases the rate of scour decreases as shown. While this derived solution is not unique (other orientations could be found for the tested case) it does exemplify the potential to predict and discern the difference between an orientation effect and a distance effect.

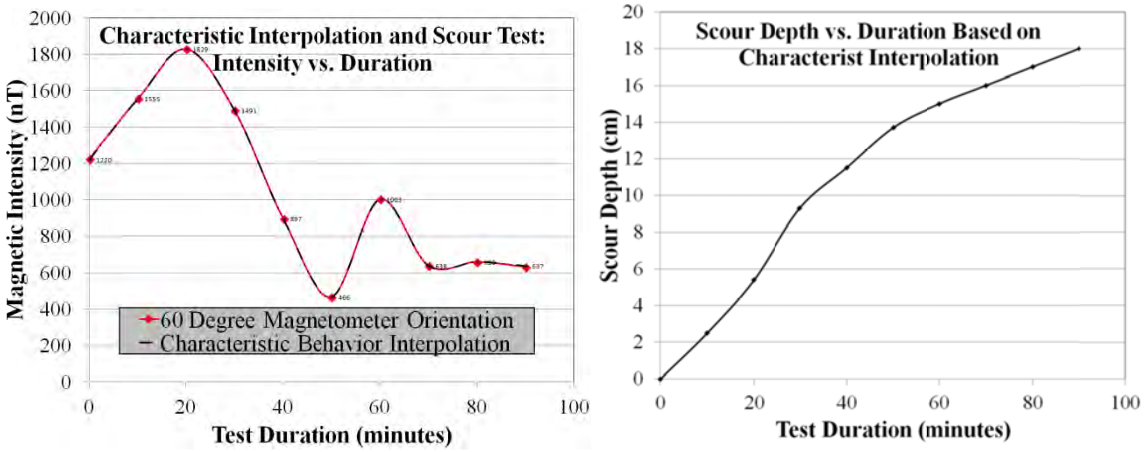

(a) Characteristic Behavior (b) Scour Scenario Derived from Characteristic Behavior

Figure 3.40 Scour Process Scenario Derived from Characteristic Behavior

Table 3.2 Characteristic Behavior Curve Fit Data Compared to Scour Test Measurements

Axis of Orientation	Angle of Orientation	Scour Depth	Time of Measurement	Interpolation Points	Characteristic Measurement	Actual Test Results
Units	Degrees	cm	minutes	nT	nT	nT
z	90	0	0	1310, 1171	1220	1225
z	75	2.5	10	1975, 1537	1555	1555.3
z	45	5.4	20	1984, 1540	1829	1828.5
z	75	9.3	30	1537, 1484	1491	1491.3
y	75	11.5	40	1184, 766.5	897	897.4
x	0	13.7	50	554, 356	466	466.2
z	180	15	60	1084, 955.4	1003	1003.2
y	165	16	70	808, 578	638	637.9
x	150	17	80	837, 637	659	659.5
x	150	18	90	637	637	632.3

Intensity-distance Curves of a Large Magnet: To acquire cleaner characteristic behavior data from the prototype smart rock (102 mm or 4 in. in diameter), more tests were conducted with stronger control over the variables using a test apparatus. As a result, the characteristic behavior is more predictable and agrees with the equations relating magnetic intensity with distance from the magnet. Figure 3.41a – 3.41c compares the overall trend of the orientation effect with respect to rotation about the respective axis at each distance between the magnet (smart rock) and the measuring device (magnetometer) for various orientations.

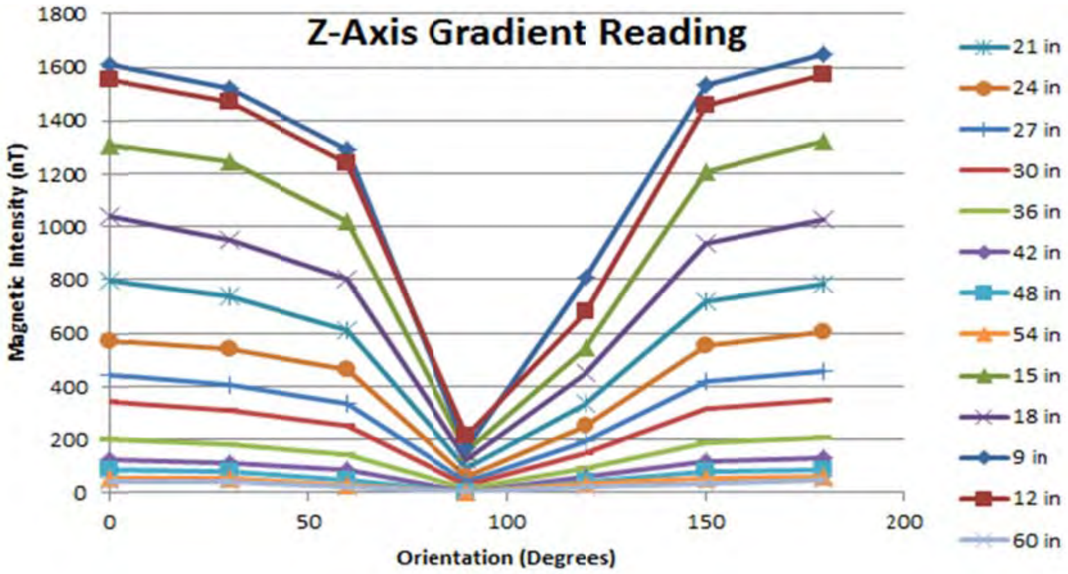

a) Rotation about *z*-axis

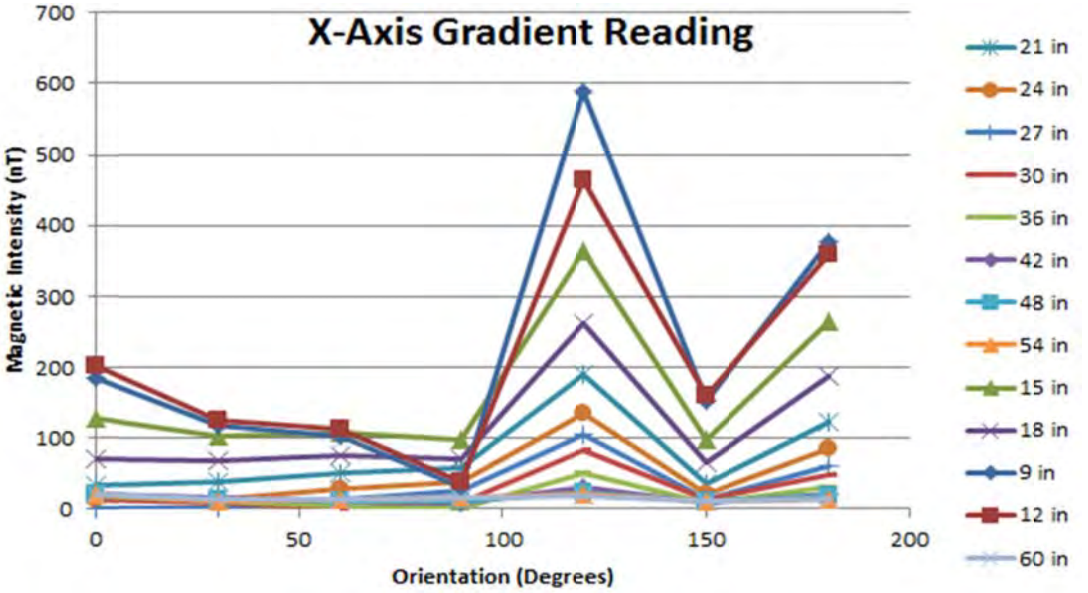

b) Rotation about *x*-axis

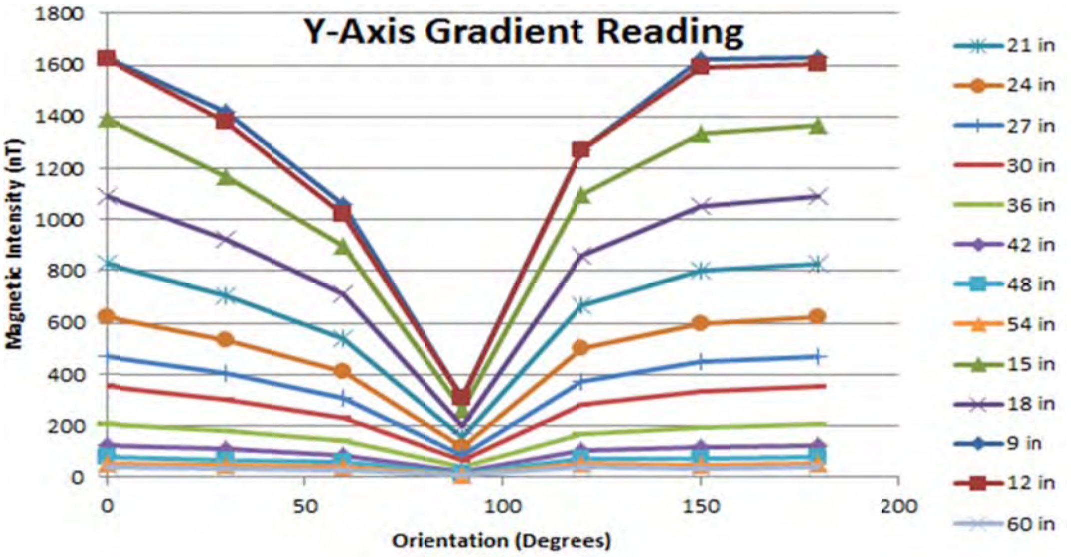

c) Rotation about *y*-axis

Figure 3.41 Comparison of the Orientation Effects along Vertical Distance Changes

Alternatively, Figure 3.42a – 3.42c compares the overall trend of the distance effect with respect to rotation about the respective axis or the relative orientation between the magnet (smart rock) and the measuring device (magnetometer). By fixing the orientation of the smart rock with respect to the magnetometer and varying the vertical distance between the two, cleaner intensity readings were recorded and plotted to emulate the natural trend of magnetic intensity as the distance increases. Note that the two measurements at short distances with 90° rotation appear to be outliers that are likely affected by the test setup.

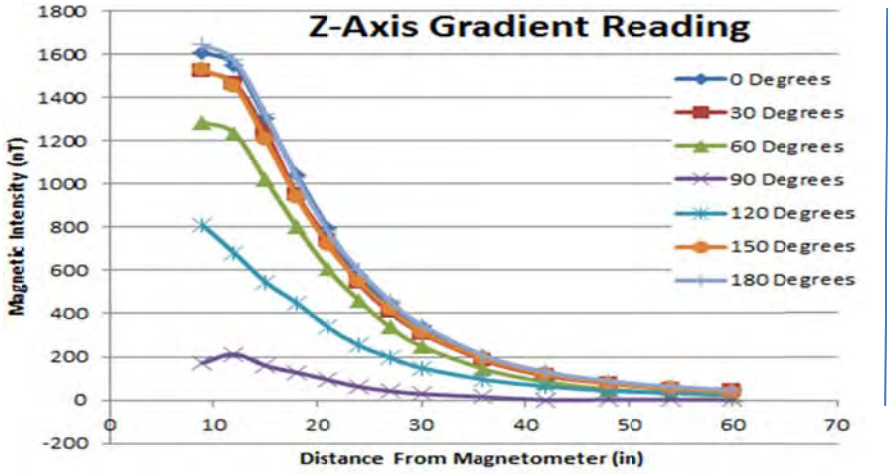

(a) Rotation about *z*-axis

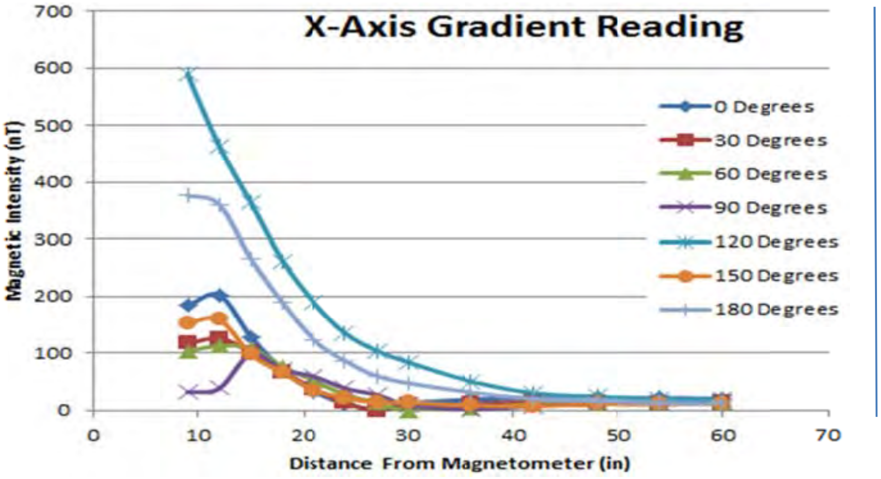

(b) Rotation about *x*-axis

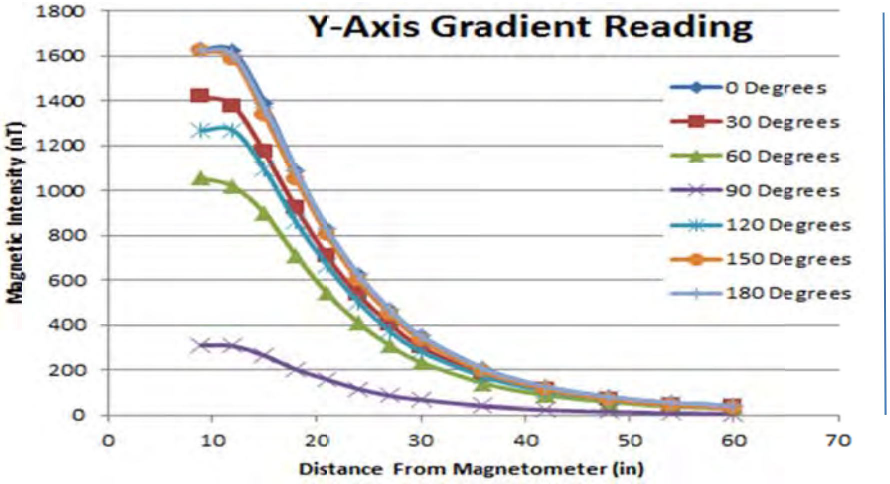

(c) Rotation about *y*-axis

Figure 3.42 Comparison of the Distance Effect along Smart Rock Orientation Changes

Design and Casting of Passive Smart Rocks for Bridge Tests: For field tests at bridge sites, two types of spherical concrete blocks with embedded magnets were cast to represent smart rocks. They included one cylindrical neodymium manget and two magnets placed in series for a larger dipole moment, respectively. Each magnet was 102 mm (4″) in diamter and 51 mm (2″) in height/length. Normal weight concrete with a specific gravity of 2.4 was used. The magnets used had a specific gravity of 7.5. The goal of passive smart rock designs was to encase magnets in concrete so that a specific gravity of at least 2.0 can be achieved. To achieve this goal, the only restriction to the passive smart rock design was geometric. Since these magnets are rare earth magnets and very brittle, a concrete cover of at least 51 mm (2″) was desired. To consider the same overall dimentions of the two smart rocks, the stronger smart rock with two magnets was the limiting factor; it was designed as a spherical concrete block with 254 mm (10″) in diameter as shown in Figure 3.43a. Figure 3.43b shows the finishing product of two prototype smark rocks for field testing. Figures 3.44a and 3.44b illustrate the casting process of spherical concrete blocks with embedded magnet.

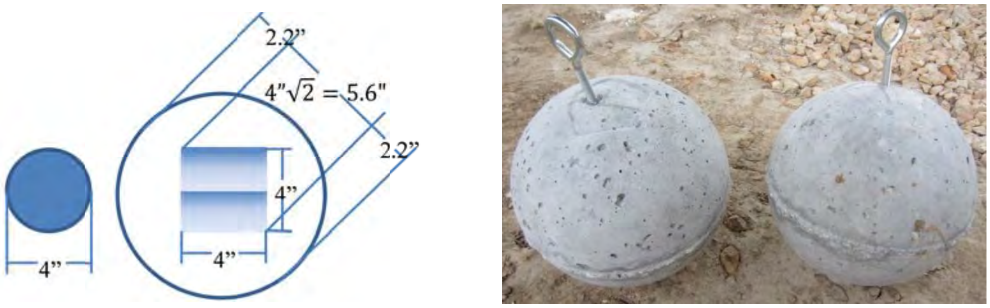

(a) Geometry of Magnets and Encasement (b) Prototype in Spherical Shape

Figure 4.43 Design and Prototype of Magnets and Passive Smart Rocks

(a) Bottom Half a Concrete Encasement (b) Top Half of a Concrete Encasement

Figure 3.44 Placement of a Magnet and Casting of Spherical Concrete Block

Field Test Procedure and Matrices: At the I-44 Roubidoux Creek Bridge, Pulaski County, MO, two groups of 12 tests were conducted on October 3, 2012, and summarized in Table 3.3. One group of tests (all but Case 8 in Table 3.3) were performed with the magnetometer set at predetermined locations, as illustrated in Figure 3.45, while a smart rock was manually dragged in parallel with Pier 7 as shown in Figure 3.46 between downstream (north or N) and upstream (south or S). The other group of tests (Case 8 in Table 3.3) were performed after one smart rock was settled about 1.2 m (4′) east of Pier 7 while the magnetometer was moved slowly on the north shoulder of the bridge deck. Each test case in one line orientation of the two magnetometer sensor heads as defined in Table 3.3 was performed four times to understand the repeatability of test data. For convenience in discussion, a test identification (ID) code (bridge identification:case number:line orientation of two sensor heads) was developed. For example, 44:01:0 represents the test case #1 of I-44 bridge with the two magnetometer sensor heads oriented along the river flow direction.

Figure 3.45 I-44 Roubidoux Creek Bridge, Pulaski County, MO Test Layout

Figure 3.46 Manual Movement of a Prototype Smart Rock near a Bridge Pier

Table 3.3 Test Matrix for I-44 Roubidoux Creek Bridge Supporting Westbound Traffic

Case	Magnetometer Location	Sensor Heads Orientation		Magnetomer Movement	Smart Rock Movement	Note
1	Underneath the bridge near Pier 8 (west side)	90	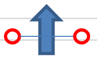	Fixed	N -> S	The weaker smart rock was moved slowly.
		90		Fixed	S -> N	
		90		Fixed	N -> S	
		90	River flow	Fixed	S -> N	
		0	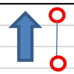	Fixed	N -> S	
		0		Fixed	S -> N	
		0		Fixed	N -> S	
		0	River flow	Fixed	S -> N	
2	On the downstream shoulder of bridge deck at Pier 7	0	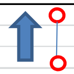	Fixed	N -> S	
		0		Fixed	S -> N	
		0		Fixed	N -> S	
		0	River flow	Fixed	S -> N	
3	On the downstream shoulder of bridge deck at Pier 8	0	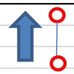	Fixed	N -> S	
		0		Fixed	S -> N	
		0		Fixed	N -> S	
		0	River flow	Fixed	S -> N	
4	On the downstream shoulder of bridge deck at Pier 6	0	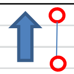	Fixed	N -> S	
		0		Fixed	S -> N	
		0		Fixed	N -> S	
		0	River flow	Fixed	S -> N	
5	On the downstream shoulder of bridge deck at Pier 6	0	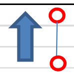	Fixed	Fixed	The weaker smart rock was placed at the bottom of the river at 4 ft away from Pier 7 (east side).
		0		Fixed	Fixed	
		0		Fixed	Fixed	
		0	River flow	Fixed	Fixed	
6	On the downstream shoulder of bridge deck at Pier 7	0	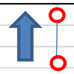	Fixed	Fixed	
		0		Fixed	Fixed	
		0		Fixed	Fixed	
		0	River flow	Fixed	Fixed	
7	On the downstream shoulder of bridge deck at Pier 8	90	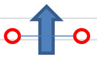	Fixed	Fixed	
		90		Fixed	Fixed	
		90		Fixed	Fixed	
		90	River flow	Fixed	Fixed	
		0	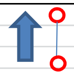	Fixed	Fixed	
		0		Fixed	Fixed	
		0		Fixed	Fixed	
		0	River flow	Fixed	Fixed	
8	On the downstream shoulder of bridge deck slowly moved between Pier 8 to Pier 6	90	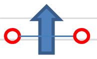	Pier 8 to Pier 6	Fixed	
		90		Pier 6 to Pier 8	Fixed	
		90		Pier 8 to Pier 6	Fixed	
		90	River flow	Pier 6 to Pier 8	Fixed	
		0	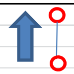	Pier 8 to Pier 6	Fixed	
		0		Pier 6 to Pier 8	Fixed	
		0		Pier 8 to Pier 6	Fixed	
		0	River flow	Pier 6 to Pier 8	Fixed	
9	On the downstream shoulder of bridge deck at Pier 8	90	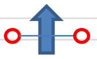	Fixed	N -> S	The weaker smart rock was placed at the bottom of the river at 4 ft away from Pier 7. The stronger smart rock was slowly moved along Pier 8 (west side).
		90		Fixed	S -> N	
		90		Fixed	N -> S	
		90	River flow	Fixed	S -> N	
		0	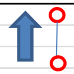	Fixed	N -> S	
		0		Fixed	S -> N	
		0		Fixed	N -> S	
		0	River flow	Fixed	S -> N	
10	On the downstream shoulder of bridge deck at Pier 7	90	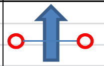	Fixed	N -> S	
		90		Fixed	S -> N	
		90		Fixed	N -> S	
		90	River flow	Fixed	S -> N	
		0	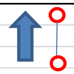	Fixed	N -> S	
		0		Fixed	S -> N	
		0		Fixed	N -> S	
		0	River flow	Fixed	S -> N	
11	on the shoulder of bridge near downstream at Pier 6	90	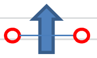	Fixed	N -> S	
		90		Fixed	S -> N	
		90		Fixed	N -> S	
		90	River flow	Fixed	S -> N	
		0	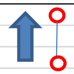	Fixed	S -> N	
		0		Fixed	N -> S	
		0		Fixed	S -> N	
			River flow			
12	Underneath the bridge near Pier 8 (west side)	90	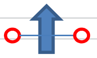	Fixed	N -> S	
		90		Fixed	S -> N	
		90		Fixed	N -> S	
		90	River flow	Fixed	S -> N	
		0	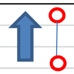	Fixed	N -> S	
		0		Fixed	S -> N	
		0		Fixed	N -> S	
		0	River flow	Fixed	S -> N	

Field Test Results and Discussion: Figures 3.47-3.49 present a consolidated sample of data collected from the passive sensor testing at Roubidoux Creek. Figures 3.47a – 3.47c represent the gradient change when the magnetometer remained stationary and the passive smart rock was moved along the same path between downstream (north or N) and upstream (south or S). Though the smart rock was moved along the same path each time, the distance from the magnetometer is different when the magnetometer was located in Pier 6 to Pier 8. As the magnetometer was relocated further from the sensor path, the angle spanned from the magnetometer to Point A (farthest upstream) and Point B (farthest downstream) decreased, which in turn reduced the change in distance experienced by the magnetometer and resulted in less change in magnetic gradient measurement from Pier 7 to Pier 6 or Pier 8.

Figures 3.47a – 3.47c demonstrate a general decaying trend of the magnetic field intensity as the smart rock moves away from the magnetometer. The local fluctuations along this trend are likely due to the change in magnetic orientation as the smart rock was dragged and moved along the riverbed topography.

Figure 3.48 presents the magnetic field gradient as a function of distance as the magnetomter was moved away from Pier 6 to Pier 8 when the weaker smart rock was placed near Pier 7. While the overall trend of the intensity-distance curve is the decreasing of magnetic intensity with distane, a significant fluctuation exists in this case likely due to different blind zone effects of the sensor heads and abrupt change in near-field magnetic strength as indicated in Figures 3.9 and 3.10. Note that the span length between Piers 6 and 7 is 24.4 m (80′) while the span length between Piers 7 and 8 is 30.5 m (100′).

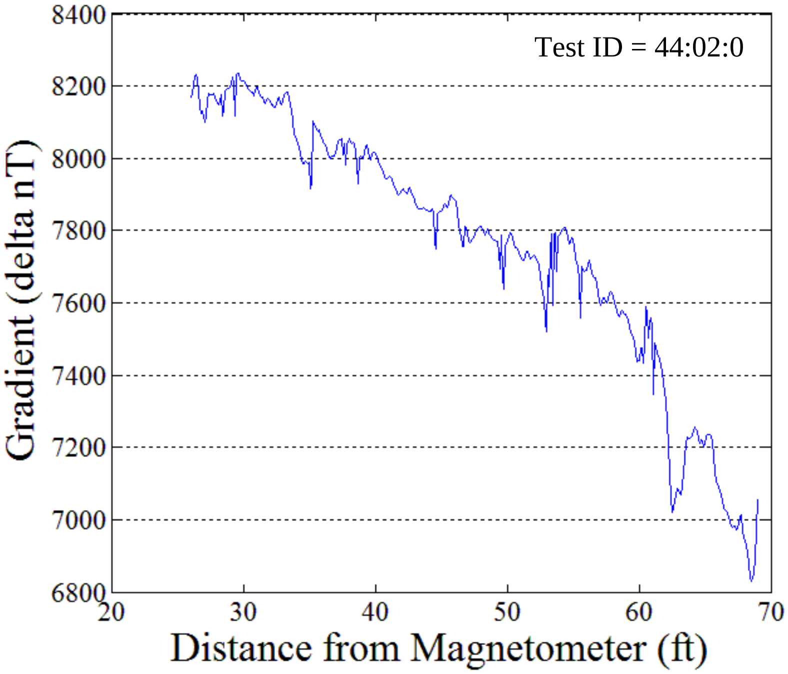

(a) Magnetometer Stationed above Pier 7

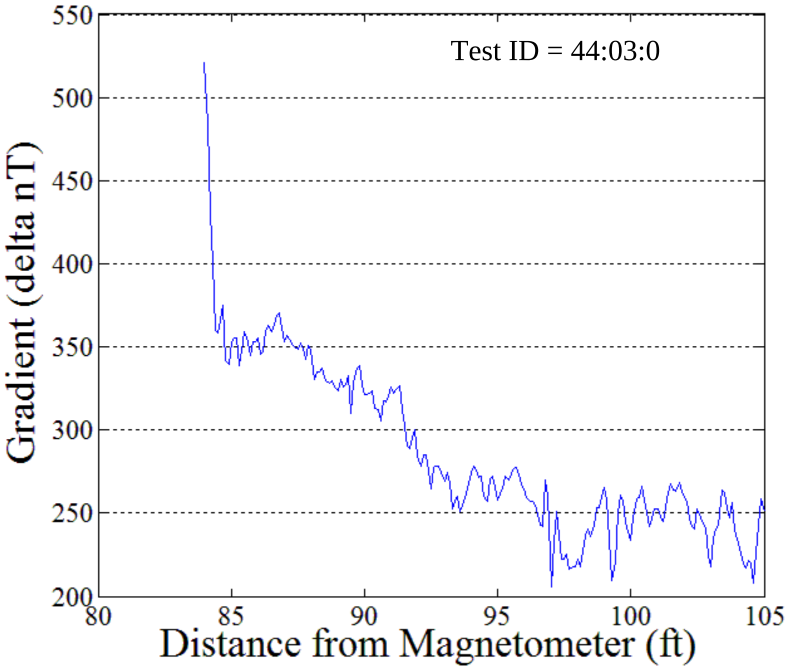

(b) Magnetometer Stationed above Pier 8

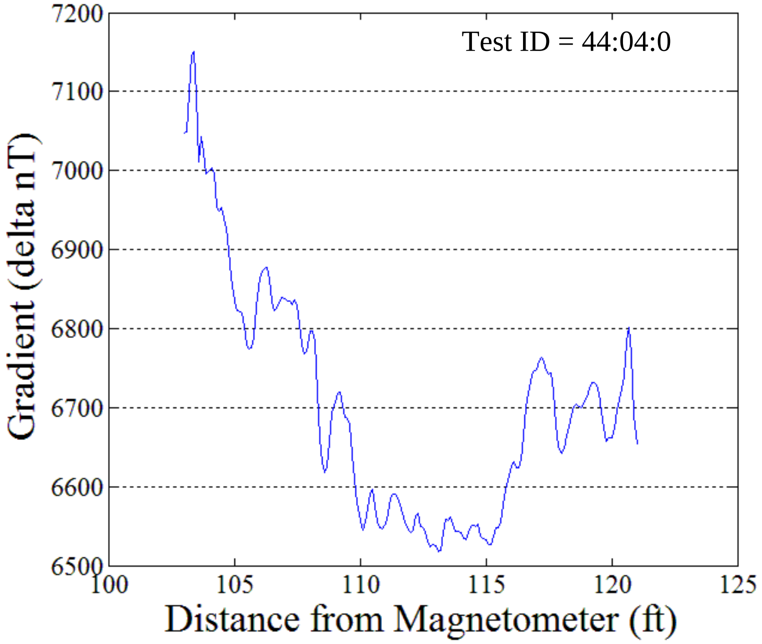

(c) Magnetometer Sationed above Pier 6

Figure 3.47 Magnetic Gradient versus Distance Relations

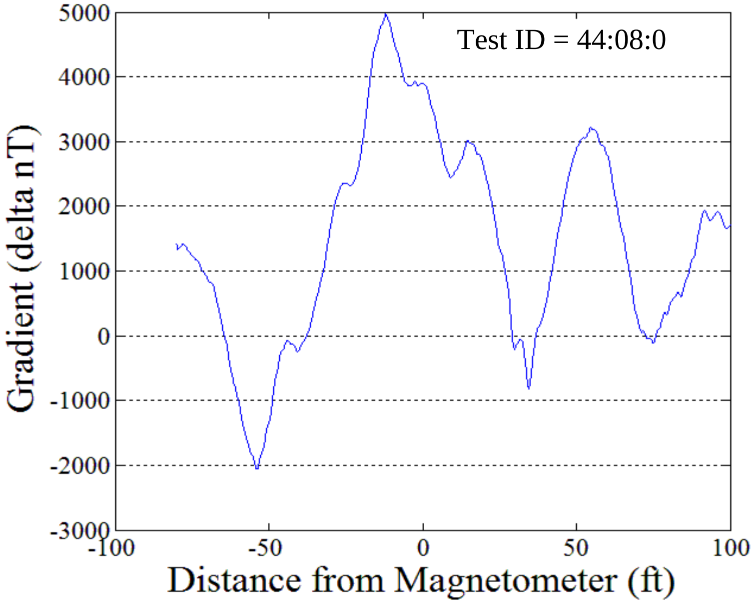

Figure 3.48 Magnetometer Movement from the Smart Rock at 1.22 m from Pier 7

Figures 3.49a – 3.49d confirm the same trend as indicated by Figures 3.47a – 3.47c. However, the field intensities in Figures 3.49a – 3.49d seem to decrease with distance more rapidly than those in Figures 3.47a – 3.47c since they were measured with two sensor heads of the magnetometer aligned perpendicular to the water flow direction. Additionally, these tests were performed with the weaker smart rock placed at the bottom of the river 1.22 m (4 ft) away from Pier 7 and the stronger smart rock was moved along the river bank on the west side of Pier 8. The distance in Figures 3.49a – 3.49d was measured from Pier 8 instead of Pier 7 in Figures 3.47a - 3.47c and Figure 3.48. Each individual test point given in Figures 3.47 – 3.49 represents an average of four (except for Case 11 with three data points) runs of the same test with the same parameters. However, a few variables were not controlled during the test to replicate a practical application. For example, the orientation of the two sensor heads of the magnetometer as it is moved along the path cannot be percisely controlled and may thus cause a slight change between different tests. By taking an average of four test runs, this change can be minimized.

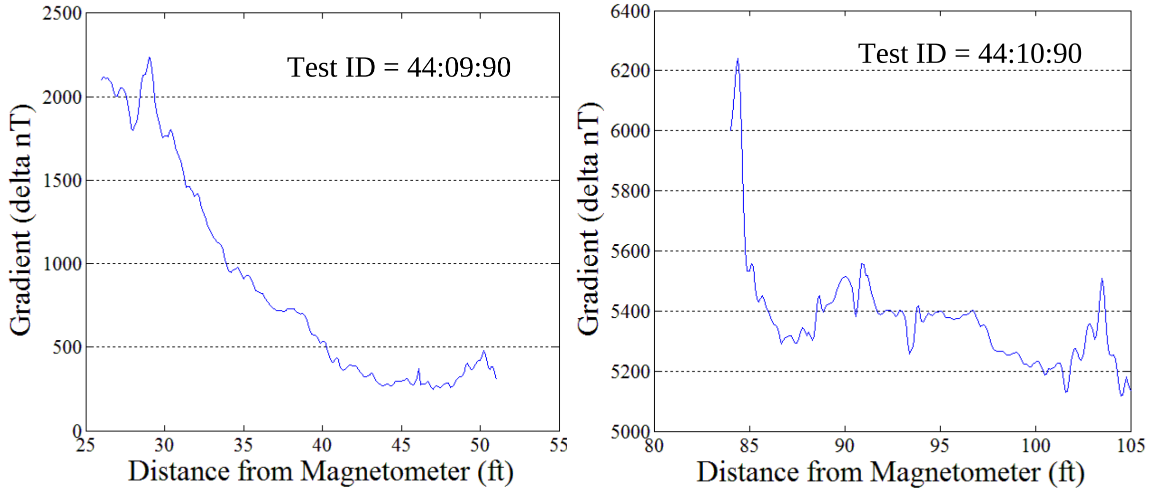

(a) Magnetometer at Pier 8 (b) Magnetometer at Pier 7

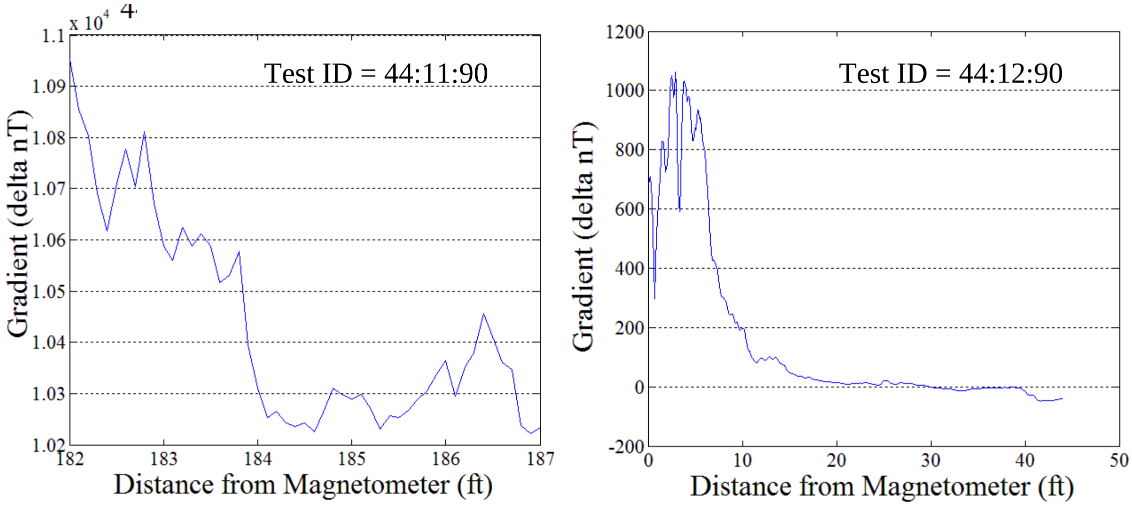

(c) Magnetometer at Pier 6 (d) Magnetometer at Pier 8

Figure 3.49 Magnetic Field Gradient versus Measurement Distance when Weaker Smart Rock Placed at 1.22 m east of Pier 7 and Stronger Smart Rock Moved near Pier 8

Concluding Remarks on Field Tests: The data acquired from this series of tests at Roubidoux Creek show promise in utilizing rare Earth magnets and a magnetometer as a passive sensing system for bridge scour monitoring as scour occurs. The overall decaying trend is consistent and repeatable as demonstrated with local fluctuations due to changing orientation of the neodymium magnet. Note that the results obtained from the two bridges are consistent. On October 4, 2013, one smart rock was retrieved as shown in Figure 3.50 after the August 7, 2013, flood event. The smart rock was found in the small hole near the foundation of the pier in US63 Bridge. It appeared in a good condition and remained effective for magnetic field intensity measurement.

Figure 3.50 Retrieved Passive Smart Rock after the August 7, 2013 Flood

3.3 Localization of a Magnet with Unknown Orientation

Figure 3.6 illustrates the magnetic fields of the Earth and a permanent magnet that is oriented towards the North Pole or near geographical south of the Earth. However, Section 3.2.2 repeatedly demonstrated the significant influence of magnet orientation on the intensity-distance relation. In general cases, the orientation of the magnet is unknown and the total intensity of the combined Earth and magnet's magnetic fields is derived below.

3.3.1 General Solution of the Total Magnetic Field

For a general case, the orientation of a magnet can be defined by three rotational angles (α, β, γ) with respect to a reference coordinate system as shown in Figure 3.6. Here, the reference coordinate system is referred to as XYZ as illustrated in Figure 3.51. The general position of the magnet is defined in the new coordinate system xyz with y-axis pointing to the south pole of the magnet, which is also shown in Figure 3.51. The new coordinate system can be established by first rotating the XYZ coordinate system around X-axis by α angle, then around Y-axis by β angle, and finally around Z-axis by γ angle, respectively. The final position of the rotated XYZ coordinate system is represented by the new xyz coordinate system.

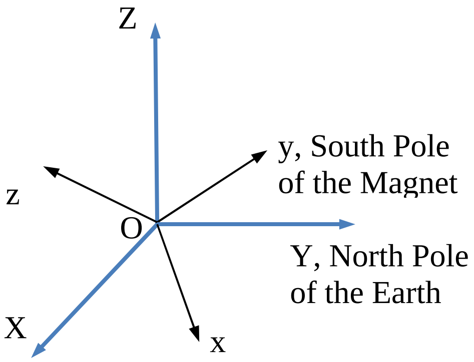

Figure 3.51 Reference (XYZ) and New (xyz) Coordinate Systems

For each rotation about X-axis, Y-axis, or Z-axis, the old and new positions of the XYZ coordinate system can be related to each other by a transformation matrix $\mathbf{T}_X$, $\mathbf{T}_Y$, and $\mathbf{T}_Z$, respectively. By simple derivations, the transformation matrices can be expressed into:

$$\mathbf{T}_X = \begin{bmatrix} 1 & 0 & 0 \\ 0 & \cos\alpha & \sin\alpha \\ 0 & -\sin\alpha & \cos\alpha \end{bmatrix}, \ \mathbf{T}_Y = \begin{bmatrix} \cos\beta & 0 & -\sin\beta \\ 0 & 1 & 0 \\ \sin\beta & 0 & \cos\beta \end{bmatrix}, \ \mathbf{T}_Z = \begin{bmatrix} \cos\gamma & \sin\gamma & 0 \\ -\sin\gamma & \cos\gamma & 0 \\ 0 & 0 & 1 \end{bmatrix} \tag{3.6}$$

Therefore, the total transformation matrix from the XYZ coordinate system to the xyz coordinate system can be expressed into:

$$\mathbf{T} = \mathbf{T}_Z\mathbf{T}_Y\mathbf{T}_X = \begin{bmatrix} a_{xX} & a_{xY} & a_{xZ} \\ a_{yX} & a_{yY} & a_{yZ} \\ a_{zX} & a_{zY} & a_{zZ} \end{bmatrix}$$

$$= \begin{bmatrix} \cos\beta\cos\gamma & \cos\alpha\sin\gamma + \sin\alpha\sin\beta\cos\gamma & \sin\alpha\sin\gamma - \cos\alpha\sin\beta\cos\gamma \\ -\cos\beta\sin\gamma & \cos\alpha\cos\gamma - \sin\alpha\sin\beta\sin\gamma & \sin\alpha\cos\gamma + \cos\alpha\sin\beta\sin\gamma \\ \sin\beta & -\sin\alpha\cos\beta & \cos\alpha\cos\beta \end{bmatrix} \tag{3.7}$$

in which each column of Matrix **T** represents the directional cosine factors of X, Y, or Z axis in the new coordinate system xyz. In other words, the coordinates (x, y, z) of any point in the new xyz coordinate system can be related to the coordinates (X, Y, Z) in the XYZ coordinate system by the **T** matrix.

The approximate magnetic field intensity of a magnet can be derived in exactly the same way as Eq. (3.3). The components of the Earth's magnetic field in XYZ coordinate system can be expressed into $\begin{Bmatrix} 0 & B_E\cos\theta & B_E\sin\theta \end{Bmatrix}^T$. In the xyz coordinate system, the intensity components can be transformed into:

$$\begin{bmatrix} a_{xX} & a_{xY} & a_{xZ} \\ a_{yX} & a_{yY} & a_{yZ} \\ a_{zX} & a_{zY} & a_{zZ} \end{bmatrix} \begin{Bmatrix} 0 \\ B_E \cos\theta \\ B_E \sin\theta \end{Bmatrix} = \begin{Bmatrix} B_E[\sin\gamma\cos(\theta-\alpha) - \sin\beta\cos\gamma\sin(\theta-\alpha)] \\ B_E[\cos\gamma\cos(\theta-\alpha) + \sin\beta\sin\gamma\sin(\theta-\alpha)] \\ B_E\cos\beta\sin(\theta-\alpha) \end{Bmatrix}$$

As a result, the three intensity components and the total intensity of the combined Earth and magnet magnetic fields can be expressed into:

$$B_x = k\frac{3xy}{r^5} + B_E[\sin\gamma\cos(\theta-\alpha) - \sin\beta\cos\gamma\sin(\theta-\alpha)] \tag{3.8a}$$

$$B_y = k\frac{2y^2 - x^2 - z^2}{r^5} + B_E[\cos\gamma\cos(\theta-\alpha) + \sin\beta\sin\gamma\sin(\theta-\alpha)] \tag{3.8b}$$

$$B_z = k\frac{3zy}{r^5} + B_E\cos\beta\sin(\theta-\alpha) \tag{3.8c}$$

$$B = \sqrt{B_x^2 + B_y^2 + B_z^2} \tag{3.8d}$$

in which $0 \le \alpha < 360°$, $0 \le \beta < 360°$, and $0 \le \gamma < 360°$. Note that Eq. (3.8) shows the total magnetic field intensity components when a magnet is located at the origin of the coordinate system. In general cases where a magnet is placed at coordinates (x_M, y_M, z_M), (x, y, z) in Eq. (3.8) must be changed to ($x-x_M$, $y-y_M$, $z-z_M$). Given the coefficients k and θ as well as the Earth's magnetic intensity B_E for a project site, the total magnetic intensity of the Earth and a magnet, B, at any point (x, y, z) is a function of (x_M, y_M, z_M) and (α, β, γ). To accurately determine the location and orientation of a magnet from measured total intensities, measurements must be taken at a minimum of six stations in practical applications.

3.3.2 Magnet Localization Algorithm with Unknown Orientation

Assume that n number of measurements, $B_i^{(M)}$ (i=1, 2, …, n), are taken at n stations around a bridge pier (x_i, y_i, and z_i, i=1, 2, …, n). At each station, the theoretically predicted intensity $B_i^{(P)} = B$ can be calculated when $x = x_i$, $y = y_i$, and $z = z_i$ are introduced in Eq. (3.8d). Therefore, the square-root-of-the-sum-of-the-squared (SRSS) error between the calculated intensity $B_i^{(P)}$ and the measured intensity $B_i^{(M)}$, $J(x_M, y_M, z_M, \alpha, \beta, \gamma)$, can be evaluated by:

$$J(x_M, y_M, z_M, \alpha, \beta, \gamma) = \sqrt{\sum_{i=1}^{n}[B_i^{(P)} - B_i^{(M)}]^2} \tag{3.9}$$

To minimize the SRSS error, the following six partial differential equations must be satisfied:

$$\frac{\partial J(x_M, y_M, z_M, \alpha, \beta, \gamma)}{\partial x_M} = 0 \tag{3.10a}$$

$$\frac{\partial J(x_M, y_M, z_M, \alpha, \beta, \gamma)}{\partial y_M} = 0 \tag{3.10b}$$

$$\frac{\partial J(x_M, y_M, z_M, \alpha, \beta, \gamma)}{\partial z_M} = 0 \tag{3.10c}$$

$$\frac{\partial J(x_M, y_M, z_M, \alpha, \beta, \gamma)}{\partial \alpha} = 0 \tag{3.10d}$$

$$\frac{\partial J(x_M, y_M, z_M, \alpha, \beta, \gamma)}{\partial \beta} = 0 \tag{3.10e}$$

$$\frac{\partial J(x_M, y_M, z_M, \alpha, \beta, \gamma)}{\partial \gamma} = 0 \tag{3.10f}$$

from which both the coordinates (x_M, y_M, z_M) and orientations (α, β, γ) of a permanent magnet can be determined. Note that the orientations are defined in the relative sense with respect to the Earth's geographical south.

3.4 Localization of a Magnet with Known Orientation

Eq. (3.10) gives three coordinates and three orientations of a magnet in general placement. However, it requires a significant time to derive a solution of six unknowns, which could be critical for emergency responses in real time scour monitoring and result in uncertainties as smart rocks continue rotating. Furthermore, to determine six unknowns require more measurements at various stations and the orientations of a magnet are not really needed for the practical design and maintenance of bridge foundations. Therefore, it is desirable to develop a new passive smart rock with its embedded magnet always remaining in certain direction so that only the coordinates (x, y, z) are required to be evaluated in scour monitoring and assessment.

3.4.1 An Automatically Pointing to South System

Like a compass that has been widely used for direction and navigation around the world, the magnet embedded inside a smart rock can be designed such that it always points to the North Pole or near geographical south of the Earth. Such a magnet and its supporting components constitute an Automatically Pointing to South System (APSS) proposed and developed in this study. The key to this design is to create a frictionless mechanism that makes a magnet free to rotate at all times.

Figure 3.52 shows the schematic of an APSS design. This design consists of an inside organic glass ball, an outside organic glass ball, liquid filled in between the two balls, one cylindrical magnet placed into the inside ball, a level indicator, and some copper beads distributed as balanced weights. The magnet is 10 cm in diameter and 5 cm in height. Its side face is glued to the surface of the inside ball with a diameter of *d*. The outside ball has a diameter of *D*. The inside ball with the magnet, the level indicator, and copper beads is designed to remain in equilibrium or to be free to rotate once the inside ball floats inside the outside ball. Therefore, the magnet in the APSS will always point to the North Pole of the Earth's magnetic field, which is near the geographical South of the Earth.

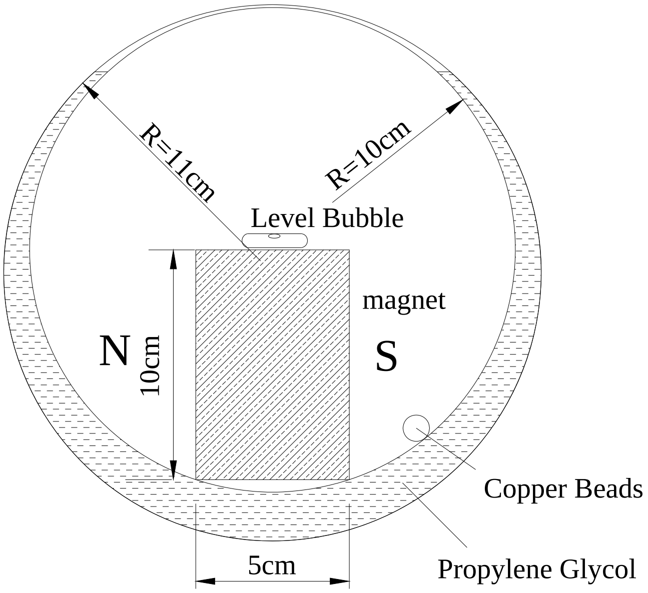

Figure 3.52 Schematic View of an APSS Design

Diameter Selection: The selection of ball diameter mainly depends upon three factors: commercial availability of two halves, smart rock size, and floating requirement of inside ball. To ensure that the inside ball can float in the liquid between the inside and outside balls, the average density of the inside ball with embedded magnet and other components is slightly less than that of the liquid. To start with, a trial value of d = 20 cm is considered. In this case, the mass of inside ball is equal to the sum of magnet (3.06 kg), organic glass ball and copper beads (total 0.5 kg), and glue and level indicator (negligible). That is, $\rho_0(\pi)(0.2)^3/6 = 3.06+0.5$ or ρ_0=850 kg/m^3, which is less than water density (1000 kg/m^3). Therefore, an inner diameter of 20 cm is a viable choice for the inside ball. The inner diameter of outside ball can be approximately selected to be 22 cm, which will leave sufficient spacing for lubrication liquid in between the inside and outside balls.

Liquid Selection: The liquid in between the inside and outside balls must be selected such that the inside ball with magnet can always float without creating any friction force on the inside ball as it rotates in the outside ball. For a 20-cm-diameter inside ball, the liquid density must exceed 850 kg/m^3. Although water is a viable candidate in terms of density and nontoxicity requirements, water does not provide sufficient lubrication between the two balls. Lubrication oil is good for minimum friction but insufficient in mass density for inside ball floating requirement. Consequently, propylene glycol with a mass density of 1040 kg/m^3 is chosen for satisfactory lubrication and nontoxicity requirements.

Fabrication Process: As shown in Figure 3.52, a light level indicator with bubble was glued on one side of a magnet, the opposite side of the magnet was glued to the bottom of a small half sphere with attached copper beads near the magnet, and the other small half sphere was attached and sealed to form a complete inside ball. Then, the complete inside ball was placed in a large half sphere and covered and sealed by the other large half sphere to complete the outside ball. Next, a 1-cm-diameter hole was drilled on the outside ball and propylene glycol liquid was injected into the outside ball until the inside ball completely floated and the top of the inside ball was in contact with the outside ball to avoid a large drift of the inside ball. Finally, the injection hole was sealed by a small piece of plastic and glue. Figure 3.53 shows a prototype APSS. The prototype APSS is ready for embedment into a concrete encasement or a natural rock to form a smart rock.

Figure 3.53 Overall View of a Complete APSS Prototype

It is noted that copper beads are needed to ensure the axis of the magnet remains horizontal. Since the dip angle θ of the Earth's magnetic field is greater than 60° in Rolla, MO, the axis of the magnet is slightly off the horizontal plane in the fabrication process. Specifically, the South Pole of the magnet is slightly higher than the North Pole with a small non-zero angle between the magnet axis and the horizontal plane. To remove the small angle, copper beads were added inside the ball as balancing weights on the south side of the magnet until the bubble level is horizontal. In this case, the South Pole of the magnet points to exactly the south direction and parallel to the horizontal plane.

3.4.2 Magnet Localization Algorithm with Known Orientation

With $\alpha=0$, $\beta=0$, and $\gamma=0$, the first three equations of (3.8) degenerates into Eq. (3.3) and the SRSS error in Eq. (3.9) is simplified into $J(x_M, y_M, z_M)$ in which $B_i^{(P)} = B$ can be evaluated by Eq. (3.4). In this case, the coordinate system xyz is the same as the XYZ. As such, only the first three equations in (3.10) are required to derive a solution for a minimum J value or the SRSS error. For clarity, the three partial differential equations are re-written in Eq. (3.11) as.

$$\frac{\partial J(x_M, y_M, z_M)}{\partial x_M} = 0 \tag{3.11a}$$

$$\frac{\partial J(x_M, y_M, z_M)}{\partial y_M} = 0 \tag{3.11b}$$

$$\frac{\partial J(x_M, y_M, z_M)}{\partial z_M} = 0 \tag{3.11c}$$

3.4.3 Validation of Localization Algorithm

A field teat was carried out in Ber Juan Park, Rolla, MO, to validate the accuracy of the magnet localization algorithm. The test layout is shown in Figures 3.54a and 3.54b with the preliminary implementation of an APSS concept as shown in Figure 3.7. Three locations of the 10-cm-diamter magnet, designated by M1, M2, and M3 in Figure 3.54, were selected to take into account a combination of horizontal positions and depths in bridge scour monitoring. M1, M2, M3 were well spaced as clearly shown in Figure 3.54a in horizontal plane. M2 and M3 also had significantly different depths. To locate each magnet, a sensor head of the G858 Magnetometer was respectively stationed at S1, S2, S3, S4, and S5 as shown in Figure 3.54. The sensor head was placed on top of five wooden poles that are fixed to the ground. As illustrated in Figure 3.55a, the sensor head faced the ground and was ensured to be perpendicular to the ground by a level bubble attached onto the sensor head. Moreover, a total station as indicated in Figure 3.55b was applied to measure the coordinates of three magnet locations and five sensor positions, which are measured from the centers of the magnet and the sensor head, respectively. To facilitate the precise measurement of magnet location, a prism was placed on top of the magnet as shown in Figure 3.55b.

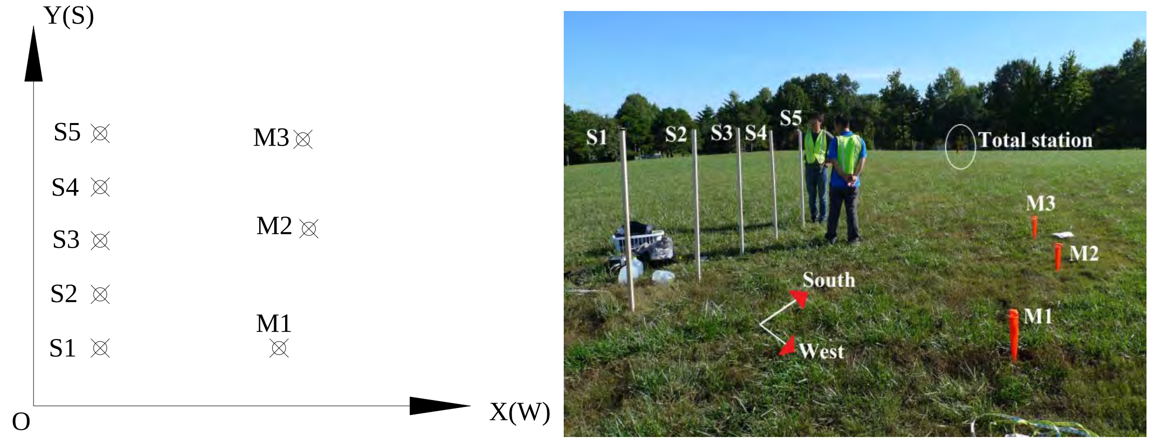

(a) Horizontal Positions of Magnet and Sensor (b) Sensor and Magnet Layout

Figure 3.54 Test Setup and Layout of Sensor Head and Magnet

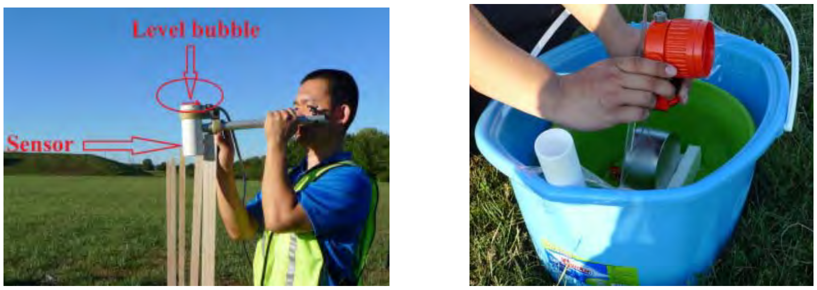

(a) Sensor Head Placement (b) Prism Placement

Figure 3.55 Sensor Head and Magnet Preparation for Total Station Measurements

Table 3.4 shows the measured coordinates (X, Y, Z) and intensity ($B_i^{(M)}$) of the magnet at locations S1 to S5, respectively, compares the predicted with the measured coordinates of the magnet Location M1, and provides the SRSS errors in location and field intensity for M1 estimation. Tables 3.5 and 3.6 show similar results for the magnet located at M2 and M3, respectively. By comparing the prediction errors at Locations M1 to M3, it can be observed that the SRSS prediction error in location ranges from 1.2% (0.058 m over a measurement distance of 4.96 m) to 2.4% (0.090 m over a measurement distance of 3.68 m). This relative prediction error corresponds to a measurement distance of 21 to 42 m for a 0.5 m or less localization accuracy – a performance criterion set forth for bridge scour monitoring with smart rocks in this study.

Table 3.4 Predicted and Measured Data for Magnet Location M1

Sensor Head	**X (m)**	**Y (m)**	**Z (m)**	$B_i^{(M)}$ **(nT)**
S1	0.0457	-36.53	0.391	51962.83
S2	0.0250	-35.57	0.397	52412.25
S3	-0.0192	-34.72	0.419	52643.57
S4	-0.0686	-33.79	0.398	52684.01
S5	-0.0183	-32.90	0.383	52658.24
Predicted Magnet Location M1	3.003	-36.69	-0.520	
Measured Magnet Location M1	3.025	-36.72	-0.475	
Location Prediction Error for M1	-0.022	-0.030	-0.044	
SRSS Error in Coordinate	0.058 m over a distance of 3.11 - 4.96 m			
SRSS Error in Magnetic Intensity, *J Value*	0.657 nT			

Table 3.5 Predicted and Measured Data for Magnet Location M2

Sensor Head	**X (m)**	**Y (m)**	**Z (m)**	$B_i^{(M)}$ **(nT)**
S1	0.0457	-36.533	0.391	52173.21
S2	0.0250	-35.565	0.397	52067.95
S3	-0.0192	-34.720	0.419	52137.05
S4	-0.0686	-33.789	0.398	52338.78
S5	-0.0183	-32.899	0.383	52506.43
Predicted Magnet Location M2	3.530	-34.833	-0.511	
Measured Magnet Location M2	3.566	-34.805	-0.581	
Location Prediction Error for M2	-0.036	-0.028	0.070	
SRSS Error in Coordinate	0.084 m over a distance of 3.72 - 4.17 m			
SRSS Error in Magnetic Intensity, *J Value*	1.049 nT			

Table 3.6 Predicted and Measured Data for Magnet Location M3

Sensor Head	**X (m)**	**Y (m)**	**Z (m)**	$\boldsymbol{B_i^{(M)}}$ **(nT)**
S1	0.0457	-36.533	0.391	52334.55
S2	0.0250	-35.565	0.397	52204.32
S3	-0.0192	-34.720	0.419	52080.26
S4	-0.0686	-33.789	0.398	52057.91
S5	-0.0183	-32.899	0.383	52202.33
Predicted Magnet Location M3	3.367	-33.192	-0.960	
Measured Magnet Location M3	3.409	-33.250	-0.906	
Location Prediction Error for M3	-0.042	0.058	-0.054	
SRSS Error in Coordinate	0.090 m over a distance of 3.68 - 4.88 m			
SRSS Error in Magnetic Intensity, *J Value*	0.286 nT			

3.5 Summary and Observations

In this section, the concept, measurand, and measurement principle of passive smart rocks were introduced, the combined magnetic field intensity of a permanent magnet and the Earth was formulated for general cases, two smart rock localization algorithms were proposed with known and unknown magnet orientations, and various intensity-distance curves and the localization algorithms were validated with field tests. The effects of magnet geometry, volume, and rotation as well as the type of magnetometer on the magnetic intensity of a magnet were investigated. Based on the extensive tests and analysis, the following observations can be made.

3.5.1 Magnetic Intensity Sensitivity to Various Test Parameters

For a given size, rod and plate magnets appeared to induce stronger magnetic fields than other shapes. A hollow magnet like a tube induced a comparable magnetic intensity to that by a solid magnet like a rod when their outside dimensions are the same. With a 12.7 mm × 25.4 mm (diameter × length) rod magnet, the maximum measurement distance was 7.95 m with the G-858 Magnetometer but 1.7 m only with the mini MGM Magnetometer due to coarse resolution. The G-858 Magnetometer not only had a longer measurement distance, but also provided a magnetic field gradient of the magnet with two sensor heads. The measurement distance for the 12.7 mm × 25.4 mm rod magnet can be increased to 21.3 m when each side of the magnet is extended by 0.35 m No. 13 rebar. A 50.8 mm × 50.8 mm rod magnet provided a maximum measurement distance of more than 40.7 m. For simplicity and effectiveness, rod/cylinder magnets were selected for further studies.

Cell phones, watches, and other ferromagnetic substances in close proximity to the sensor head of a magnetometer can significantly affect the magnetic intensity measurement of a magnet. In practical applications, portable items such as cell phones and watches should be removed prior to any intensity measurements and other permanent objects such as steel reinforcement in bridge piers must be taken into account. For example, the magnetometer can be set up at exactly the same position for various tests over time so that the effect of steel reinforcement can be subtracted out from the baseline measurement.

Due to the limited sampling rate of G858 Magnetometer (10 readings per second), the dynamic effects of rapid switching of the dipole of magnets were not fully observed during various tests. However, the layout directions of magnet rotations significantly increased the measured strength of electromagnetic field since the dipoles of the magnet rotated in different planes.

3.5.2 Test Results with a Small-scale Pier Model in Large Flume

The 11.1 mm × 25.4 mm (diameter × length) Grade N42 cylinder magnet embedded in a 28.6 mm acrylic ball can resist a dragging force of water flow at 56 - 65 cm/sec when placed on top of the sand particles glued to a flat bottom of the small flume at TFHRC. This velocity slightly exceeded the velocity (approximately 50 cm/sec) around the small-scale bridge pier model tested in the large flume at TFHRC.

Three scour tests with one, two, and five smart rocks, each with an embedded 11.1 mm × 25.4 mm magnet, were conducted around a circular pier (114 mm in diameter) and a rectangular pier (225 mm long in water flow direction by 750 mm wide by 500 mm deep) in the large flume at TFHRC. All three scour simulations resulted in the same scour depth correlation. This repeatability is very promising for the validity of the passive smart rocks.

During the scour tests, the designed smart rocks always rolled and remained at the bottom of a scour hole, giving the maximum scour depth. The total effect of a group of smart rocks was measured each time. The measured average intensity per smart rock and the observed scour depth around the rectangular pier were in good agreement with the intensity-distance curves derived from the calibration tests. At the completion of the three scour tests, a scour depth of 20 cm was estimated without prior knowledge on the magnet orientation. The 20 cm prediction was compared with the actual 18 cm scour depth.

3.5.3 Total Magnetic Field and Magnet Localization

The total magnetic field intensity of an arbitrary magnet and the Earth is a function of three coordinates and three orientations. When the magnet is free to rotate in the automatically pointing to south system (APSS) embedded in a smart rock, the total intensity can be formulated into a function of three coordinates only, which can greatly simplify the localization of smart rocks in practical applications.

In the total magnetic field theory, three parameters must be calibrated before the magnetic intensity can be used to locate smart rocks in real time bridge scour monitoring. The constant k is proportional to the magnetic moment of a magnet and the permeability of vacuum. The intensity B_E and the dip angle θ of the Earth magnetic field can change from one place to another. For the 10-cm-diamter and 5-cm-height magnet, $k = 37060\times10^{-9}$ Nm^2/A. In Rolla, MO, with latitude and longitude coordinates of approximately 37°57′12″N and 91°45′27″W, B_E = 52442 nT with a standard deviation of 0.18 nT and θ = 64.3 º with a standard deviation of 0.283º.

For a smart rock with an embedded APSS, the total magnetic field of the embedded magnet and the Earth is symmetric only about the vertical plane passing through the axis of the magnet. With the use of APSS, the localization algorithm derived from minimizing the SRSS error of the magnetic intensity is easy to solve and simple to apply in practice. The location prediction error in coordinates ranged from 1.2% to 2.4% based on the five measurements on a smart rock placed at 3.68 m to 4.96 m away.

3.5.4 Test Results and Discussion at Bridge Sites

One concrete ball with 254 mm in diameter was deployed at the US63 Gasconade River Bridge on September 24, 2012, and another concrete ball of the same size was deployed at the I-44 Roubidoux Creek Bridge on October 3, 2012. Each concrete ball included a 102-mm-diameter and 51-mm-high cylindrical neodymium magnet that was covered by at least 51 mm concrete. Futher tests on an irregular basis were performed at both bridges, e.g. on July 23, 2013 on the US63 Gasconade River Bridge and on July 25, 2013, on the I-44 Roubidoux River.

On October 4, 2013, one smart rock was retrieved from the US63 Bridge after the August 7, 2013, flood event. The smart rock was retrieved from a small hole near the bridge foundation of the pier in US63 Bridge. It appeared in a good condition and remained effective for magnetic field intensity measurement.

The magnetic intensity measured at a fixed station around the I-44 Roubidoux Creek Bridge site showed a decreasing trend with increasing measurement distance as the smart rock was manually dragged away from the magnetometer. The overall intensity-distance trend followed the calibration curves with some local fluctuations as a result of the river bottom topology variation or unknown orientation of the magnet. The measured intensities were consistent at the two bridge sites and over time at each bridge.

4 ACTIVE SMART ROCKS WITH MAGNETO-INDUCTIVE WIRELESS COMMUNICATION

4.1 Conceptual Design of an Active Smart Rock System

Active smart rocks are rocks with embedded sensors and electronics. Sensors may include a 3-axis accelerometer, a 3-axis magnetometer, a gyroscope, a pressure transducer, a battery indicator, a timer, a calendar, and an ID. Electronics may include one or two batteries and an antenna for both transmitting and receiving functions that is controlled by a switching relay.

Figure 1.5 shows the proposed concept of an active smart rock positioning system for bridge scour monitoring. For scour countermeasure effectiveness monitoring, active smart rocks with embedded electronics and various sensors are mixed with natural rocks and deployed around a bridge foundation. As the smart rocks move under flow water, the rip-rap scour mitigation measure begins to lose its effectiveness. The extent of smart rock movement is an indication of the effectiveness of the mitigation measure. The smart rock system can be monitored from a mobile vehicle platform or base station at a bridge deck with magneto-inductive communication links.

4.1.1 Potential Outcomes in Application Scenarios

Figure 4.1 shows three possible smart rock network mapping scenarios looking down from the bridge deck into the river (top view). The bridge has two rectangular piers shown in dark grey. The smart rocks are represented by circular objects, color-coded for easy movement recognition. In practical applications, each smart rock is equipped with a unique identification number so that it can be clearly identified on an outcome map.

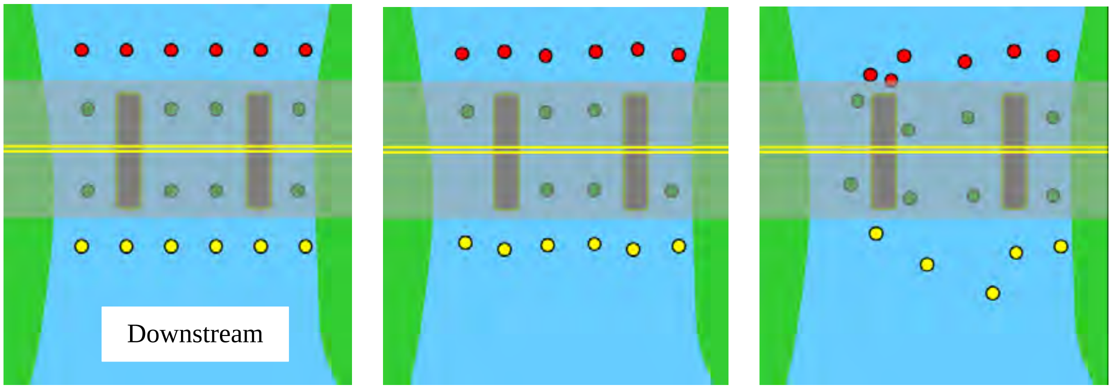

(a) Deployed Smart Rocks (b) No Significant Movement (c) With Significant Movement

Figure 4.1 Active Smart Rock Movement Scenarios

Figure 4.1a shows the initial locations of deployed smart rocks. A total of 10 smart rocks are deployed around each bridge pier. The sensors inside the smart rocks stay in sleep mode with little power consumption and can be activated by an external demand (wakeup signal), a timer or a movement (due to scour and flood). After the initial deployment, the smart rocks can be networked locally or globally with the base station that is often set up on the bridge deck. They are monitored for any movement on a regular basis, either with an automatic base station or by scheduled visiting to the bridge site. The outcome of each monitoring session is a map of the deployed smart rocks. For example, Figure 4.1b and 4.1c indicates two cases without and with significant rock movement, respectively.

As indicated in Figure 4.1b, some smart rocks move slightly. So long as their movement is within a pre-set measurement accuracy of 0.5 m, this scenario is classified as little movement on the monitoring map. Other smart rocks are shown to disappear from the monitoring map due to potential sensor failure, water leakage, or battery discharge. In such a case, the malfunctional smart rocks may be retrieved and reused after repair or can be v replaced with new units.

As indicated in Figure 4.1c, several smart rocks move due to scour effect. By comparing the current map with the reference map when smart rocks are initially deployed, the process of scour development can be evaluated. Note that some smart rocks experience significant movement and eventually disappear from the monitoring map area. In that case, additional smart rocks can be added into the existing smart rock network as needed.

4.1.2 Active Smart Rock Positioning System

Smart rocks are sized and weighed to ensure that they roll down to the bottom of a scour hole when deployed within the scour area and lost their supporting deposits. Their location in space (particularly in horizontal plane) can be identified from the so-called received signal strength indicator or RSSI (Tumanski 2006, Sun and Akyildiz 2009, Abdou et al. 2011, Yu et al. 2011, Yusof and Kabir 2011, Dionigi et al. 2012, Gulbahar and Akan 2012) so that the scour depth can be estimated or the effectiveness of a scour countermeasure can be evaluated. To verify or directly determine the scour depth, a pressure sensor can be integrated into the design of smart rocks. To further understand the process of scour, the orientation and tilt of smart rocks can be measured with a 3-axis accelerometer, a 3-axis magnetometer, or a gyroscope.

Each smart rock reports to the base station its own ID, battery voltage, orientation, water pressure, and a set of other parameters such as the RSSI of wake-up signal as observed on a board, command acknowledgement, and memory content. For easy communication/ localization, antennas can be permanently embedded into a bridge during construction so that a monitoring mobile vehicle can connect to them and use the same antenna structure /topology each time, minimizing possible errors due to receiving antennas misplacement during a monitoring session.

An active smart rock system includes:

- Smart Rock core electronic board with hardware and embedded software
- Base Station with receiver and wake-up/command transmission modules
- Graphical User Interface (GUI) for base station modules with corresponding hardware drivers implementation

- Digital Signal Processing (DSP) software implementation for the base station
- Smart Rock network communication and corresponding protocols
- Housing of Smart Rock electronic boards for field deployment and testing
- Localization Scheme for Smart Rock network mapping and association with actual geographical locations and depth

The Base Station and Smart Rocks are communicated with a magneto-inductive link by loop antennas operating at 125 kHz. Such a low antenna frequency is selected because:

1) The propagation of electromagnetic waves (EM) suffers from very high loss in water due to its conductivity. The propagation loss is proportional to the communication signal frequency and thus less at lower frequencies.
2) The smart rock communication occurs in near-field region since the EM wavelength (2.4 km or 1.5 miles at 125 kHz) is significantly larger than the required receiver-to-transmitter distance (up to 30 m) in the rock positioning system. Therefore, either electric or magnetic near-field communication can be used separately. Although the electric near-field communication cannot operate in slightly conductive water, the magnetic near-field communication can penetrate even salt water and propagate over a long distance.
3) On the other hand, low frequency communication requires the use of large antennas for efficient operation. With the limited size of smart rocks, 125 kHz is considered to be a lower-bound frequency for EM communication.
4) A communication frequency of 125 kHz can be shared with acoustic communication links to be discussed in Section 6. For acoustic underwater communication, 125 kHz is within a suitable frequency range.

4.2 Electronic Board Design

Throughout the project duration, three versions of electronic board have been designed and tested for smart rocks. Two of them are presented below for various laboratory and field tests, which are referred to as basic and advanced smart rock boards in this report.

4.2.1 Basic Smart Rock Board (v2.5)

A basic Printed Circuit Board (PCB), v2.5, was originally designed in accordance with specifications for the laboratory tests of small-scale bridge models. The board was designed to be in circular shape and not exceed 2″ in diameter. The board was placed in approximately 2.5″ diameter spheres together with a small antenna and two CR123A batteries. It was used for June 2012 laboratory tests and September 2012 field tests.

Figure 4.2 shows a prototype of the v2.5 board with main components noted. The v2.5 board has the following features:

- Compact and low power accelerometer/magnetometer LSM303DLHC-LGA14
- Integrated calendar module for long-term timer operation
- Possible connection to the receiver module by Serial Peripheral Interface (SPI) eliminating I2C-SPI bridge
- Separate tuning capacitor banks for receiving/transmitting coil connection

- Schematic/footprint fixes
- H-Bridge/transmission circuit to be replaced by ATA5276 125kHz transmitter Integrated Circuit (IC)

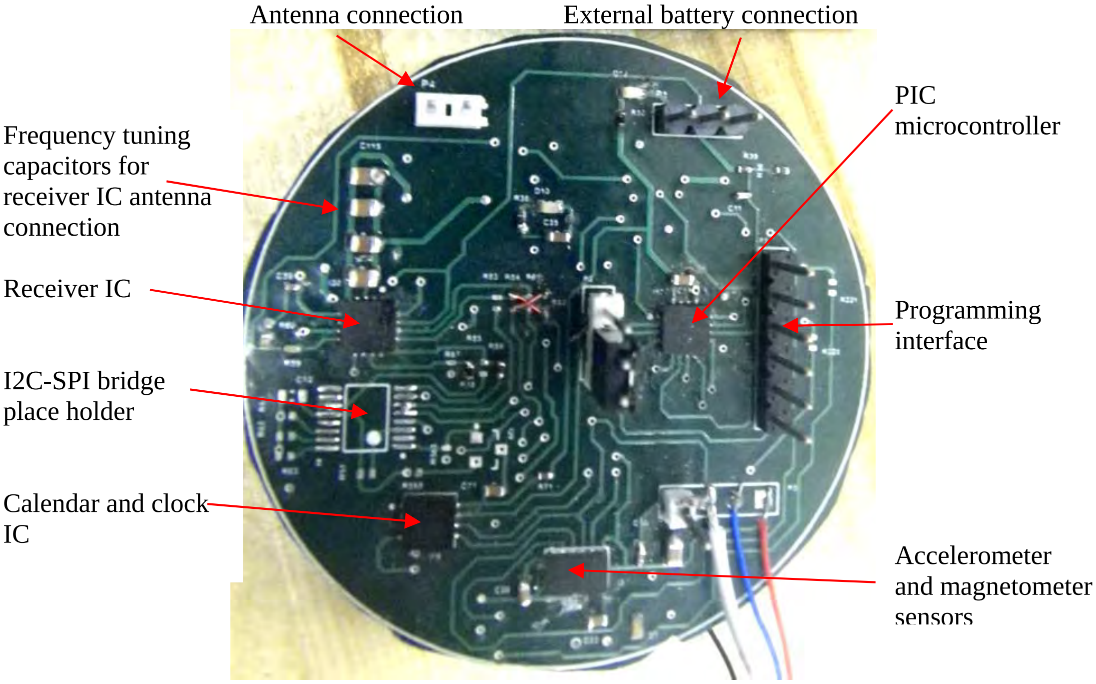

(a) Top View

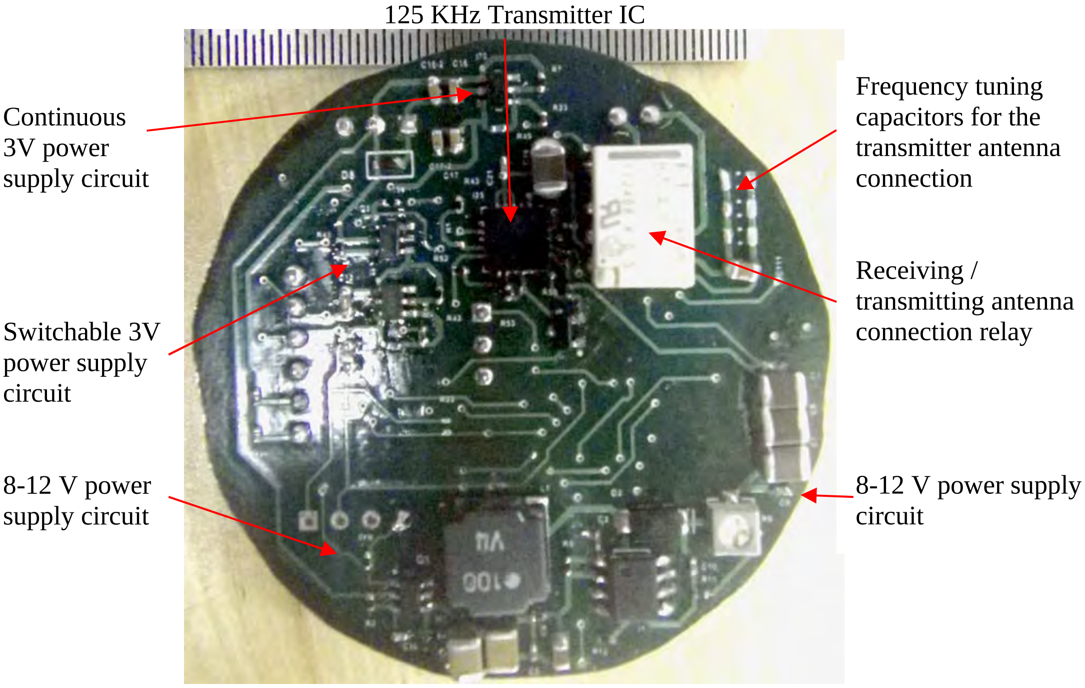

(b) Bottom View

Figure 4.2 Smart Rock v.1 Board and Electronics

As indicated in Figure 4.2a, the accelerometer/magnetometer sensor (LSM303DLHC-LGA14) was applied in the v2.5 PCB. Both accelerometer and magnetometer sensor data were obtained from one unified I2C address accessible by different registers. The v2.5 PCB required only one 3V battery supply and 14 pins trace routing.

The real-time clock and calendar module (PCF8523) provided a possibility to use flexible timer (seconds to years delay time) for the smart rock wakeup and data transmission. The time-stamp data can be obtained from this module for accurate interrupt (rock movement) events log arrangement.

The on-board receiver module (AS3930) can generate a wakeup interrupt on demand based on the received external modulated signature signal at 125 kHz. It is configurable by the SPI bus and can directly communicate with a PIC microcontroller by using the SPI protocol. The PIC microcontroller can control both SPI and I2C interfaces, both sharing the same PIC-pins. With alternative direct connections and special programming techniques made available on the board, the PIC microcontroller can independently process SPI and I2C requests.

Due to size limitation, some components were placed on the bottom side of the v2.5 board. Specifically, most of the ICs were placed on the top side as indicated in Figure 4.2a, while all power supply circuits and some modulation/antenna connection elements were mounted from the bottom side as illustrated in Figure 4.2b.

The v2.5 board has integrated a special 125 kHz transmitter IC that allows a further reduction of the board size as needed in the future and provides a more stable and power-effective operation during data transmission. It was tested and found to receive clear signals at 10 m distance, which is sufficient for small-scale tests in laboratory.

Figure 4.3 shows a schematic view of a packaged smart rock module. It shows a model of a spherical smart rock test module with ferrite antenna, smart rock PCB, and battery module placement. The rechargeable battery will be charged by a through-hole connection interface at the module wall.

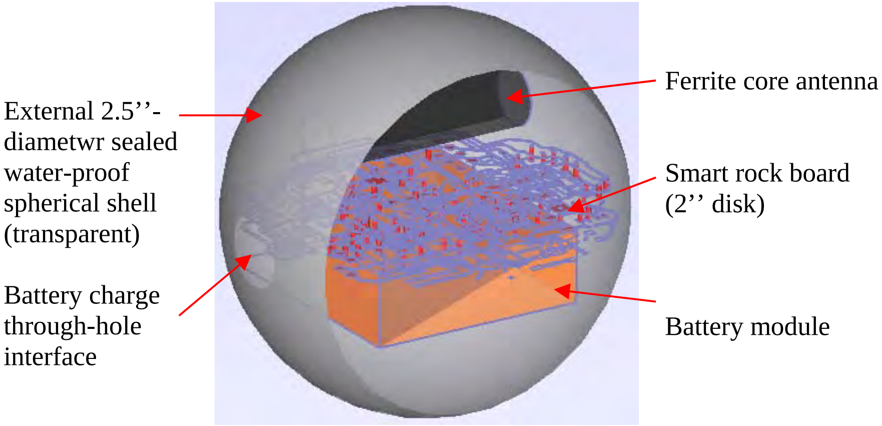

Figure 4.3 Spherical Smart Rock Module Scheme (cut-away view)

Figure 4.4a shows a pair of Smart Rock PCB in operation condition with attached ferrite-core based antennas. Each board has a unique assigned ID, which was used for board data processing and on-demand particular board wakeup for data acquisition. The mounted LEDs were for test/debug purposes only, and would be deactivated in practical applications in order to reduce board current consumption. Figure 4.4b shows a prototype of the assembled Smart Rock v2.5 board in a plastic shell.

(a) v2.5 Board with Attached Ferrite-core Antennas (b) Board in a Plastic Shell

Figure 4.4 Active Smart Rock Boards v2.5 with Attached Ferrite-core Antennas

Figure 4.5 shows the inside detail of the assembled prototype v2.5 board during the assembling stage. It can be seen that the antenna was placed perpendicular to the board for most effective signal transmission. To provide the required weight, brass balls were glued on the inside wall of the plastic shell. The v2.5 board was placed inside a plastic bag to avoid moisture invasion.

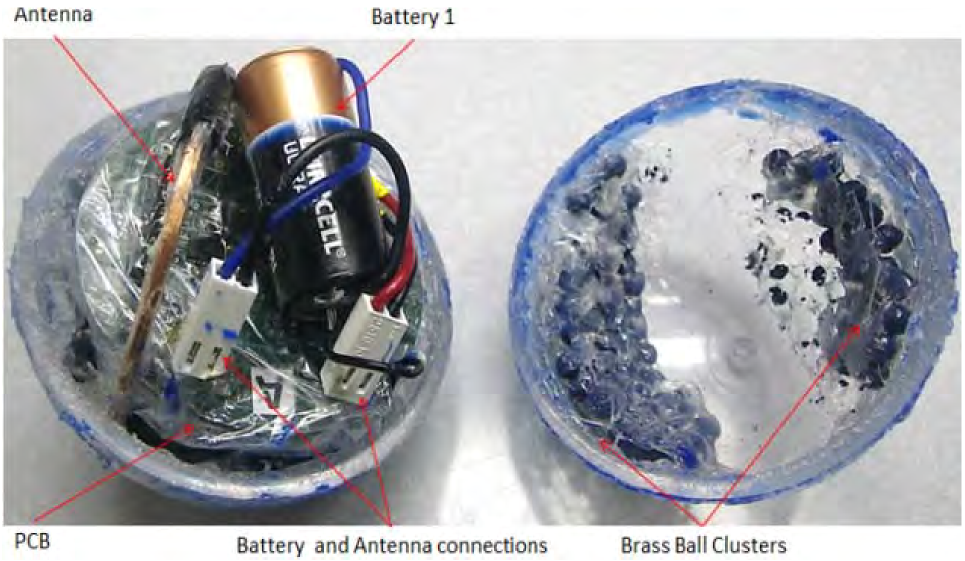

Figure 4.5 Detail of the Prototype Smart Rock

4.2.2 Advanced Smart Rock Board (v3.0)

Figure 4.6 shows a prototype of the latest generation of advanced electronic board (v3.0) that was designed in November 2012. The new design provides the following updates:

- Upgraded **PIC16LF1829** microcontroller (more I/O pins and program memory)
- Gyroscope (ST Microelectronics **L3G4200D**)
- On-board flash memory (Atmel **AT24C1024B-TH-B**)
- Alternative current-driven solution for antenna excitation

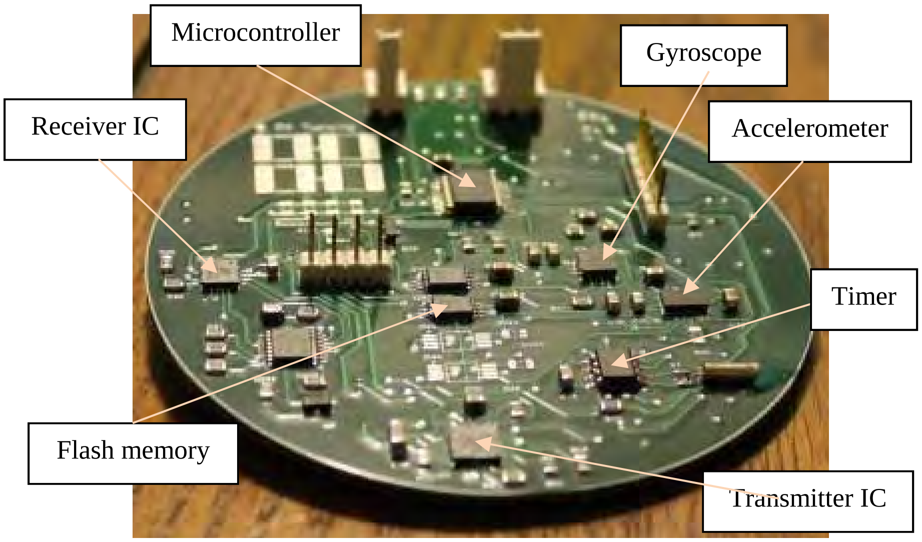

Figure 4.6 Smart Rock v3.0 Electronics

The new microcontroller provides a larger program space and more pins for interrupt/ control processing. The Gyroscope is a new addition for further development of Smart Rock movement trajectory recovery/better orientation monitoring. It uses an ST Microelectronics IC, similar to the accelerometer used on the board, accessible by I^2C bus.

Smart Rock v3.0 supports up-to four flash memory ICs, accessible by I2C with Atmel AT24C1024B-TH-B, each providing 1 MB memory space. Depending on the Smart Rock operation mode, it is sufficient to store up to a few thousands of data records. Two operation scenarios are considered for memory usage:

- High-rate data recording during relatively fast movement
- Data storage for Smart Rock inter-sensors network communication (RSSIs, IDs, Sensors).

The Smart Rock v3.0 boards provide two ways for antenna excitation: voltage driven and current driven. A jumper switch selects the modes. The current driven transmission is preferable for the RF magneto-inductive link, and the voltage driven transmission is preferable for acoustic transducer usage to be discussed in Section 6. Providing both configurations on the same board allows flexible switching between RF and acoustic communication.

The v3.0 board maintains a small size (3 inch in diameter), making it applicable in both laboratory and field environments. Whenever possible, IC components are selected to be in SOP packages and passive components (resistors/capacitors) are at least 0806 size, which makes it easier to assemble in comparison with the Smart Rock v2.5 design. However a few IC components (Gyroscope, Accelerometer, and Receiver) are only available in small QFN package.

4.3 Base Station Design

A base station or link control system was designed to control the operation of active smart rocks. Presented in this report are two versions of the base station designs that are referred to as basic and advanced base stations. Following is a presentation of each base station design.

4.3.1 Basic Base Station Design

As shown in Figure 4.7, the circuitry of a basic base station design was packaged into two professional enclosures: base station receiver (left) and wakeup signal transmitter controller/amplifier (right), making the overall system portable and easy to use for laboratory and field tests. All the required power supplies (±6 V, ±15 V and +12 V) were integrated into the enclosures. The two base station units were used in field tests since September 2012.

Figure 4.7 Two Main Modules of the Analog Base Station

Figure 4.8 shows a schematic of the Analog Demodulator module, a key component of the analog base station. The PCB-based module is well controllable and mechanically stable. The design is based on the Analog Devices 8032 single supply voltage feedback amplifiers and provides control for easy tuning of demodulation threshold settings.

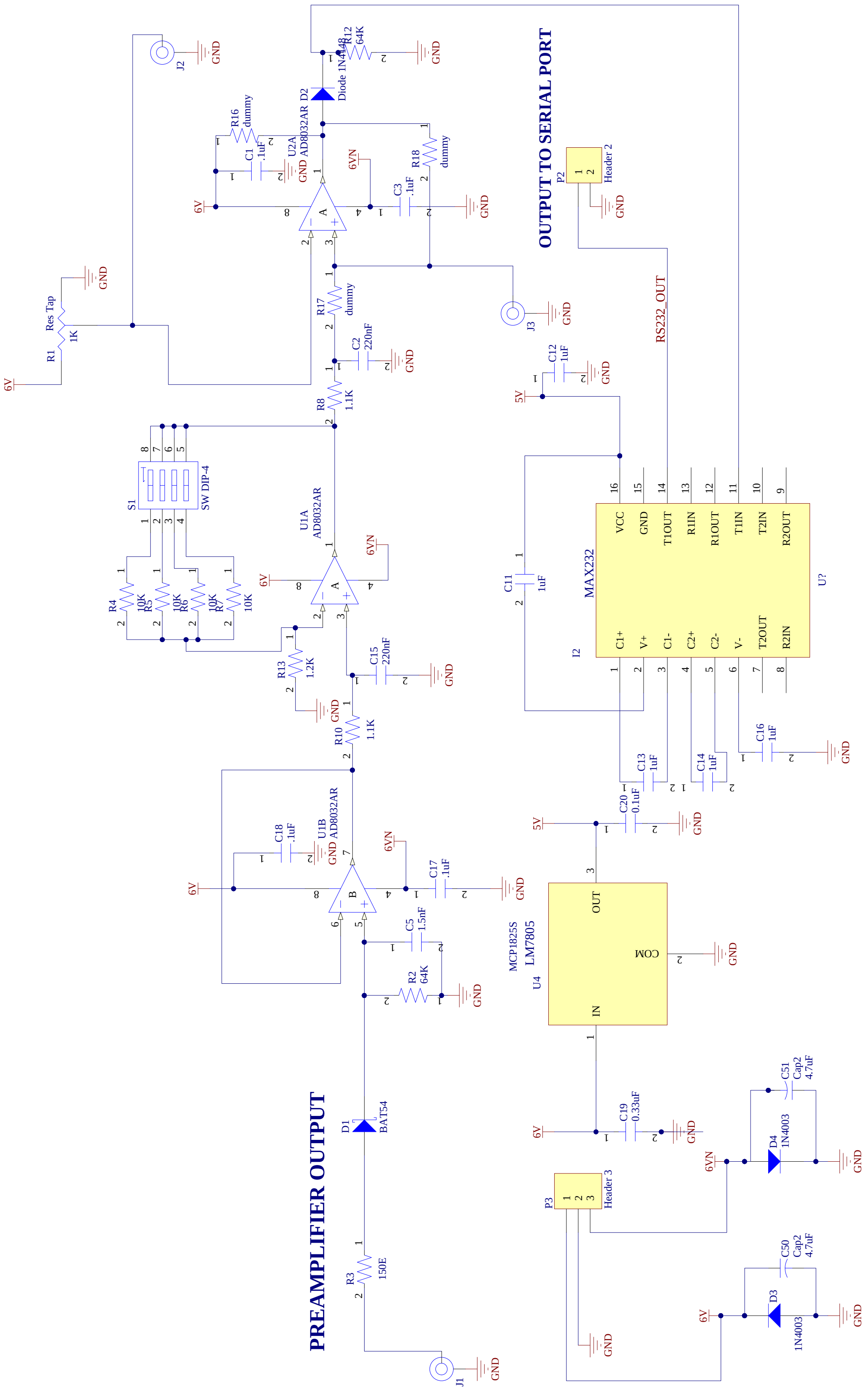

Figure 4.8 Analog Demodulator Schematic

As shown in Figure 4.9a, the analog base station receiver includes:

- EMI filter for reducing noise coupling from power line to the system
- ±6 V linear power supply
- 4 filters: 125 kHz band-pass filters / preamplifiers for antennas connection
- 4 port log detector
- Demodulator with RS232 output interface

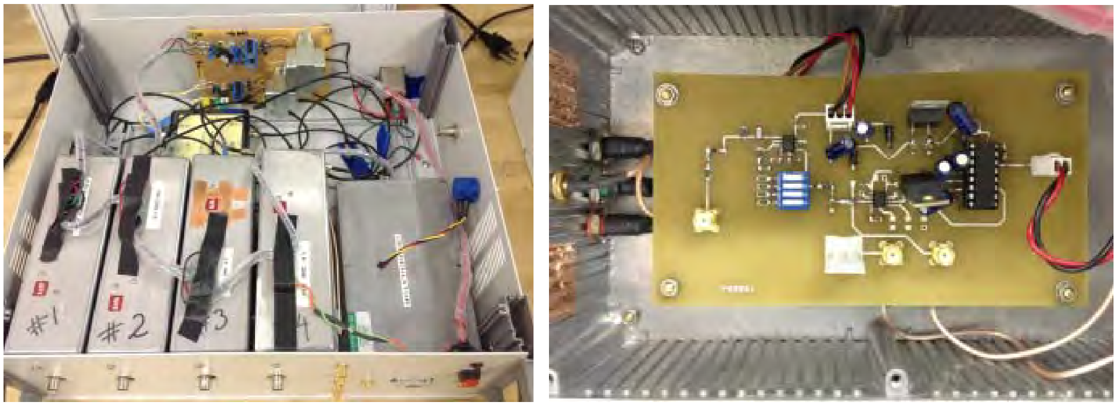

(a) Modular Structure (b) Demodulator Board with I/O Connections

Figure 4.9 Analog Base Station Receiver

All four channels had independent filter/amplifier configurations; any channel can be connected to the demodulator board for data acquisition. Figure 4.9b presents a prototype demodulator board of the design as schematically shown in Figure 4.8. The demodulator is integrated into one of the modules in the Base Station system, as shown in Figure 4.9a.

4.3.2 Advanced Base Station Design

Digital signal processing (DSP) can improve sensitivity and filtering features, resulting in a more stable communication link for Smart Rock data acquisition even over a longer distance. It also allows various filter settings tailored to local noise environments. Therefore, a DSP board with audio interface/codec was designed and built. To convert signals from the Smart Rock operating frequency of 125 kHz to the audio frequency range, a down mixing concept was implemented in the advanced Base Station design. As a side feature, the advanced design also contains an analog demodulator circuitry, generating the standard RS232 output. Figure 4.10 shows a block diagram of the analog pre-amplifier unit in the advanced Base Station design.

The input of the preamplifier is connected to the 125 kHz antenna. The received signal is passed through a low-frequency band-pass-filter, amplified and mixed down to 20 kHz at the first stage of frequency downshifting. The 20 kHz signal is further mixed down to 800 Hz at the second stage of frequency downshifting, which can be connected to any computer sound card and easily loaded into standard software like MATLAB or LabView with signal processing capabilities. Three RSSI estimations are available for the original signal and two intermediate frequency downshifting stages, providing a more robust dynamic response of the base station system.

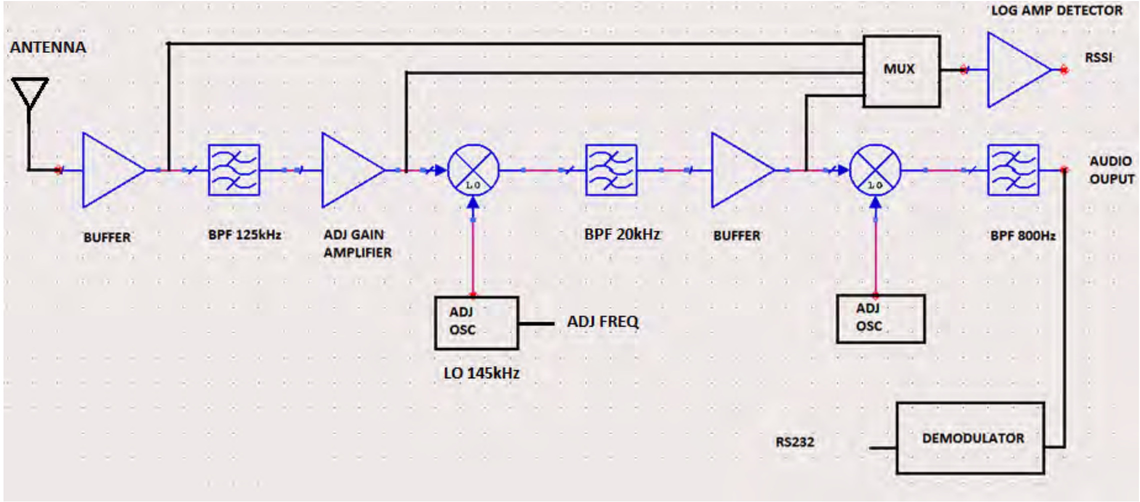

Figure 4.10 Preamplifier Module Block Diagram in the Advanced Base Station

Figure 4.11 shows a layout of all control components in the base station preamplifier PCB. In addition to the analog demodulation in the basic base station design, the advanced design is capable of signal filtering, amplification, three-step log-detection for RSSI estimation, and conversion from the 125 kHz signal to 800 Hz audio band.

Figure 4.12 shows a prototype of the advanced base station receiver unit and the multi-layer arrangement of four PCBs inside the receiver unit. The station provides four independent channels for signal processing. The four printed circuit boards are stacked inside the enclosure as shown in Figure 4.12b and controlled at the front panel of the unit. Apart from the audio output (DSP input), each channel can also be individually tuned and used as a demodulator with the COM port interface.

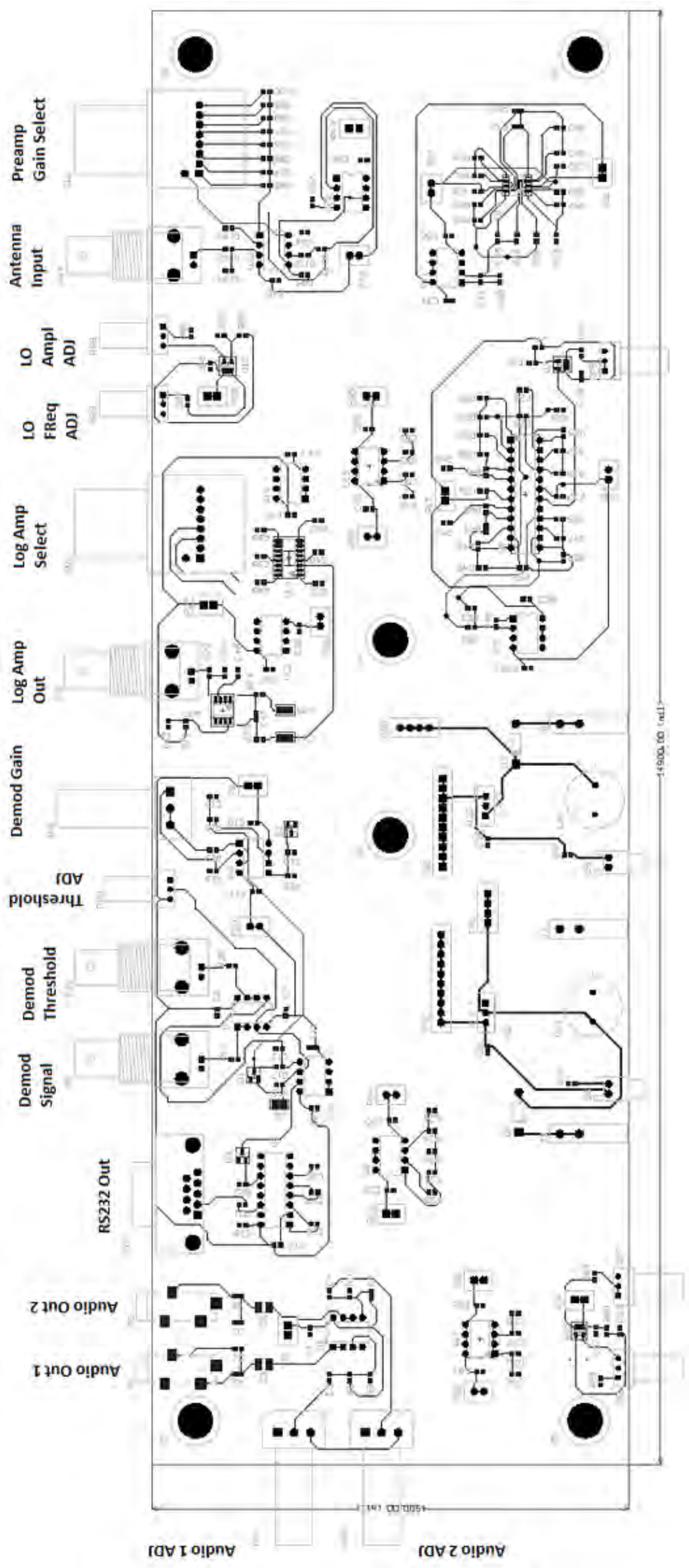

Figure 4.11 Preamplifier Module Layout of the Base Station Design

(a) Receiver Unit (b) Receiver PCBs inside the Unit

Figure 4.12 Prototype of the Advanced Base Station Receiver Design

4.3.3 Digital Signal Processing Capabilities

Various algorithms were used in the Base Station designs and example test results to illustrate their functionalities in digital signal processing. The Smart Rock board microcontroller operates at 125 kHz and is capable of generating amplitude-shift keying (ASK) modulated signals with a configurable baud rate. The baud rate, however, cannot be specified arbitrarily and must be selected from the following equation:

$$\text{Baud Rate} = \text{Fosc}/(4*(N+1)) \tag{4.1}$$

where N is an int8 value and Fosc can be set from a list of the fixed values [31 kHz, 31.25 kHz, 62.5 kHz, 125 kHz, 250 kHz, 500 kHz, 1 MHz, 2 MHz, 4 MHz, 8 MHz, 16 MHz and 32 MHz]. The carrier frequency of the modulated output signal can be configured into Fosc divided by any of [2, 4, 8, 16, 32, 64, 128] values.

Real Time DSP Demodulator Algorithm. The algorithm implemented on the DSP board to demodulate the signal sent from the Smart Rock is illustrated with the flow chart shown in Figure 4.13. The following description refers to the data variables shown in the algorithm flow chart and used in the actual implemented code.

The Smart Rock was programmed to send data at a rate of 250 bits/second, corresponding to 384 samples/bit with a DSP sampling rate of 96 kHz. Since asynchronous clocks were used between the Smart Rock and the DSP, the data sent from the Smart Rock was never perfectly aligned with the DSP. One method to improve the reliability in asynchronous communication is to divide the 384 samples/bit into multiple bins and have the bins to vote to see if the bit should be a zero or a one. Dividing each bit into 3 bins allows 128 samples per bin. The number of samples per bin actually used in the data processing can be determined based on the following equation:

$$N_{SamplesPerBin} = F_{SampleRate} / N_{BinsPerBit} / N_{BitsPerSecond} \tag{4.2}$$

when $\mathrm{N_{SamplesPerBin}}$ is close to a whole number. In this study, $\mathrm{N_{SamplesPerBin}}$ is 128 since $\mathrm{F_{SampleRate}}$ is 96 KHz, $\mathrm{N_{BinsPerBit}}$ is 3, and $\mathrm{N_{BitsPerSecond}}$ is 250.

The processBuffer() function in Figure 4.13 contains all of the processing steps required by the algorithm. First, 128 bits are copied from the ping or pong buffer to x[]. The Fast Fourier Transform, fft of x[], is then calculated, and the magnitude of each data point in x is calculated and stored in gXmag[]. When sent from the Smart Rock, a high bit is presented in Figure 4.14, indices 21 and 43 of gXmag[] spike. A low bit is presented in Figure 4.15. A small amount of carrier frequency harmonics is still shown up on the signal. The low bit harmonics have a much lower magnitude than the high bit harmonics and occur at different indices.

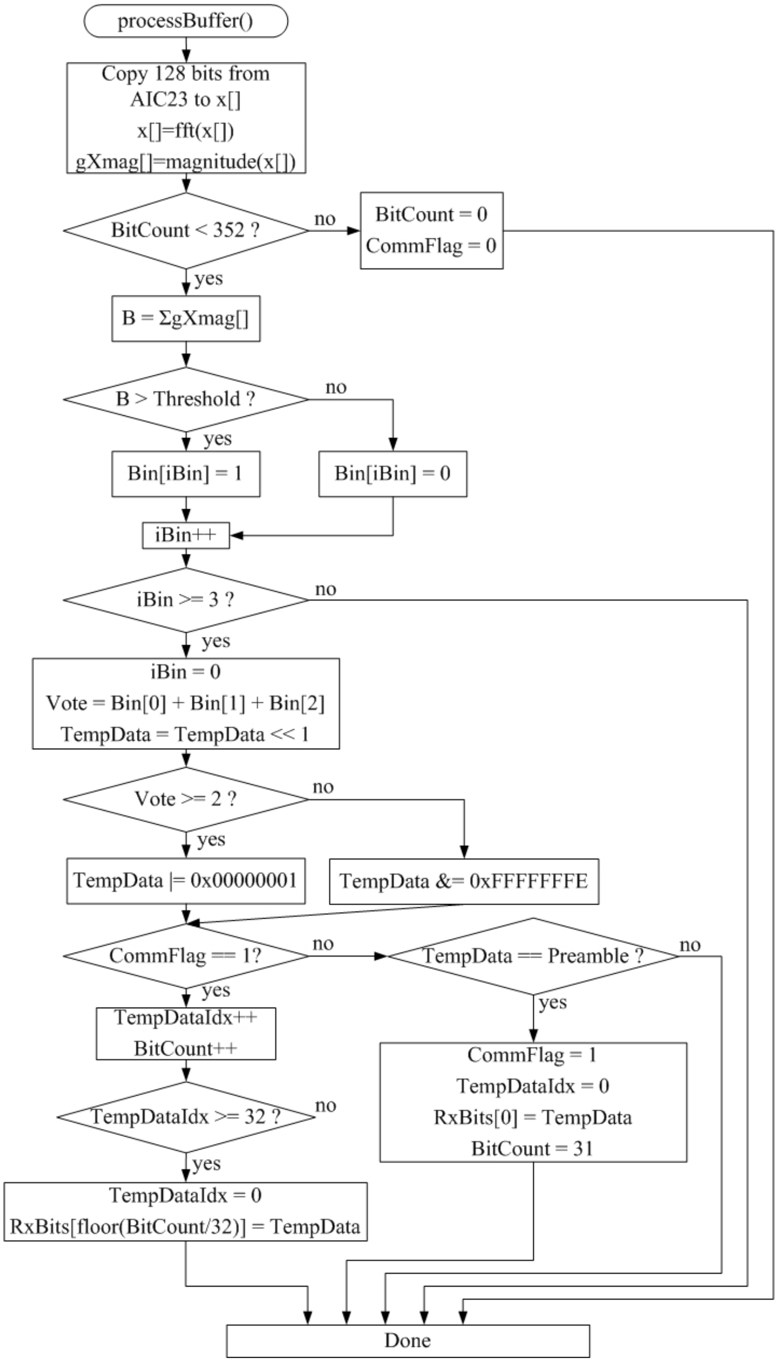

Figure 4.13 Flow Chart of the DSP Demodulator Algorithm

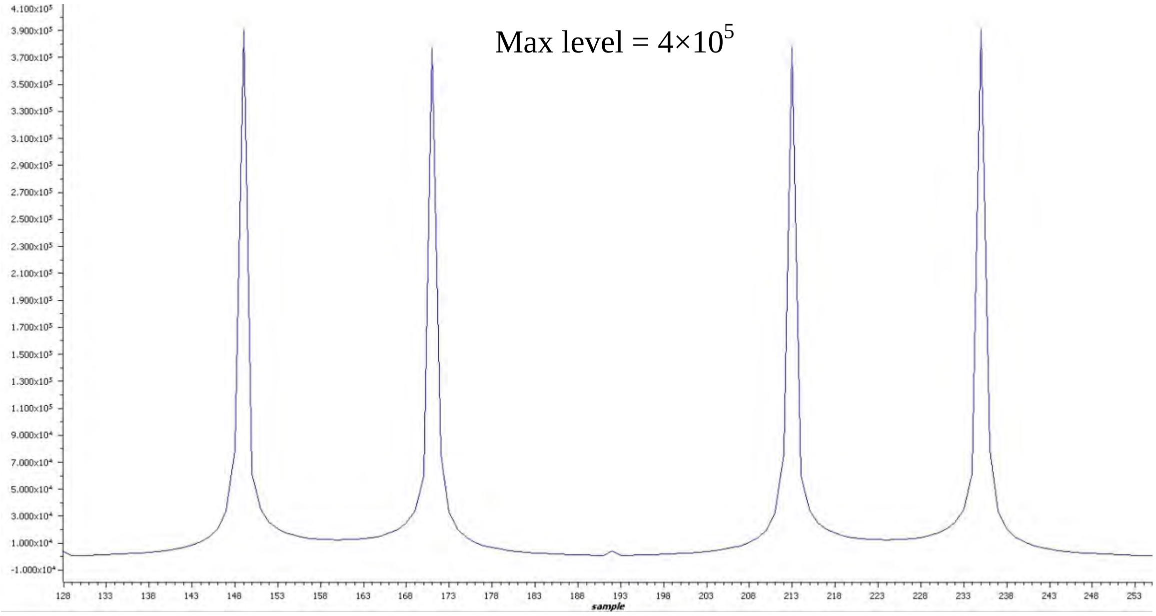

Figure 4.14 gXmag[] of a 1-bit Received from the Smart Rock (spike level = 4×10^5)

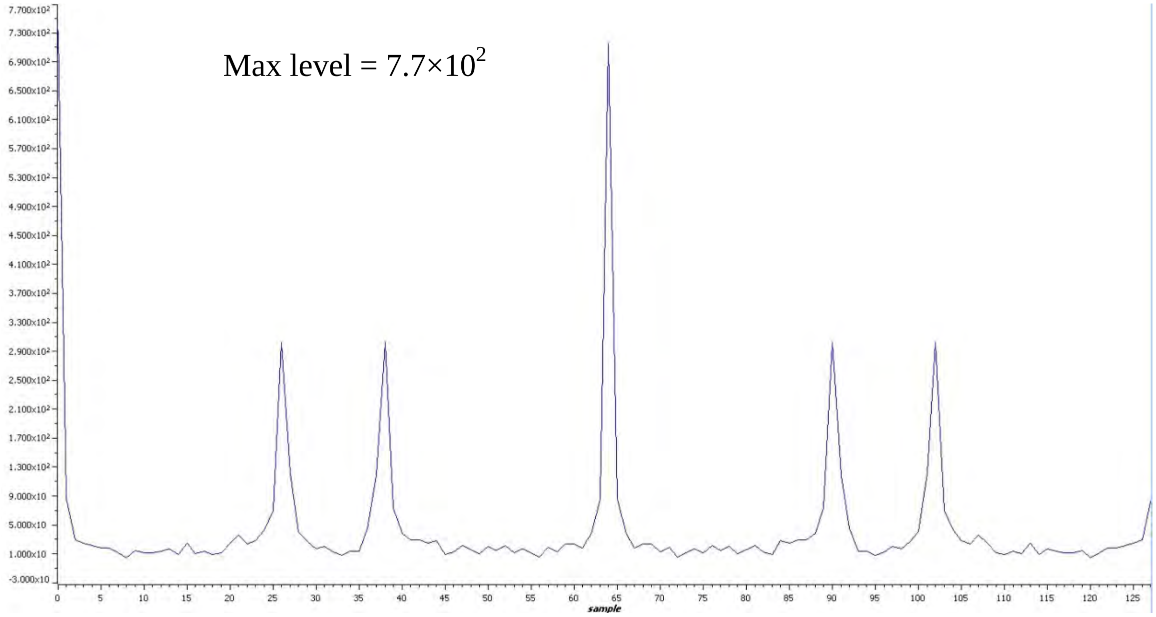

Figure 4.15 gXmag[] of a 0-bit Received from the Smart Rock (spike level 3×10^2)

Next, the number of bits received is verified. If 352 bits or more have been received, the entire packet of data has been received and communications can stop. In this case, eleven 32-bit integers are used to store the incoming data stream from the Smart Rock (11*32=352). The DSP then returns to the state where it is looking for the preamble. If less than 352 bits have been received, the values of gXmag[] are summed to see if the bin should be a 0 or 1.

The indices of gXmag[] to be summed are chosen by comparing the values of gXmag[] when no signal is connected to the AIC23, with the values of gXmag[] when the carrier signal is connected to the AIC23. The indices of gXmag[] with the greatest difference are used to determine if the bin should be a 0 or 1. If the sum exceeds a predetermined threshold, the bin is a 1. Otherwise, it is a 0. If the number of bins is greater than or equal to 3, the bins 'vote' to see if the resulting bit should be a 1 or 0. The resulting bit 1 or 0 is then shifted to TempData.

If the DSP is in a state where it is looking for the preamble, TempData is compared with the (32-bit) preamble. If TempData matches the preamble, the DSP is changed to a state where it is receiving data. If the DSP is already in a state where it is receiving data, it checks to see if 32 bits have been received yet. If 32 bits have been received, TempData is written to the RxBits array. After RxBits is full, it is sent to a computer file via a 'write' data to file' breakpoint in Code Composer Studio. For more effective DSP-PC-communication, the corresponding breakpoint is set up to send Integer (32-bit) data as hex values.

Allowance Preamble Bit Errors. For noisy environments or for debugging, it is useful to allow for preamble detection with a few bit errors. To do this, TempData is XORed with the preamble, and the resulting bits are summed to get the number of bit errors between TempData and the preamble. If the number of bit errors is less than or equal to the error threshold, CommFlag is set to one, which will start data recording. To allow for zero bit errors in the preamble, the error threshold is set to zero.

Multiple Bit Voting. The DSP must take the modulated signal and accurately convert it back to a digital signal. Figures 4.16a - 4.16c show various cases with an input signal of alternating 1's and 0's. In the ideal case in Figure 4.16a, the three voting bins will be in sync with the digital signal. In the non-ideal case in Figure 4.16b, the digital signal is out of sync with the voting bins, resulting in bit errors. If the DSP is checking for a preamble, it will only find the preamble shown in Figure 4.16a, and miss the preamble in Figure 4.16b. One solution to this is to have multiple bits voting, as shown in Figure 4.16c. In this case, Bits2 and Bits3 generate alternating 1's and 0's, while bits1 generates an error. The data resulting from Bits1, Bits2, and Bits3 is checked against the preamble. Whenever there is a match, that bit number is used for recording the data stream. This allows for more robustness in checking for the preamble and data recording.

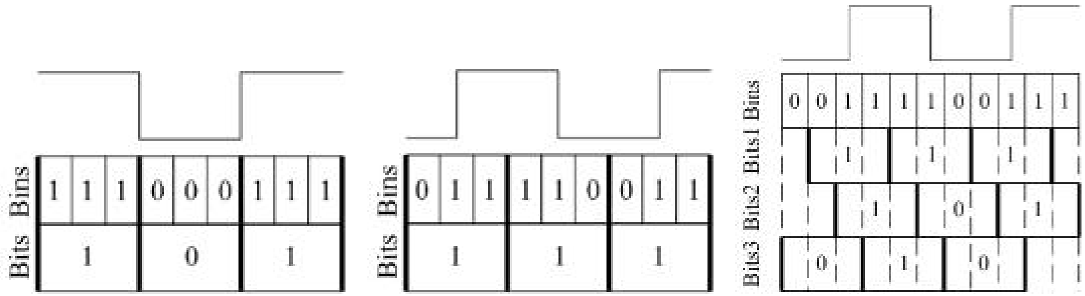

(a) Ideal Signal (b) Non-ideal Signal (c) Multiple Bit Voting

Figure 4.16 Three Scenarios of Bits Voting

Test Results. Figure 4.17 shows a packet of data sent by a Smart Rock module. The data packet starts with a long carrier burst (~0.18 sec.) and a digital modulated signal consisting of a preamble marker 1111111010010001 followed by a set of alternating 0-1 bits and the coded data from accelerometer and magnetometer sensors. Finally, the data packet is finished with additional alternating 0-1 bits and a carrier wrap-up. Figure 4.18 details the header and preamble data portion.

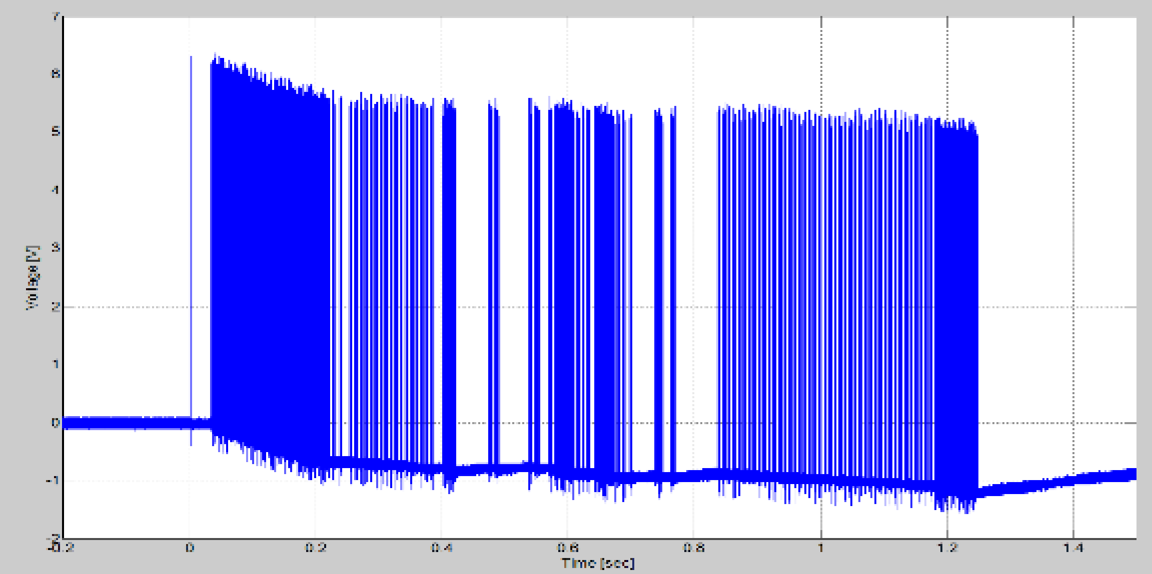

Figure 4.17 Example Signal Sent by a Smart Rock Module

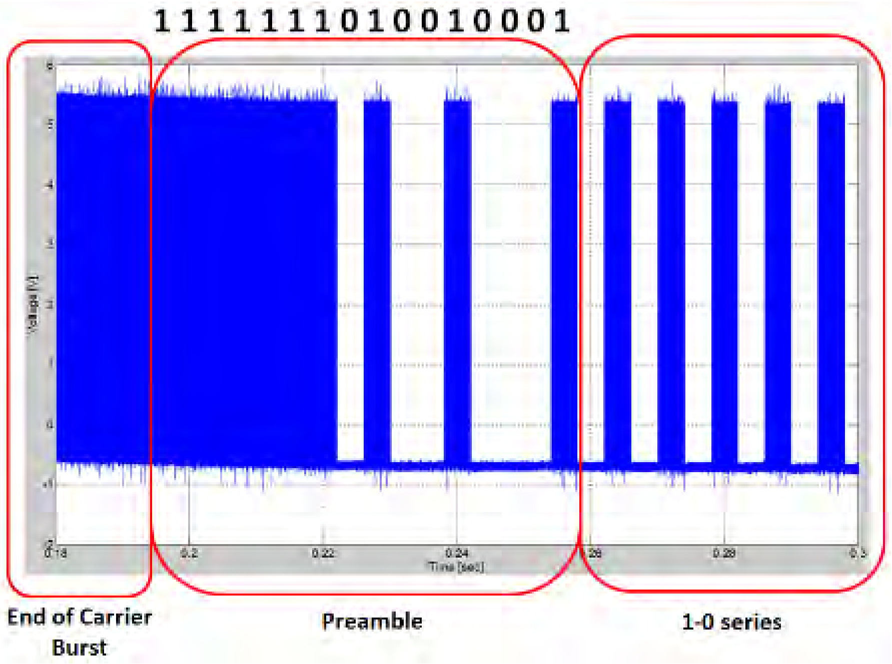

Figure 4.18 Details of the Header and Preamble Data

Accelerometer Data Processing. With the implemented real time DSP system, acquisition of smart rock on-board sensors can be performed. For example, Figure 4.19 shows the schematic view of a 3-axis accelerometer. The acquired data is processed and used to determine the 3D orientation of a smart rock PCB with respect to the gravity field. Similarly, the data from a 3-axis magnetometer is used to determine the 3D orientation of a smart rock with respect to the Earth magnetic field. The output port of the smart rock board is directly connected to the DSP board for rapid data transmission.

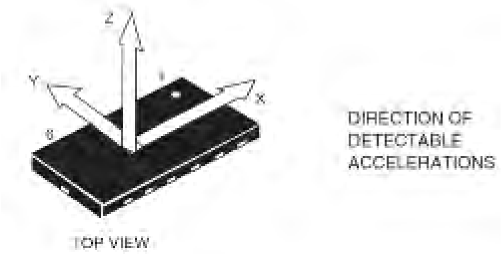

Figure 4.19 Three Components of a 3-axis Accelerometer

The accelerometer output data consists of two byte values for each X/Y/Z axis: LOW byte and HIGH byte of a 16 bit signed integer. After recombination of LOW/HIGH bytes, a clear indication of the accelerometer vector can be obtained. Figure 4.20 shows three components of an acceleration vector as a function of time observed during tests. The PCB with the accelerometer was initially oriented parallel to ground (dominant +Z component) and then flipped over (dominant -Z component). Next, a few other distinctive orientations were tested with dominant X and Y components.

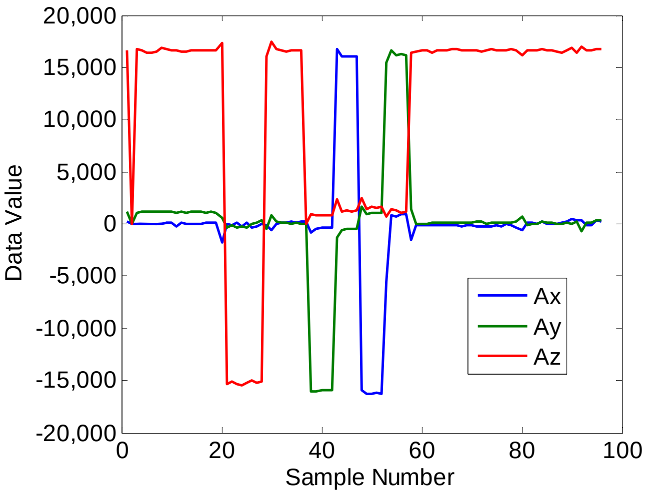

Figure 4.20 Accelerometer Output with Three Components

In practical applications, the data packet of a Smart Rock module contains data from the ID, battery meter, accelerometer, magnetometer, gyroscope, and pressure sensor. However, for the purpose of RealTime DSP code development, only acceleration data was processed, while most of other data parts were replaced by alternated 1-0 sequences.

For a convenient data transmission from the DSP Board to a PC, the acquired data was combined and provided as Uint32 values. Figure 4.21 shows the structure of an output file stored on the PC side.

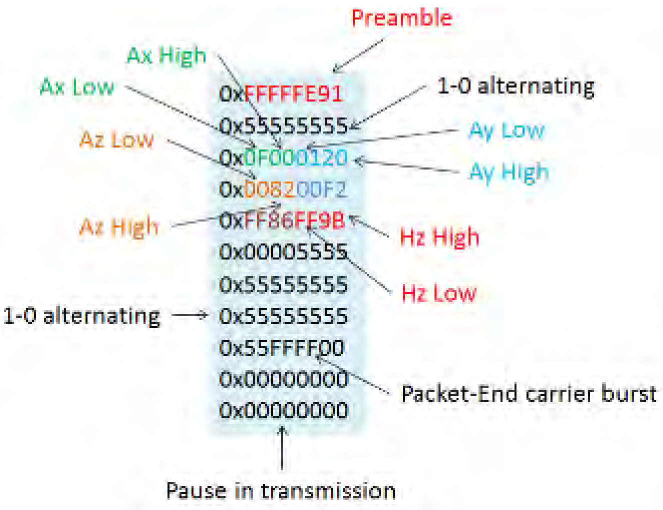

```
0xFFFFFE91
0x55555555
0x0F000120
0x008200F2
0xFF86FF9B
0x00005555
0x55555555
0x55555555
0x55FFFF00
0x00000000
0x00000000
```

Figure 4.21 Extraction from Stored Output File with Processed Smart Rock Data

Each data-value sent by the DSP board is a 32 bit unsigned integer. The data packet starts from the preamble code and is followed by the alternating 1-0 sequence, which translates to a ‘0x55555555’ record. Then, the accelerometer readings are provided by LOW-HIGH bytes pairs. The data packet also contains the magnetic field sensor reading, the second 1-0 alternating sequence, the packet-end carrier burst, and a zero-signal record which corresponds to pause in smart rock transmission. Using the MATLAB code, the recorded data shown above is decoded and processed as independent values.

4.4 Smart Rock Remote Reconfiguration/Command

The remote reconfiguration commands set was implemented in the Smart Rock embedded software utilizing features of the on-board receiver IC (AS3930). The IC analyzed the incoming signal and detected preamble matches that trigger a wake-up interrupt for the microcontroller. The interrupt enabled the IC for data stream decoding, which makes it possible to implement a remote reconfiguration of a Smart Rock unit based on a pre-defined command/action table.

The length of the command stream is not limited and depends on the embedded software requirements. Currently 16 bits of <command>:<data> pair are used for the configuration settings. Table 4.1 gives a list of sample commands. The bit sequence command line shows a 16 bit sequence where the ‘x’ symbol represents a place holder for a bit and the ‘d’ symbol shows valuable bits used in command recognition. The command/ reconfiguration include the setting timer, memory, ID settings, and smart rock updating. The command protocol can easily be expanded to support additional configuration settings.

Table 4.1 A List of Sample Commands

Bit Sequence Command	**Description/Action**
0 0 x x x x x x x x x x x x x x	Start two zeros / direct command
0 0 0 0 0 1 x x x x x x x x x x	Respond with current sensors data only
0 0 0 0 1 0 d d d d x x x x x x	Respond sending data from memory (up to 0b<dddd> records)
0 0 0 0 1 1 x x x x x x x x x x	Clear memory content (with acknowledgement transmission)
0 0 1 1 1 1 x x x x x x x x x x	Send own data and wake up all the known rock in the network
0 0 1 1 0 1 d d d d x x x x x x	Don’t send own data, but wake up rock 0b<dddd>
1 1 x x x x x x x x x x x x x x	Start two ones / reconfiguration command
1 1 0 1 0 0 x x x x x x x x x x	Set the wake up timer
1 1 0 1 0 0 0 d d d d d d d d x	Set the wake up timer for 0b<dddddddd> minutes
1 1 0 1 0 0 1 d d d d d d d d x	Set the wake up timer for 0b<dddddddd> hours
1 1 0 1 0 1 d x x x x x x x x x	Set the accelerometer interrupt (d = ON/OFF)
1 1 0 1 1 1 x x x x x x x x x x	Set the data recording into memory (d = ON/OFF)
1 1 1 1 0 1 0 d d d d d x x x x	Set own ID of the rock to 0b<ddddd>
1 1 1 1 0 1 1 d d d d d c c c c	Add/Overwrite a new rock into the known network list (rock 0b<cccc>, ID 0b<ddddd>)

4.5 Laboratory Validation on Smart Rock and Communication Link Designs

4.5.1 Smart Rock Sensor Assembly

For laboratory tests at the Turner-Fairbank Highway Research Center Hydraulics Laboratory, Washington D.C., the Smart Rock v2.4[1] electronic boards were used in June 2012. As indicated in Figure 4.5, the Smart Rock boards were enclosed into plastic spheres of 64 mm (2.5″) in diameter. Each assembled module included a PCB with electronics circuit, receiving/transmitting coil antenna, two CR123A batteries in parallel as shown in Figure 4.22, and a set of 3.5-mm-dia.brass balls (more than 160 grams) to ensure that the module be sufficiently heavy to remain under water. The brass balls were painted to avoid electric conductive contact within the set, and then glued inside the plastic spheres using glue or super glue. The coil antennas integrated into the assembly were placed perpendicularly to the Smart Rock electronic board to decrease possible detuning of the antenna by metal parts of the board. To assure waterproof properties, the spheres were sealed using silicone adhesives and tight wrapping by electric tapes.

---

[1] The Smart Rock v2.4 used the voltage-driven antenna excitation with H-bridge circuitry while the Smart Rock v2.5 used the current-driven antenna excitation with 125 kHz antenna driver transmitter IC.

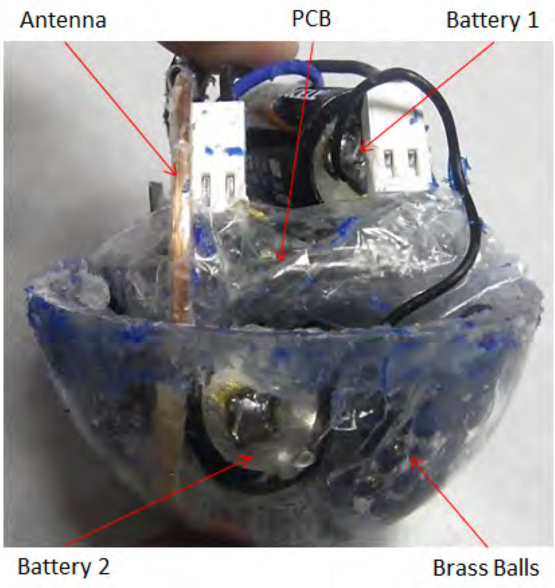

Figure 4.22 Two Batteries Shown in Each Smart Rock Module

During the tests, four Smart Rock units were used. Two of them were programmed for continuous sensors data acquisition and transmission with predefined timer delays. The other two were programmed to respond to the external wake-up signal interrupt. Data transmission and processing were performed using the analog signal processing procedures; transmission was arranged using the RS232 protocol and ASCII code without data encoding/compression and error recovery. These features are needed in the future version of smart rocks, v3.0, which uses digital signal processing routines.

4.5.2 General Scheme of Tests

Figures 4.23 and 4.24 show a general scheme and a photo of the actual test setup and environment. As shown in Figure 4.23, smart rocks are placed in a water channel mixed with natural rocks in comparable size. Four antennas can be deployed around the water channel for receiver signal strength intensity (RSSI) detection and smart rock localization. The base station control system supports up to four antennas for processing. For sensors data acquisition, a separate large square loop antenna is placed above the water channel.

During actual tests as shown in Figure 4.24, only two RSSI-antennas were deployed on top of a small flume and outside the smart rocks area, thus giving the rock locations along the small flume or water flow in 1D environment. The control PC was connected to both the data channel demodulator unit and the oscilloscope, providing RSSI estimations from localization antennas.

A smart rock (Smart Rock B in Figure 4.24) was placed into the upstream water channel, and moved to the downstream water channel following the water flow. The time required for a smart rock to complete the path varied from 10 seconds to a few minutes, depending on the water flow speed and the arrangement of nearby natural rocks. During the tests, the natural rocks were distributed along the channel such that the water flow of varying velocities was created and the active rock was accelerated or decelerated along the way.

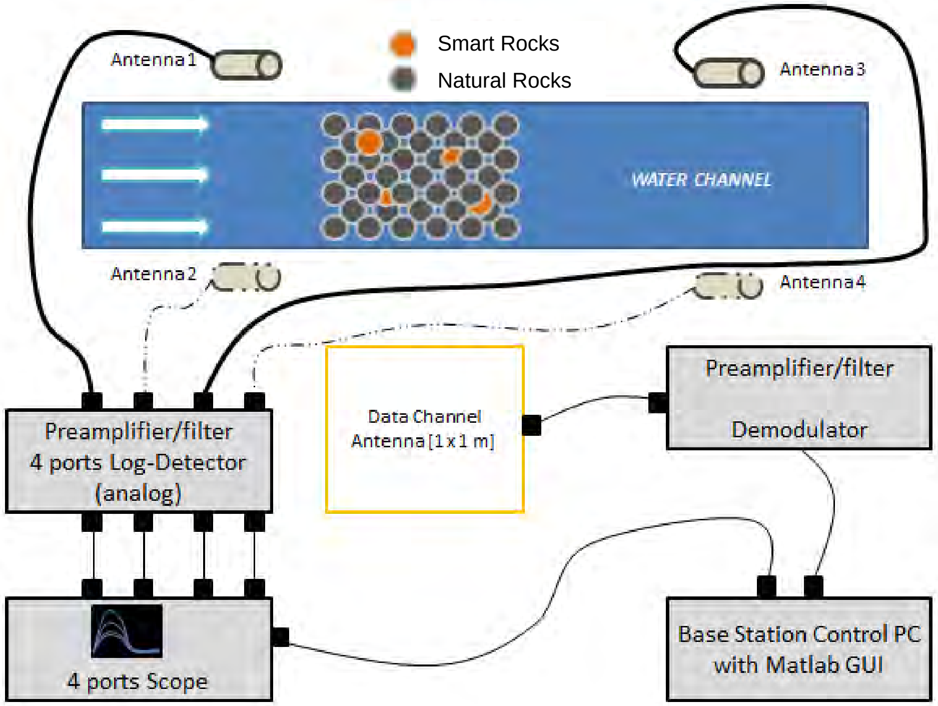

Figure 4.23 General Scheme of Test Setup for Smart Rock Localization

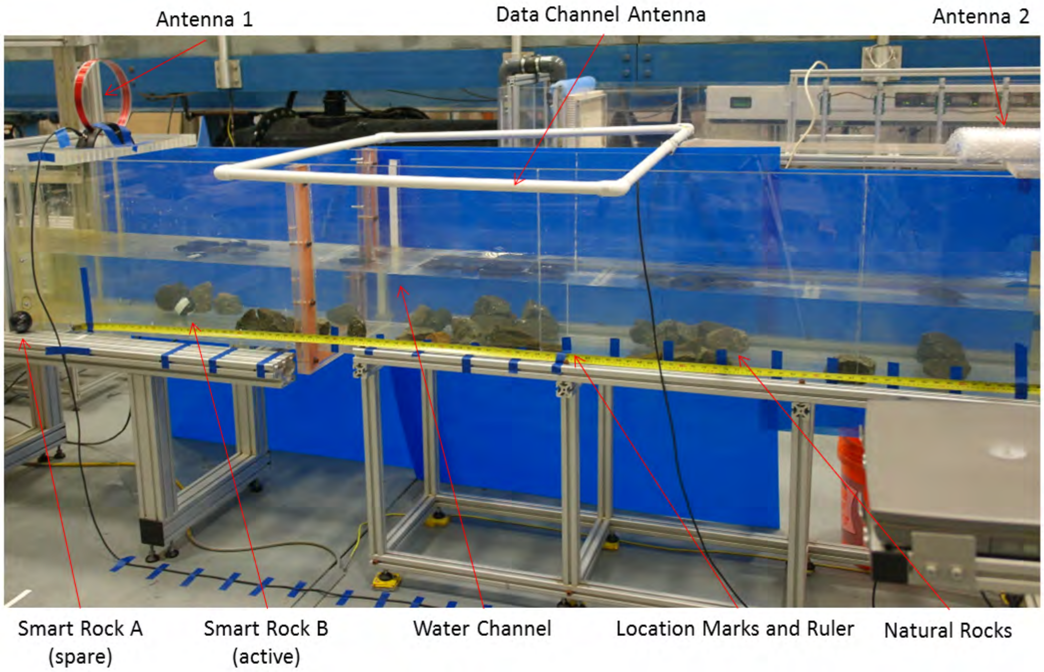

Figure 4.24 Test Setup for Smart Rock Localization

4.5.3 Calibration

To adjust localization routines to a particular laboratory environment, various antennas and smart rock modules were calibrated in the laboratory. For RSSI measurements, external electronic devices, power supplies, chargers, high-speed cameras, pump controllers, and motors are sources of noise in the hydraulic laboratory environment from an electromagnetic point of view. In such a noisy environment, the smart rock signal-to-noise ratio degrades, which could lead to potential issues with data decoding and wake up signal processing. Therefore, prior to testing and calibration, the laboratory was inspected to identify and remove several significant noise sources.

A calibration procedure is illustrated in Figure 4.25. A sample Smart Rock module was manually moved along the path with a fixed distance step (approximately10 cm). At each position, RSSI readings from localization antennas were taken and stored. The procedure was repeated three times for three orientations of the Smart Rock integrated antennas at a total of 15 locations along the channel.

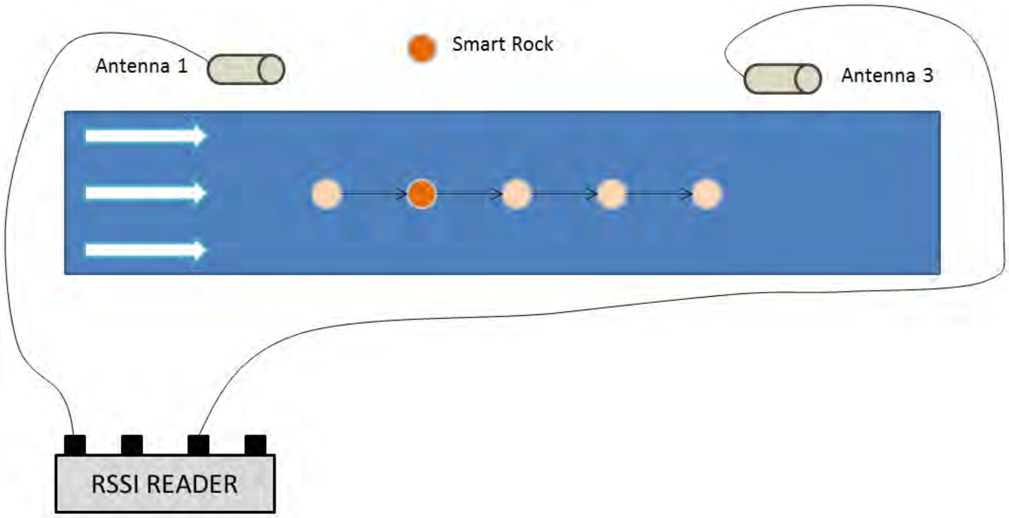

Figure 4.25 Calibration Procedure

For reference, X-axis follows the direction of water flow in a small flume or water channel, and Y-axis and Z-axis are perpendicular to X-axis in horizontal and vertical planes, respectively. Figure 4.26 shows a photo of the calibration test setup. Calibration was performed without water in the channel, using a Smart Rock module fixed in a styrofoam box at specified positions.

Figures 4.27a - 4.27c show average RSSI antenna readings for each rock orientation: X-, Y-, and Z-axis. In these figures, the horizontal axis represents the numbered position along the water channel and the vertical axis shows the voltage at the base station preamplifier/filter output port, which corresponds to the signal strength received by an antenna. Figure 4.27d shows an average of the three RSSI ratios in three directions, each representing the ratio between ‘Antenna 1’ and ‘Antenna 2’ RSSI readings. This curve was used as a baseline for a location estimate of arbitrarily oriented smart rock modules.

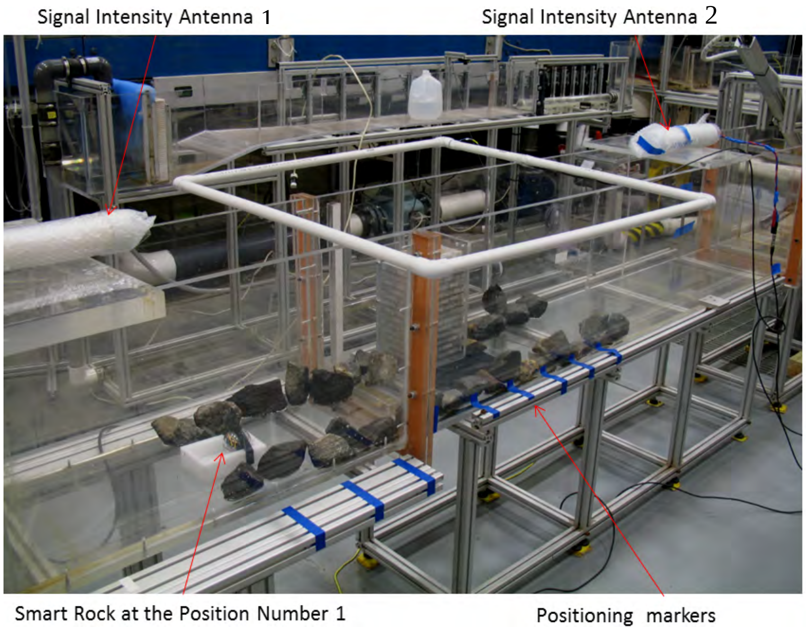

Figure 4.26 Calibration Test Setup

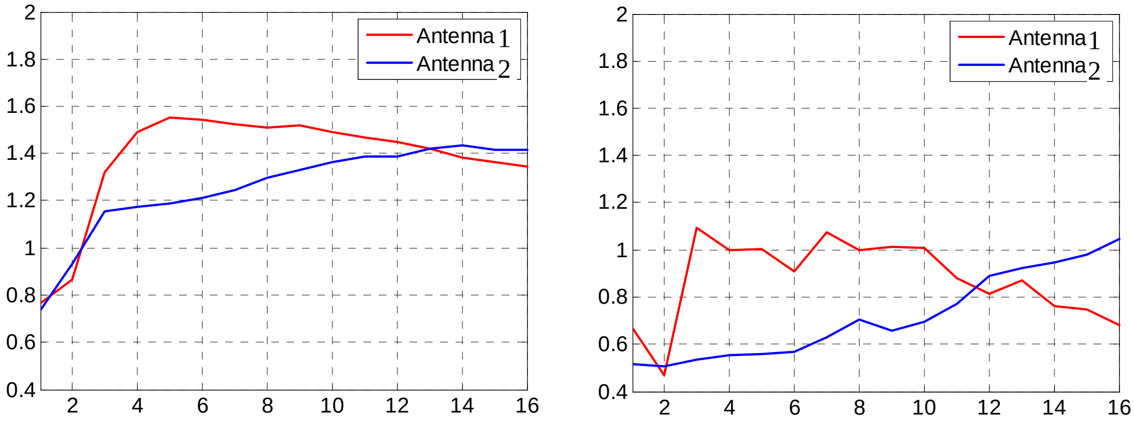

(a) X-axis Direction

(b) Y-axis Direction

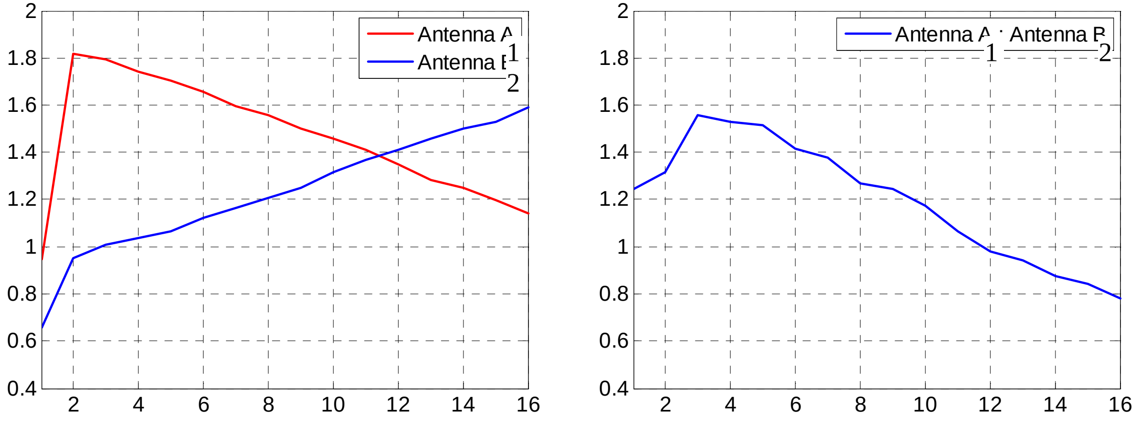

(c) Z-axis Direction

(d) Average RSSI Ratio

Figure 4.27 Calibration Voltage-location Curves

4.5.4 Laboratory Test Results and Discussion

To test the functionality of various sensors, two active smart rocks with external wake-up signal processing were moved manually one-by-one inside the small flume at 30-40 cm steps. In each position, data from every rock was collected from individual rocks. The last step was to return the two rocks to their start positions, respectively. Figure 4.28 shows a screenshot from the Control GUI with the RSSI data, pitch & roll, heading and the estimated position information from the RSSI readings and the calibration curves. Sample #1 and #6 represent the start and end positions of the two rocks, respectively. The top left graph displays the RSSI readings from Antenna 1 (Figure 4.24) in solid curve and from Antenna 2 (Figure 4.24) in dashed line. The top right graph shows pitch in solid curve and roll in dashed line for smart rocks. Note that the control interface supports a simultaneous visualization of the data from four smart rocks (A to D) and only A and B were used in this test.

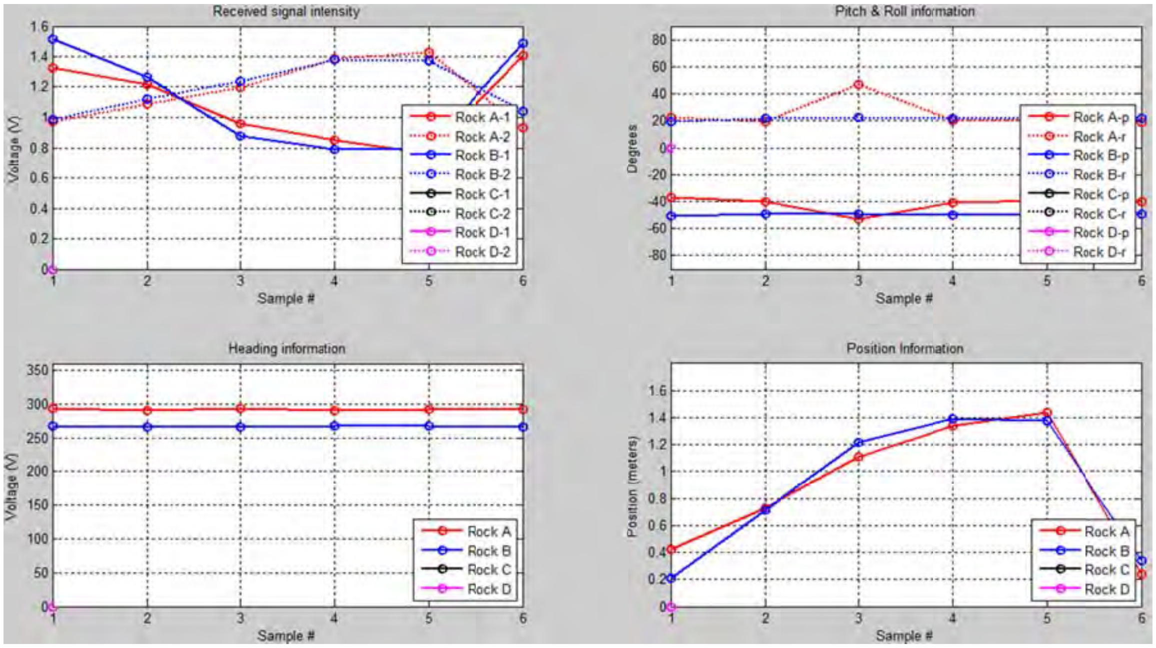

Figure 4.28 Test Results from Two Active Smart Rocks (A & B) Moved Manually

It can be seen from Figure 4.28 that there was no sign of significant change in pitch, roll and heading since the two rocks experienced translational movement manually. The position information from each rock shown in the bottom right graph was in good agreement with the physical locations of the rocks during tests. In particular, the accuracy of position estimation seems to be ±15 cm as indicated in the comparison between samples #1 and #6.

General tests were then performed by placing one or two smart rocks in the small flume and letting them move along with the water flow between Antennas 1 and 2 as shown in Figure 4.26. The time required to complete one test varied from 10 second to several minutes, depending on the water flow velocity. As shown in Figure 4.26, natural rocks were also placed in the flume to potentially create spatially-varying velocities and accelerate/decelerate the active smart rocks.

Figure 4.29 shows the test results when one smart rock (B) moved along the water flow. While the smart rock generally moved in the forward direction, the position information indicates possible moves of the rock opposite to the water flow. These local changes were likely attributed to the rocking motion (sample # 4-6) and lateral movement (sample #6 and #7) of the smart rock, both causing an alternation of the RSSI readings from Antennas 1 and 2. Sample #7 to 8 indicated that the rock temporarily stopped at one position.

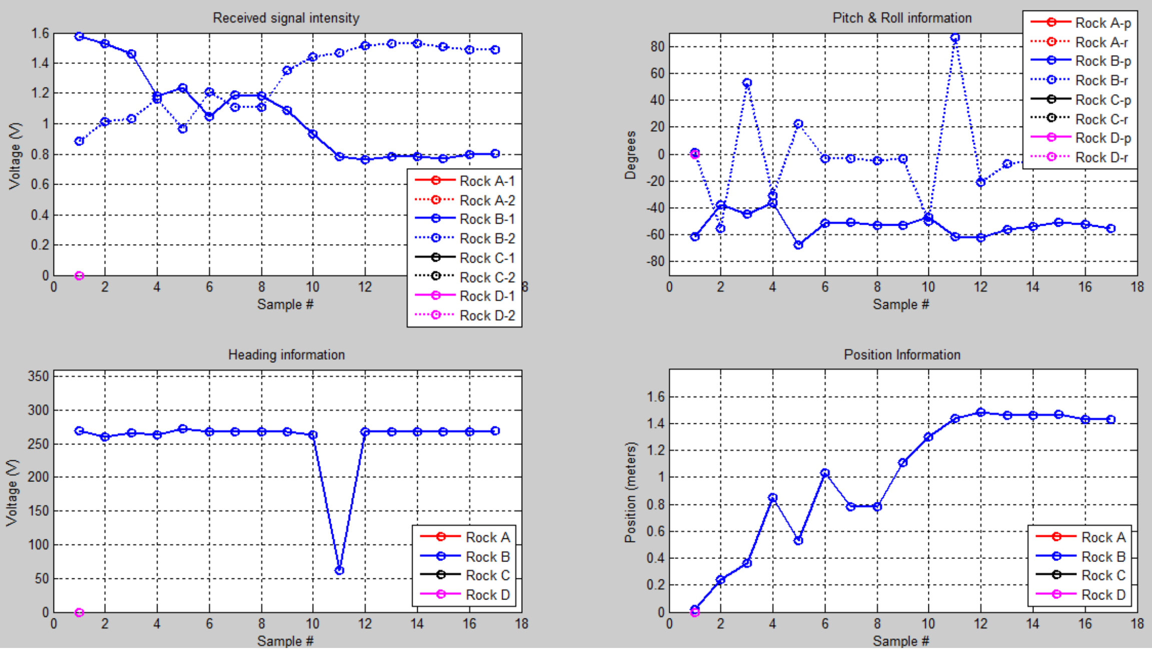

Figure 4.29 Results from Active Smart Rock B under Flow Water

Figure 4.30 shows the test results when two smart rocks were placed in the small flume and moved along with the water flow. It was visually observed that Rock ‘A’ traveled through the measurement area more rapidly than Rock ’B’. However, Rock ‘A’ stopped at the exit of the test range after the 5th step. Rock ‘B’ temporarily stopped in the middle of the flume when Samples # 4-7 were recorded. These physical observations are the evidences why there are 5 reading steps for Rock ‘A’ and 11 steps for Rock ‘B’ over the same travel distance. Overall, this test case indicated that the position monitoring task with active smart rocks was performed successfully and the rock localization algorithm is stable and reliable.

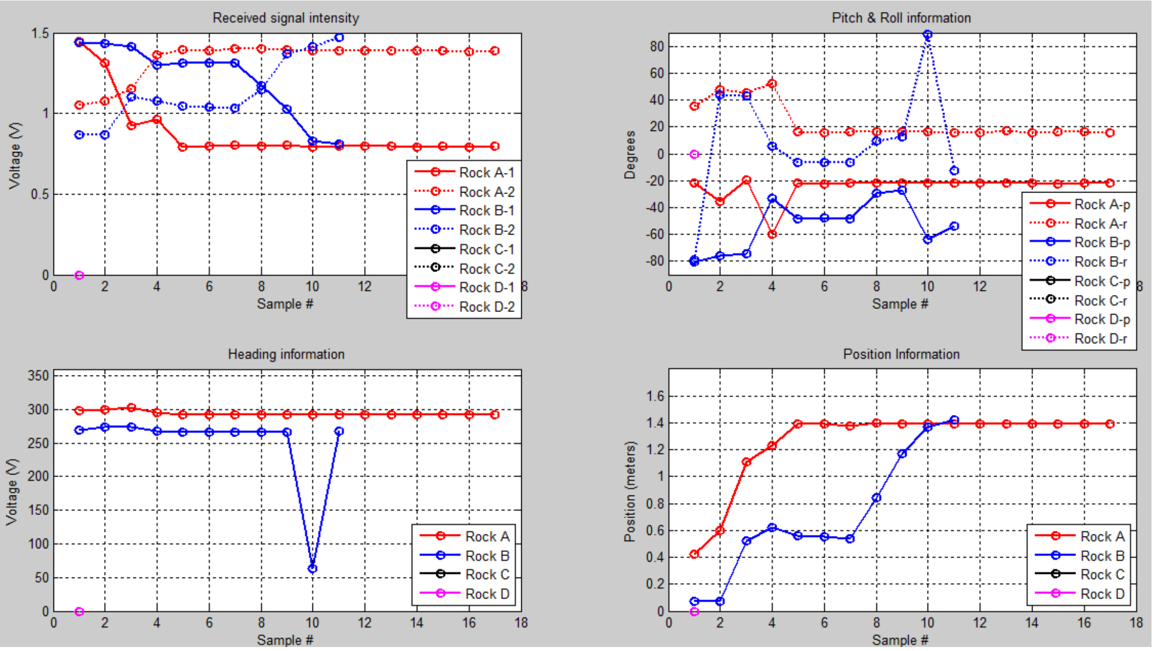

Figure 4.30 Results from Two Active Smart Rock A & B under Flow Water

The final test in the TFHRC Hydraulic Engineering Laboratory was performed in the large flume with two small-scale pier models (circular and rectangular) supported by sand deposits. The goal of this test was to understand the capability of the designed smart rocks for wireless and continuous data transmission. To this end, an active smart rock was placed near the circular pier as illustrated in figure 4.31 and was monitored for one hour. Figure 4.32 shows the overall pitch and roll data as well as zoomed-in roll data of the active smart rock recorded within 80 minutes. The most significant changes occurred during the first 10 minutes. After that, the smart rock rotated back and forth within a scour hole, showing approximately ±3° rocking.

Figure 4.31 An Active Smart Rock Deployed around the Circular Pier in Large Flume

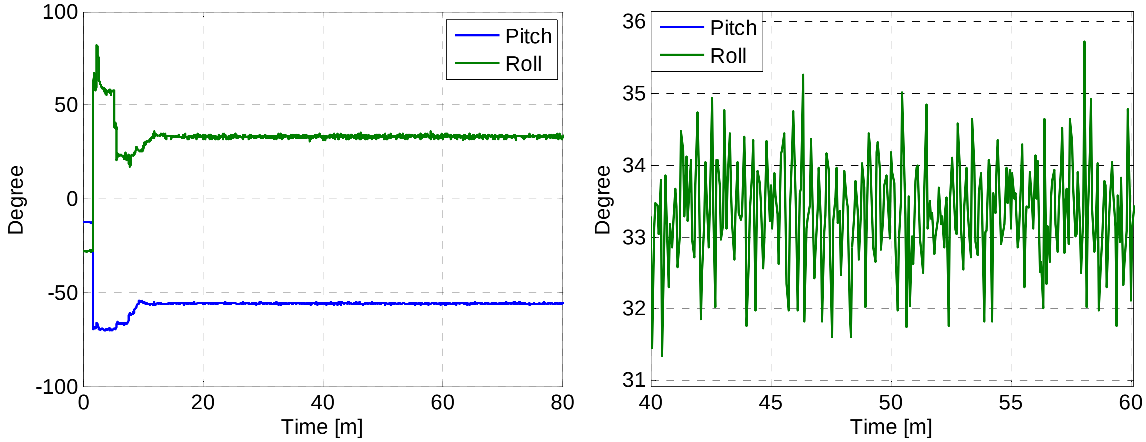

(a) Overall Pitch and Roll Data (b) Zoomed-in Roll Data

Figure 4.32 Pitch and Roll Information from Continuous Monitoring of Small-scale Circular Pier Model in the Large Flume

During various laboratory tests, the following functions of active smart rocks have been demonstrated to be successful:

- Smart rock modules waterproof and sinking properties
- Communication with smart rock modules by assigned IDs
- Smart rock wakeup and data acquisition by timer
- Low power consumption (no battery issues occurred during tests)
- Effective antennas tuning
- Reasonable accuracy of the initial version of the localization/calibration algorithm and procedure

4.6 Field Validations on Smart Rock and Communication Link Designs

As discussed in Section 3, two bridges in Missouri were selected for smart rock field testing: US Route 63 over Gasconade River near Vienna, MO, and Interstate I-44 over Roubidoux Creek near Waynesville, MO. The two bridges are significantly different in physical structure and river flow.

4.6.1 Field Tests on September 24, 2012, with the US63 Bridge

Two active smart rocks were deployed at the US63 Bridge on September 24, 2012. As illustrated in Figure 4.33a, each rock was built with a concrete shell and a concrete cap with a plastic bucket embedded in the center for electronics installation. The rocks were placed in proximity to the north bridge pier and communication was attempted from both the river bank and the bridge deck. Figure 4.33b shows the four antennas hung down from the bridge deck at the US63 Bridge. The antennas were hung downward at the tip of wood members in approximately 2.5 m from the rail with the intent of being close to the rocks but more importantly away from the massive steel girders. The bridge deck is approximately 17-18 m above water so that the distance from the bridge deck to the rocks is approximately 20 m.

(a) Active Smart Rocks Deployed (b) Four Antenna Holders Hung on Bridge Rail

Figure 4.33 US63 Bridge, Two Smart Rocks, and Four Antennas Setup

Figure 4.34 shows the base station test setup at the river bank and over the bridge deck. The base station receiver and wakeup signal transmitter controller/amplifier as shown in Figure 4.7 were set on a table. Both modules were controlled by a laptop computer as shown in Figure 4.34.

(a) At River Bank (b) Over Bridge Deck

Figure 4.34 Base Station Setup for Field Tests at US63 Bridge

During communication tests, operation of each rock was tested. Both smart rocks deployed underwater promptly responded to wakeup signals and transmitted pitch and roll data about their current orientations from the accelerometer and magnetometer.

Figure 4.35 shows the data signal patterns received from the two rocks in response to the wakeup signal transmission. The peak-to-peak noise levels observed have been approximately 50 mV when the peak-to-peak signal level was approximately 150 mV. For initial tests at large distance from the rocks (approximately 20 m), the signal quality was considered to be quite good. In this case, the preamplifier gain was set to 500, leaving room for further distances at higher gains. Therefore, the signal levels were proven sufficient for data processing; the wakeup interface demonstrated robust operation.

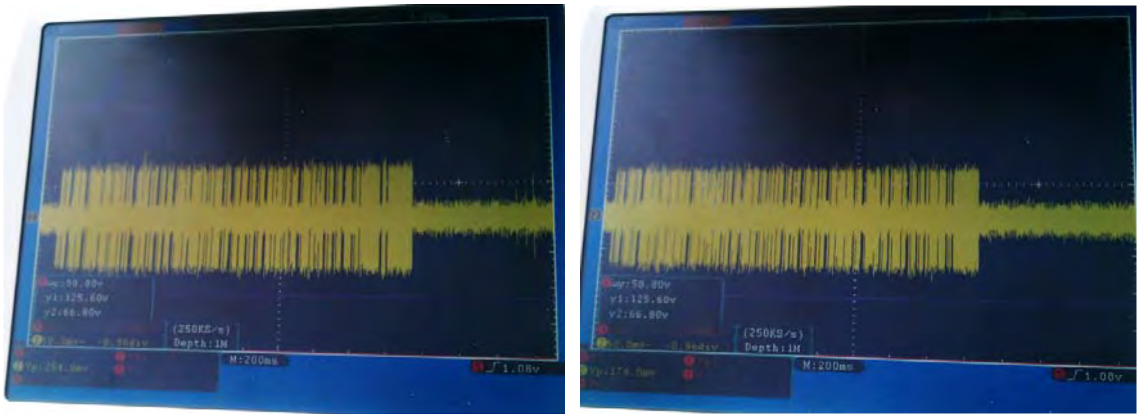

(a) Smart Rock A (b) Smart Rock B

Figure 4.35 Signal Responses from Two Active Smart Rocks

During the tests, the communication link between the base station and the underwater smart rock was validated. The maximum communication distance depended on co-orientation of the smart rock antenna and the receiving antenna. The communication distance exceeded approximately 10 m and 20 m when the base station was set at the river bank and over the bridge deck, respectively.

The US 63 Bridge was revisited in 10 weeks after the initial smart rocks deployment. Both smart rock units responded to the wakeup commands. Thus, the waterproof casing of the smart rock electronic components was validated. Initial pitch and roll parameters of the placed smart rocks were stored. Stability of the power source batteries was also validated. Batteries pack can continuously supply the required current amount for smart rock effective operation.

4.6.2 Field Tests on July 25, 2013

Battery Test. For these field tests, Tadiran Pulse Plus TLP93111/A/S batteries were selected. These batteries provided 19 Ah capacity and 3 A peak current supply. They were tested for continuous transmission of typical smart rock data signals. A typical data signal from a smart rock was transmitted more than 1250 times on a single battery till test was terminated by the user.

Pressure Sensor Integration. An APG PT-500 submersible pressure transducer (http://www.apgsensors.com/sites/default/files/PT-500.pdf) was integrated into a smart rock unit. Figure 4.36 shows a general view of the pressure sensor. The tip of the sensor as shown in Figure 4.36 contains a membrane that can be directly exposed to river water. The other end of the sensor is connected with a watertight electrical wire for pressure reading. The sensor can measure a maximum pressure of 15 psi or a maximum water depth of 10 m. It was calibrated in water of varying depths and demonstrated to produce a linear relation between the pressure and the water depth as illustrated in Figure 4.37.

Figure 4.36 An APG PT-500 Pressure Sensor

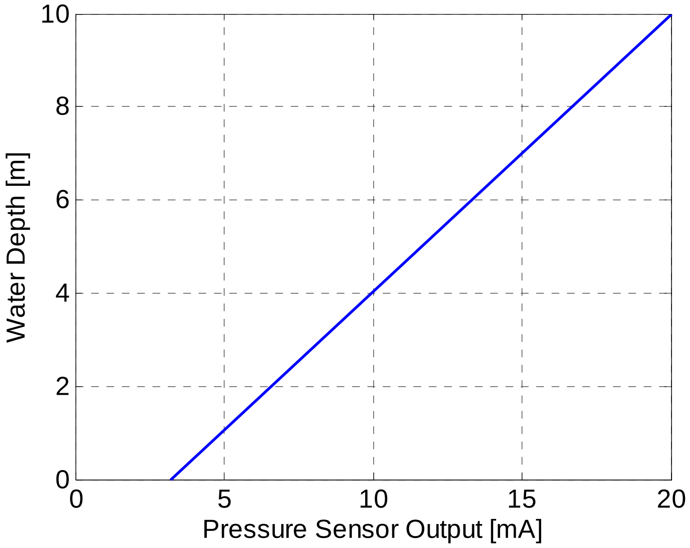

Figure 4.37 The Calibration Curve between Pressure Sensor Output and Water Depth

The pressure sensor has a simple electrical connection as shown in Figure 4.38 and is powered up by a voltage source of 10V-28V DC. It produces a pressure-dependent current output in the range of 3.2 mA - 20 mA.

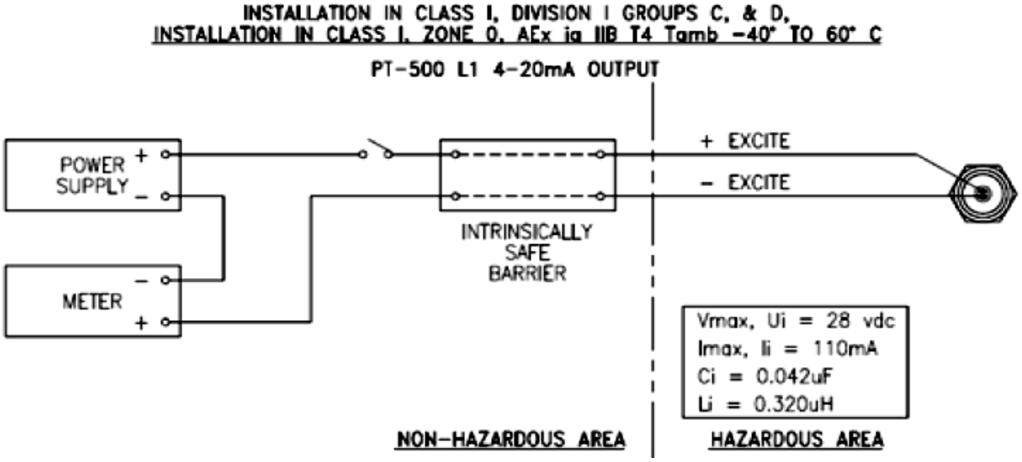

Figure 4.38 The Electrical Connection Scheme of the Pressure Sensor

The smart rock electronic boards already contain a voltage source of 10 V with a microcontroller pin for Analog-to-Digital converter. Therefore, minimal design updates are required on the electronic board in order to read the pressure sensor. However, integration of the sensor into a smart rock unit requires specific mechanical work to ensure a watertight interface between the pressure sensor and electronic compartment. Figure 4.39 shows a mechanical design of the smart rock unit with an integrated pressure sensor.

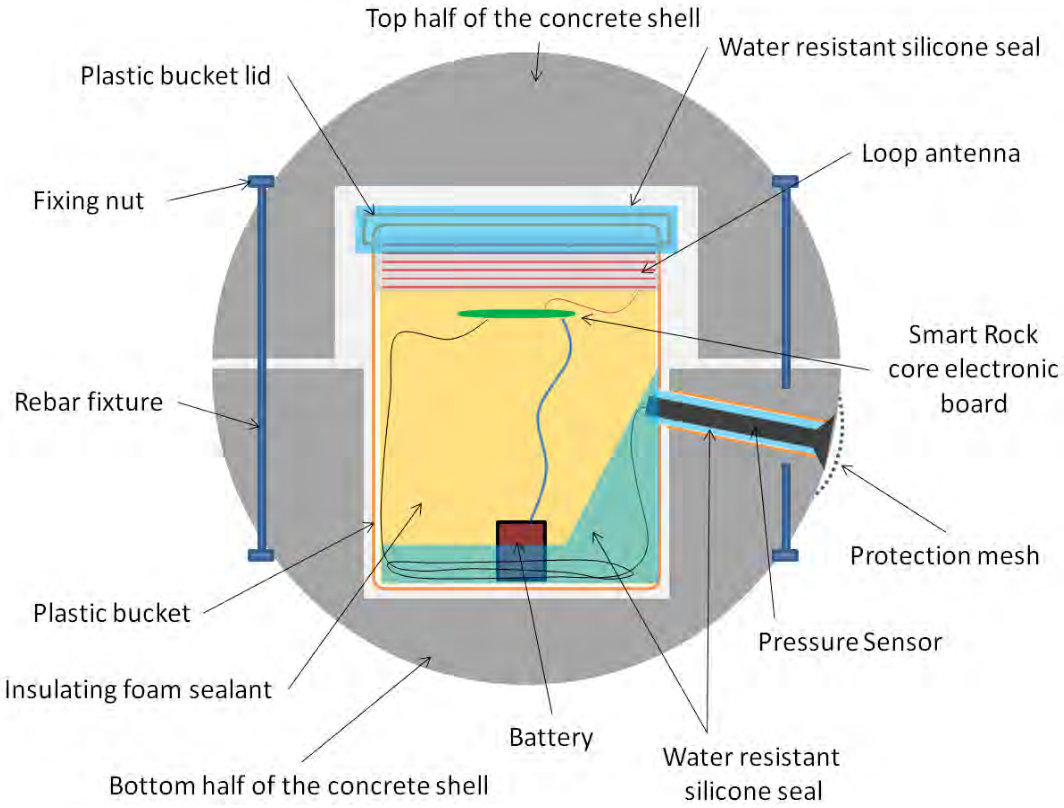

Figure 4.39 A Schematic View of Pressure Sensor Integration into a Smart Rock

Smart Rock Fabrication and Deployment. For field testing, two half-shell concrete encasements were cast with a center cavity for the installation of electronics in a plastic bucket with a pre-cut hole on its wall as shown in Figures 4.40a and 4.40c. The two halves were connected into one smart rock by at least three threaded steel bars and nuts at their ends, as illustrated in Figure 4.40b. For pressure sensor installation, an approximately 4-cm-diameter PVC tube was embedded into the bottom half of the concrete encasement as shown in Figure 4.40c, and aligned with the hole cut on the wall of the plastic bucket. The pressure sensor was then placed inside the PVC tube and the gap between the sensor and the tube was sealed with water resistant silicone as shown in Figure 4.40d. The silicone seal continued inside the bucket to fill the hole and the bottom of the plastic bucket as illustrated in Figures 4.39 and 4.40b. In its final position, the membrane end of the pressure sensor was flush with the surface of concrete encasement as shown in Figure 4.40d.

(a) Bucket with a Pre-cut Hole in Encasement Center (b) Threaded Steel Bars

(c) PVC Pipe Alignment with the Plastic Bucket (d) Sensor Flush with Concrete Surface

Figure 4.40 Installation of Pressure Sensor in a Smart Rock

The bucket was then filled with insulating foam sealants till the level of loop antenna as shown in Figure 4.40b for mechanical stability of the electronic components inside the bucket as shown in Figure 4.41a. The electronic board was placed in plane with the loop antenna so that the embedded on-board accelerometer defines the orientation of the board and the loop antenna, both in parallel to the lid of the plastic bucket. The pressure sensor was directly wired to the microcontroller pin and the power supply pin as illustrated in Figure 4.41b.

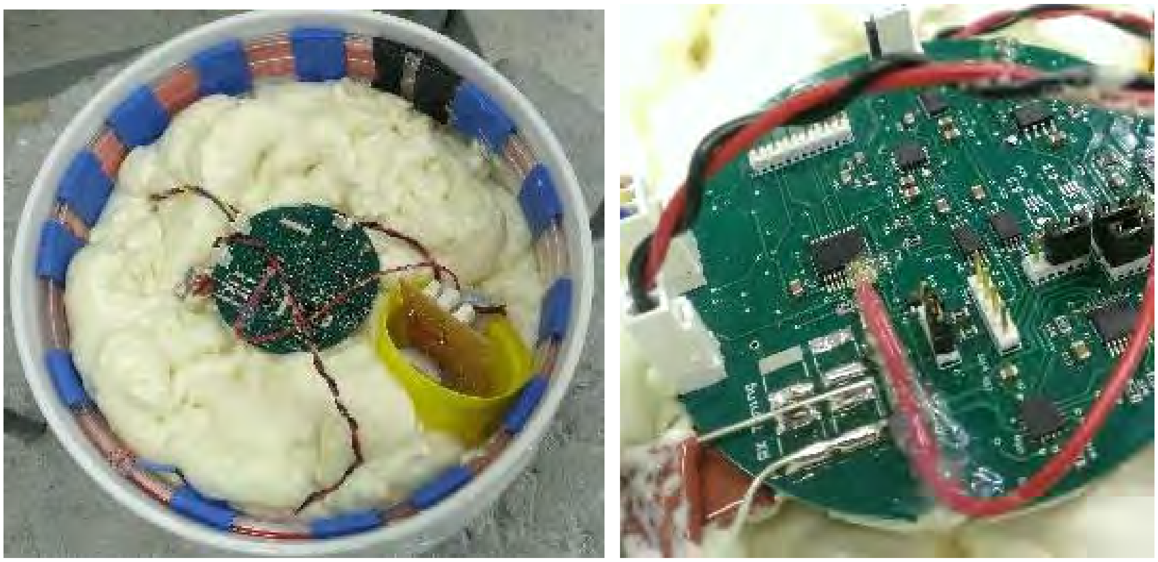

(a) Filled with Insulating Foam (b) Electric Connections of Sensor with PCB

Figure 4.41 Placement of Electronic Board in the Smart Rock

Finally, the lid of the plastic bucket was in place and completely covered with a thick layer of silicone as shown in Figure 4.42a. The two halves of a concrete encasement with the installed pressure sensor, shown in Figure 4.42a, were connected into a complete smart rock as shown in Figure 4.42b. To protect the fragile pressure sensor membrane from direct mechanical contact with natural rocks/debris in the river, at least two layers of metallic mesh were used to cover the pressure sensor tip as seen in Figure 4.42c. The fabricated smart rock was dragged into the river at approximately 1.5 m depth near the bridge pier as illustrated in Figure 4.43.

(a) Two Halves of Encasement (b) Complete Encasement (c) Sensor Protection Mesh

Figure 4.42 Finished Assembly of a Smart Rock

Figure 4.43 Deployment of an Active Smart Rock near the I-44 Bridge Pier

US63 Bridge Tests. At the US63 Bridge over the Gasconade River near Vienna, MO, five active smart rocks were deployed. Figure 4.44 shows the five core boards labeled ‘A’ to ‘E’ used in this test. Each board has a specific ID used in communication with the base station and among smart rocks in a rock-to-rock network. An ID is an 8-bit integer, ranging from 0 to 255 as illustrated in Table 4.2, and used as a primary code in on-demand wakeup signal generation sent by the base station or by another smart rock in the network. On a core board, the AS3930 IC analyzes an incoming signal, performs its demodulation and decoding (when Manchester coding is enabled), and compares its own preprogrammed ID with the received ID. If the IDs are matched, the corresponding active smart rock wakes up and performs the required operations (e.g. sensors data acquisition, RSSI estimation, data transmission to the Base Station). To improve the accuracy in ID recognition and avoid the false wakeups of nearby rocks, the numerical values of various IDs must be significantly different in binary representation. Table 4.2 provides a list of the numerical IDs for the five rocks deployed at the US63 Bridge.

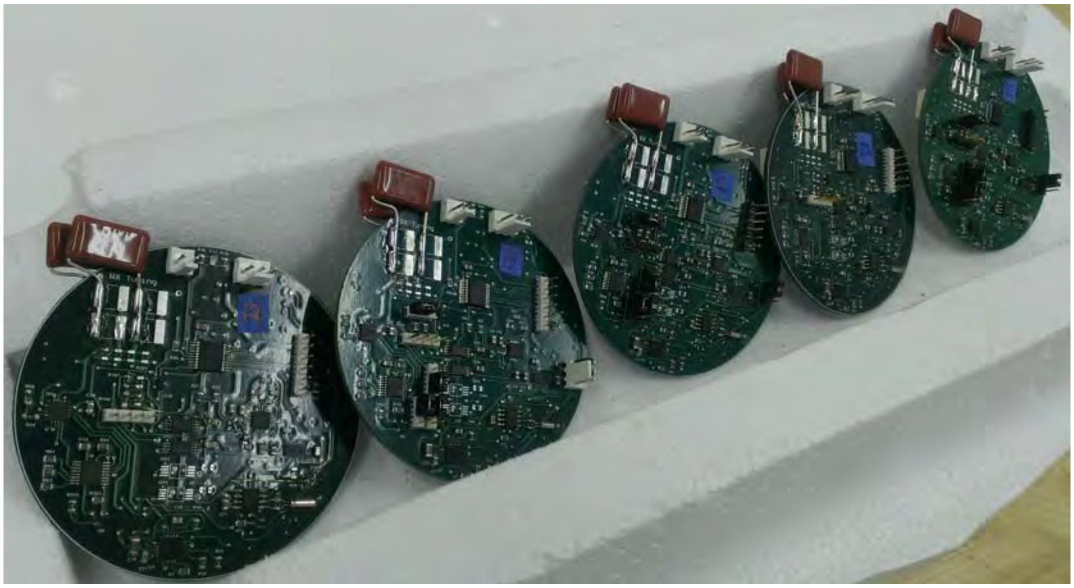

Figure 4.44 Five Core Electronic Boards Ready for Inclusion in Smart Rocks

Table 4.2 ID Assignment of the Five Smart Rocks Deployed at the US63 Bridge

Smart Rock Designation	Numerical ID (binary :: decimal)
A	0b01000101 :: 69
B	0b01111000 :: 120
C	0b00001011 :: 11
D	0b01010000 :: 80
E	0b01100111 :: 103

The five active smart rocks used for the US63 Bridge tests were fabricated similarly to those detailed in Figures 4.40 - 4.42 except no pressure sensor installed. Figure 4.45 shows the final assembling of a few active smart rocks at the US63 Bridge site prior to their deployment.

Figure 4.45 Field Assembling of Active Smart Rocks at the US63 Bridge Site

The five active smart rocks were deployed around the north pier of the US63 Bridge on the upstream side. Their distribution is schematically illustrated in Figure 4.46 in the top view of the bridge. The brown polygon depicts the bridge pier, the light blue arrow indicates the water flow direction, and the dark blue circles represent the installed smart rocks. The location of the rocks was determined with a precision survey instrument. The X-axis was oriented north along the bridge centerline. Y-axis was perpendicular to X-axis in horizontal plane, starting from Rock E.

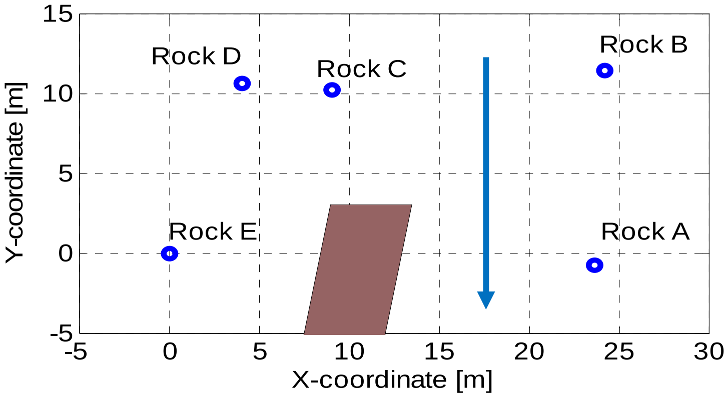

Figure 4.46 Active Smart Rock Distribution near the North Pier of US63 Bridge

Figure 4.47 shows the horizontal distances among Rocks A to E and their depths. The maximum distance between any two rocks was approximately 27 m, which is achieved between Rocks E and B. The minimum distance between any two rocks was approximately 5 m, which represents the spacing between Rocks C and D. The maximum water depth above all rocks is approximately 1.8 m, which is achieved at Rock E.

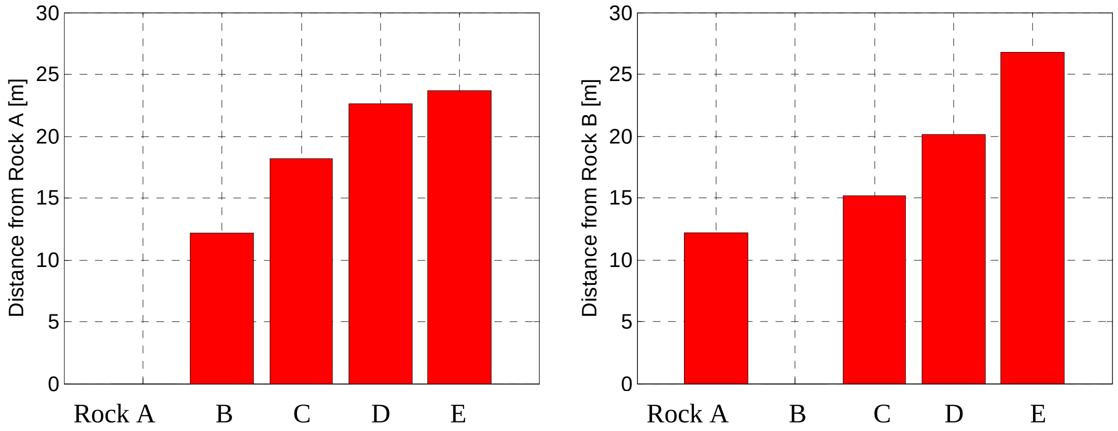

(a) Distance from Rock A (b) Distance from Rock B

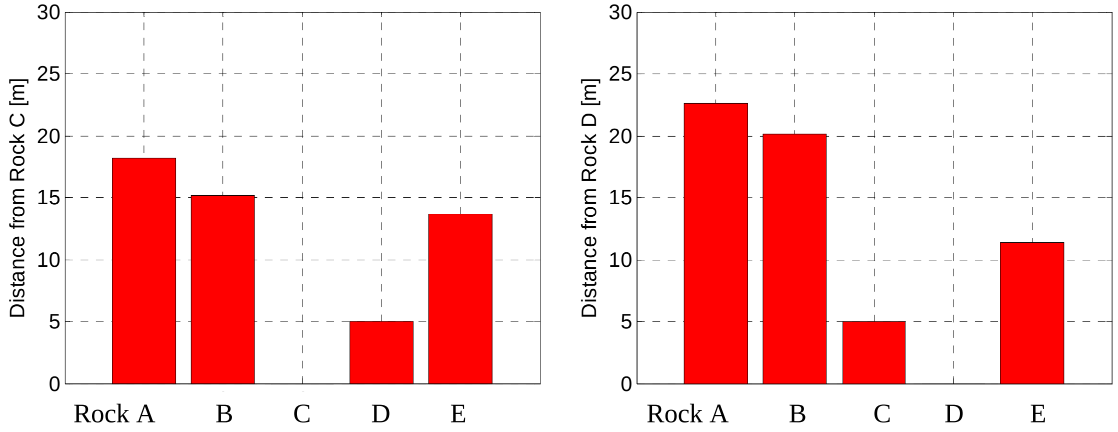

(c) Distance from Rock C (d) Distance from Rock D

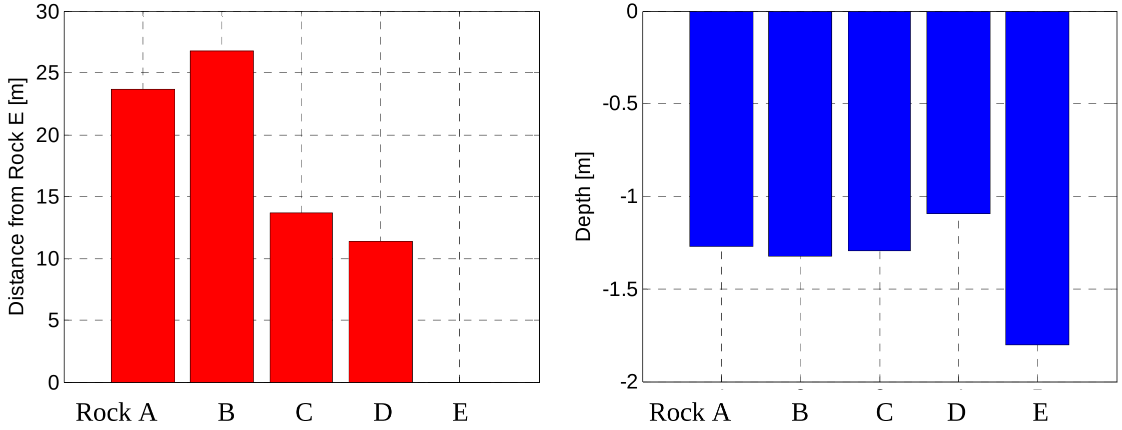

(e) Distance from Rock E (f) Water Depth above Rocks

Figure 4.47 Distances and Water Depth of Smart Rocks

One week after the rocks deployment, the bridge site was revisited and communication with the rocks was performed from a Base Station at the bridge deck, which is over 18 m above the water surface. Over 50 global communications from the Base Station to each of Rocks B, C, and D were all successful. The rocks were demonstrated to have accurately recognized the base-station command.

Local rock–to–rock underwater communications between rock pairs were also demonstrated to be successful. In addition, data was successfully transferred between the located pair of Rocks B and E, demonstrating the stable wakeup functionality at 27 m distance in the field environment at the bridge site.

The embedded accelerometer sensor data was acquired from the deployed rocks. As pointed out previously, the normal vector to a smart rock core board defines the orientation of its in-plane loop antenna. If the plane of the core board remains horizontal in the X-Y plane of a XYZ Cartesian coordinate system, the normal vector of the board is parallel to the Z-axis. Based on the obtained data, the orientation of the rocks or the angle between the normal vector and the Z-axis was estimated as listed in Table 4.3. Therefore, the misalignment between Receiver and Transmitter antennas was less than 20°, which results in relatively low polarization loss as demonstrated by numerical simulations later.

Table 4.3 The Measured Orientations of Three Smart Rocks

Rock	**B**	**C**	**E**
Angle between the normal vector of core board and Z axis	4.8515 °	17.839 °	7.2294 °

I-44 Bridge Tests. At the I-44 Bridge over Roubidoux Creek near Waynesville, MO, one active smart rock was deployed. This unit was equipped with the APG PT-500 pressure sensor and programmed to collect and transmit data at 10:10 am every four days. In the installation day, the rock was scheduled for initial operations as described in Figure 4.48.

Figure 4.48 shows raw data received from the smart rock unit. The empty cells correspond to the times when the rock was transported from the laboratory in Rolla to the bridge site or was being prepared for installation so that data was not recorded at the Base Station. The data from 3:25 am to 8:15 am were recorded in Rolla, MO, at the elevation of approximately 340 m when the smart rock was in the Electromagnetic Compatibility (EMC) Laboratory. The data from 10:15 to 11:50 am were recorded at the I-44 Bridge near Waynesville MO, at the elevation of approximately 240 m when the smart rock was place on the river bank. The data after 12:00 pm were recorded at the bridge site when the smart rock was placed in the river at approximately 1.5 m depth.

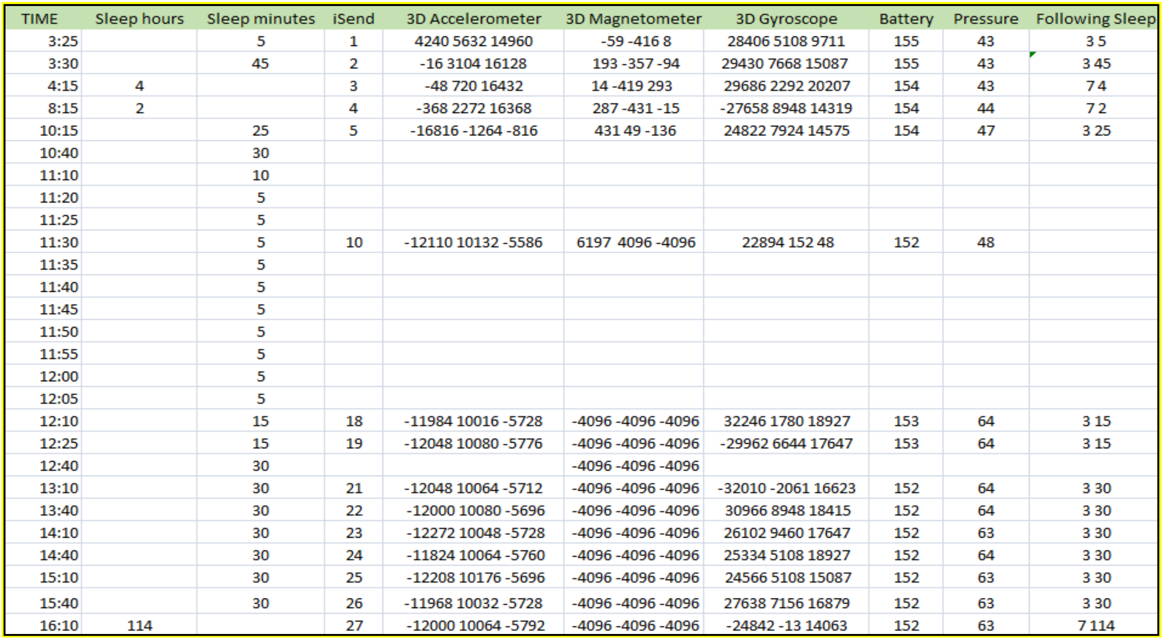

TIME	Sleep hours	Sleep minutes	iSend	3D Accelerometer	3D Magnetometer	3D Gyroscope	Battery	Pressure	Following Sleep
3:25		5	1	4240 5632 14960	-59 -416 8	28406 5108 9711	155	43	3 5
3:30		45	2	-16 3104 16128	193 -357 -94	29430 7668 15087	155	43	3 45
4:15	4		3	-48 720 16432	14 -419 293	29686 2292 20207	154	43	7 4
8:15	2		4	-368 2272 16368	287 -431 -15	-27658 8948 14319	154	44	7 2
10:15		25	5	-16816 -1264 -816	431 49 -136	24822 7924 14575	154	47	3 25
10:40		30							
11:10		10							
11:20		5							
11:25		5							
11:30		5	10	-12110 10132 -5586	6197 4096 -4096	22894 152 48	152	48	
11:35		5							
11:40		5							
11:45		5							
11:50		5							
11:55		5							
12:00		5							
12:05		5							
12:10		15	18	-11984 10016 -5728	-4096 -4096 -4096	32246 1780 18927	153	64	3 15
12:25		15	19	-12048 10080 -5776	-4096 -4096 -4096	-29962 6644 17647	153	64	3 15
12:40		30			-4096 -4096 -4096				
13:10		30	21	-12048 10064 -5712	-4096 -4096 -4096	-32010 -2061 16623	152	64	3 30
13:40		30	22	-12000 10080 -5696	-4096 -4096 -4096	30966 8948 18415	152	64	3 30
14:10		30	23	-12272 10048 -5728	-4096 -4096 -4096	26102 9460 17647	152	63	3 30
14:40		30	24	-11824 10064 -5760	-4096 -4096 -4096	25334 5108 18927	152	64	3 30
15:10		30	25	-12208 10176 -5696	-4096 -4096 -4096	24566 5108 15087	152	63	3 30
15:40		30	26	-11968 10032 -5728	-4096 -4096 -4096	27638 7156 16879	152	63	3 30
16:10	114		27	-12000 10064 -5792	-4096 -4096 -4096	-24842 -13 14063	152	63	7 114

Figure 4.48 Schedule Table and Sensor Data in the Installation Day

Figure 4.49 shows the corresponding plots of accelerometer, magnetometer, gyroscope and pressure sensor readings given in Figure 4.48. The X-axis shows the accumulated time when the readings were captured in the installation day. It can be seen from Figure 4.49 that, after the smart rock has been placed in the river, the readings remained quite stable. The exception to the general observation is the gyroscope X-component readings that suddenly changed sign around 12 hours. This unusual reading is likely attributed to the initial stability of the gyroscope when the rock was in final position. In addition, the magnetometer readings were returned to -4096 for three components after the rock was in final position in the river. This was likely caused by the presence of strong magnets embedded in the passive smart rocks and located in close proximity to this active smart rock. Thus, the magnetic field strength generated by the passive smart rock overfilled the embedded on-board magnetometer readings. In the event that both active and passive rocks must be deployed in close proximity, the orientation of the active smart rock can be determined from the gyroscope readings or accelerometer readings.

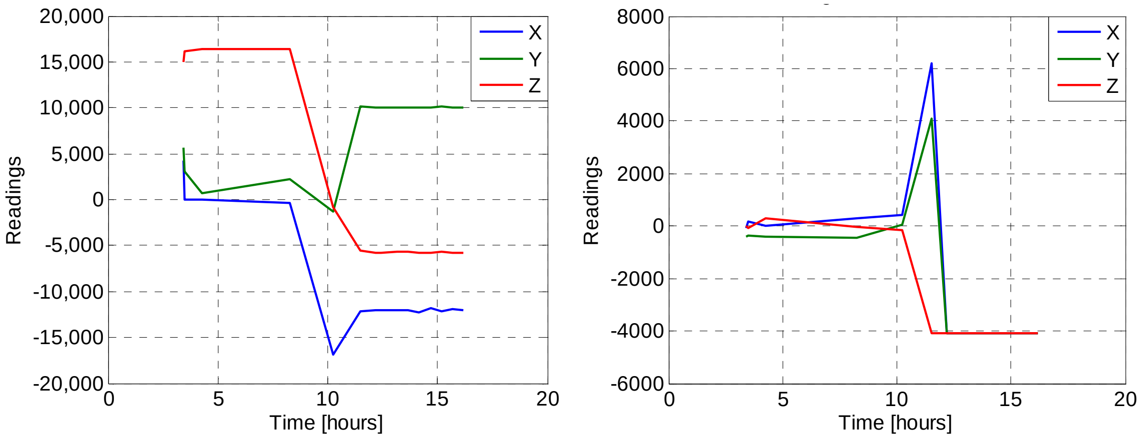

(a) Accelerometer Data (b) Magnetometer Data

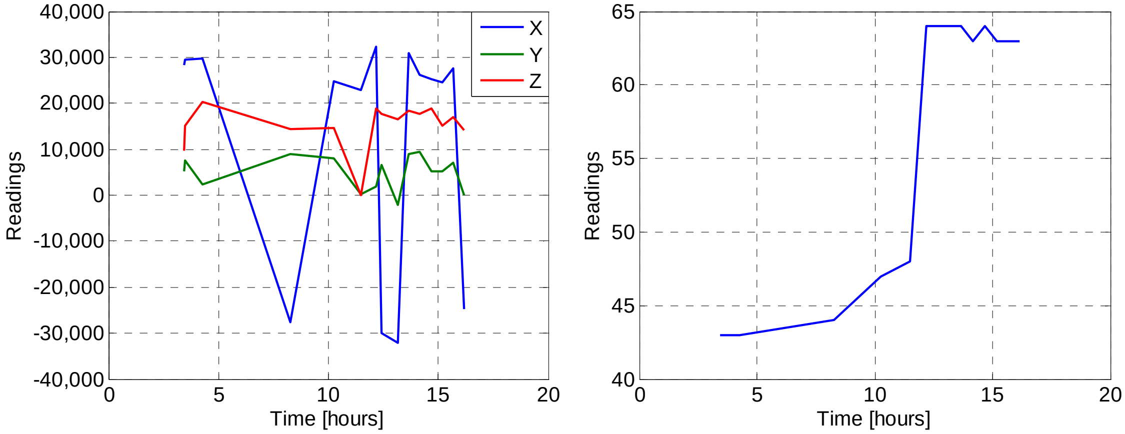

(c) Gyroscope Data (d) Pressure Sensor Data

Figure 4.49 Time Histories of Readings from Various Sensors

When the rock was placed in water, the pressure sensor reading remained approximately 64, corresponding to a current of 4.76 mA according to the sensor specifications or a water depth of approximately 1 m based on the calibration curve in Figure 4.37. Due to rotation/roll of the smart rock with the embedded pressure sensor, the pressure sensor membrane can be located at different levels in the range of the rock diameter or about 50 cm change in water depth. Thus, the estimated water depth from the smart rock was accurate within approximately 50 cm as observed during the test.

4.6.3 Field Tests after the August 7, 2013, Flood

On August 6 and 7, 2013, Rolla area experienced a flood event with over 100-year return period. Both the US63 and I-44 roadways were flooded near the two bridges monitored with smart rocks. This event (a disaster to local residents) represented an opportunity for the research team to understand the performance of the deployed smart rocks. The water level in the Gasconade River near the US63 Bridge exceeded 15 m. Since the smart rocks and sensors were not tested in such an extreme condition, they were retrieved for inspection.

The US63 Bridge was revisited on September 4, 2013, to check the state of the installed smart rocks. Attempts were made to first establish the communication with the deployed smart rocks and find out whether they were still near the bridge pier, and then visually inspect the area to locate the smart rocks. Figure 4.50a shows the base station setup at the river bank in an effort to wake up the deployed smart rocks. To facilitate the retrieval of located smart rocks, a specially designed raft shown in Figure 4.50b was used to lift the located smart rocks from the river. Figures 4.50c and 4.50d show the three retrieved smart rocks (A, B, and C) and the buckets with electronics from the retrieved rocks, respectively. Although the buckets inside the retrieved rocks were crushed under the excessive water pressure during the flood event, they were not leaked and the electronic circuitry inside the buckets was found undamaged. Due to deep water and strong current after the flood event, the movement of the retrieved smart rocks was not measured. However, the three rocks were found to have generally moved towards downstream to various degrees but remained near the bridge pier. The other two (Rocks D and E) were not found until the following visit on October 4, 2013 when the water level subsided to a workable environment.

(a) Base Station Setup (b) Special Raft for Rock Retrieval

(c) Retrieved Smart Rocks (d) Retrieved Buckets inside the Rocks

Figure 4.50 Active Smart Rock Retrieval Efforts

4.7 Smart Rock Network Design and Analysis

To locate a source in a network, triangulation schemes are often implemented by evaluating phase/time differences of arrival at multiple receiving nodes. With the magneto-inductive communication link used in the smart rock system, however, phase-difference measurements are unreliable since the low operation frequency of 125 kHz results in a wavelength of 2.4 km and a small change in meter-scale distance at bridge sites will not be observable in phase difference. Therefore, the RSSI data at multiple receiver nodes is used in this study.

4.7.1 RSSI Reading Test at Component Level

The electronic board in a smart rock was equipped with a low-frequency receiver IC AS3930 that is capable of sensing RSSI from other nearby smart rocks. To test the AS3930 RSSI sensitivity, the output cable from an Agilent A5181A analog signal generator, Figure 4.51a, was connected to the AS3930 receiver IC input pins on a Smart Rock PCB, Figure 4.51b. Continuous sinusoidal signals of 125 kHz frequency were used during the sensitivity tests. The acceptable input voltage for the RSSI estimation ranged from 43 to 43000 uVrms. Out of this range, the RSSI readings from the AS3930 IC were recorded to be either zero or an overflow value, which is not useful.

(a) Agilent A5181A Signal Generator (b) Smart Rock PCB with AS3930 Chip

Figure 4.51 RSSI Sensitivity Test

The RSSI register of the AS3930 provides a 5-bits value with each step representing 2 dB. Figures 4.52a and 4.52b compare the sensitivity from the datasheet with that from the tests. It can be seen from Figure 4.52 that the tested IC demonstrated a good correlation between the test results and the datasheet, validating the RSSI reading range and the embedded software routines for data processing.

The dynamic range of the AS3930 RSSI reader is approximately 60 dB. Within this range, the AS3930 IC provides a very good weak-signal input voltage (~ 43 uV), but has a limited strong-signal input voltage (approximately 43,000 uV). If two smart rocks are located at short distance, the rock-to-rock signal strength can exceed this limit. The dynamic range of a RSSI reader can be extended by adding a secondary RSSI-reader circuitry to the Smart Rock electronic board or by providing an attenuation / antenna damping mechanism.

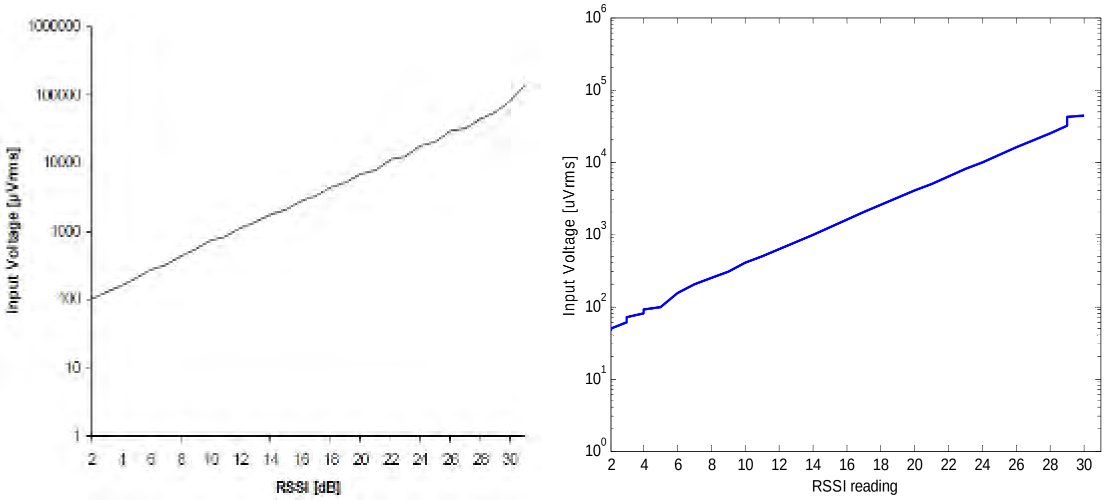

(a) Based on Datasheet (b) Test Results

Figure 4.52 Comparison between Datasheet and Test RSSI Sensitivities

4.7.2 RSSI Reading Test at System Level

The RSSI readings were also tested for a smart rock system. In this case, RSSI values were acquired through rock-to-rock communication links. The RSSI readings were processed by the PIC microcontroller through a SPI bus connection and transmitted to the Base Station by the connected loop antenna. This case introduced additional uncertainties such as antenna tuning, orientation, and relation to the ground. The RSSI dynamic range estimation in relation to the distance between rocks was performed in an outdoor environment with the test setup shown in Figure 4.53.

The transmitting Smart Rock electronic unit was located at a stationary place near the Base Station receiver. The receiving Smart Rock unit was placed on a cart and moved away from the transmitter. The distance range was tested within the RSSI acquisition limits. As illustrated in Figure 4.54, the system tests were performed in three relative orientations between two rocks: (a) co-axial with the two collinear rocks perpendicular to the ground, (b) co-planar with the two co-planar rocks parallel to the ground, and (c) perpendicular with the two perpendicular rocks perpendicular to the ground.

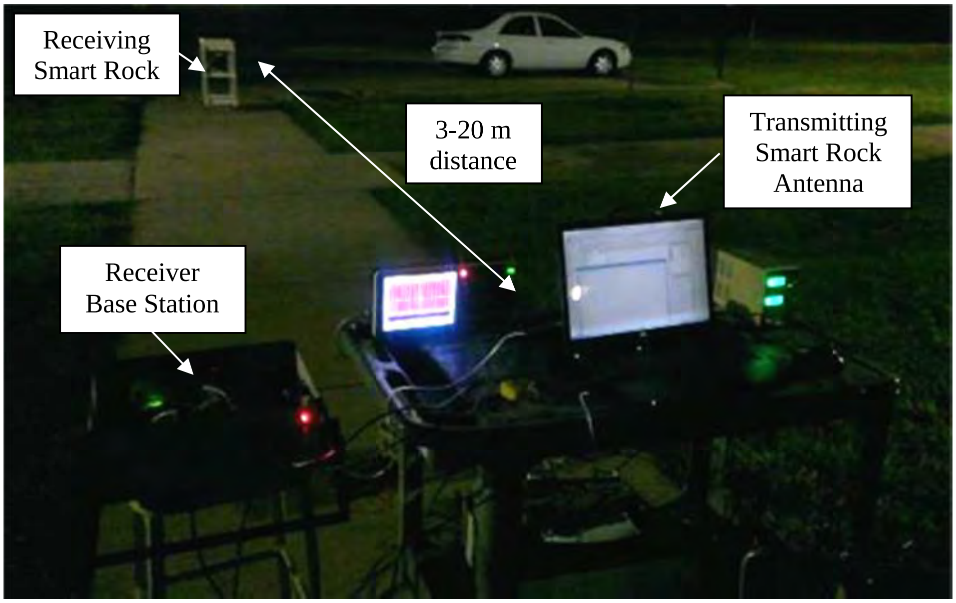

Figure 4.53 Test Setup for RSSI Readings of a Smart Rock Network

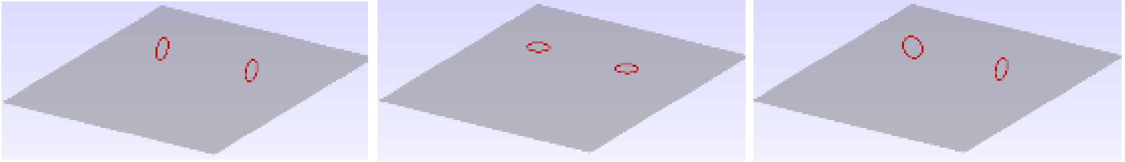
(a) Co-axial (b) Co-planar (c) Perpendicular

Figure 4.54 Test Cases with Relative Transmitting and Receiving Coil Orientations

Figure 4.55 shows the RSSI readings in dB as a function of distance between the rocks. The RSSI had an approximately 60 dB field strength dynamic range. The test results indicated that the AS3920 IC has provided sufficient sensitivity and dynamic range for over 15 m distance. In both co-axial and co-planar orientations, the RSSI readings were valid up to 19 m distance. The co-planar orientation yielded an about 3 dB weaker output up to 11 m distance and an about 2 dB stronger output over 11 m distance than the co-axial orientation did. This is likely due to the effect of ground. The system tests were repeated twice for each configuration and were found to have excellent repeatability.

In the perpendicular orientation (90° cross-orientation in Figure 4.55), significant polarization loss was observed. As such, the communication/RSSI estimation was limited to short ranges only. This is a known issue that must be taken into account in the design of smart rocks. However, the likelihood of having this scenario seems low, and missing one link in a network of many rocks will only have a slight effect on the location estimation accuracy when redundant smart rocks are deployed in practical applications.

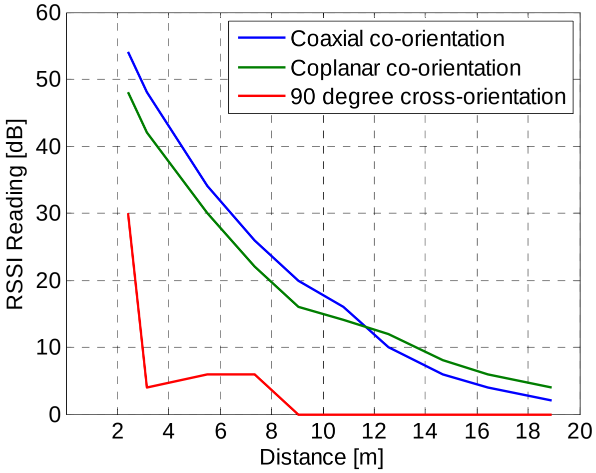

Figure 4.55 RSSI Readings as a Function of Distance

4.8 Communication Link Modeling

To further optimize communication links and achieve large communication distances, the Grundig AN-200 antennas used in the smart rocks deployed at bridge sites was modeled as shown in Figure 4.56. The double-coil antenna contains several turns for excitation and a coupled resonant coil that is the actual antenna for communication. For simplicity of the analysis (and tuning), the feeding structure of the antenna was modified; the short ‘feed-coil for excitation’ was disconnected and the outer coil for communication was excited by an external source directly. The geometrical parameters of the communication coils are given in Table 4.4.

(a) Grundig AN-200 Antenna (b) Antenna Model

Figure 4.56 Modeling of a Grundig AN-200 Antenna

Table 4.4 Coil Parameters of a Grundig AN-200 Antenna

Parameter	Value
Wire radius	0.4 mm
Coil radius	11.35 cm
Number of turns	28
Turn-on-turn height	2.3 cm

The inductance of the coil can be measured using an LCR meter, calculated from the analytical expression, and obtained from the Static 3D modeling in Electromagnetic Compatibility (EMC) Studio as shown in Figure 4.56b. For self-inductance extraction using a Static 3D simulation, the coil was placed in free space. The coil wire with a total length of approximately 20 m was divided into 1662 segments with around 1.2 cm long meshes. The DC-resistance of the coil is 0.8 Ohm. Table 4.5 summarizes and compares the coil inductances evaluated in different ways. The Static 3D simulation result matches well with the measured data. The analytical expression gives a 9% smaller inductance than the measurement. In the following study, a coil inductance of 349 uH will be used.

Table 4.5 Comparison among Various Coil Inductances

Approach	Coil Inductance
Measurement	348 uH
Analytical expression	317 uH
EMC Studio Static 3D simulation	349 uH

For transmission and receiving in smart rocks, the coil was tuned to a resonant frequency of 125 kHz by using capacitors. The resonant frequency can be related to the inductance (L) and capacitance (C) by the following LC-resonance equation:

$$\mathrm{f} = \frac{1}{2\pi\sqrt{\mathrm{LC}}} \tag{4.3}$$

In the Static 3D simulation, the exact capacitance required to achieve 125 kHz resonant frequency is 4.64 nF. Simulations were performed in full wave using the EMCoS (EMC Studio Method of Moments (MoM) solver) and in Agilent Advanced Design System (ADS) as an L-C circuit for the Rx/Tx antennas part of the system (S-parameters solver).

Figure 4.57 compares the simulated with the measured input impedance of the tuned coil antenna. It can be seen from Figure 4.57 that the two simulations (EMC Studio and ADS) agree to each other, both matching well with the measurements particularly in the non-resonance region. The resonant frequency in simulations is very accurate as also indicated in Table 4.5. However, the simulations overestimated the input impedance since loss was not fully taken into account or a higher Q-factor was used in the simulation model. To make the model more accurate, skin effect and additional losses were introduced into the model. The skin effect was represented by an equivalent impedance implemented in the full-wave MoM solver. Figure 4.58 shows both the overall and detailed updated simulation results for the receiving antenna. The blue curve in Figure 4.58 matches well with the measured antenna response in terms of both resonant frequency and impedance amplitude.

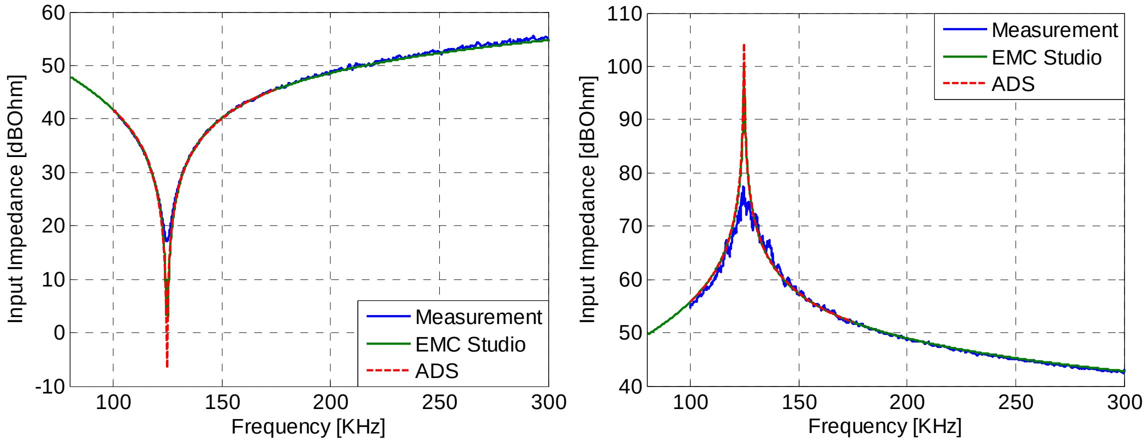

(a) Tx Coil: C in Series (b) Rx Coil: C in Parallel

Figure 4.57 Input Impedances of Transmission and Receiving Antennas

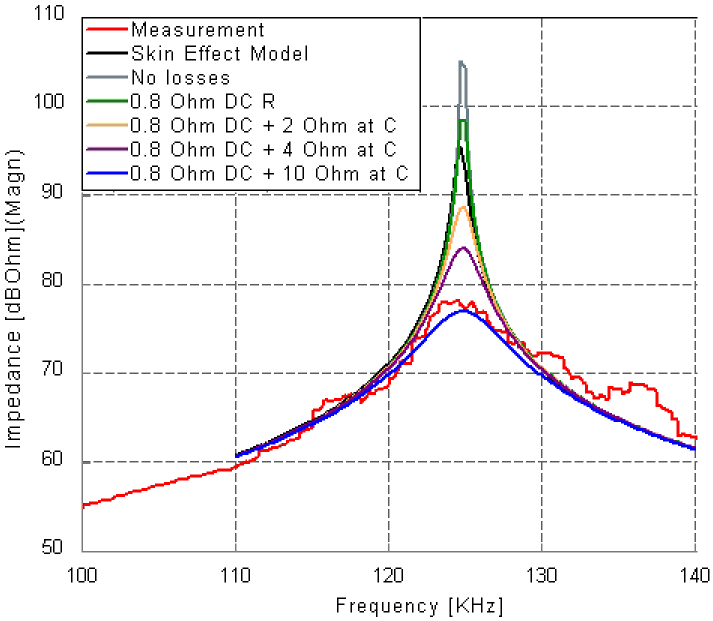

Figure 4.58 Updated Impedance Curves with Rx Antenna Loss Tuning

In smart rocks, antenna coils were embedded into approximately 0.5-m-diameter concrete shells as shown in Figures 4.33a and 4.40-4.42 such that, when placed at the river bed, the antenna may be 15-40 cm above the ground. The above-the-ground distance could cause detuning of the antenna. To estimate how much the presence of ground and the rock shell rotation affect the self-inductance of the coil, a series of simulations were performed. Figure 4.59 presents two antenna models corresponding to 0 and 75° rotation. For comparison, the center of the two antennas was kept at the same height.

(a) 0° (b) 75°

Figure 4.59 Two Antenna Models at 0° and 75° Rotations

Figure 4.60 shows the change in simulated self-inductance of the coil at 30 cm above the PEC ground as a function of rotation. It can be observed that the presence of the ground plane reduced the simulated inductance of the coil by 1.1-1.85 uH only. That is, L=349.5 uH when the antenna is in free space, L = 348.4 uH when parallel to the ground, and L = 347.65 uH when perpendicular to the ground. Correspondingly, the presence of the ground plane can increase and then detune the antenna by 0.19-0.32 kHz in comparison with the free space estimation. The effect of rotation alone at 30 cm height can detune the antenna by 0.12 kHz. Therefore, the tuning capacitance tolerance due to the above-the-ground height can detune the antenna more significantly than the effect of rotation. Table 4.6 lists the effect of tuning capacitance tolerance on the degree of detuning.

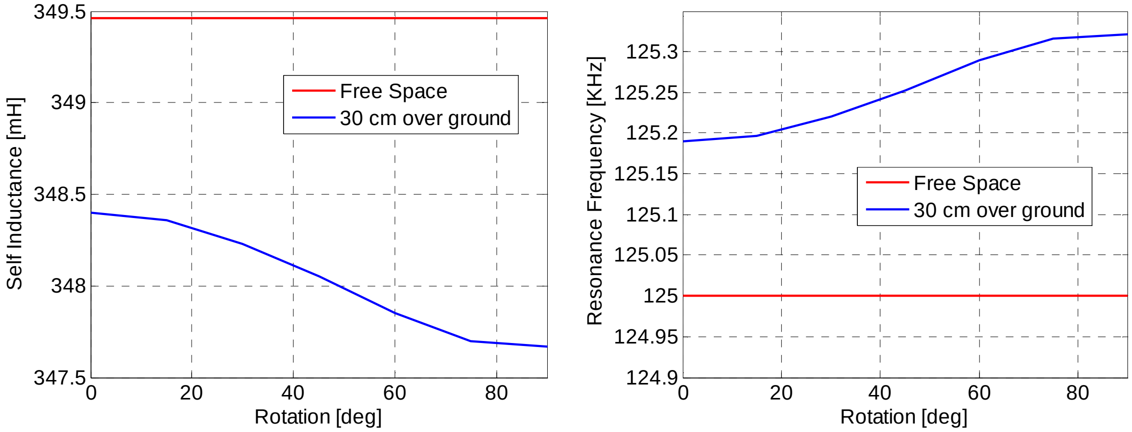

(a) Change in Coil Inductance (b) Change in Resonance Frequency

Figure 4.60 Effect of Coil Rotation at 30 cm above the Ground

Table 4.6 Effect of Tuning Capacitance Tolerance on Detuned Resonance Frequency

Capacitance Tolerance	**1%**	**2%**	**5%**	**10 %**	**20%**
Frequency detuning(±)	~0.6 kHz	~1.2 kHz	~3 kHz	~6 kHz	~14 kHz

The coupling effect between two identical antennas was then analyzed. To simplify the simulation, the transmission (Tx) antenna was replaced by an impressed current source - equivalent driving 1 Ampere current. The centers of excitation and receiver (Rx) antenna coils are along one vertical line as the receiver antenna is rotated to estimate the polarization loss factor. This configuration is similar to smart rock application cases when a communication channel was established from a bridge deck. Figure 4.61a shows the geometrical relation between the two simulated antenna coils where r is the distance between the two coils and α is the tilt angle of the receiver coil that is defined as the deviation from an orientation parallel to the Tx coil. Figure 4.61b shows the receiver antenna port model. A pair of resistors, 0.4 Ohm each, was placed in series with the coil to represent the DC resistance of the coil (the coil wire is generally set as PEC), a 4.64 nF capacitor is provided to tune the coil to resonance, and a 1 kOhm resistor represents the loading by the receiver input.

The voltage across the 1 kOhm resistor is observed and numerically evaluated with the MoM in EMC Studio. Figures 4.62a and 4.62b show the changes in coupled voltage as a function of distance between the Tx and the Rx antennas and as a function of rotation of the Rx antenna at a fixed Tx-Rx distance. It can be seen from Figure 4.62 that the coupled voltage curves for various parameters are generally in parallel. As such, the changes in coupled voltage in Figures 4.62a and 4.62b can be represented by two characteristic curves with α = 0° and r = 1.25 m as shown in Figure 4.63a and 4.63b, respectively. The antenna response attenuates according to $1/r^3$ and up to 20 dB for an angle mis-alignment of less than 85°. The antennas polarization loss is less than 6 dB if the angle mis-alignment is within 60°. The normalized coupled voltage is analytically estimated using the following formula (Sun and Akyildiz 2009);

$$\frac{P_r}{P_t} \cong \frac{\mu^2 \omega^2 a_t^3 a_r^3 N_t N_r sin^2 \alpha}{8r^6} \frac{1}{4R_0(2R_0 + 0.5j\mu\omega N_t)}$$

where P_r and P_t represent the voltages of receiving and transmitting coils, respectively, R_0 is the resistance of the loop per unit length, ω is equal to 2π times frequency, N_t is the number of turns in transmitting coil, N_r is the number of turns in receiving coil, a_t is the radius of transmitting coil, a_r is the radius of receiving coil, α is the angle between the coils, r is the distance between the coils, μ is the permeability equal to $2\pi\times10^{-7}$.

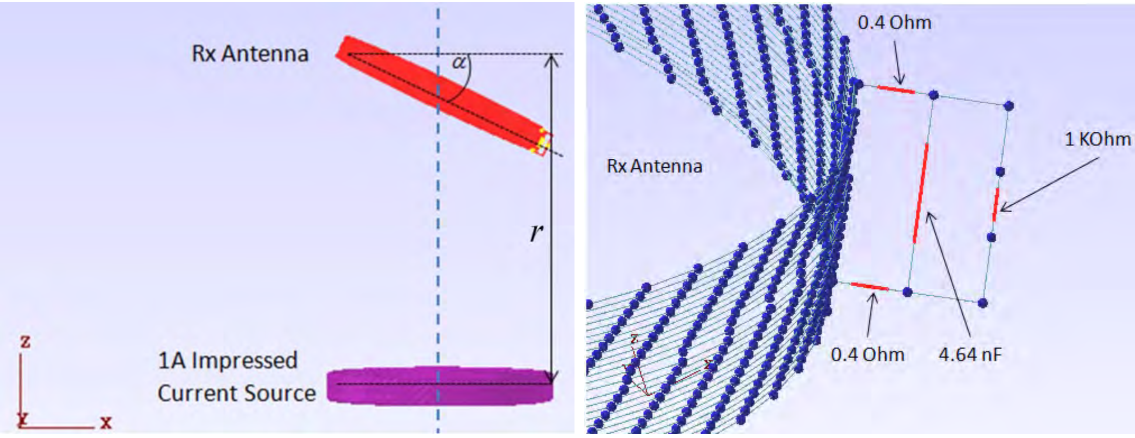

(a) Geometrical Relation between Two Coils (b) Receiver Antenna Port Model

Figure 4.61 Modeling of Coupling Effect of Two Antennas

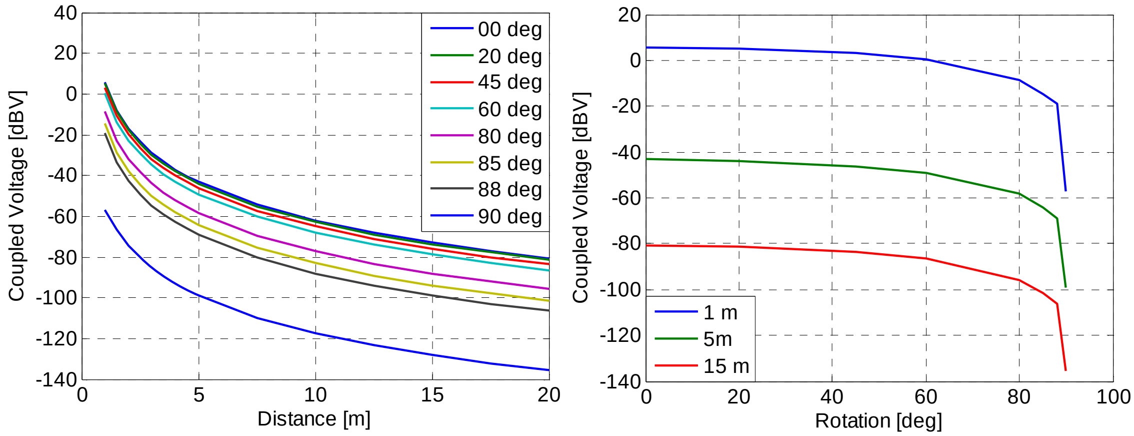

(a) Effect of Tx-Rx Distance (b) Effect of Rx Antenna Rotation

Figure 4.62 Change in Coupled Voltage with Antenna Distance and Rotation

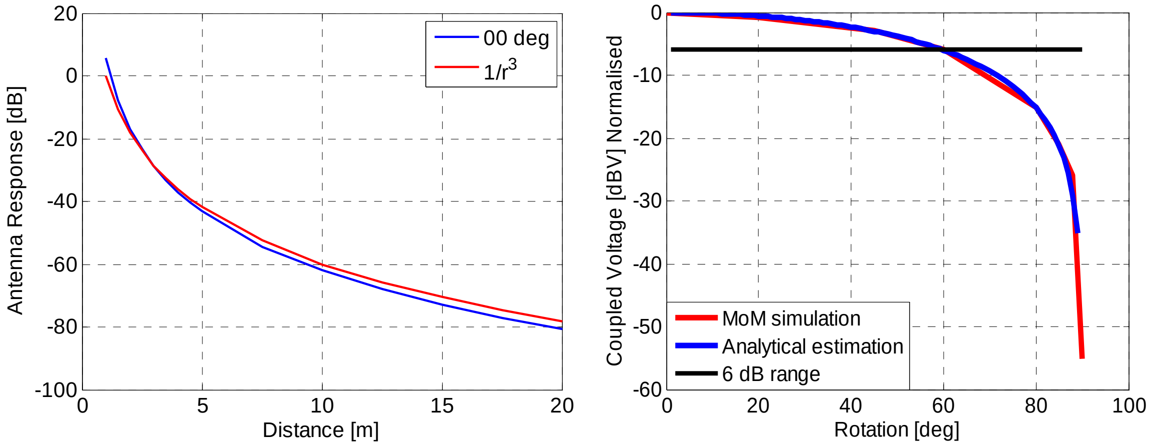

(a) $1/r^3$ Fit to MoM Simulation (b) Fit to MoM Simulation and 6 dB Range

Figure 4.63 Antenna Responses to Changes in Antenna Distance and Rotation

4.9 Localization Scheme Development

4.9.1 General Concept

Active smart rocks include embedded individual IDs and can be located in practical applications. In this study, a two-step localization technique is developed and illustrated with an example smart rock network. The first step involves the architectural mapping of a local communication network of smart rocks, defining the relative positions among the smart rocks. The second step involves the architectural mapping of a global communication network between a subset of select smart rocks and the base station, defining the absolute position of the local smart rock network. The use of the local smart rock network in the first step can improve the measurement accuracy of relative distances among smart rocks.

The general concept of the localization technique is implemented for bridge scour monitoring by first arranging communication among a set of smart rocks in such a way that each rock sequentially pings all other rocks and receives relative RSSI values. The rock-to-rock RSSI data received at the base station is then processed to generate a relative positioning map of all the smart rocks (Awad et al. 2007). Finally, the absolute location of a few select rocks is determined from additional RSSI data between the known base station and the select rocks to map the relative rock positions over the plan view of the bridge near the monitored pier. Alternatively, one smart rock can be mounted / fixed to the bridge pier with known location. The select smart rocks are those rocks that are critical to the accurate positioning of the entire rock network and close to the base station for accurate acquisition of RSSI data.

4.9.2 Illustrative Example with Deployed Smart Rocks at the US63 Bridge Site

To illustrate the localization technique, a network of five smart rocks implemented at the US63 Bridge site was considered and numerically tested with full-wave modeling based on the Method of Moments – an EMC Studio simulation tool at Missouri University of Science and Technology. The five smart rocks designated as A to E were distributed as shown in Figure 4.46. For clarity, Figure 4.64 reproduces the relative positions of all five rocks with approximate distances among a few rocks to provide a general notion about the problem scale. In this model, all the smart rocks are oriented in the same direction with the normal vector of their co-planar loop-antennas pointed upward. In practical applications, the rotational polarization loss factor between antennas can be taken into account with known orientations of the antennas based on accelerometer and magnetometer measurements from each smart rock.

Five simulations were performed with one rock as a transmitting unit and other four rocks as receiving units in each simulation. The transmitting rock was excited by a 1 A current source. The voltage at the receiving rocks was numerically obtained. A complete matrix of the mutual coupled voltage [dBV] is presented in Table 4.7.

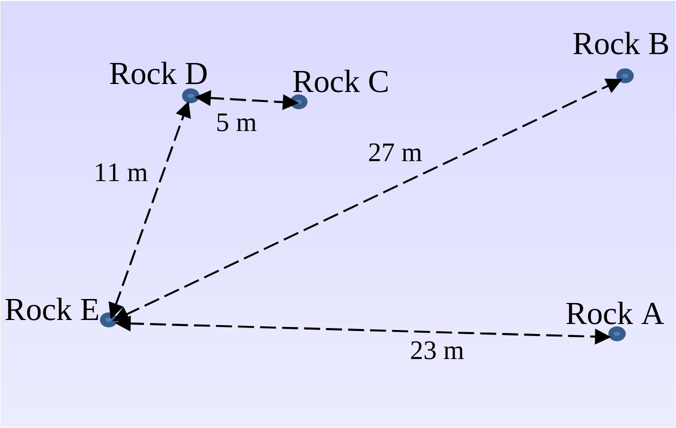

Figure 4.64 Distribution of Five Smart Rocks with Approximate Distances

Table 4.7 Mutual Coupled Voltage among Smart Rocks [dBV]

Rock	**A**	**B**	**C**	**D**	**E**
A	N/A	-36.28	-46.75	-52.38	-53.60
B	-36.29	N/A	-42.07	-49.42	-56.87
C	-46.74	-42.06	N/A	-13.12	-39.27
D	-52.38	-49.41	-13.12	N/A	-34.47
E	-53.58	-56.84	-39.27	-34.46	N/A

Similar to Figure 4.63, the coupled voltage between two antennas can be related to their distance from a calibration test or from a separate simulation with two antennas spaced 0.5 to 30 m. The resulting voltage-distance curve is presented in Figure 4.65. For localization, the two coupled voltages in Table 4.7 were averaged for each pair of rocks and then translated into the estimated distance (d_{ij}, i,j=1,…,5) as shown in Table 4.8.

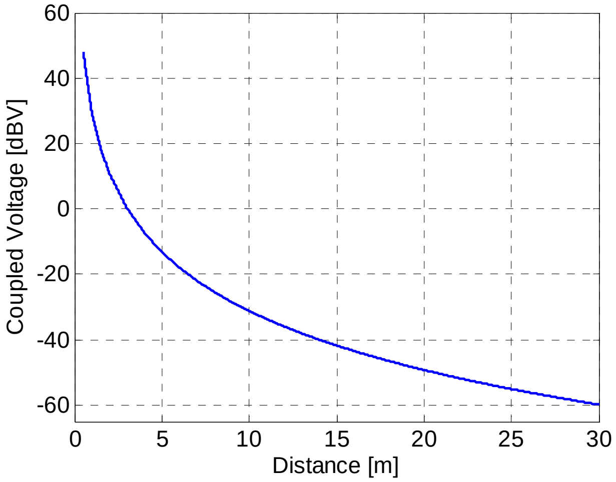

Figure 4.65 Voltage-Distance Calibration Curve

Table 4.8 Simulation-based Estimated Distance between Two Rocks [m]

Rock	**A**	**B**	**C**	**D**	**E**
A	N/A	12.2	18.2	22.6	23.7
B	12.2	N/A	15.2	20.2	26.8
C	18.2	15.2	N/A	5.0	13.7
D	22.6	20.2	5	N/A	11.4
E	23.7	26.8	13.7	11.4	N/A

With the determined mutual distances among the rocks, the relative rock location map can be constructed by the following procedure:

1) The first rock in the network is set into the origin of a Cartesian coordinate system (0,0).

$$X_1 = 0, Y_1 = 0$$

2) The second rock in the network is placed at the right side of the first rock with coordinates (d_{12},0).

$$X_2 = d_{12}, Y_2 = 0$$

3) The third rock is positioned from the known locations of the first two rocks and the distances from the third rock to the first and second rocks (d_{31} and d_{32}), resulting in the X and Y coordinates:

$$X_3=\frac{(d_{12}-d_{32}+d_{31})}{2d_{12}},\ Y_3=\sqrt{{d_{32}}^2-(d_{12}-X_3)^2}$$

4) Each additional rock (designated as i^{th} rock) is positioned by triangulation from the first three rock locations and the distances from the rock to each of the first three rocks (d_{i1}, d_{i2}, and d_{i3}), resulting in the X and Y coordinates:

$$X_i=\frac{(d_{12}-d_{i2}+d_{i1})}{2d_{12}},\ Y_i=\frac{2Y_3\pm\sqrt{4Y_3^2-4(Y_3^2+(X_i-X_3)^2-{d_{i3}}^2)}}{2}$$

Note that the X coordinate is calculated in the same way as for the third rock but the Y coordinate is different with two candidate solutions. The Y coordinate that contributes to a lower difference between some known distances and their corresponding calculated values is selected.

The relative rock location map is finally aligned to the actual bridge site by translational movement, rotation, and/or mirror reflection. Figure 4.66 shows the resulting relative location map of the five rocks. To evaluate the mapping accuracy, the positions of the five smart rocks were surveyed at the US63 Bridge site as presented in Figure 4.46. To align the simulated localization map with the survey result, Rock E in Figure 4.66 was set to (0,0) coordinate and the coordinate system was rotated to make the X-axis from Rock E to Rock A. The aligned relative rock position map or the reconstructed map of five rocks is presented in Figure 4.67a. For comparison, the survey data in Figure 4.46 are re-plotted in Figure 4.67b to show the actual map of the five smart rocks. The absolute difference between each rock's estimated and surveyed X (Y) coordinates is calculated and listed in Table 4.9. The maximum location error is less than 5 cm for the 5-rock network simulation.

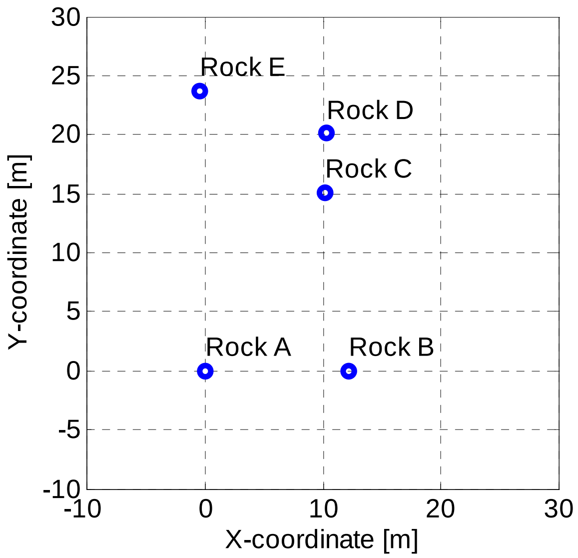

Figure 4.66 Relative Smart Rock Map

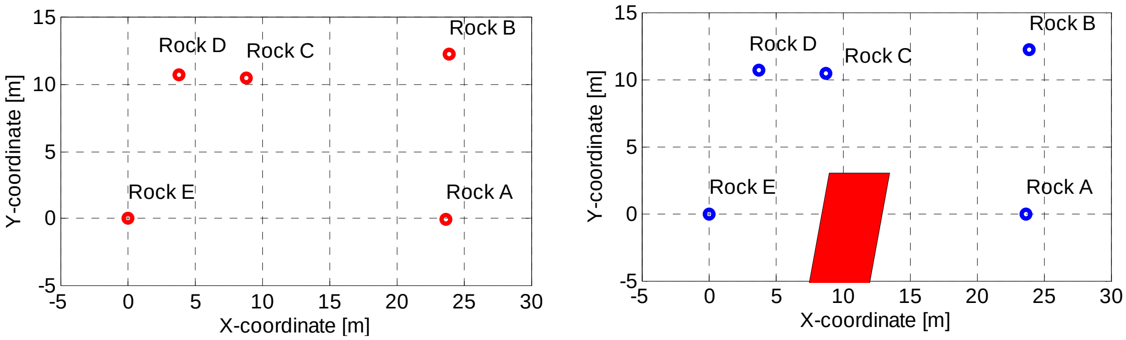

(a) Estimated Smart Rock Map (b) Actual Smart Rock Map

Figure 4.67 Comparison of Estimated and Acutal Rock Positions

Table 4.9 Rock Location Error for the 5-rock Network Simulation

Rock	**A**	**B**	**C**	**D**	**E**
Location error [m]	0.0428	0.0360	0.0279	0.0248	

The localization accuracy is affected by a number of uncertainties, including:

- Current in the transmitting antenna
- Antenna impedance tuning (resonance)
- Antenna detuning due to local environment at the deployment location
- RSSI acquisition dynamic range
- RSSI acquisition quantization
- Effect of large metal / steel components in bridge construction
- Antenna misalignment / polarization loss compensation

In the current design of the core smart rock electronic boards, the embedded receiver IC AS3930 is used to perform the RSSI estimation. The IC has 60 dB dynamic range and uses a 5-bit register for RSSI values. This results in 2 dB quantization over 30 quantization levels of non-zero RSSI readings. Further simulation of data processing was performed to understand the effects of the RSSI dynamic range and the number of quantization levels on the localization accuracy for the considered 5-rock network.

Let the received signal strength at 30 m distance be the minimum RSSI sensitivity. The 60 dB dynamic range can then be used over a measurement distance of 3 to 30 m in the voltage-distance calibration curve in Figure 4.65. Figure 4.68 shows the modified voltage-distance calibration curve including the RSSI dynamic range and the quantization level. Figure 4.69 shows the quantization level as a function of distance with each black circle marking the middle distance relative to that quantization level. This analysis assumes no polarization loss, and will thus need to be modified to compensate the loss based on the known mutual orientation between the antennas from accelerometer and gyroscope measurements in practical applications.

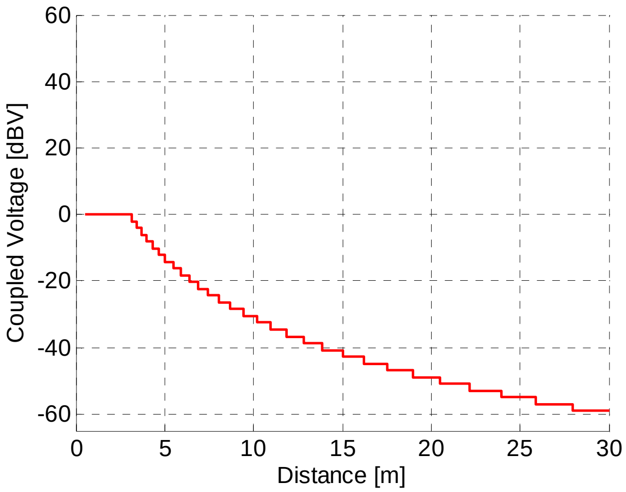

Figure 4.68 Voltage-displacement Curve with 60 dB Dynamic Range and 30 Quantization Levels

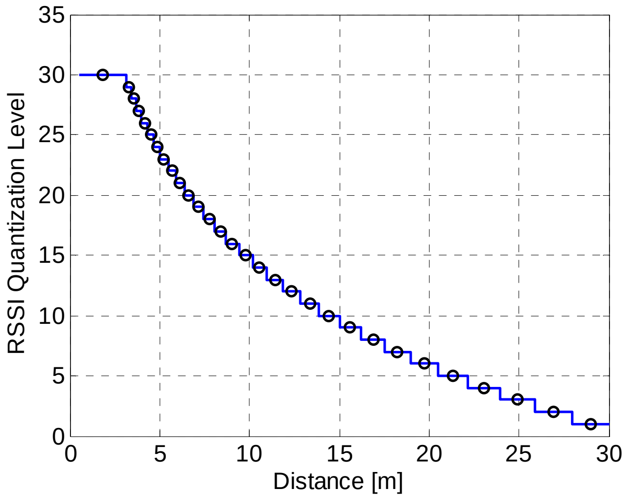

Figure 4.69 Quantization Levels vs. Distance

The mapping algorithm for smart rocks is based on the knowledge of the distances among the rocks. Its performance is thus affected by the quantization on the distance information as evaluated through the following parametric study. The number of quantization levels ranges from 8 to 256 corresponding to 3 to 8 bit Analog to Digital conversions. It can be seen from Figure 4.69 that the largest distance estimation error due to RSSI quantization occurs at the largest distance. Thus, the distance range for the lowest RSSI reading defines the maximum distance error between a pair of transmitting and receiving rocks. In the smart rock network model, however, distances among the rocks are calculated in a set of many rocks. As a result, errors can accumulate during a series of distance estimations and be significantly increased.

Figure 4.70a shows the distance range at the lowest RSSI quantization level in red color and the simulated distance estimation inaccuracy in the 5-rock network with 30 m special range in black color. The distance inaccuracy and the distance inaccuracy follow the same trend, both significantly decreasing as the number of quantization levels increases. The rock-to-rock distance inaccuracy is about 0.5 m for 7-bit RSSI resolution (128 quantization levels) and can be as high as 2 m for 5-bit resolution (30 quantization levels as used in AS3930 IC). Figure 4.70b shows the maximum location error observed in the simulated 5-rock network mapping. For 150 quantization levels or higher, the maximum location error is less than 0.5 m. This result is in general agreement with the distance inaccuracy conclusion.

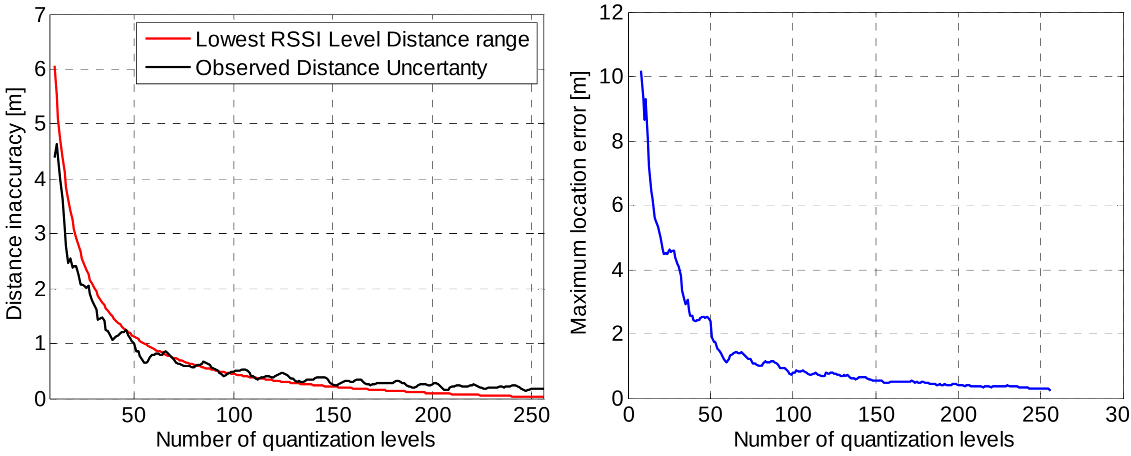

(a) Distance Inaccuracy (b) Location Error

Figure 4.70 Effects of RSSI Quantization Levels on Distance and Location Estimation

The above parametric studies showed that an 8-bit RSSI acquisition circuitry can provide the required resolution for accurate mapping of a smart rock network. The distance inaccuracy and location error are both within 0.5 m for the 5-rock smart rock network deployed at the US63 Bridge site.

4.10 Summary and Observations

In this section, active smart rocks with embedded electro-mechanical modules for magneto-inductive communication with a base station and among the smart rocks were proposed and developed as a rock positioning system from which bridge scour can be inferred. The battery-powered electronics received command from the base station, sensed the movement of rocks, and transmitted information back to the station. To save power, smart rocks were set in sleep mode until they received a wakeup signal from the base station. Based on a series of proof-of-concept tests and analyses, the following conclusions can be drawn:

- Both laboratory and field tests consistently indicated that smart rocks were waterproofed with no leakage. The designed rocks all remained near the monitored bridge pier even after the August 7, 2013, flood with a return period of over 100 years.

- Wireless communications with smart rocks were individually established by pre-assigned IDs.
- Smart rocks were successfully waken up by timer and sent measurement data accordingly over a distance of 30 m at bridge sties.
- The communication system was efficiently tuned with demonstrated low power consumption.
- For the 5-rock smart rock network deployed at the US63 Bridge site, an 8-bit RSSI acquisition circuitry with 60 dB dynamic range can provide the required resolution for accurate mapping of the smart rocks, i.e., within 0.5 m in distance and location estimation error.

5 SEMI-ACTIVE SMART ROCKS WITH FLIPPING MAGNETS

Sections 3 and 4 discussed passive smart rocks with embedded permanent magnets and active smart rocks with embedded electro-mechanical modules, respectively. The passive smart rocks were based on the measurement of static magnetic field strength. The active smart rocks were wirelessly connected and responded to a base station through magneto-inductive communication. In this section, the technologies presented in Sections 3 and 4 are integrated to develop semi-active smart rocks with controllable embedded magnets so that the dynamic magnetic field strength can be measured for improved measurement distance and an effective separation of magnets' effect from passing-by ferrous objects in practical applications.

5.1 Flipping Controllable Magnets Embedded in Smart Rocks

5.1.1 Concept of a Controllable Flipping Mechanism

A magnetometer (i.e. G858) measures the total magnetic field strength at any point in space, combining the effects of the Earth, a nearby magnet, and other ferrous objects. In general, the Earth magnetic field is dominant and the remaining part is significantly less. As a result, detecting a small change of the field strength induced by the magnet embedded in a passive smart rock limits the measurement distance in applications. More importantly, the static magnetic field characteristics of the magnet and the ferrous objects are similar, presenting a challenge to separate their effects with periodical monitoring.

To overcome the practical challenges with a passive smart rock, the magnet inside the rock is flipped in a controllable fashion so that a time-varying magnetic field is generated. The resulting unit is referred to as a semi-active smart rock since the total magnetic field strength measured by a magnetometer includes the effect of external excitation to flip the magnet. To control the rock flipping motion with minimum energy consumption, a special mechanical design of the smart rock with a least-effort magnet flipping mechanism is proposed. For proof-of-concept tests in this study, a frictionless surface between a concrete shell and the inside magnet is introduced in the design of a semi-active smart rock. The flipping control of the magnet in the semi-active smart rock is designed by extending the circuitry of the same PCB as used for a magneto-inductive active smart rock in Section 4.

5.1.2 Design of Semi-active Smart Rocks with Rotating Magnets

To make the magnet inside a smart rock rotate with minimum energy, a low friction or frictionless interface between the magnet and the concrete shell of the smart rock must be created. The initial design first included a magnet encased within a hollow sphere with an outside diameter of 38 mm. The encased magnet was then placed inside a larger hollow sphere with an outside diameter of 51 mm. Finally, a membrane of general motor oil was applied between the two spheres to reduce the friction in between as displayed in Figure 5.1. However, this design was prone to a weight imbalance due to the variability of the magnet placement within the inner sphere. In an effort to overcome the weight imbalance, a second version of the “frictionless” surface was developed.

Figure 5.1 Oil encased magnet

The second version of the packaging sphere design had a few variations from the first design. For a correction of the weight imbalance problem, the new inner sphere was completely solid. A 13 mm hole was drilled through the center of the sphere at a depth of 32 mm. This ensured that the 25 mm long magnet with 11 mm in diameter would be centered and balanced within the sphere. The hole was then filled with a two-part acrylic resin of the same specific gravity as the rest of the acrylic sphere. In addition, instead of general motor oil, a clear silicone fluid with a low viscosity of 5 cSt and a surface tension of 19.7 dynes/cm was used and acted as the “frictionless” membrane between the two spheres. The lower surface tension ensured less energy needed to rotate the magnet encased in the inner sphere.

5.1.3 Design of Magnet Flipping Control Circuitry

To flip the magnet inside a semi-active smart rock, a co-axial current coil of over one hundred turns was designed and wrapped around a cylindrical core that was tightly fitted outside the outer sphere of the encased magnet as shown in Figure 5.2. To control the magnet flipping, a special extension board based on an H-bridge component was designed and connected to the free Input/Output (I/O) pins on the PIC microcontroller of the Smart Rock v3.0 PCB. As schematically shown in Figure 5.3, Input A and Input B of the H-Bridge were connected to the PIC microcontroller I/O pins. The H-bridge has a connection to 6V and two outputs – Output A and Output B. The coil and a series resistive load (for current limiting purpose) were connected to the H-bridge output. When current passes through the coil, a relatively strong magnetic field is generated within the coil core.

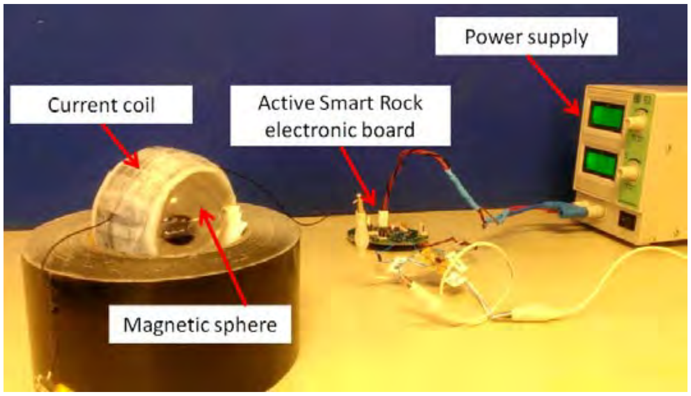

Figure 5.2 Current Coil on a Cylindrical Core and Extension Board Connection to Smart Rock v3.0 PCB

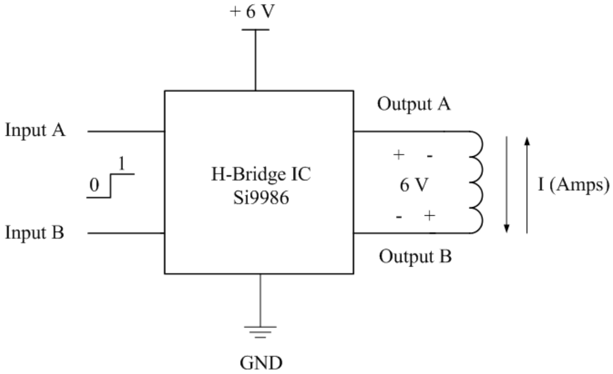

Figure 5.3 Flipping Magnet Extension Circuitry

Figures 5.4 and 5.5 show a model of the current coil in a semi-active smart rock and its induced magnetic field lines as current passes through the coil, respectively. The field strength generated depends on the current magnitude, number of coil turns, and coil dimensions. The unrestrained magnet inside the smart rock placed within the coil is free to rotate and aligned along the magnetic field vector or the coil axis. If the direction of the current flow in Figure 5.5b is changed, the magnetic field vector will flip, causing rotation of the magnet.

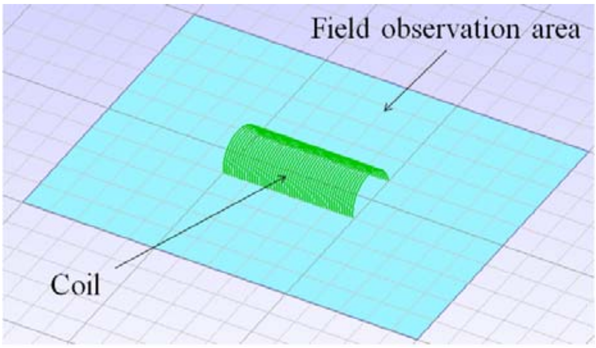

Figure 5.4 A Solenoid Coil Driven by a Current Source

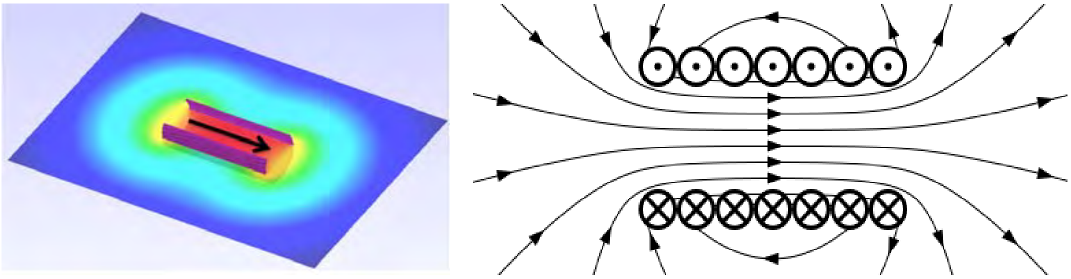

(a) Simulation Results (b) Schematic View

Figure 5.5 Magnetic Field Distribution and Direction within the Solenoid Coil

The above designed semi-active smart rock with the v3.0 PCB and its extension board is a comprehensive system that can be woken up by an external radio frequency (RF) signal through magneto-inductive communication, acquire data from embedded sensors, and wirelessly transmit data to the base station. More importantly, the magnet inside the smart rock can be remotely flipped following a pre-programmed sequence as current was applied to the current coil.

5.2 Preliminary Study

5.2.1 Test Setup

To test the flipping magnet mechanism, the dynamic magnetic field induced by the flipping magnet, and the performance of current-controlling circuitry, a laboratory setup was prepared as shown in Figure 5.2. The test setup included a free-to-rotate magnet in the magnetic sphere, a current coil on the cylindrical core, an Active Smart Rock v3.0 electronic board, a magnet flipping extension board, and power supply. The applied current is basically a periodical change of 0 and 1 A at a predefined interval. The magnetometer for field strength measurement was set up at 305 mm away from the magnet. Laboratory tests indicated that the current consumption required to effectively flip the magnet was 0.3 A, which is significantly less than the available 1 A for magneto-inductive communication links with coil-antenna RF transmission. Therefore, the magnet flipping function does not require any additional power source or any power redistribution in the Smart Rock v3.0 electronic circuitry.

5.2.2 Results and Discussion

Figure 5.6 shows the dynamic magnetic intensity measured over time from the flipping magnet and its corresponding static magnetic field intensity from a 25 mm long cylinder magnet with 11 mm in diameter. It can be observed from Figure 5.6 that the static intensity basically represents the low bound of the dynamic intensity. The maximum dynamic intensity is approximately five times as high as the static intensity. The dynamic magnetic intensity is also a nearly periodical function corresponding to the applied current period of 3.1 sec. The exception to the periodical observation is the missing of one cycle at approximately 20 sec when the magnet accidentally stopped rotating likely due to loose connection in the extension board. Overall, the repeatability and periodicity are obviously seen from the measurement.

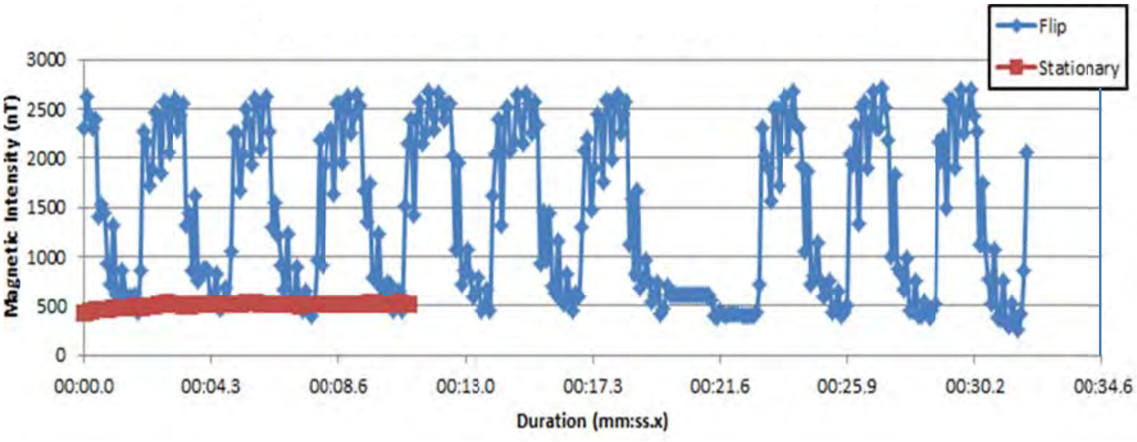

Figure 5.6 Static and Dynamic Magnetic Intensity over Time

Figure 5.6 also indicates a significant difference in pattern of the two magnetic intensity curves over time: alternating with the semi-active smart rock and stationary with the passive smart rock. Such a difference allows the distinction between the effects of a magnet and any nearby ferromagnetic substances. As a result, the identified location of the rock based on the magnetic field strength of the magnet is more accurate.

A detailed examination on the tested magnet indicated that the applied 0.3 A current induced the maximum magnetic strength of 0.75 mT inside the coil.

Furthermore, the semi-active smart rock with a magnet flipping mechanism allows a significantly larger dynamic range of measurement than the passive smart rock with an embedded permanent magnet. This is because, by rotating the magnet, the maximum and minimum magnetic field strengths in the magnet rotation plane can be obtained. In applications, the maximum and minimum strength measurements depend on several factors including the sampling rate of a magnetometer and the speed of magnet flipping that is in turn a function of the time required to change the current in coil and the potential friction at the interface between the inner and outer sphere in the semi-active smart rock.

5.3 Summary and Observations

In this section, a semi-active smart rock with a flipping magnet is proposed, designed, and tested for its performance in terms of the dynamic range of measurement, data repeatability, and differentiability between the effects of magnet and other ferromagnetic substances. Based on the limited tests, the following conclusions can be drawn:

- The mechanism to make a magnet free to rotate is quite effective. Its performance is consistent and repeatable over time.

- The magnet flipping control circuitry requires a minimum extension from the Active Smart Rock v3.0 electronic board.
- The dynamic range of measurement of a semi-active smart rock can be five times as large as that of a passive smart rock.
- The magnetic field strength induced by a flipping magnet is repeatable and can be periodic if the current applied to the coil wrapped around the semi-active smart rock is a periodic function of time. The periodic measurement allows additional verifications on the quality of obtained data.
- The time-varying magnetic field strength taken from a semi-active smart rock is significantly different from the time-invariant strength taken from a passive smart rock. This difference allows the separation of magnet effect from the effect of other ferromagnetic substances in practical application, further reducing the rock localization error.

6 ACTIVE SMART ROCKS WITH ACOUSTIC COMMUNICATION

Alternative to magneto-inductive communication discussed in Section 4 is acoustic communication between smart rocks and gateway nodes at river banks as illustrated in Figure 1.5. When placed together with natural rocks near a bridge pier for bridge scour monitoring, the smart rocks with transmitters (Tx) can send underwater acoustic signals to the receivers (Rx) at the gateway nodes. The time difference of arrival (TDOA) among various receiver channels can be used to estimate the locations of smart rocks. The estimated locations of smart rocks carry the critical information about the maximum scour depth that is needed in engineering design and maintenance of bridges. As shown in Figure 1.5, the gateway nodes can relay the localization data via cellular networks to the engineer-in-charge of scour monitoring program or the headquarters of bridge engineering design and maintenance offices.

Utilizing the TDOA for localization with acoustic communication has some advantages over the RSSI used in the magneto-inductive communication discussed in Section 4. Since the acoustic waves propagate at a much smaller velocity (nominal 1,500 m/s) than the magneto-inductive waves (300,0000,000 m/s), using TDOA for short distance measurement between smart rocks and gateway nodes in water is feasible by acoustic waves and the TDOA evaluated from the phase difference of signals is not sensitive to signal attenuation, which is often affected largely by the transmitter and receiver orientations and path loss of the propagation channels. However, commercial underwater acoustic communication systems are not only expensive, but also difficult to adapt to this application because they are mostly designed for medium or long range (over 1 km) communications. Therefore, custom-designed hardware for underwater acoustic communication system for smart rocks is developed, implemented, and field tested.

Three main technical challenges for improving the localization accuracy in underwater acoustic communication of smart rocks were identified: (a) multipath propagation (Chandrasekhar et al. 2006, Stojanovic and Preisig 2009) that can result in stronger late arrivals than the direct line of sight path, (b) timing synchronization among multiple gateway node receivers deployed at two sides of the river, as shown in Figure 6.1, and (c) timing calibration of the localization signals at transmitters of the rock nodes. In this study, these issues are addressed in the hardware design that is currently based on the Texas Instruments (TI) Digital Signal Processor (DSP) platform TMS320C6713.

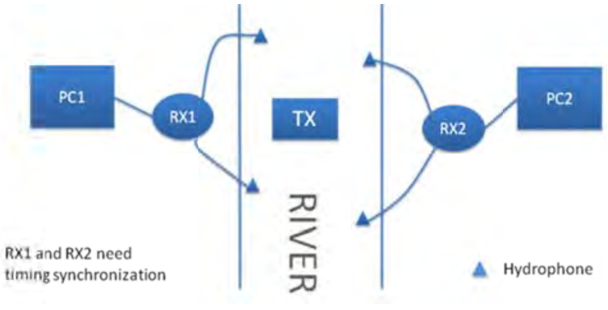

Figure 6.1 A Schematic Acoustic Communication System with one Smart Rock Transmitter and Two Receivers in a River, each Receiver with two Hydrophones

6.1 The Acoustic Communication System

The proposed acoustic communication link is a combined data transmitter and receiver system or an acoustic transceiver as shown in Figure 6.2. In essence, a transmitter first encodes information bits, combines them with one or two preamble sequences, and modulates the resulting data sequence to the carrier frequency with On-Off Keying (OOK). Zeros (gaps) are then padded to form N bits per block. A digital-to-analog convertor (DAC) is used to convert digitally modulated signals to analog signals. A power amplifier and a load matching network are used to tune the signal output to the acoustic projector.

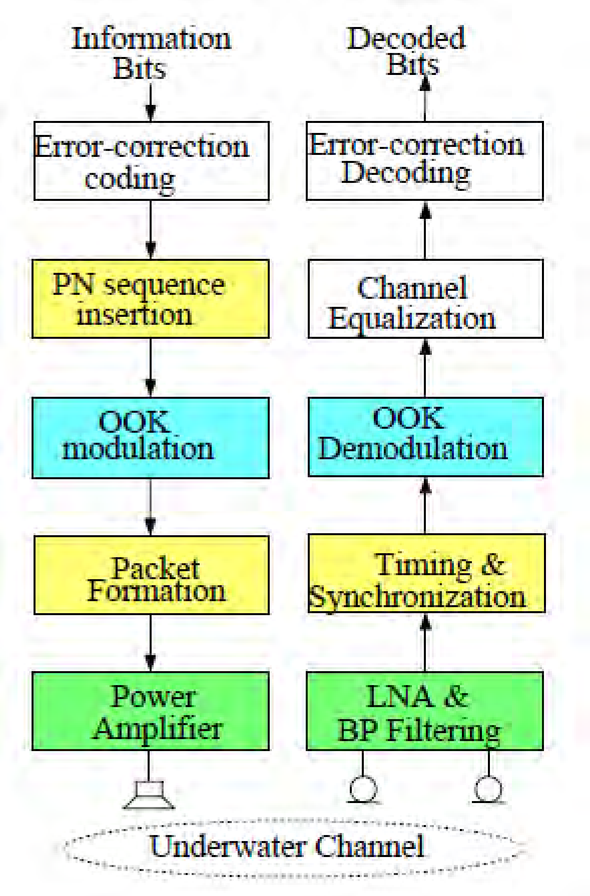

Figure 6.2 Acoustic Transceiver Block Diagram

The frame structure of each block of N bits transmitted data is presented in Figure 6.3, including four zones for Preamble 1, Preamble 2, Payload, and Zero-padding, respectively. In this study, two block structures were designed, each having N=250 bits at a bit rate of 5000 bps. Design #1 included $N_1 = 63$ bits preamble of the maximum length PN sequence, $N_2=0$ preamble, $N_3 = 16$ bits payload length, and $N_4 = 171$ padded zeros. Design #2 included two identical preambles $N_1 = N_2 = 64$ (a 63-bit main sequence plus a padded one), $N_3 = 15$ bits payload length that can be adjusted if needed, and $N_4 = 107$ padded zeros.

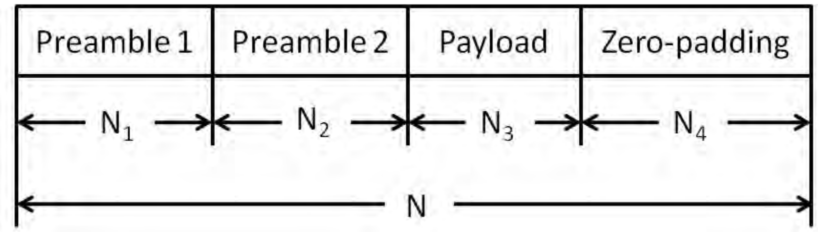

Figure 6.3 Transmitted Signal Frame Structure for Localization

The receiver applied a bandpass filter and a low-noise amplifier to remove interference from the received signals and amplify the desired signals for further data processing. Analog-to-digital convertors (ADCs) were used to convert the zero intermediate frequency (IF) signals to the digital format. A simple non-coherent rectifier was used to demodulate the OOK signal to baseband symbols. Timing and bit synchronizations were then estimated by correlating the PN sequence with the demodulated signal and peaks were detected to estimate the start indices of blocks. If strong multipaths are present, channel estimation and equalization must be used to reduce the inter-symbol interference (ISI) before bits were detected.

The transmitter hardware consisted of a TI TMS320C6713 starter board, a 12-bit DAC, a power amplifier and matching network (BII model 5000), and an acoustic projector (BTech 1201 model). The data blocks were transmitted repeatedly for localization purposes with payload bits changed block by block. The OOK modulation was implemented in the DSP, where bit 1 represented the memory bank of a pre-computed cosine wave of frequency $f_c = 125$ kHz at a sampling rate of 3 mHz, and bit 0 represented the DC voltage. The DSP board used the memory transfer method to send the modulated OOK signals to the DAC. The receiver consisted of two channels of hydrophones, analog bandpass filters, low-noise amplifiers (LNA), and ADC units. The two 12-bit ADC channels were interfaced with one C6713 board using the external memory interface (EMIF). The sampling rate at the receiver was *55* kHz to yield a bandpass sampling carrier at 15 kHz and 11 samples per bit.

Figure 6.4 shows a hardware diagram of the acoustic receiver on the DSP. When multiple DSP receivers with multiple channels are required for field deployment, for example, at both sides of a river, timing synchronization among the receivers is critical to the TDOA localization method. Several options for the timing synchronization of multiple receivers have been researched and simulated. In this study, a commercial global positioning system (GPS) timing module was selected and integrated into each DSP receiver. The GPS timing module provided the one pulse per second (1PPS) signal to the DSPs of all the receivers that are placed at different locations. Therefore, sampling and recording of the hydrophones at the receivers were synchronized by the 1PPS reference.

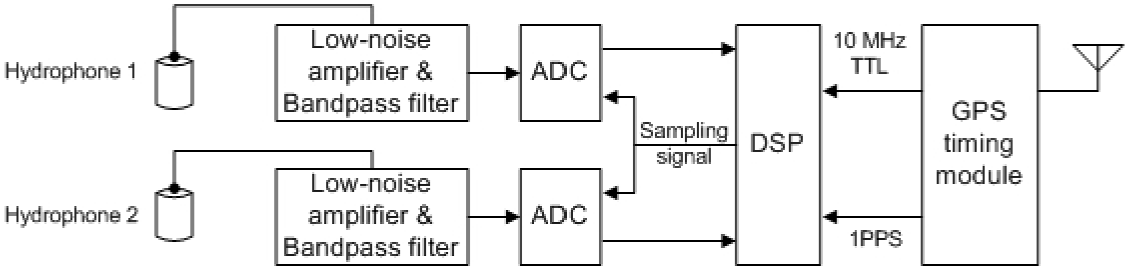

Figure 6.4 Receiver Structure Based on DSP

Figure 6.5 shows the hardware setup for timing synchronization. The 1 PPS signal from the GPS timing module triggers the DSP as an external interrupt and the DSP then generates 55 kHz sampling signals for the ADCs. This method can accommodate the difference of the sampling frequencies between the transmitter and multiple receivers, which is significant in this application since the 5 – 10 PPM (part per million) frequency accuracy of the ovenized piezo-electrical crystal oscillators used on the DSP boards results in a drift of one to two samples every two seconds of the transmitted signals. This accuracy is not sufficient for accurate long-term timing estimation. Therefore, a calibration procedure to reduce the drift was considered at the transmitter side. Similar efforts were made at the receiver side to synchronize the data inputs and recording. With the aid of GPS, the synchronization accuracy was improved to 0.5 PPM from the 10 PPM accuracy without GPS modules.

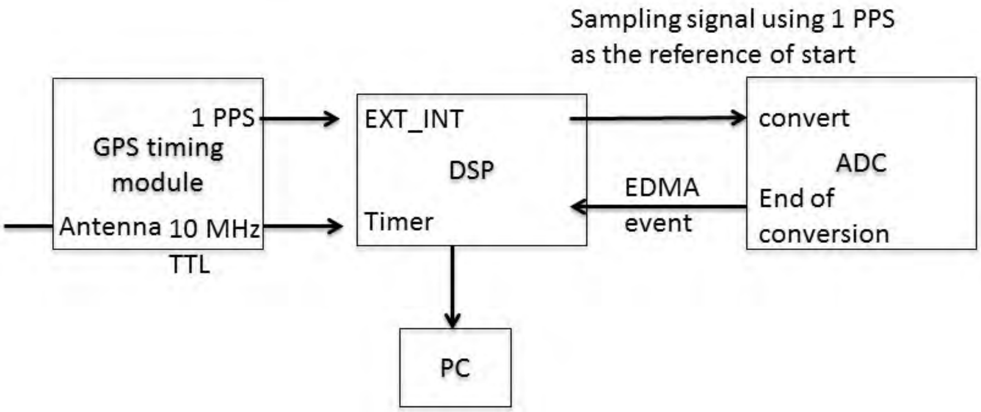

Figure 6.5 GPS Interfaces with DSP

By measuring the time indices between the correlated peaks from four or more hydrophones, the TDOAs between the hydrophones can be obtained. With the TDOA information, the localization algorithms such as Cooperative Localization in (Patwari et al. 2005, Tan et al. 2011) can be implemented effectively. To this end, the propagation speed of acoustic wave in water must be determined, which changes with water temperature and can be estimated from the following empirical formula (Bilaniu and Wang 1993)

$$c = 1.403 \times 10^3 + 5.038T - 5.805 \times 10^{-2}T^2 + 3.320 \times 10^{-4}T^3 - 1.445 \times 10^{-6}T^4 + 2.994 \times 10^{-9}T^5 \tag{6.1}$$

where T and c represent the water temperature in Celsius and the speed of sound in water in m/s, respectively. As an example, when T=5 °C, $c = 1426$ m/s. This speed corresponds to a distance resolution of *0.2852* m/bit. By taking *11* samples per bit, the range resolution becomes *0.026* m/sample.

6.2 TDOA Estimation in Laboratory Tests

Indoor laboratory tests were conducted by wiring the transmitter signals directly to receiver inputs without the power and low noise amplifiers. The hardware is shown in Figure 6.6. The tests identified a timing drift of the transmitter because the ovenized crystal oscillator (OCXO) on the TI DSP board had an accuracy of 5-10 PPM, which caused the drift measured in the tests. The timing drift was then corrected by adjusting the length of the last transmitted bit of each block through transmitter C++ programs. The resulting timing drift after the calibration was reduced to 1 sample in 20 seconds.

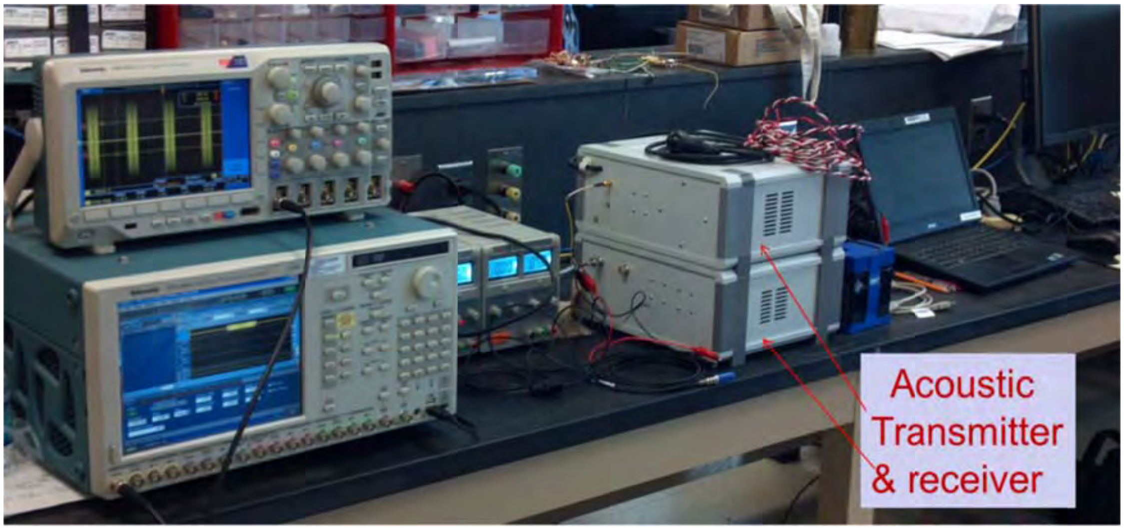

(a) Indoor Test Setup

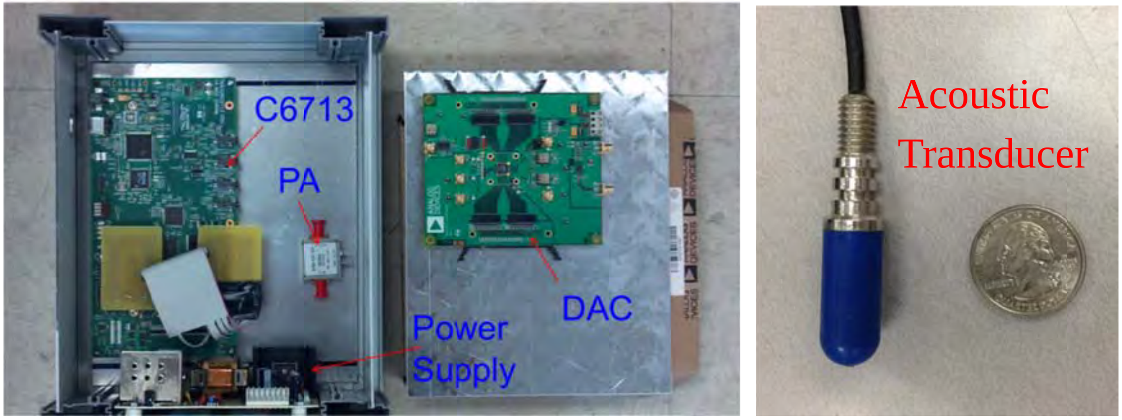

(b) Inside the Transmitter Box (c) The Acoustic Transducer

Figure 6.6 Transmitter and Receiver Hardware

6.3 TDOA Estimation in Field Tests

The underwater acoustic localization system has been tested in swimming pool, pond, lake, and river during the last seven months. A total of ten experiments were conducted in different conditions such as range, environment, and water conditions (i.e. temperature and flow speed). Four field tests are discussed below. They demonstrated the effectiveness of the acoustic communication system. When the Tx-Rx distance varied from 2 to 90 m, the TDOA algorithm achieved a localization error of 0.3 m (Zheng et al. 2013).

6.3.1 Test 1

The underwater acoustic localization experiments using one receiver with two hydrophones were conducted in a pond at the Lions Club Park, Rolla, MO, in March 2013. The pond and its wooden deck are shown in Figure 6.7a. The relative locations of the projector and hydrophones are shown in Figure 6.7b. The transmission distance ranged from *2* to *30* m. The signal reception was pretty good with a signal-to-noise ratio (SNR) of over 20 dB.

(a) Experimental Site near the Deck

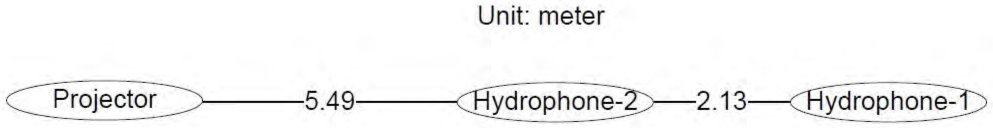

(b) Relative Locations of the Projector and Hydrophones with Distance in Meter

Figure 6.7 Experimental Setup for Field Test 1

The C6713 DSP at the receiver processed the 2-channel signals simultaneously and calculated the distance difference and bit error rate (BER). Typical received passband carrier signals at the two hydrophones are presented in Figure 6.8. They clearly indicated two major propagation paths. However, the first arrival was always stronger than the second. Therefore, by a simple cross-correlation between the received signal and the PN sequence, the first-arrival peak was detected from each channel and its time index was recorded. The TDOA between the two channels suggested that the mean distance between the two hydrophones was approximately *2.18* m with multiple runs. The estimation error between the acoustic measurement and the ground truth was *0.05* m.

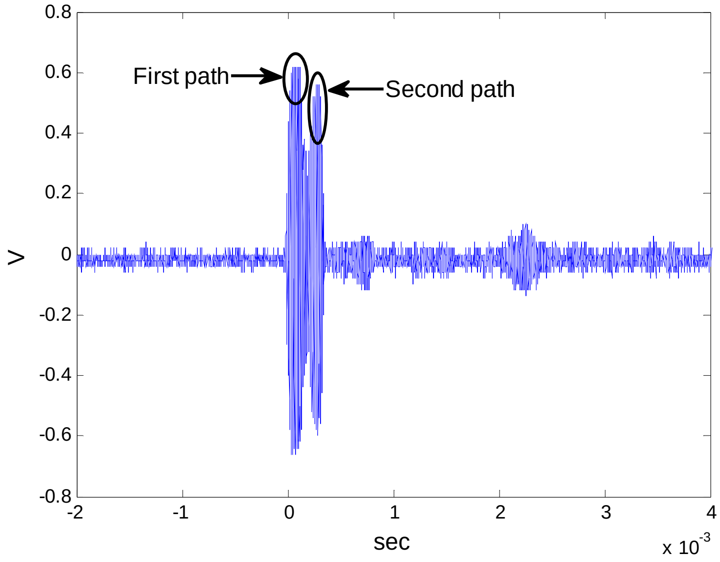

(a) Receiver 1

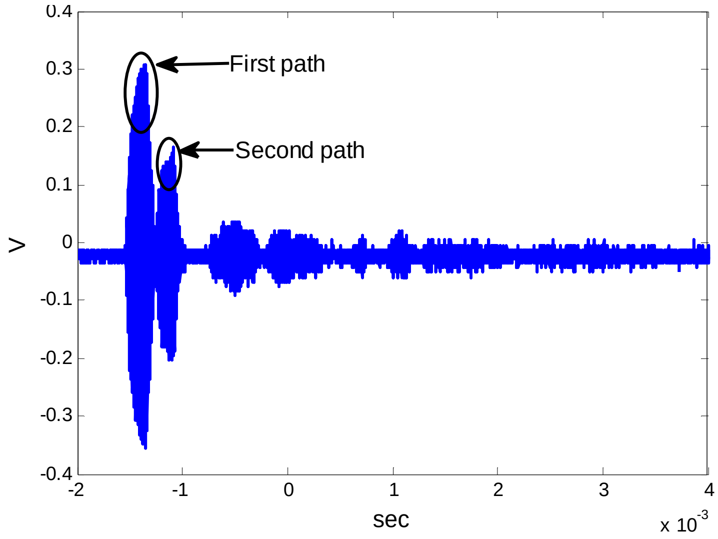

(b) Receiver 2

Figure 6.8 Received Passband Signals at Two Hydrophones

6.3.2 Test 2

Three field tests were conducted in May 2013 at a small wooden bridge on the Pine Lake, near Pine Forest Drive, Rolla, MO. The area and the lake are shown in Figure 6.9, where the wooden bridge runs across the island and the south side of the lake. Two receivers, each with two hydrophones, were placed at two ends of the wooden bridge, respectively. The two channels of the first receiver (Rx1) were designated as Ch1 and Ch2, and the other two channels of the second receiver (Rx2) as Ch3 and Ch4.

(a) Experimental Site at Pine Lake, Rolla, MO

(b) Locations of Transmitters and Receivers

Figure 6.9 Setup for Field Test 2

Table 6.1 True Locations of Tx and Rx in Field Test 2 at Pine Lake

Point	**(x,y) Coordinates (m)**	**Tx/Rx**	**Transducer Type**
1	(-13.054, 11.194)	Rx1 Ch1	BII Hydrophone
2	(-17.214, -9.767)	Rx1 Ch2	BII Hydrophone
3	(-2.011, 12.300)	Rx2 Ch3	BTech Transducer
4	(-3.694, -13.491)	Rx2 Ch4	BTech Transducer
5	(-8.155, 3.615)	Tx	BTech Transducer
6	(-6.915, 2.258)	Tx	BTech Transducer
7	(-8.403, 2.466)	Tx	BTech Transducer

The relative locations of the projector (transmitter) and hydrophones (receivers) are marked as *1 - 7* in Figure 6.9, whose true locations were measured by a total station and presented in Table 6.1. The transmitter was located at Point *5* to Point 7 at any time. Overall, 16 trials were conducted, each collecting data over a period of 2 to 5 min.

The signals received at all channels were very noisy and contained the effect of long and strong multiple paths. The multi-path delay spread was as large as *40 - 50* bits long. The TDOA was estimated by correlating the received pass-band signals with the upsampled 63-bit PN sequence and detecting the correlation peak. The sample index corresponding to the peak was considered the first arrival of the PN sequence as shown in Figure 6.10. The two examples show the frame start index detected in Trial 16. Since a simple rectifier was used for demodulation, the correlation output as shown in red curve is very spiky. Therefore, a left sliding window and a right sliding window were used to average the correlation output. The averaged correlation curves were proportional to the energy of the signal in the windows, as shown in green and blue curves in Figure 6.10. By comparing the amplitudes of the two curves, the energy of the OOK PN sequence can be detected, within which the peak index was searched and the index corresponding to the maximum peak was taken as the frame start index. The detected indices are used to compute the TDOA for locating the transmitter.

Three challenges were encountered in these experiments. First, two peaks may be present in each acquisition of the two channels per receiver, as shown in Figure 6.10. Second, multipath echoes may cause large estimation errors because later arrivals may be stronger than the first arrival, as shown in Figure 6.11. Third, sampling frequencies between the transmitter and receivers may drift due to the loss of GPS synchronization. For example, Figure 6.12 shows that Ch3 and Ch4 experienced a significant index drift that was attributed to the inaccurate 1PPS signals. Sometimes Ch1 had no peaks due to low SNR.

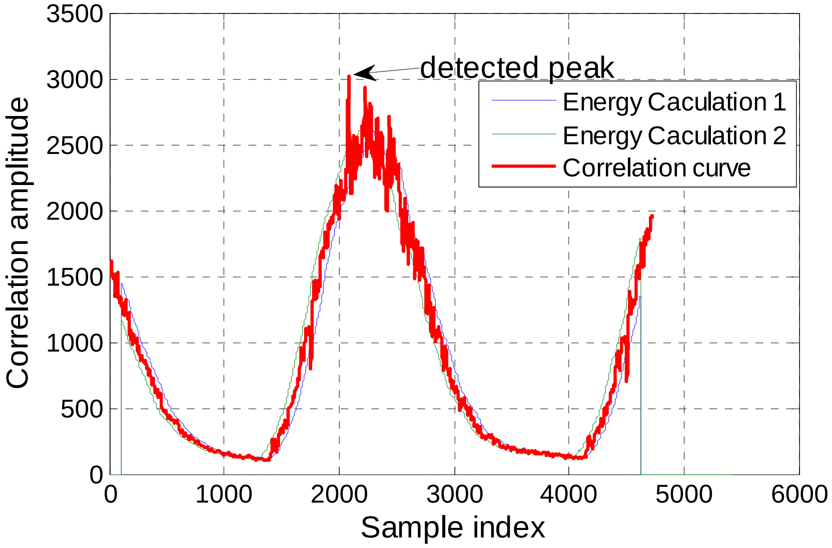

(a) Ch 1(Rx1): Detected Index 2084

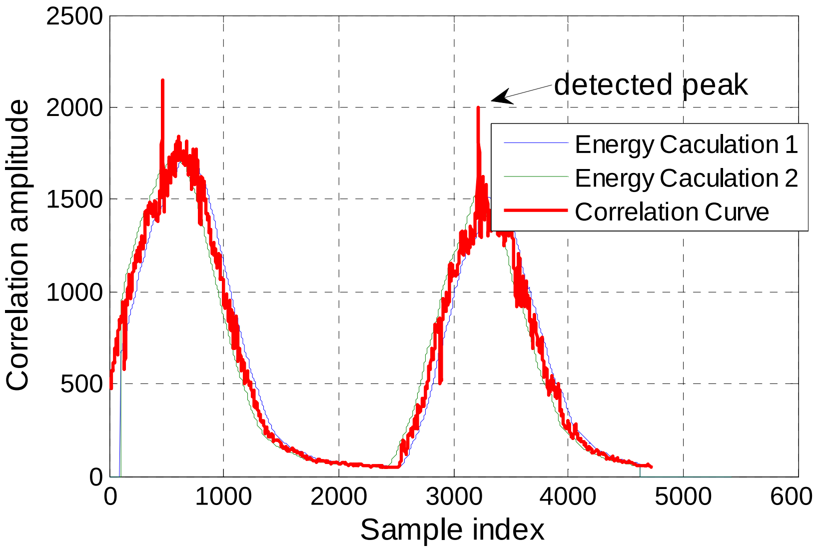

(b) Ch 3 (Rx2): Detected Index 3218

Figure 6.10 Successful Frame Start Index Detection: the First Second in Trial 16

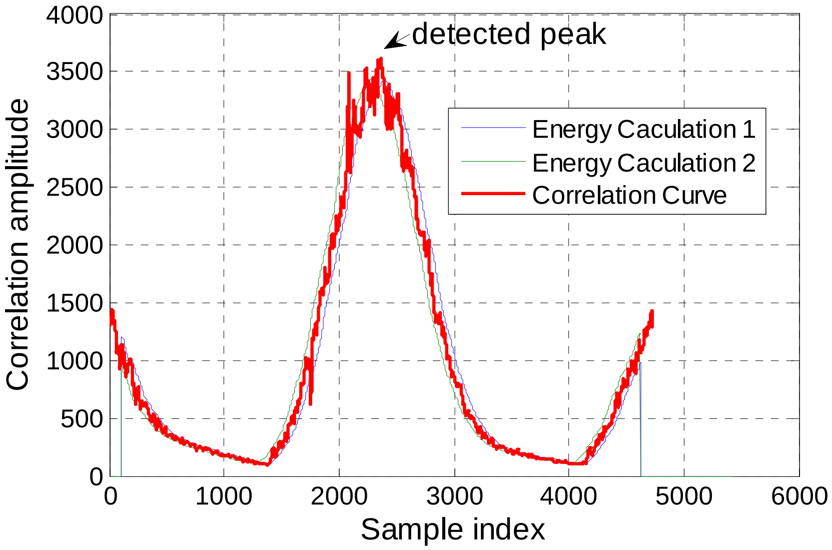

(a) Ch 1 (Rx1) in 6th Second, Detected Index 2343

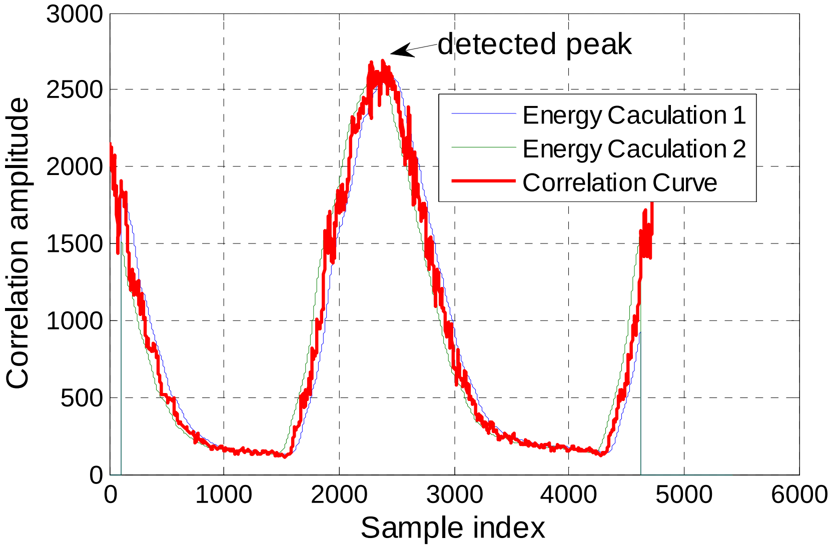

(b) Ch 2 (Rx1) in 12th Second, Detected Index 2385

Figure 6.11 Unsuccessful Frame Start Index Detection: Trial 16

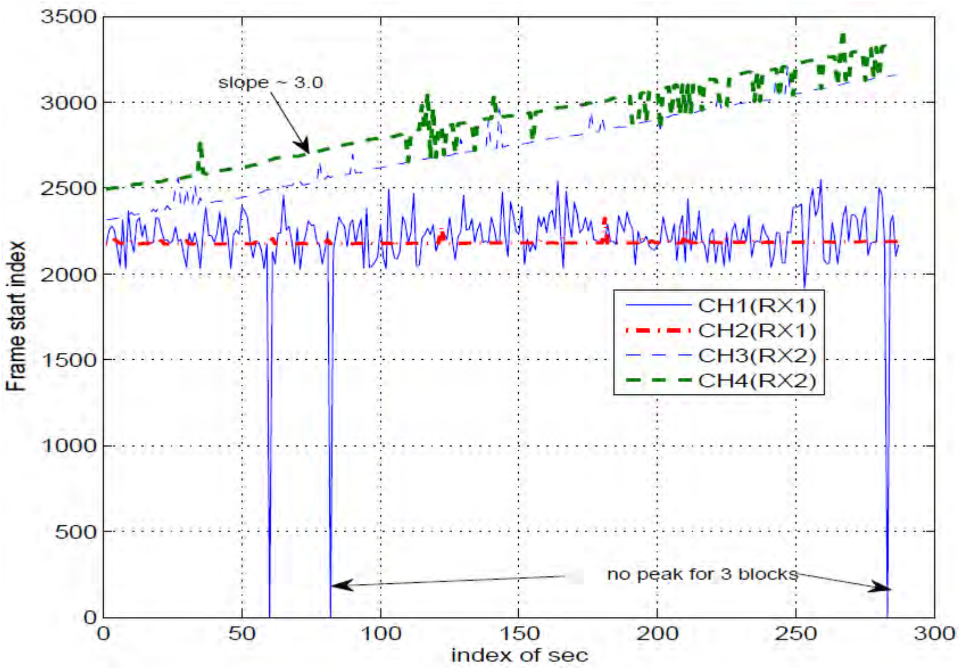

Figure 6.12 Detection of Frame Start Index in Trial 12

The following observations can be made from Figures 6.10 – 6.12:

- The estimated frame start indices in receiver 1 are generally larger than the true indices mainly due to strong multipath echoes that added favorably to a later arrival time.
- When the peak detection includes significant errors, the bit detection experiences large BER.

- Satisfactory BER performance corresponds to accurate peak detection. However, accurate peak detection may not guarantee the satisfactory BER performance.

6.3.3 Test 3

After the frequency drift at the transmitter side has been removed, the third field test was conducted in July, 2013, in Roubidoux Creek, Waynesville, MO. The surveyed locations of the transmitter and the receivers are listed in Table 6.2. The locations of the transducers and the area map are shown in Figure 6.13. All transmitter and receivers used BTech transducers.

Table 6.2 True Locations of Tx and Rx in Field Test 3 at Roubidoux Creek Bridge

Tx/Rx	**(x,y) Coordinates (m)**	**Distance to Tx (m)**
Rx1 Ch1 (point 2)	(-6.167, -26.312)	6.717
Rx1 Ch2 (point 1)	(-11.859, -35.728)	6.132
Rx2 Ch3 (point 3)	(0.530, -29.656)	7.665
Rx2 Ch4 (point 4)	(-3.028, -40.967)	8.609
Tx (point 5)	(-6.355, -33.026)	0

Figure 6.13 Experimental Site for Field Test 3 at I-44 Roubidoux Creek Bridge

The receiver passband signals in ten trials were recorded, each lasting for 1 to 2 min. Their SNR values are higher than those recorded in Field Test 2 but lower than those in Field Test 1. Typical peak detection performance is demonstrated in Figure 6.14, where the frame start index was all detected except for the first five blocks due to data recording time needed in the hardware setup. A few intermediate blocks also led to wrong detection due to strong interference or low SNR. The BER of the unequalized PN sequence is shown in Figure 6.14. To improve the robustness of the average TDOA estimation, the blocks whose raw BER values were under a certain threshold level, say 0.2 or 0.3, were selected to calculate the TDOA and distance difference between channels while the blocks with high BER were removed from the average. When the water temperature is T=29 °C, the estimated range differences between the channels are listed in Table 6.3.

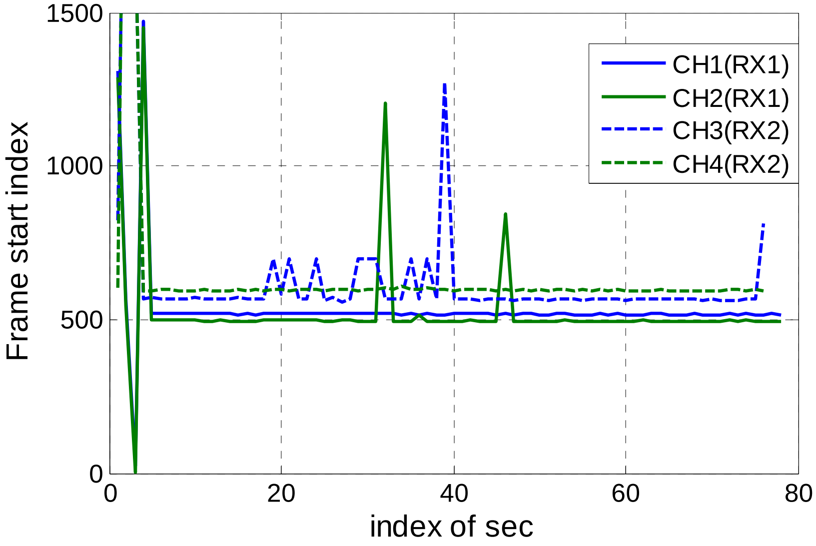

(a) Detection of Frame Start Index from Rx1

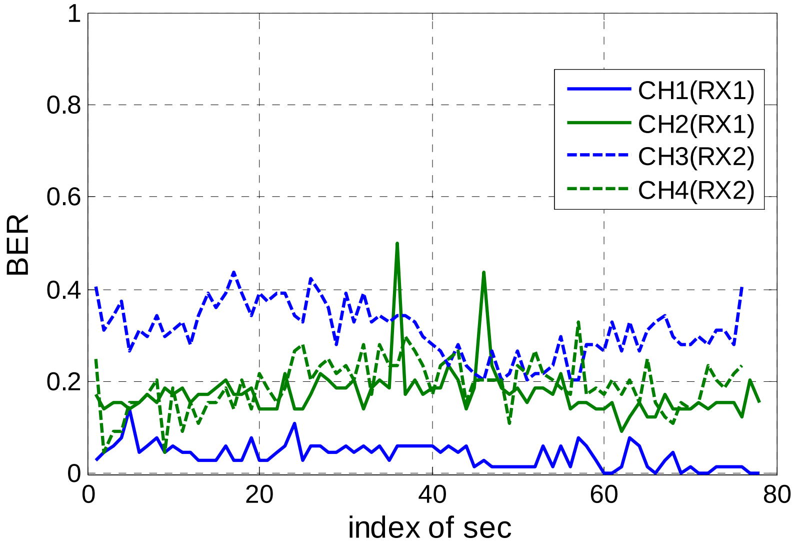

(b) Raw BER of Uncoded PN Sequences

Figure 6.14 Performance of Trial 10, Field Test 3

Table 6.3 Measured Rx-Tx Range Differences in Field Test 3

Rx-Tx Range	**Ground Truth**	**Measured Mean**	**Standard Deviation**
Ch1-Tx and Ch2-Tx	0.585 m	0.618 m	2.71×10^{-2} m
Ch1-Tx and Ch3-Tx	-0.949 m	-1.305 m	4.36×10^{-2} m
Ch3-Tx and Ch4-Tx	-0.944 m	-0.824 m	8.06×10^{-2} m

Let the estimated Tx coordinates be $\hat{\mathbf{x}}$, the true coordinates of Tx, Ch1, Ch2, Ch3, and Ch4 be $\mathbf{x}$, $\mathbf{x}_{\mathrm{ch1}}$, $\mathbf{x}_{\mathrm{ch2}}$, $\mathbf{x}_{\mathrm{ch3}}$, and $\mathbf{x}_{\mathrm{ch4}}$, respectively, the distance difference between Ch1-Tx and Ch2-Tx be d_{12}, and the distance difference between Ch3-Tx and Ch4-Tx is d_{34}. Then, the following two equations can be formulated:

$$\begin{cases} \left\|\hat{\mathbf{x}}-\mathbf{x}_{ch1}\right\|_2 - \left\|\hat{\mathbf{x}}-\mathbf{x}_{ch2}\right\|_2 = d_{12} \\ \left\|\hat{\mathbf{x}}-\mathbf{x}_{ch3}\right\|_2 - \left\|\hat{\mathbf{x}}-\mathbf{x}_{ch4}\right\|_2 = d_{34} \end{cases}, \tag{6.2}$$

where $\left\|\bullet\right\|_2$ is the l_2-norm. With $\mathbf{x}_{\mathrm{ch1}}$, $\mathbf{x}_{\mathrm{ch2}}$, $\mathbf{x}_{\mathrm{ch3}}$, $\mathbf{x}_{\mathrm{ch4}}$, d_{12}, and d_{34} given in Tables 6.3 and 6.4, Eq. (6.2) leads to $\hat{\mathbf{x}}=\left(-6.120,-33.200\right)\mathrm{m}$. The l_2-norm error of the localization of the Tx is $\left\|\hat{\mathbf{x}}-\mathbf{x}\right\|_2 = 0.292\,\mathrm{m}$.

6.3.4 Test 4

After the frequency drift at the transmitter side has been removed, the fourth field test was conducted on September 4, 2013, in the Gasconade River, Vienna, MO. The locations of the transducers are shown in Figure 6.15. The surveyed locations of the transmitter and the receivers are listed in Table 6.5.

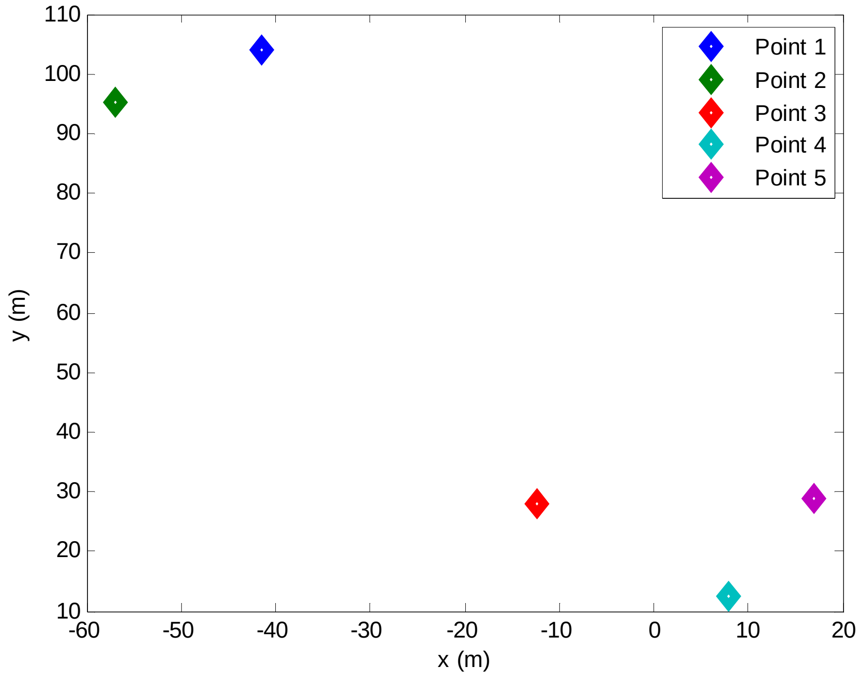

Figure 6.15 Transducer Locations in the Gasconade River for Field Test 4

Table 6.4 True Locations of Tx and Rx in Field Test 3 in the Gasconade River

Tx/Rx	(x,y) Coordinates (m)	Distance to Tx (m)
Rx1 Ch1 (point 2)	(-56.879, 95.262)	80.699
Rx1 Ch2 (point 1)	(-41.441, 104.122)	81.518
Rx2 Ch3 (point 4)	(7.884, 12.453)	25.477
Rx2 Ch4 (point 5)	(17.023, 28.974)	29.349
Tx (point 3)	(-12.320, 27.987)	0

Table 6.5 Measured Rx-Tx Range Differences in Field Test 4

Rx-Tx Range Difference	Ground Truth	Measured Mean
Ch1-Tx and Ch3-Tx	55.224 m	55.284 m
Ch3-Tx and Ch4-Tx	-3.871 m	-3.795 m

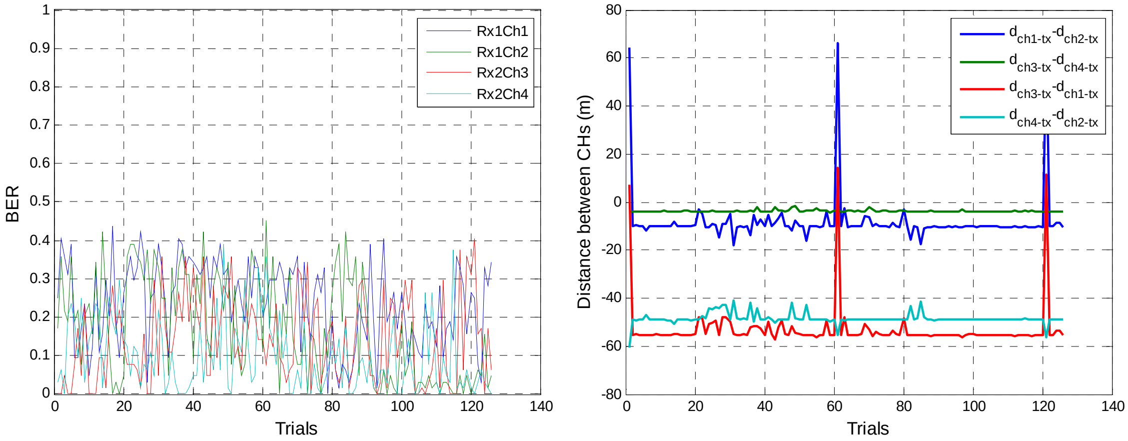

(a) Raw BER of Uncoded PN Sequence (b) Rx-Tx Distance Difference

Figure 6.16 The Received Data at 13:30 on September 4, 2013, for Field Test 4

With the Ch1 , Ch3, and Ch4 coordinates, the range difference between Ch1-Tx and Ch3-Tx, and the range difference between Ch3-Tx and Ch4-Tx, and the two hyperbolic Eq. (6.2), the Tx coordinates was estimated to be (-2.015, 28.011) m. Compared with the survey data, the average Euclidean error of the localization of TX is 0.296 m.

6.4 Summary and Observations

In this section, an underwater acoustic localization system for bridge scour monitoring has been designed and tested both in laboratory and field conditions. The system hardware included GPS receivers for timing synchronization, ADC and DAC for data reception and transmission, and TI DSP for digital processing. The main system software included the TDOA algorithm that was developed to locate the acoustic transmitter. To demonstrate the effectiveness of the localization system, ten field tests have been conducted in swimming pools, ponds, lakes, and rivers. Several challenges in achieving accurate timing and TDOA estimation have been addressed in our hardware and software designs. In the event of strong multipath acoustic channels, robust algorithms for PN sequence correlation peak detection can be further improved. Without involving data fusion and optimization algorithms, the field test results have demonstrated that the underwater acoustic localization system achieved a high accuracy of 0.3 m in 2 – 90 m.

7 TECHNOLOGY READINESS AND RECOMMENDATIONS

In this section, the readiness of various smart rock technologies is briefly discussed and recommendations for their field implementation studies are presented. The technology readiness and recommendations are organized in the order of passive smart rocks, active smart rocks with magneto-inductive communications, semi-active smart rocks, and active smart rocks with acoustic communication.

7.1 Technology Readiness for Implementation Study

Common to all types of smart rock technologies is the design of rocks or concrete encasements. To date, the concrete encasements were designed based on the density requirement to ensure they can remain at the bottom of river without being washed away in strong water current. The ad-hoc design for smart rocks was proven effective during the August 7, 2013, flood event with a return period of over 100 years in Rolla, MO. The so-designed smart rocks were demonstrated to consistently roll to the deepest area of scour with multiple laboratory tests. However, the size and density of concrete encasements have not been optimized based on the bridge and river geometries, hydraulic environments, and riverbed profile and materials.

7.1.1 Passive Smart Rocks

Critical to the localization of smart rocks by triangulation, the intensity-distance relation of a passive smart rock with an embedded permanent magnet was significantly affected by the polarization of the magnet. This effect can be effectively removed from a unique mechanism design to make the magnet be always oriented with the Earth magnetic field. It is practically challenging to separate the effects of individual magnets in a group.

A measurement distance of over 50 m has been demonstrated in field condition. In laboratory tests, 2 cm accuracy was achieved for scour depth measurement of approximately 18 cm. The magnetometer can be set up for measurement in less than 10 minutes in field condition. The cost for one cylinder magnet (102 mm in diameter and 51 mm in height) embedded in each smart rock and deployed at bridge sites is approximately $300.

Overall, a single or a few passive smart rocks with Earth magnetic field oriented magnets are recommended as a cost-effective solution for bridge scour monitoring in real time, which gives the maximum scour depth only. They are ready for implementation studies.

7.1.2 Active Smart Rocks with Magneto-inductive Communication

The electro-mechanical modules in active smart rocks were demonstrated to be waterproofed with no leakage even during the August 7, 2013, flood event. They successfully provided battery-powered magneto-inductive communication, whenever needed, for individual rocks and transmitted sensor data with low power.

Initial test modules installed at the I-44 Bridge on July 25, 2012, were still responding on August 27, 2013. Therefore, the rock was underwater for over a year and survived all the weather changes.

A measurement distance of over 20 m in field condition was tested. A distance and localization error of less than 0.5 m can be achieved based on numerical simulations. The cost for electro-mechanical modules in each active smart rock is approximately $100 plus over $300 for a pressure sensor. Additional cost for electronic components at the base station may be $800-$1,000. The total material cost for each smart rock transmission and receiving is approximately $200.

Overall, a network of 10 to 20 active smart rocks is recommended as a comprehensive solution for bridge scour monitoring in real time, which gives water depth and tilt/head/rock data at the location of individual rocks in addition to the maximum scour depth. They will be ready for implementation studies after the electro-mechanical modules and localization algorithm have been further characterized and validated in field conditions.

7.1.3 Semi-active Smart Rocks

In addition to the advantages with passive smart rocks and active smart rocks with magneto-inductive communication, semi-active smart rocks can provide individual rock positions, increase the dynamic range of measurement or measurement distance, enhance the quality of data, and reduce the distance and location estimation errors. The material cost for one semi-active smart rock is approximately $400.

Overall, a few semi-active smart rocks with flipping magnets are recommended as the most reliable solution for bridge scour monitoring in real time. They will be ready for implementation studies after they have been characterized for their performance indices in laboratory and field conditions.

7.1.4 Active Smart Rocks with Acoustic Communication

The transmitter in smart rocks and receiver (hydrophones) modules have been demonstrated to be robust and functional as designed based on ten laboratory and field tests. The field test results indicated that the underwater acoustic localization system achieved a localization accuracy of 0.3 m over a measurement distance of 2 to 90 m. The cost for one transmitter and one receiver (hydrophone) is approximately $900 due to the high price of the acoustic transducers with non-recurring engineering cost. The cost of a transducer unit can be reduced to 50% if over 100 units are ordered at once.

Although the TDOA localization algorithm with acoustic communication is potentially advantageous over the RSSI with magneto-inductive communication in that the received signals are less affected by signal attenuation and measurement distance, the acoustic transmitter has not been embedded into concrete encasement for field testing and the transmitter/receiver modules have not been packaged into a system for laboratory and field tests. The potential effect of concrete encasement on the acoustic wave propagation needs to be studied. How smart rocks with multiple transmitters can help more accurately locate the rocks and then determine the scour depth in real time requires further investigation. As such, the acoustic communication system is recommended for implementation study after extensive packaging and system integration tests have been completed.

7.2 Future Studies

The current proof-of-concept study has demonstrated the feasibility of deploying various smart rocks for bridge scour monitoring in real time. Properly designed smart rocks can automatically find the deepest point in a scour hole and remotely provide the maximum scour depth estimation with other useful data such as water depth, rock orientation, and battery level. However, a pilot implementation study on smart rock technologies is still required with several select bridges distributed in the continental U.S. before the smart rock technologies can be widely applied for real-time bridge scour monitoring. The implementation study will quantify the field performance of smart rocks either by comparing the smart rocks' collected data sets with ground truths or comparing the smart rock technologies with other scour monitoring techniques, develop a design procedure for smart rocks (size and density) based on computational fluid dynamics simulations and laboratory tests, and develop user-friendly software for tracking smart rock movement at bridge sites.

Specific technical issues that are warranted for further investigation are discussed below for each of the four types of smart rock technologies. Most of the technical issues are expected to be addressed in the early part of the implementation study.

7.2.1 Passive Smart Rocks

The rock localization algorithm needs further calibrations and validations in field conditions. In particular, the Earth magnetic field varies from one place to another and its effect on the field strength of magnets must be quantified at each bridge site.

7.2.2 Active Smart Rocks with Magneto-inductive Communication

Hardware Challenges The communication distance between a smart rock and the base station needs to be extended. This can be achieved by integrating a battery powered pre-amplifier directly at the receiving antenna output connection, thus compensating potential signal degradation due to antenna detuning/loading by a long coaxial cable. Alternative receiver antennas with more turns in coil can also be evaluated and applied.

The dynamic range and resolution of on-board RSSI estimation is limited. This limitation can be lifted by using an extended version of the receiver IC that offers an analog RSSI output. To further improve the RSSI accuracy, three antennas can be integrated and arranged in an 'omnidirectional' configuration as shown in Figure 7.1. Such an extension requires updating in the mechanical design of a smart rock unit. To process data from all three channels independently, the extended version of the receiver IC can be used.

Figure 7.1 “Omnidirectional” Three-Channel Receiver Antenna for Each Smart Rock

Smart rock loop antennas can detune due to rock roll, mechanical construction, and nearby environmental conditions, resulting in change in transmitted power. For more accurate RSSI estimation, the current passing through the smart rock transmitting coil must be known. The current can be measured by adding a sensing resistor in series with the transmitting coil. At the base station, digital signal processing hardware will be integrated and implemented.

Software Challenges. The extended version of the receiver IC discussed under the hardware challenges can be used to improve the IC design stability and optimize the inter-rock communication network. The data obtained from the gyroscope sensor can be better utilized for the improvement of orientation determination.

At the base station, user-interface software will be developed and implemented. More importantly, localization algorithms will be improved by compensating antenna/channel losses. Specifically, the 3D localization mapping algorithms will be developed and implemented using Particle Swarm Optimization for the rocks mapping optimization towards a minimum error target function.

7.2.3 Semi-active Smart Rocks

The coil flipping circuitry can be optimized by including a capacitor across the resistor so that a much higher current can flow at the beginning in order to break the flipping magnet loose. It must also be scaled up for large magnets with other corresponding mechanical and electrical design updates.

7.2.4 Active Smart Rocks with Acoustic Communication

The effects of various packaging materials and structures (to embed transmitters in smart rocks) can be studied by building and testing smart rock prototypes in laboratory and field conditions. The performance of an integrated transmitter/receiver acoustic communication system can be investigated with multiple transmitters and multiple receivers as did with the magneto-inductive communication. In this case, multipath acoustic wave propagation and timing synchronization are the two technical issues to address systematically. In addition, the current hardware design on the TI DSP platform TMS320C6713 can be migrated to low-power microcontroller for rock node.

8 REFERENCES

Abdou, A. A., Shaw, A., Mason, A., Al-Shamma'a, A., Cullen, J., and Wylie, S. (2011). "Electromagnetic (EM) wave propagation for the development of an underwater wireless sensor network (WSN)." *IEEE Sensors*, 1571-1574.

Ali, K. H. M., and Karim, O. (2002). "Simulation of flow around piers." *Journal of Hydraulic Research*, 40(2), 161–174.

Anderson, N. L., Ismael, A. M. and Thitimakorn, T. (2007). "Ground-penetrating radar: a tool for monitoring bridge scour." *Environmental and Engineering Geosciences*, 12(1), 1-10.

Ansari, F. (2007). "Practical implementation of optical fiber sensors in civil structural health monitoring." *Journal of Intelligent Material Systems and Structures*, 18(8), 879-889.

Avila, C. M. C., Racin, J. A., and Davies, P. (1999). "Talk to your bridges and they will talk back - Caltrans Bridge Scour Monitoring Program." *Proceedings of ASCE Hydraulics Conference*, New York.

Awad, A., Frunzke, T., and Dressler, F. (2007). "Adaptive distance estimation and localization in WNS using RSSI measures." *10th EUROMICRO Conference on Digital System Design - Architectures, Methods and Tools*.

Bilaniu, N., and Wang, G.S.K. (1993). "Speed of sound in pure water as a function of temperature." *Journal of Acoustic Society of America*, 93(3), 1609 – 1612.

Boorstin, R. O. (1987). "Bridge collapses on the thruway: trapping vehicles." *The New York Times*, CXXXVI (47), 101–108.

Briaud, J. L., and Hunt, B. E. (2006). "Bridge scour & the structural engineer." *Structures Magazine*, 58-61.

Browne T. M. (2010). "Underwater acoustic imaging devices for portable scour monitoring." *International Conference on Scour and Erosion 2010 (ISCE-5), Scour and Erosion*, 931-940.

Butch, G. (1996). "Evaluation of scour monitoring instruments in New York." *Proceedings of 1996 ASCE North American Water and Environment Congress, Bridge Scour Symposium*, ASCE, Hydraulics Division, Anaheim, CA.

Chandrasekhar, V., Seah, W. K., Choo, Y. S., and Ee, H. V. (2006). "Localization in underwater networks - survey and challenges." *ACM International Conference on Mobile Computing and Networking (MobiCom)*, New York, NY, USA, 33–40.

Chang, W. Y., Lai, J. S., Tsai, W. F., Lee, L. C., Lin, F., and Loh, C.H. (2012). "Multi-lens pier scour monitoring and scour depth prediction." *Proceedings of the ICE Water Management*, 1-17.

Chen, G. D., Pommerenke, D., Zheng, R.Y., Huang, Y., Radchenko, A., Shinde, S., Schafer, B. P. (2012). "A new methodology for bridge scour monitoring with wireless smart rocks." *Proceedings of NDE-NDT for Highways and Bridges: Structural Materials Technology (SMT) Conference, New York, NY.*

Chen, S., Chen, Z. J., and Wang, W. (2010). "Multi-scale detection technics for local scour monitoring in river bed: case study at Sutong Bridge." *ASCE Conference on Earth and Space*, 2431-2441.

Chen, S., Sun, Y. X., and Liu, D. W. (2012). "Monitoring technique for local scour around bridge pier." *ASCE Conference on Earth and Space,* 914-919.

Chiew, Y. M. (1992). "Scour protection at bridge piers." *ASCE Journal of Hydraulic Engineering*, 118(9), 1260-1269.

Cigada, A., Ballio, F., and Inzoli, F. (2008). "Hydraulic monitoring unit." Application for International Patent, No. PCT/EP2008/059075.

Derby, N., and Olbert, S. (2009). "Cylindrical magnets and ideal solenoids." *American Journals of Physics*, 1-11.

Dionigi, M., Costanzo, A., Mastri, F., Mongiardo, M. (2012). "Magnetic resonant wireless power transfer." *Chapter 5 of Wireless Power Transfer, edited by Johnson I A.*, River Publishers, Algade, Denmark, 157-198.

Dowing, C. H., and Pierce, C. E. (1994). "Use of time domain reflectometry to detect bridge scour and monitor pier movement." *Proceedings of Symposium and Workshop on Time Domain Reflectometry in Environmental Infrastructures and Mining Applications*, Northwestern University, Evanston, IL, 579-587.

Ettema, R., Nakato, T., and Muste, M. (2006). "An illustrated guide for monitoring and protecting bridge waterways against scour." Iowa Department of Transportation, Report No. TR-515. Iowa.

Fan, W., Wang, H., Wang, C., and Chen, M. (2008). "Piezoelectric type real-time scouring monitoring sensor at the foundation of bridge pier." *World Forum on Smart Materials and Smart Structures Technology*, CRC Press.

Forde, M. C., McCann, D. M, Clark, M. R., Broughton, K. J., Fenning, P. J., and Brown, A. (1999). "Radar measurement of bridge scour." *NDT&E International*, 32, 481-492.

Fukui, J., and Otuka, M. (2002). "Development of the new inspection method on scour condition around existing bridge foundations." *First International Conference on Scour of Foundation* (ICSF-1), University Drive East, College Station, Texas.

Gorin, S. R., and Haeni, F. P. (1989). "Use of surface-geophysical methods to assess riverbed scour at bridge piers." *U.S. Geological Survey Water-Resources Investigations Rep. No. 88-4212*, Federal Highway Administration, 33.

Gulbahar, B., and Akan, O. (2012). "A communication theoretical modeling and analysis of underwater magneto-inductive wireless channels." *IEEE Transactions on Wireless Communications*, 11(9).

Hayes, D. C., and Drummond, F. E. (1995). "Use of fathometers and electrical-conductivity probes to monitor riverbed scour at bridges and piers." *Water Resource Investigations Rep. No. 94-4164*, U.S. Geological Survey, Hartford, Connecticut.

Horne, W. A. (1993). "Scour inspection using ground penetrating radar." *Proceedings of National Conference on Hydraulic Engineering*, San Francisco, 1888–1893.

Huang, L. Q., Wang, D. J., and Zhou, Z. (2007). "A new type of optical FBG-based scour monitoring sensor." *Pacific Science Review*, 9(1), 103-109.

Hunt, B. E. (2005). "Scour monitoring programs for bridge health." *Proceedings of the 6th International Bridge Engineering Conference: Reliability, Security, and Sustainability in Bridge Engineering*, Transportation Research Board, Boston, 531–536.

Hunt, B. E. (2005). "Practices for monitoring scour critical bridge." *NCHRP Report 205*, Transportation Research Board, National Research Council, National Academy Press, Washington, D. C.

Hunt. B. E. (2009). “Monitoring scour critical bridges: a synthesis of highway practice.” *NCHRP Synthesis Report 396*, Transportation Research Board, National Research Council, National Academy Press, Washington, D. C.

Jesse, T. H., and Jack, A. P. (2011). “Near real-time scour monitoring system: application to Indian River Inlet, Delaware.” *Journal of Hydraulic Engineering*, 137(9), 1037-1046.

Joan, R. C., and Paulo, J. S. C. (2003). “Fiber optic sensors for bridge monitoring.” *Journal of Bridge Engineering*, 8(6), 362-373.

Isley, II, J., Saafi, M., Jow, J., Rose, K., and Romine, P. (2007). “Sensor networks for bridge stability safety monitoring during flood induced scour.” *Structural Engineering Research Frontiers*, 1-10.

Ko, Y. Y., Lee, W. F., Chang, W. K., Mei, H. T., and Chen, C. H. (2010). “Scour evaluation of bridge foundations using vibration measurement.” *International Conference on Scour and Erosion*, 884-893.

Lagasse, P. F., Richardson, E., Schall, J., and Price, G. (1997). “Instrumentation for measuring scour at bridge piers and abutments.” *NCHRP Report 396*, Transportation Research Board, National Research Council, National Academy Press, Washington, D.C.

Lagasse, P. F., Clopper, P. E., Pagán-Ortiz, J. E., Zevenbergen, L. W., Arneson, L. A., Schall, J. D., and Girard, L. G. (2009). “Bridge scours and stream instability countermeasures: experience, selection and design guidance.” *Hydraulic Engineering Circular No. 23*, Volume I, FHWA NHI HEC-23, Department of Transportation, Federal Highway Administration, Washington, D.C.

Lagasse, P. F., Zevenbergen, L. W., Schall, J. D., and Clopper, P. E. (2001). “Bridge scour and stream instability countermeasures.” *Hydraulic Engineering Circular. Report* No. FHWA-NHI-01-003 No. 23.

Landers, M. N., and Mueller, D. S. (1996). “Evaluation of selected pier scour equations using field data.” *Journal of Transportation Research Record*, No. 1523, 186-195.

Lauth, T. J., Papanicolaou, A. N. (2008). “Experimental/feasibility study of radio frequency tracers for monitoring sediment transport and scour around bridges.” *Proceedings of the World Environmental and Water Resources Congress*, 1-10.

Lin, Y. B., Chang, K. C., Lai, J. S., and Wu, I. W. (2004). “Application of optical fiber sensors on local scour monitoring.” *IEEE Sensors*, 2, Vienna, Austria, 832–835.

Lin, Y. B., Chen, J. C., Chang, K. C., Chern, J. C., and Lai, J. S. (2005). “Real-time monitoring of local scour by using fiber Bragg grating sensors.” *Smart Materials and Structures*, 14(4), 664–670.

Lin, Y. B, Lai, J. S, Chang, K. C., and Li, L. S. (2006). “Flood scour monitoring system using fiber Bragg grating sensors.” *Smart Materials and Structures*, 15, 1950-1959.

Lin, Y. B., Lai, J. S., Chang, K. C., Chang, W. Y., Lee, F. Z., and Tan, Y. C. (2010). “Using MEMS sensors in the bridge scour monitoring system.” *Journal of the Chinese Institute of Engineers*, 33(1), 25-35.

Li, H. N., Li, D. S., and Song, G. B. (2004). “Recent applications of fiber optic sensors to health monitoring in civil engineering.” *Engineering Structure*, 26, 1647-1657.

Lu, D., and Cai, C. S. (2010). “Bridge scour: prediction, modeling, monitoring and countermeasures - review.” *Practice Periodical on Structural Design and Construction*, 15(2), 125-134.

Lu, J. Y., Hong, J. H., Su, C. C., Wang, C. Y., and Lai, J. S. (2008). “Field measurements and simulation of bridge scour depth variation during floods.” *Journal of Hydraulic Engineering*, 134(6), 810–821.

Lueker, M., Marr, J., Ellis, C., Hendrickson, A., and Winsted, V. (2010). “Bridge scour monitoring technologies: development of evaluation and selection protocols for application on river bridges in Minnesota.” *Proceedings of* the *International Conference on Scour and Erosion*, 949-957.

Manzoni, S., Grotti, G., Cigada, A., Inzoli, F., and Ballio, F. (2010). “Monitoring bridge scour by Bragg grating array.” *International Conference on Scour and Erosion (ICSE-5), Scour and Erosion*, 941-948.

Mason, R. R., and Shepard, D. M. (1994). “Field performance of an acoustic scour-depth monitoring system.” *Fundamentals and Advancements in Hydraulic Measurements and Experimentation*, New York, 366–375.

Measures, R. (2001). “Structural monitoring with fiber optic technology.” Academic, London.

Melville, B. W., Ettma, R., and Jain, S. C. (1989). “Measurement of bridge scour.” *Bridge Scour Symposium*, Turner-Fairbank Highway Research Center, Federal Highway Administration and Subcommittee of Sedimentation, OWDC, USGS, 183-194.

Millard, S. G., Bungey, J. H., Thomas, C., Soutsos, M. N., Shaw, M. R., and Patterson, A. (1998). “Assessing bridge pier scour by radar.” *NDT&E International*, 31(4), 251–258.

Ministry of Works and Development (1979). “Code of practice for the design of bridge waterways.” Civil Division Publication CDP 705/C, Ministry of Works and Development, Wellington, New Zealand.

Mueller, D. S., and Landers, M. N. (1999). “Portable instrumentation for real-time measurement of scour at bridges.” *Federal Highway Administration Report* No. FHWA-RD-99-085. McLean, VA.

Mueller, D. S., and Wagner, C. R. (2002). “Field observations and evaluations of streambed scour at bridges.” *Federal Highway Administration Report* No. FHWA-RD-01-041, Washington, D. C..

Nassif, H., Ertekin, A. O., and Davis, J. (2002). *Evaluation of Bridge Scour Monitoring Methods*, FHWA-NJ-2003-009, Hydraulic Engineering Circular, Federal Highway Administration, Washington, D. C.

NTSB (1998). “Collapse of New York Thruway (I-90) Bridge over the Schoharie Creek, near Amsterdam, New York, April 5, 1987.” *Highway Accident Report*: NTSB/HAR-88/02, National Transportation Safety Board, Washington, D.C.

Okoshi, M., and Fukui, J. (2001). “Present of investigation technique for scouring.” *The Foundation Engineering and Equipment*, 29(9), 19-21.

Park, I., Lee, J., and Cho, W. (2004). “Assessment of bridge scour and riverbed variation by ground penetrating radar.” *Proceedings of the 10th International Conference on Ground Penetrating Radar*, GPR 2004, Delft, The Netherlands, 411–414.

Patwari, N., Ash, J. N., Kyperountas, S., Hero, A. O., Moses, R. L., and Correal, N. S. (2005). "Locating the nodes: cooperative localization in wireless sensor networks." *IEEE Signal Process*ing *Magazine*, 22(4), 54–69.

Pu, C. C., Pu, C. H., Lee, H. J. (2011). "Indoor location tracking using received signal strength indicator." *Chapter 11 of Emerging Communications for Wireless Sensor Networks*, Edited by Foerster, A., and Foerster, A., ISBN 978-953-307-082-7, InTech (open access book).

Radchenko, A., Pommerenke, D., Chen, G. D., Maheshwari, P., Shinde, S., Pilla, V., and Zheng, Y. R. (2013). "Real-time bridge scour monitoring with magneto inductive field coupling." *Proceedings of Sensors and Smart Structures Technologies for Civil, Mechanical, and Aerospace Systems, SPIE 2013 Conference*, San Diego, CA.

Richardson, E. V., and Davis, S. R. (2001). "Evaluating scour at bridges." *Hydraulic Engineering Circular 18, 5th Edition*, FHWA NHI 01-001, Federal Highway Administration, U.S. Department of Transportation, Washington, D. C.

Salaheldin, T. M., Imran, J., and Chaudhry, M. H. (2004). "Numerical modeling of three-dimensional flow field around circular piers." *Journal of Hydraulic Engineering*, 130(2), 91–100.

Schall, J. D., Price, G. R., Fisher, G. A., Lagasse, P. F., and Richardson, E. V. (1997a). "Sonar scour monitor – installation, operation and fabrication manual." *NCHRP Report 397A*, Transportation Research Board, National Research Council, National Academy Press, Washington, D.C.

Schall, J. D., Price, G. R., Fisher, G. A., Lagasse, P. F., and Richardson, E. V. (1997b). "Magnetic sliding collar scour monitor – installation, operation and fabrication manual." *NCHRP Report 397B*, Transportation Research Board, National Research Council, National Academy Press, Washington, D.C.

Schall, J. D., and Price, G. R. (2004). "Portable scour monitoring equipment." *NCHRP Report 515*, Transportation Research Board, National Research Council, National Academy Press, Washington, D.C.

Shin, J. H., and Park, H. (2010). "Development and application of a 3-dimensional scour monitoring system for sea-crossing bridge piers." *International Journal of Offshore Polar Engineering*, 20(4), 292-297.

Stojanovic, M., and Preisig, J. (2009). "Underwater acoustic communication channels: propagation models and statistical characterization," *IEEE Communication Magazine*, 47(1), 84–89.

Sun, Z., and Akyildiz, I. (2009). "Underground wireless communication using magnetic induction." *Proceedings of IEEE Communications Society*.

Tan, H., Diamant, R., Seah, W., and Waldmeyer, M. (2011). "A survey of techniques and challenges in underwater localization," *Ocean Engineering*, 38(14–15), 1663–1676.

Tao, J. L., Yu, X. B., and Yu, X. (2013). "Real-time TDR field bridge scour monitoring system." *Proceedings of ASCE Structure Congress*, 2996-3009.

Tumanski, S. (2006). "Induction coil sensors – a review." *Measurement Science and Technology*, 18, R31-R46.

Wang, C. Y, Wang, H. L., and Ho, C. C. (2012). "A piezoelectric film type scour monitoring system for bridge pier." *Advances in Structural Engineering*, 15(6), 897.

Webb, D. J., Anderson, N. L., Newton, T., and Cardimona, S. (2000). "Bridge scour: application of ground penetration radar." *Federal Highway Administration and Missouri Department of Transportation Special Publication*,1-19.

Xiong, W., Cai, C. S., and Kong, X. (2012). "Instrumentation design for bridge scour monitoring using fiber Bragg grating sensors." *Applied Optics*, 51(5), 547-557.

Yankielun, N. E., and Zabilansky, L. (1999). "Laboratory investigation of time domain reflectometry system for monitoring bridge scour." *Journal of Hydraulic Engineering*, 125(12), 1279–1284.

Yao, C., Darby, C. B., Yu, O. Y., Hurlebaus, S., Chang, K. A., Price, J., Hunt, B., and Briaud, J. L. (2010). "Motion sensors for scour monitoring: laboratory experiment with a shallow foundation." *GeoFlorida: Advances in Analysis, Modeling and Design*, 970-979.

Yu, X., and Zabilansky, L. J. (2006). "Time domain reflectometry for automatic bridge scour monitoring." *Geotechnical Special Publication*, 149, 152–159.

Yu, X. B., and Yu, X. (2007). "Algorithm for time domain reflectometry bridge scour measurement system." *Proceedings of the 7th International Symposium on Field Measurements in Geomechanics*, FMGM 2007, Boston, 1–10.

Yu, X. B., and Yu, X. (2009). "Time domain refectometry automatic bridge scour measurement system: principles and potentials." *Structural Health Monitoring*, 8(6), 463-476.

Yu, X. B., and Yu, X. (2010). "Laboratory evaluation of time-domain reflectometry for bridge scour measurement: comparison with the ultrasonic method." *Advances in Civil Engineering*.

Yu, X. B., and Yu, X. (2011). "Development and evaluation of an automation algorithm for a time-domain reflectometry bridge scour monitoring system." *Canadian Geotechnique Journal*, 48(1), 26-35.

Yu, X. B., and Yu, X. (2011). "Assessment of an automation algorithm for TDR bridge scour monitoring system.", *Advances in Structural Engineering*, 14(1), 13-24.

Yu, X. B., Zhang, B., Tao, J., and Yu, X. (2013). "A new time domain reflectometry bridge scour sensor." *Structural Health Monitoring*, 12(2), 99-113.

Yusof, M., and Kabir, S. (2011). "Underwater communication system: a review." *Progress in Electromagnetic Research Symposium Proceedings*, Morocco.

Zarafshan,,A., Iranmanesh, A., and Ansari, F. (2012). "Vibration-based method and sensor for monitoring of bridge scour." *Journal of Bridge Engineering*, 17(6), 829-838.

Zheng, Y. R., Yang, Z., Hao, J., and Han, P. (2013). "Hardware implementation of underwater acoustic localization system for bridge scour monitoring." MTS/IEEE OCEANS 2013, San Diego, CA, 1-6.

Zhou,.Z., Huang, M. H., Huang, L. Q., Ou, J .P., and Chen, G. D. (2011). "An optical fiber Bragg grating sensing system for scour monitoring." *Advances in Structural Engineering*, 14(1), 67-78.